Non-aromatic building blocks for metallosupramolecular assemblies

Valentyna Slyusarchuk

A thesis submitted to Keele University for the degree of Doctor of Philosophy

Supervisor: Dr Chris Hawes

March 2023

Table of Contents

Acknowledgements

First and foremost I would like to thank my supervisor, Dr Chris Hawes, for his endless patience and guidance throughout my PhD. I am incredibly lucky to have had a supervisor who was both an excellent mentor and a great friend, who has shown me the kind of academic I aspire to be someday. Without his support during the more difficult periods of the last three years, the body of work that I am proud to present in this thesis would not have been possible. Thank you also to my co-supervisor, Dr Matthew O'Brien, who (to my knowledge) happily worked through the more challenging NMR data with me, I'm yet to bring him a spectrum that he can't crack.

Thank you to Sian, Neil, JC, Dave, Leanne and the technical staff, who have made sure everything ran smoothly throughout my PhD, even when the instruments did not make this particularly easy. Thank you also to Prof. Dr. Anna McConnell and the group and technical staff at the Christian-Albrechts-Universität zu Kiel in Germany, for all of their help with the NMR studies and for being so welcoming during my visit. I am especially grateful to the Turing Scheme for funding the month-long visit to Kiel to carry out the NMR studies, and to the School of Chemical and Physical Sciences at Keele University for funding my PhD.

Throughout the last three years, I have had the pleasure of working alongside some wonderful people, who both inspired me to be a better chemist and provided entertainment during the tougher days - particularly those in LJ1.60. Conor – it was such an honour to share the lab with a fellow Wolfe Tones fan, I think we did a good job of maintaining a strong Irish presence in Lennard-Jones. Ren – thank you for always being so supportive of me, but more importantly, so *approachable*. Your regular reminders of "You got this!" were always perfectly timed, and particularly needed in the final stretch of the three years. Jack – I've always admired your appreciation of everything here at Keele, especially the fresh country air. Laura – I am so lucky to have shared all of my three years at Keele with you, and I am so glad that you are part of so many memories I'll have of the PhD. I think I would have had a much more difficult time without you going through it with me.

Cæcilie – it is difficult to summarise all the ways in which I am grateful to you. Throughout the last three years you have been an incredible role-model to me both personally and professionally, and I am so grateful and proud to call you my friend. It has been such an honour to work alongside you and in particular to be in the final stages of our PhDs together – there is no one I would rather have shared this with. Thank you to Peter (Cambridge P-Diddy), who has taught me several valuable life lessons, such as the art of the passive-aggressive email, how *not* to squeeze grease out of a tube and how to speak proudly of my work, none of which were easy. To Nat and Sian – our weekly KPA trips were the therapy I didn't know I needed to make it through the last year of the PhD. Thank you both for your friendship and for assuring me that there is, in fact, life beyond the PhD. Kirsty and Farida, thank you both for being such incredible friends and housemates, and for celebrating every small milestone with me this year, you managed to make my final year much more enjoyable than it is for most.

To my wonderful friends in Dublin, thank you for your endless support and encouraging words during these three years and for managing to keep me (mostly) sane, I imagine this wasn't an easy task. Conor – I have lost count of how many pep talks you have given me, but each of them pushed me one step closer to the finish line. Róisín – thank you for always giving me much needed perspective and for always being a call away when I needed it most. Aaron – thank you for being proud of the work I've done and reminding *me* to also be proud. Bríd and Megan, thank you both for giving me much needed encouragement when I struggled to motivate myself. Thank you also to my mum, Iryna, who has always been my greatest supporter and biggest inspiration. She has always taught me than I can achieve anything I set my mind on, and after three years of regular reminders, I finally believe her.

Finally, I would like to thank the entire staff and student body of the Lennard-Jones School of Chemical and Physical Sciences. When, in my final year, the war in Ukraine began, the support I received from everyone in the department, and in the wider Keele community – both in the form of kind words and donations during the humanitarian aid collection, were invaluable.

Україна була, є і буде.

Abstract

This study investigates the metallosupramolecular chemistry of coordinating ligands that contain a rigid aliphatic unit *via* the study of their coordination complexes when combined with *d*- and *f*-block metal ions. The aim was to investigate whether these aliphatic units would mimic the rigidity of aromatic ligands, to be able to sustain permanent porosity in their subsequent coordination materials, while also observing their geometric diversity. With this goal, ten ligands containing a rigid aliphatic unit were prepared, none of which had previously appeared in the coordination chemistry literature, and from these, twenty-four novel coordination compounds have been prepared and characterised.

The metallosupramolecular chemistry of aliphatic derivates of 4-picolyl ligands was investigated, to gain an initial understanding of the short contacts arising from the aliphatic components of these ligands *via* Hirshfeld surface analysis. Protonated heteroatoms were most likely to partake in short contacts, followed by the most polarised aliphatic protons, and finally by the most accessible protons.

These observations were then applied to more complex fused-ring tropinone-derived ligands. Functionalisation at the amine and α-positions of nortropinone generated di- and tritopic ligands that yielded polymeric assemblies, including a gadolinium(III) MOF which maintained most of its porosity after exposure to ambient air.

Functionalisation of nortropinone at the amine and carbonyl moieties produced cyclohexyl-bridged ligands, which yielded discrete and polymeric silver(I) coordination cages. The *N*-aryl ligands exclusively formed truncated tetrahedron $M_{12}L_6$ cages, while the *N*-methyl-substituted nortropinone yielded a cubic M_8L_6 cage. The discrete cages were analysed *in-situ via* NMR techniques, and their behaviour mirrored the solid-state observations.

Finally, a spirocyclic ligand, spiro[3.3]heptane dicarboxylic acid (Fecht's acid) was prepared, and its coordination chemistry was studied in zinc(II) and ytterbium(III) MOFs, which were compared to analogous aromatic MOFs. The aliphatic MOFs demonstrated a relatively higher thermal stability and reduced interpenetration, however, no preservation of permanent porosity.

Abbreviations

ADP	Atomic Displacement Parameter	**MIL**	Matériaux de l′Institut Lavoisier
ATR	Attenuated Total Reflectance	**MOC**	Metal-Organic Cage
BDC	Benzene-1,4-dicarboxylic Acid	**MOF**	Metal-Organic Framework
BET	Brunauer, Emmett and Teller	**MOP**	Metal-Organic Polyhedron
BTC	Benzene-1,3,5-tricarboxylic Acid	**NMR**	Nuclear Magnetic Resonance
CCS	Carbon Capture and Sequestration	**OTf**	Trifluoromethanesulfonate (Triflate)
COSY	Correlation Spectroscopy	**ppm**	Parts Per Million
D	Diffusion Coefficient	**PSE**	Post-Synthetic Exchange
DMF	Dimethyl Formamide	**PSM**	Post-Synthetic Modification
DMSO	Dimethyl Sulfoxide	**PXRD**	Powder X-Ray Diffraction
DOSY	Diffusion Ordered Spectroscopy	**RCSR**	Reticular Chemistry Structure Resource
dpe	1,2-Di(4-pyridyl)ethylene	**SALE**	Solvent-Assisted Ligand Exchange
ESMS	Electrospray Mass Spectrometry	**SBU**	Secondary Building Unit
HKUST	Hong Kong University of Science and Technology	**SCXRD**	Single-Crystal X-Ray Diffraction
HSAB	Hard Soft Acid Base (Theory)	**TBA**	Tetrabutylammonium
ICSD	Inorganic Crystal Structure Database	**TGA**	Thermogravimetric Analysis
IR	Infrared	**THF**	Tetrahydrofuran
IRMOF	Isoreticular MOF	**UiO**	Universitetet i Oslo
L	Ligand	**UV-Vis**	Ultraviolet-Visible
M	Metal	**ZIF**	Zeolitic Imidazolate Framework

Atom Colour Scheme

Black: Carbon

White: Hydrogen

Red: Oxygen

Light blue: Nitrogen

Green: Chlorine, Fluorine

Orange: Antimony

Cyan: Copper, Ytterbium

Dark blue: Cobalt

Grey: Silver, Zinc

Purple: Gadolinium

Chapter 1

· Introduction ·

1.1 Preamble & Scope

This study focuses on the effects of incorporating cyclic aliphatic functionalities into metallosupramolecular assemblies, and their impact on the network of close contacts and therefore the crystal packing of the resultant coordination materials. Aliphatic character is not commonly encountered in these materials due to difficulties associated with ligand rigidity and synthesis. The ligands presented in this thesis were designed to incorporate a rigid aliphatic unit into the backbone of the molecule – either in the form of a fused-ring or a spirocyclic component. This results in limited rotation around the carbon-carbon bonds in the ligand molecule which, in theory, would provide the molecule with rigidity comparable to that of common aromatic molecules, while still introducing aliphatic character. As aliphatic, and in particular, cyclic aliphatic components are typically non-planar, the geometry of resultant coordination assemblies was also theorised to reflect this, yielding materials with atypical and novel geometries which are inaccessible using planar aromatic ligands.

This question was first approached by designing simple, representative cyclic amines in order to study the trends in the close contacts arising from the aliphatic components of the ligands. This knowledge was then applied to the design of more complex, tropinone-containing systems. Due to the wide range of possible modifications that can be carried out on the tropinone core, a majority of this thesis is devoted to the discussion of these functionalisations and the subsequent coordination assemblies arising from the ligands. Finally, a spirocyclic dicarboxylate ligand was studied along with its coordination chemistry. In contrast to the tropinone-containing ligands, the heteroatoms were limited to the two coordinating carboxylate moieties, significantly reducing the range of possible short contacts in the system, to potentially tackle the problem of interpenetration in porous coordination assemblies.

The fused-ring and spirocyclic aliphatic ligands studied in this project provide a level of rigidity comparable to their aromatic counterparts, with the added hydrophobicity provided by their aliphatic nature. Throughout the discussion of the complexes of these ligands, comparisons will be made to analogous aromatic coordination complexes, and their resulting geometries and physical properties. Particular attention was paid to the coordination of these ligands to first-row transition metal and lanthanide ions, to better understand their behaviour when paired with metals with a variety of coordination preferences. The interactions within and between the complexes that govern the crystal packing were analysed using a combination of single-crystal X-ray diffraction and subsequently Hirshfeld surface analysis, providing insight into the structural diversity resulting from the use of these non-traditional ligands in the assemblies. Structural analyses were also supported by solution-state spectroscopic studies to probe the dynamic behaviour of these assemblies and their properties towards guest uptake and exchange, with a view towards developing water-stable CO_2 capture materials.

1.2 Supramolecular Chemistry

Supramolecular chemistry was described by Lehn as the "chemistry of molecular assemblies and of the intermolecular bond".[1] For many years prior to this definition, the focus of synthetic chemistry research has been on the design of increasingly more complex molecules *via* the manipulation of covalent bonds.

However, since this definition there has been a growing interest in gaining a better understanding of the reversible, non-covalent intermolecular bonds, to then be able to control and manipulate them, and apply this to more complex systems. With better understanding of these interactions comes the ability to create large, organized arrays in which these intermolecular interactions govern the properties of the material. This intentional manipulation of interactions can lead to a variety of materials with tuneable properties and therefore advance the application-driven design of supramolecular materials.

Supramolecular chemistry is intrinsic to the in-depth understanding and analysis of coordination materials. These non-covalent supramolecular interactions themselves encapsulate a wide variety of interactions such as van der Waals interactions, hydrogen bonding, halogen bonding and π-π interactions, all of which vary in strength and directionality, and are typically less than fifty kilojoules per mole in strength.[2] The analysis of coordination materials goes far beyond the coordination bond itself, as the understanding of the interactions that govern the crystal packing of the material *i.e.* association of adjacent coordination materials within the crystal, is just as vital in understanding the material itself and its properties. This can be particularly important for materials designed to participate in host-guest systems, in which these non-covalent interactions dictate the nature of association of the host and guest. This focus on interactions between a "host" and "guest" is abundant in nature, in interactions between enzymes and their substrates, and ion transport across various membranes.[3,4] In a synthetic laboratory, early examples of host-guest complexes include crown ethers for binding metal cations, first synthesised by Pedersen,[5] katapinands for binding simple anions, first synthesised by Simmons and Park in 1968,[6] followed closely by cryptands for cation-binding, developed by Lehn and co-workers,[7] and some examples of these are shown in Figure 1.1.

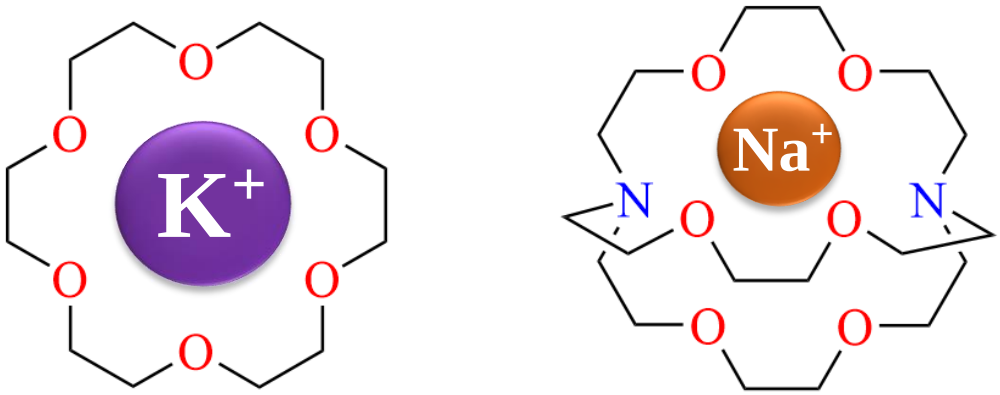

Figure 1.1. 18-crown-6 crown ether binding a K+ ion (left), cryptand [2.2.2] binding a Na+ ion (right).

The field has now evolved to designing much more elaborate host-guest complexes for increasingly niche applications, using the same fundamental techniques of utilising these reversible interactions. For example, the understanding and ability to manipulate these interactions is central to the design of materials such as metal-organic frameworks (MOFs), which rely on host-guest interactions for many of their applications, such as capturing guests,[8] or as sensors to detect specific guests and their concentrations,[9] among other uses.

By understanding and gaining control over these interactions, the complexity of these materials and their applications have expanded dramatically and will continue to do so as more knowledge is gained about their properties and assembly. Single-crystal X-ray diffraction (SCXRD) is one of the central techniques in the observation and analysis of these interactions in crystalline materials such as MOFs, and has been utilised throughout the work presented in this thesis. Other informative techniques include spectroscopic methods such as UV-Vis and fluorescence spectroscopy, which are very sensitive to small changes in the interactions present in supramolecular systems, and do not require the formation of crystalline solids.

Supramolecular materials tend to form *via* self-assembly, which is the spontaneous arrangement of constituents into well-defined assemblies, which results in the most thermodynamically stable product. By understanding the interactions that govern the process of self-assembly, more control can be gained over their formation.[10] Self-assembly is a concept that is not unique to synthetic supramolecular systems,

however, and has been seen for many years in nature, such as in the formation of the DNA double helix and the self-assembly of lipids to form the cell membrane.[11] This concept has been utilised in the design of functional materials, both in the biological and chemical fields,[12-14] and has resulted in the 1987 Nobel Prize in Chemistry to be awarded to Donald J. Cram, Jean-Marie Lehn and Charles J. Pedersen "for their development and use of molecules with structure-specific interactions of high selectivity".[15]

1.3 Coordination Chemistry

Since this early work by Cram, Lehn and Pedersen in their utilisation of these reversible intermolecular interactions, the field of supramolecular chemistry has grown dramatically, and has been particularly aided by the study of coordination chemistry. Coordination chemistry involves the study of materials which consist of organic ligand molecules which form coordination bonds to a metal cation centre, forming both discrete and polymeric materials. Coordination bonds are typically a few hundred kilojoules per mole in strength, and are therefore much stronger than the aforementioned non-covalent interactions such as hydrogen bonding or π-π interactions. Similarly to supramolecular chemistry, coordination chemistry is also commonly encountered in nature, such as in the protein nitrogenase which contains iron(II) and iron(III) ions and catalyses the reduction of nitrogen gas to ammonia,[16] and in vitamin B_{12} (which prevents anaemia and has some catalytic properties) containing cobalt(III) bound to a corrin ring structure.[17] Much like the DNA double helix and lipids in the cell membrane, coordination chemistry also makes use of self-assembly to form subsequent assemblies. As the coordination bond is by far the strongest interaction forming during the formation of metallosupramolecular assemblies (a term popularised by Constable in the 1990s to describe metal-containing supramolecular assemblies),[18] it is often the driving force for the assembly process.

In order to design materials with specific functions in mind, it is necessary to examine and understand the two main components in coordination or metallosupramolecular chemistry – the metal cation and the ligand molecules. Late first-row transition metal ions in their +2 oxidation state are a popular choice for building blocks in metallosupramolecular assemblies, and this is due to several factors. Firstly, salts of these metals

in their +2 oxidation states tend to be quite stable, and therefore easy to handle and could potentially contribute to the stability of resultant coordination complexes. The salts also need to be stable enough to be handled throughout the synthetic procedure, in particular if the complexes are intended for a certain application. However, there needs to be a balance between stability and reactivity, as the metal salts need to be reactive enough for it to be favourable to form coordination complexes *via* self-assembly, which faces higher energy barriers in the second and third row transition metals. Secondly, these metal salts tend to be relatively cheap, and cost is an important factor to consider, particularly if the final objective for these materials is again, large-scale production. Finally, first-row transition metals and their coordination chemistries are very well studied, and the metals have a range of predictable geometries, which can be factored into the crystal engineering or structure prediction of metallosupramolecular assemblies. In contrast, lanthanide metal ions tend to be much larger in size, and therefore offer much higher coordination numbers, which provides an interesting comparison of resulting coordination materials to those of transition metal ions. Some common transition metal coordination geometries are shown in Figure 1.2.

Figure 1.2. Common transition metal geometries, (from left to right) linear, trigonal planar, square planar, tetrahedral, trigonal bipyramidal, square-based pyramidal, octahedral.

The basis upon which the combination of a ligand molecule with a metal ion occurs, can be conveniently understood from the Hard-Soft Acid Base (HSAB) Theory.[19] The theory describes hard (Lewis) acids as small and/or highly charged materials, and these include metal cations such as cobalt(III), cobalt(II), copper(II), zinc(II) *etc*. These interact best with hard (Lewis) bases, typically *via* more electrostatic interactions, which are described as small and highly electronegative (*i.e.* non-polarisable), examples of which include carboxylate groups, aromatic amines such as pyridine and halogen ions and CO_2. On the other hand, soft acids are described as being larger in size and therefore carry a lower charge density and include

silver(I) and copper(I). These interact with soft bases, *via* more covalent interactions, and these are described as being large and less electronegative (*i.e.* more polarisable), and examples include nitrile functionalities, carbanions and thiols. This theory has aided in our understanding of trends observed in the stability of coordination materials, and following this, has simplified the metal/ligand combination screening process during the synthetic procedure.

The other building block to consider are the coordinating ligands. These can have a range of geometries, sizes, properties, and coordination modes. A large majority of ligands in coordination assemblies reported to date are aromatic in nature and this can be attributed to several factors, discussed further in Section 1.10, but it is their predictable rigidity that is considered an advantage in the reticular design of coordination materials, and in particular MOFs.[20] The connectivity of these ligands plays as vital a role in the determination of the geometry of the resulting coordination complex as the choice of metal ion. Chelating ligands can often lead to discrete complexes (discussed further in Section 1.5), whereas bridging ligands will more likely lead to polymeric species (discussed further in Section 1.6).[21] The geometry of the ligand, particularly if it is non-planar (*i.e.* often not fully aromatic) must also be considered, as this will have a marked effect on the properties of the material when interacting with guest molecules. In porous materials, the geometry of the ligand will often influence the shape of the pore openings, which can lead to size or shape-selective guest encapsulation. Finally, the composition of the ligand itself is also of great importance.[22] While the properties and chemistry of aromatic ligands in metallosupramolecular assemblies is well-studied, the impact of an aliphatic component or ligand on the properties of a coordination complex are not well understood and can lead to some exciting novel properties, which have not been accessed using aromatic ligands, which is further discussed in Section 1.10. The range of possible close contacts arising from aliphatic components will differ significantly to those in aromatic assemblies, mostly due to the absence of interactions with or between π-systems. These interactions will be largely influenced by the conformations and overall geometry of these non-planar aliphatic ligands, whose potential is yet to be appreciated and explored in the field of functional coordination materials.

1.4 Crystal Engineering

As well as the relatively strong metal-ligand coordination bond, the weaker interactions in metallosupramolecular systems must also be considered, such as hydrogen bonding. Hydrogen bonding has a significant influence over the assembly of metallosupramolecular materials and supramolecular materials in general.[23] Hydrogen bonding can be the deciding factor for the preferred orientation of multidentate ligands, which will determine the orientation of coordinating groups and will ultimately control the topology, and often dimensionality of a coordination material. An elegant illustration of this is demonstrated by Abrahams,[24] describing a network formed from perfect trigonal nodes. A two-dimensional (6,3) net forms if every trigonal node is coplanar (*i.e.* has a 0° twist between adjacent nodes). However, if along each connection is a 109.5° twist (preserving threefold symmetry), this results in a cubic, three-dimensional (10,3)-*a* net (this along with other descriptions of networks are discussed in Section 1.7), shown in Figure 1.3. A variety of other three-dimensional nets can occur by varying the degree of rotation around each connection. This rotation, or the preferred orientation of the coordinating ligands within the coordination complexes, is determined by those weaker interactions between ligand molecules.

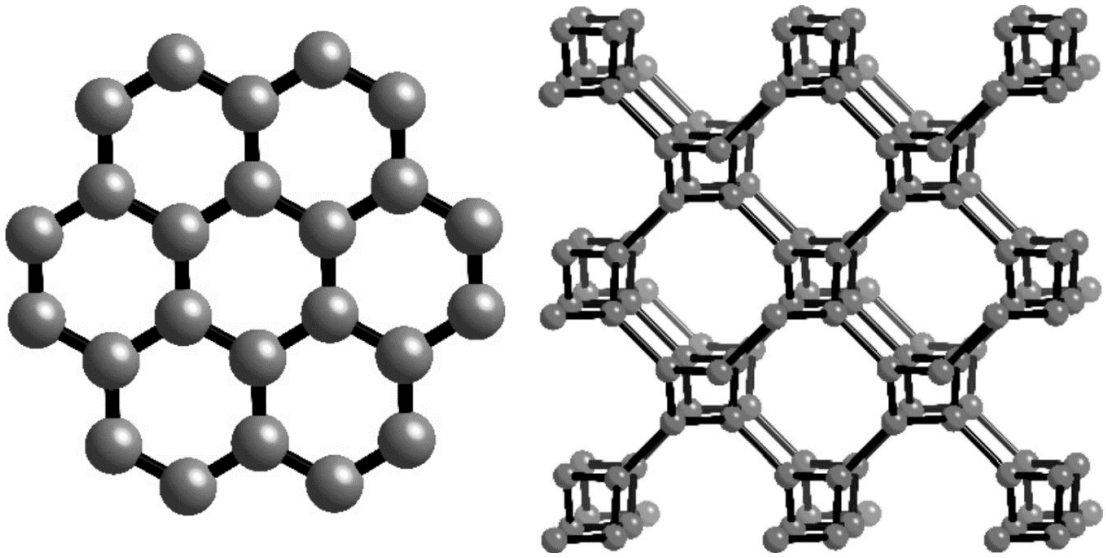

Figure 1.3. Two-dimensional (6,3) net (left) and three-dimensional (10,3)-a net formed by rotation of each connection by 109.5° (right).

Another interaction to consider is π-π interactions, and these occur when the π systems of aromatic groups overlap. While these can lead to some interpenetration (discussed in Section 1.8) in porous coordination polymers,[25] they can also serve to stabilise complexes and provide some potentially desirable properties such as photophysical activity (which can aid in the sensing of various materials), and an improved selectivity towards the encapsulation of guests. There are three main types of π-π interactions that can occur, edge-to-face T-shape, cofacial parallel stacked and parallel displaced (all shown in Figure 1.4).[26]

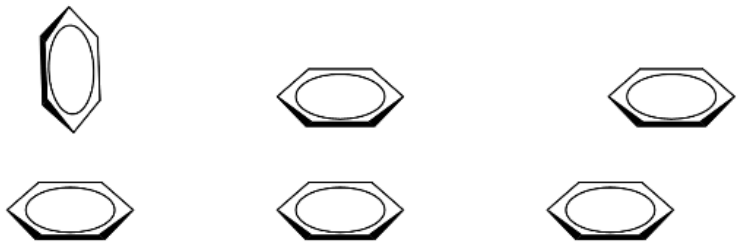

Figure 1.4. (left to right) Edge-to-face T-shape π-π stacking, cofacial parallel π-π stacking and parallel displaced π-π stacking

These interactions have been described by Hunter and Sanders,[27] and they describe a quadrupole moment in π systems that results in a partial negative electrostatic potential above both aromatic faces, and a partial positive electrostatic potential around the periphery of aromatic molecules. For this reason, most parallel π-π interactions occur at a slight offset, and edge-to-face interactions are energetically favourable. Typically, any intermolecular interactions that are observed in supramolecular materials are characterised or identified by the distances between the two interacting components, though there are no strict limits. Hydrogen bond strength is typically characterised by donor-acceptor distance and the donor-hydrogen-acceptor angle. The donor-acceptor distances tend to be up to 3.2 Å in length. A hydrogen bond acceptor is most often a nitrogen or oxygen atom (*i.e.*, an element that contains a lone pair of electrons) and a hydrogen bond donor is the moiety containing a hydrogen atom, for example an N-H or an O-H group. The shorter the distance between

the donor and acceptor atoms and the closer the donor-hydrogen-acceptor angle is to 180°, the stronger the interaction (an example of hydrogen bonding is shown in Figure 1.5).[28]

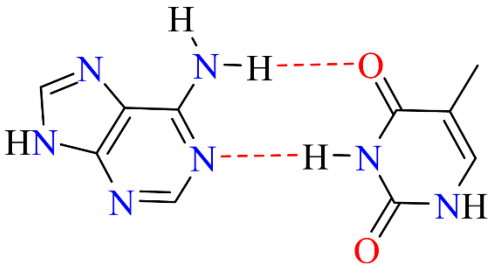

Figure 1.5. Hydrogen bonding (highlighted in dashed red lines) between adenine (left) and thymine (right).

Similar to hydrogen bonding and π-π interactions, other weak interactions such as halogen bonds, anion-π and cation-π interactions can also contribute to the preferred coordination modes and crystal packing of coordination complexes, however the latter two tend to be much weaker.[29-31] The weaker interactions tend to be much more difficult to observe, leading to some ambiguity in their identification, in particular relative to well-established, stronger coordination bonds. As these interactions and their effects on the formation of coordination polymers are becoming better understood, the rational design of functional materials incorporating these interactions is becoming more advanced. The design of coordinating ligands is becoming more meticulous, carefully engineering for the presence of these interactions, and achieving preferred ligand geometries and resultant coordination geometries.[32,33]

1.5 Discrete Assemblies

Discrete molecular assemblies (i.e. those that do not extend in any one dimension, or are zero-dimensional) occur in many forms in supramolecular chemistry such as in molecular knots,[34-36] rotaxanes,[37-39] catenanes,[40-42] and helicates,[43-45] some examples of these are shown in Figure 1.6. The knowledge of intermolecular interactions, mostly hydrogen bonding, has contributed largely to their discovery and design. Their applications range from electronic materials to catalysis,[46] with some applications found for biological purposes, for example as anti-microbial materials.[47] Coordination chemistry can also be utilised to construct

discrete metallosupramolecular assemblies in which one or multiple ligands coordinate to metal ion(s) to form a non-polymeric unit, which interacts with other discrete units *via* non-covalent supramolecular interactions, yielding a coordination compound whose properties are mainly controlled by intermolecular forces rather than intramolecular.

As with coordination polymers, these materials can be engineered by the choice in metal, ligand or synthetic conditions and include discrete complexes such as coordination cages. Discrete coordination cages have attracted a lot of attention in literature as discrete, soluble molecular cages that can interact with and selectively encapsulate guests.

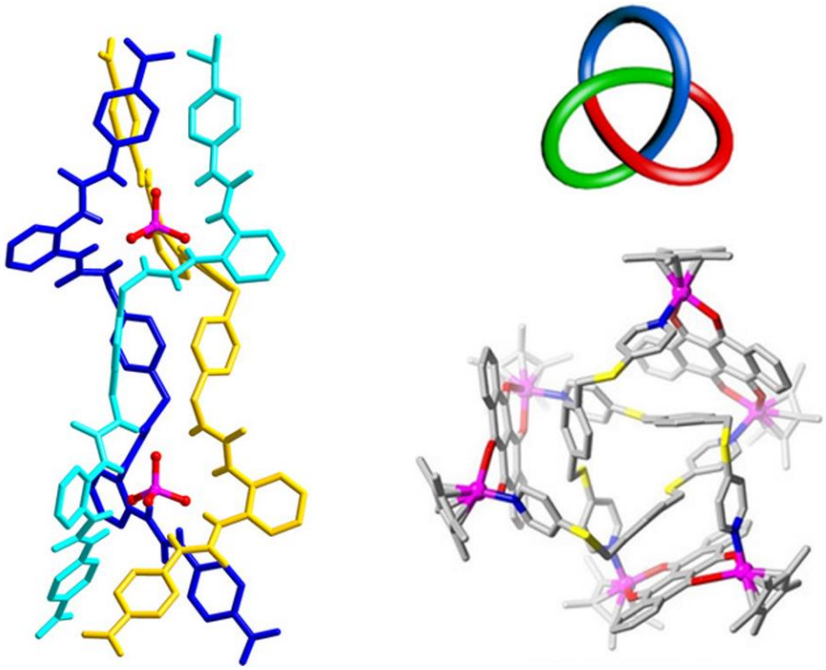

Figure 1.6. An example of an anion-coordination-driven triple helicate reported by Yang and co-workers,[44] (left) and a rhodium molecular knot (with a simplified representation shown above) reported by Jin and co-workers.[36] (right)

Metal-organic cages (MOCs) (also known as metal-organic polyhedra (MOPs)) represent finite, or discrete coordination assemblies which contain pores available for interactions with guests,[48] and some examples of discrete MOCs are shown in Figure 1.7. Their applications include drug delivery,[49] catalysis,[50] and gas storage.[51] Cage-like materials with guest-binding abilities have been studied for many years but the

development of coordination cages with permanent porosity began in the late 1980s, with landmark papers from Stang,[52] Lehn,[53] Raymond,[54] and Fujita,[55] reporting various transition metal cages with varying properties and geometries. In much of this early work, square-planar metal ions were combined with linear convergent ligands to form architectures with discrete triangular, square, and rectangular geometries. This technique was later applied to form three-dimensional polymeric architectures by using bridging ligands.

The reticular design and construction of coordination cages was elegantly summarised by Stang in 1998,[56] in which he describes the individual building blocks of MOCs as angular units and linear units, and discusses the strategic combination of the two units to achieve MOCs with predesigned geometries, making reference to some existing cages to illustrate this approach. The focus of this summary by Stang was largely the connectivity of the individual components and the resulting geometry of the cages themselves. However, as our understanding of these materials has advanced, the design of MOCs has become much more application-driven, in which the properties of the MOCs are just as, or perhaps, more important than their connectivity. The rational and systematic design of these complexes described by Stang, has shown the possible scope for the future of these materials, and has inspired a range of research since, producing MOCs with varying geometries and properties using this methodical approach.[57-59] Since the early development of metal-organic cages, there has been great progress made in the design of these materials with tuneable optical properties,[60,61] varying building block composition,[62,63] and solubilities.[64-66]

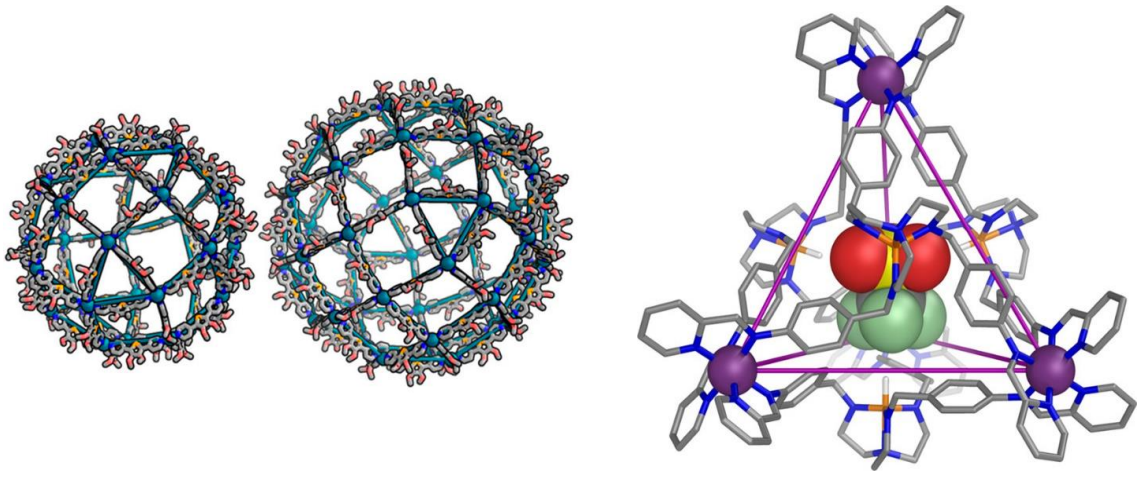

Figure 1.7. Palladium(II) $M_{30}L_{60}$ and $M_{48}L_{96}$ MOCs reported by Fujita and co-workers,[224] (left) and triflate-templated water-soluble iron(II) MOC, reported by Nitschke and co-workers.[74] (right)

The discrete nature of MOCs means that they are often quite soluble, wherein lies their benefit, and have therefore contributed to the field of porous liquids.[67] Porosity is often considered to be a property associated with solid materials, but following the work by James and co-workers,[68] porous liquids are becoming a more familiar and understood class of materials. By dissolving discrete coordination cages in a solvent that is too large to enter the cavities, the solution or liquid becomes porous itself, offering advantages over traditional solid adsorbents.[69] Cages can deform while in solution in order to encapsulate larger guests which is less commonly encountered in solid adsorbents. Much like porous solids, porous liquids can be used for a wide variety of applications, such as gas separation, catalysis and many more,[70] but combine the benefits of porous solids with the liquid phase, which could be the future of porous materials. While one of the largest deficiencies of polymeric MOFs is their instability in the presence of water,[71,72] MOCs have been shown to not only be stable in aqueous solutions, but also adsorb guests and catalyse reactions in aqueous media.[73] A recent example includes work by Nitschke and co-workers,[74] describing anion-templated self-assembly of an iron(II) coordination cage in aqueous media (shown in Figure 1.7), which utilises azaphosphatranes as anion binding units within the cage framework, which during anion displacement demonstrates a shape memory phenomenon by switching the conformation of one face of the cage from *endo* to *exo*.

Most of the applications of coordination cages, as with most supramolecular materials, involve some interaction with a guest, such as in detecting a particular substrate, selectively encapsulating a guest or the controlled release of an encapsulated guest in response to an external stimulus. Materials for sensing purposes, particularly for compounds that exist in low concentrations in a complicated mixture of compounds, are important in biomedical applications.[75] These materials often make use of fluorescence, which occurs when a material absorbs light, which in turn promotes a ground state electron to an excited state. This electron then loses some energy to nonradiative processes and proceeds to an excited state that is lower in energy than the initial excited state. The electron then returns to its ground state emitting electromagnetic radiation – *fluorescence*. In order for a cage to be an effective fluorescent sensor, it must either be luminescent itself, be attached to luminescent groups, quench or enhance the luminescence of a

bound substrate or become luminescent when bound to a substrate. The luminescence can come from either the metal, the ligand or both. The first two of those techniques are the most promising for designing fluorescent cage sensors and have been utilised to create an array of sensing cages.[76-78] Interestingly, there has also been recent progress in cages recognizing and sensing chiral molecules.[79,80]

Another interesting application for discrete coordination cages is drug delivery. Due to their discrete and polar nature, MOCs tend to be soluble in aqueous media and for this reason can be used in many biological media. Many challenges are associated with site-specific drug delivery, including solubility issues of drug molecules due to hydrophobicity, a lack of selectivity, high toxicity (and therefore harmful side effects), which results in very few drug candidates progressing past the initial stages of development. By optimising the site-specific drug delivery process, the side effects of a drug could be significantly reduced, and its efficacy improved. MOCs are an attractive potential material to address those issues, as their external and internal surfaces can be modified to encapsulate various drugs and to survive certain external conditions and only release the drug at a specific site, *i.e.* in response to contact with a certain material or at a specific pH.[81] This release can be controlled due to the dynamic reversibility of metal-ligand coordination bonds. The functionalisability of these materials is a great asset, as exposure to various materials in biological media, such as nucleophiles like cysteine and histidine, can result in premature degradation of the MOCs and therefore premature release of the drug molecule.[82,83] Ligand functionalisation and post-synthetic modifications have made increasing the stability of MOCs in various conditions much more accessible. The tuneability of the size of MOCs is also a benefit, as this allows for size-specific permeability to occur.[84,85] MOCs themselves can also be considered as drug molecules, or prodrugs, bearing some similarity in cytotoxicity to the platinum-containing drug cisplatin, as an anticancer drug.[86,87] In fact, metallodrugs in the form of discrete coordination cages have gained popularity in literature mostly as anticancer therapeutics,[88] which has meant that the by-products of the cage breakdown are not as much of a concern when the cages are themselves the drug.[89-91]

1.6 Coordination Polymers & Metal-Organic Frameworks

In contrast to discrete coordination complexes such as MOCs, coordination polymers are defined as coordination materials that extend in one-, two- or three- dimensions *via* metal-ligand coordination bonds.[92] Metal-organic frameworks (MOFs) are a class of coordination polymers that contain potential voids or pores that can be utilised for interactions with guests.[93] They consist of an organic coordinating ligand molecule, paired with a metal ion or node. These are often compared to their predecessors, zeolites, which are microporous, inorganic aluminosilicate materials in which the pores can also be utilised for interactions with guests. Zeolitic imidazolate frameworks (ZIFs) are a class of MOFs which contain imidazolate linkers and metal ions, and have structures similar to traditional aluminosilicate zeolites.[94] The advantage of MOFs and ZIFs over zeolites lies in their versatility and tuneability, which improves the specificity of their applications, and this interest is reflected in the number of reported structures as there are less than 200 known zeolites *versus* over 90,000 reported MOF structures.[95] The types of metal ions and ligands encountered in MOFs are discussed in further detail in Section 1.3, however stability and cost are among important factors to consider. Selection of metal ions is often made based on coordination number, as a preference for higher coordination numbers might increase the likelihood for the formation of a polymeric species. The ligands in MOFs must be bridging in order to form a polymeric structure, with the coordinating moieties far enough away from one another that they do not chelate. For this reason, ligands such as terephthalic acid are a popular choice, as it is a bridging dicarboxylate molecule with the two coordinating carboxylate moieties facing 180° from one another. MOFs typically possess a much higher surface area (ranging from 1,000 – 10,000 $m^2\ g^{-1}$),[96] relative to zeolites, where this figure does not exceed 2000 $m^2\ g^{-1}$. It is this advantage, combined with the high tunability of MOFs that makes them an attractive class of porous materials.

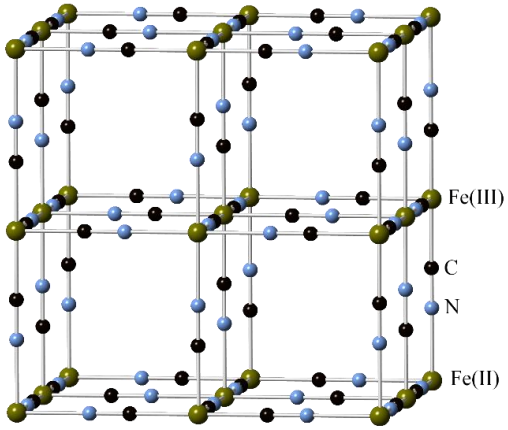

Figure 1.8. Crystal structure of Prussian Blue

The term coordination polymer was first introduced by Bailer in 1964,[97] where he compared coordination polymers with organic polymers and concluded that they can both be considered polymeric species. The first reported synthetic coordination compound was a cyano-bridged iron(II)/iron(III) complex, which is now more commonly known as Prussian Blue, shown in Figure 1.8, the structure of which was only determined in 1977,[98] more than 250 years after the discovery of this material in 1724.[99]

However, it was Robson and Hoskins in 1990,[100] who introduced the idea of a 'node and spacer' analogy to the design and synthesis of coordination materials. In this work, they use tetrahedral and octahedral ions and "rodlike connecting units" to describe the reticular design of porous three-dimensional coordination networks. In the work, they describe and hypothesise the wide range of frameworks that can be achieved by improving the understanding of these materials and their connectivity. It was this work that inspired the exponential expansion of the field since, with a huge amount of attention being focused on creating polymeric coordination materials and as the field grew, the understanding of the wide range of potential applications of these materials grew with it.

The term "metal-organic framework" was only first used in 1995, by Yaghi and co-workers to describe these materials.[101] Their work describes the synthesis of a porous cobalt(II) coordination polymer, containing a rigid tritopic ligand, 1,3,5-benzenetricarboxylic acid, and pyridine, resulting in a formula of

$CoC_6H_3(COOH_{1/3})(NC_5H_5)_2 \cdot 2/3NC_5H_5$. The MOF was shown to preferably adsorb aromatic solvents, and Yaghi and co-workers hypothesise that this is due to the π-stacking of the aromatic solvents and the 1,3,5-benzenetricarboxylic acid and pyridine ligands, and suggest that the properties of these materials can be fine-tuned by altering the properties of the bridging ligands. Since this work, the field of metal-organic framework design has expanded rapidly, pioneered by Yaghi and co-workers in their development of MOF-5 in 1999,[102] Ferey and co-workers in their development of MIL-53 in 2002,[103] and Williams and co-workers in their development of HKUST-1 in 1999,[104] all shown to contain permanent porosity, the structures of which are shown in Figure 1.9. Each of these MOFs, and many more that were synthesised from 1990 to the early 2000s, contain simple aromatic ligands, often with carboxylic acid coordinating groups.[105]

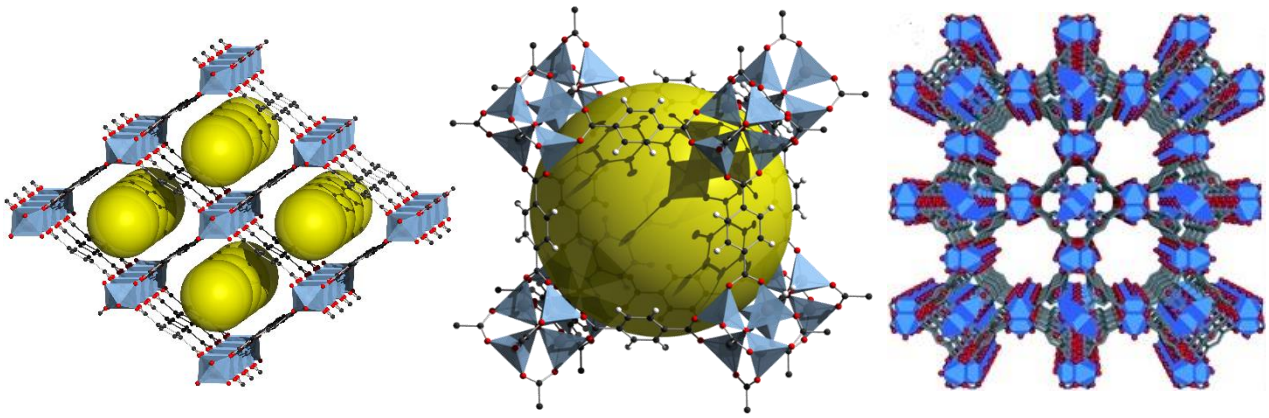

Figure 1.9. Structures of some early MOFs; (left to right) MIL-53 reported by Ferey and coworkers,[103] MOF-5 reported by Yaghi. and co-workers,[102] and HKUST-1 reported by Williams and co-workers.[225]

Since this early work by Yaghi, Ferey, and Williams, the focus of the design of MOFs has shifted from the structural features to the chemistry and properties of these materials, and fine-tuning these to adapt to an increasingly application-driven demand for their development, which requires a much more precise design strategy. The development of post-synthetic modification (PSM) has markedly advanced the synthesis of these materials, allowing for careful alterations to be made to the material, even after the formation of the core framework. Five years prior to the term "MOF" was introduced by Yaghi, Hoskins and Robson hypothesised in their landmark paper in 1990,[100] that "relatively unimpeded migration of species throughout

the lattice may allow chemical functionalization of the rods subsequent to construction of the framework", and this concept has been explored since then in terms of guest exchange in MOFs. However, it was not until over a decade later that this concept was first applied to the *covalent modification* of a MOF backbone by Cohen and co-workers,[106] in which the free amines in Yaghi's IRMOF-3,[107] are converted to amides in high yields by reaction with acetic anhydride, while preserving the crystallinity of the MOF. This breakthrough work shifted the way in which the design and synthesis of MOFs was approached, as now it was shown to be possible to modify the composition and chemistry of a MOF framework while retaining the original connectivity and maintaining crystallinity. Since then, more methods of PSM have been suggested and implemented, such as postsynthetic exchange (PSE) of ligands and solvent-assisted ligand exchange (SALE). PSE was a concept also popularized by Cohen and co-workers, in 2012, in which the NH_2-BDC and Br-BDC (BDC = benzene-1,4-dicarboxylic acid) ligands in the UiO-66 series were first exchanged with one another. Following this, the standard BDC ligand in the original UiO-66 framework was exchanged for BDC-N_3, BDC-OH and BDC-2,5-$(OH)_2$, which could not be incorporated into the UiO-66 MOF solvothermally. Prior to this, ligands have been inserted into MOFs post-synthesis, to modify their chemical properties such as gas-sorption properties by Suh and co-workers in 2010,[108] but Cohen and co-workers were the first to use the term, PSE. At a similar time to the introduction of PSE, Farha and co-workers reported the concept of solvent-assisted ligand exchange (SALE)[109] in which a ZIF – CdIF-4,[110] was exposed to a solution of 2-nitroimidazole and 2-methylimidazole and underwent ligand exchange to form either CdIF-9 or SALEM-1, which works in a similar way to PSE, but makes use of different terminology. These methods of post-synthetic modification provided access to frameworks that were previously unattainable from the *de novo* synthetic approach that was traditionally taken in the early years of the field. This, in turn, has led to a dramatic expansion of the reported structures, and provided a novel method to impart specific properties to MOFs, after the synthesis of the core frameworks.

Another important advancement in the earlier stages of MOF development includes the development of the UiO series of zirconium(IV) cluster MOFs that show remarkable hydrothermal and chemical stability. The

most well-known of these is the UiO-66 MOF, reported in 2008 by Lillerud and co-workers.[111] The weak thermal, chemical and mechanical stability of MOFs reported prior to this was the largest limiting factor in their use in large-scale industrial applications. The high stability of the UiO series arose from the combination of the strong Zr-O bonds and the ability of the octahedral Zr_6-cluster ($Zr_6O_4(OH)_4$) to rearrange reversibly upon addition or removal of μ_3-OH groups without altering the coordinating carboxylate moieties. Prior to the development of this series, the thermal stability of MOFs typically ranged from 350 – 400 °C, with only MIL-53 having stability exceeding 500 °C,[112] whereas the decomposition temperature of UiO-66, UiO-67 and UiO-68 (which differ in their linkers) was 540 °C.[113] Again, due to the strong Zr-O bonds and robust Zr_6-cluster, UiO-66 was also resistant to solvents like water, DMF, benzene and acetone as well as pressures of up to 10,000 kg cm^{-2}. The solvent stability (in particular towards water) likely arises due to the higher metal-oxygen bond strength relative to the acidity of the linker (benzene-1,4-dicarboxylic acid).[114] Among other important developments during this time, are the development of breathing/flexible MOFs which can adapt to guest molecules, improving their adsorption capacities,[115] and the development of MOF nanoparticles,[116] and MOF membranes.[117]

While the development of the UiO family of MOFs offered a potential solution to the issue of water-sensitivity in MOFs, the problem unfortunately persists in many MOFs reported to date. The labile coordination bond in MOFs is vulnerable to water displacement or hydrolysis of the metal-oxygen bonds causing a structural collapse and subsequent loss of porosity, and this water-sensitivity is widely considered to be the major weakness of MOFs. This degradation has been observed in many well-known MOFs such as MOF-5,[118] MOF-74,[119] and HKUST-1.[120] This sensitivity was addressed to an extent in the UiO series, in which inert Zr-O bonds are less sensitive to hydrolysis, however this approach limits the choice of metal ion in the preparation of MOFs. Ligand functionalisation, as well as post-synthetic modification have also been utilised in order to address this *via* the incorporation of water-repellent functionalities into the ligands, such as adding a methyl group to the terephthalic acid bridging ligand in MOF-5,[121] or by adding isopropanol to HKUST-1 to add methyl groups around the sensitive metal-ligand bond.[122-124] Another approach is to

increase the degree of aliphatic character of the bridging ligands, which results in an overall increase in the hydrophobicity of the interior pore surface of the MOF, however this area of ligand design in MOF chemistry is relatively unexplored and is further discussed in Section 1.10. This sensitivity is the largest limiting factor in the applications of MOFs, however, the aforementioned approaches to mitigate this offer promising avenues in the ever-growing interest in application-oriented MOFs.

Despite this limitation, the applications of MOFs have not ceased to expand since their emergence. As with the applications of many supramolecular systems, most applications of MOFs involve the interaction with some guest, such as in in catalysis,[125,126] drug delivery,[127,128] sensing,[129,130] and selective gas adsorption,[131,132] among many others.

In the context of catalysis, MOFs combine the benefits of both homogenous and heterogenous catalysis in terms of recyclability, selectivity, precise control of active sites and high efficiency. Their high surface area relative to traditional solid catalysts results in a highly efficient catalytic process, combined with an increased likelihood of catalyst recovery. By the careful engineering of the pore geometries along with the pore surface chemistry *via* careful ligand design, the MOFs can be fine-tuned to suit specific reactions or substrates, making them an attractive class of materials for this application. This tunability has allowed for the catalysis of chemo-, regio- or enantio-selective organic transformations.[133] The choice of metal ion or secondary building unit (SBU) can also greatly increase the specificity of these catalysts, as the metal sites act as Lewis acid centres, which often activate the substrates, and the choice of metal will affect the mechanism and efficiency of catalysis as well as determine the reaction that they catalyse. This versatility is demonstrated by the range of reported organic transformations that have been catalysed by MOFs, such as the carboxylative cyclisation of propargylic alcohols with CO_2,[134] dimerization of ethylene,[135] and oxidative halogenation reactions,[136] among many others.

The use of MOFs (and MOCs) in sensing applications is also an attractive prospect due to their fine tunability. Their efficiency has been largely aided by the use of aromatic ligands (*i.e.* those containing chromophores), as discussed in Section 1.4. Their sensing applications range from the detection of

humidity,[137] various anions,[138] volatile organic compounds,[139] and much larger molecules such as antibiotics,[140] among others. The sensing relies on the difference in luminescence of a MOF or substrate (when not bound to one another) relative to the luminescence observed upon binding or interaction of the substrate with a MOF. Lanthanide MOFs (LnMOFs) are a popular choice for applications in sensing, due to their large Stokes' shift (the difference between the band maxima of the absorption and emission spectra of equivalent electronic transitions), sharp and characteristic emissions and high colour purity.[141] Their luminescence can be enhanced by the utilisation of the "antenna effect" in which energy is transferred from the coordinating ligands to the lanthanide ions, which then generate luminescence.[142] As with catalytic MOFs and luminescent MOFs for sensing, most applications of MOFs involve an interaction with a guest, and therefore it is vital that the MOF is designed and functionalised in a way to make it as sensitive and selective towards that specific guest as is possible. This also applies when considering MOFs as selective gas adsorbents, which is discussed in further detail in Section 1.9.

1.7 Topology

While the individual components of a coordination polymer will vary significantly, it is important to be able to simplify each structure to define its connectivity, in order to better understand and observe its structural features. In coordination chemistry, there is a wide range of connectivity modes between the individual components, leading to a diverse range of larger architectures, and this diversity is the reason behind the need for some more straightforward classification. Each polymeric coordination complex can be simplified into two main components – a "node" and a "link", which was a concept popularized by Wells in 1954,[143-146] and has been used extensively since then. In any network, a node is defined as a component that connects three or more links. Links are components that connect two nodes, and if they connect three or more components, they are considered a node. The assignment of components as nodes and links is entirely arbitrary, however the goal is to simplify the structure and therefore there are some common practices when making these simplifications. Metal ions or clusters are often assigned as nodes as they likely have a coordination number higher than two, and coordinating ligands are often assigned as links which connect

or coordinate to these nodes. However, occasionally it may be more straightforward to assign a two-coordinate metal as a link and a multidentate bridging ligand as a node. An example of the simplification process is shown in Figure 1.10, in which the IRMOF series is simplified to a primitive cubic (RCSR code **pcu**, discussed further in this section) topology by assigning the basic zinc acetate, $Zn_4O(O_2C)_6$ clusters as four-connecting nodes and the terephthalic acid ligands as links.

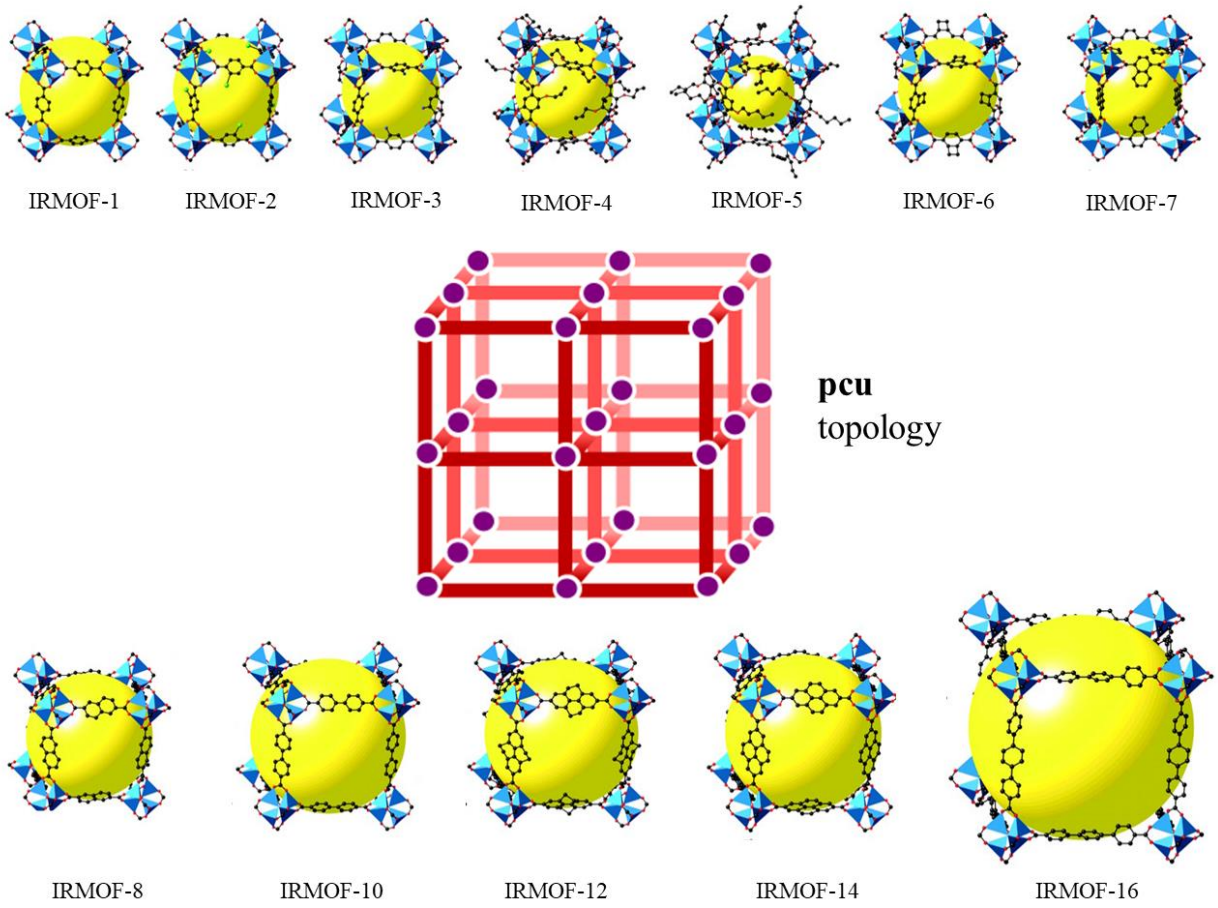

Figure 1.10. Topological simplification of Yaghi's isoreticular IRMOF series,[107] choosing $Zn_4O(O_2C)_6$ clusters as four-connecting nodes (purple spheres) and the ligands as links (red bars)

The IRMOF series in Figure 1.10 above, despite containing different chemical functionalities, different bridging distances and different physical properties, can all be represented by the **pcu** net. Two structures are described to be isoreticular if they have the same topology and remain unchanged after continuous

deformations, such as bending or stretching *i.e.* the connectivity of the materials is preserved, two isoreticular networks are shown in Figure 1.11.

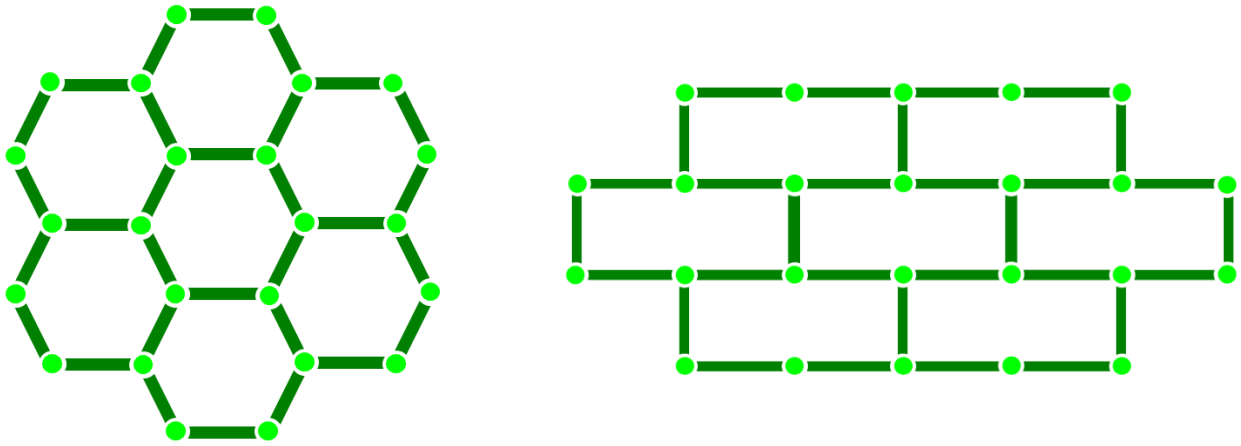

Figure 1.11. Two isoreticular networks, with the Wells symbol (6,3), with light green spheres representing three-connecting nodes, and dark green bars representing links

By reducing a structure to an array of "nodes" and "links" it is possible to assign a particular net or network type (which is an infinite array of nodes and links) to that structure. These have been widely used to classify coordination materials and there are several ways to name these nets. First, it is important to identify the "shortest circuit" in the net, which is the smallest loop containing a link-node-link fragment. If a net contains only one type of node and all of the loops are the same size, it is called a "Platonic uniform net" and is assigned the (*n*,*p*) naming system (Wells nomenclature) to classify these nets,[147] where *n* is the number of nodes in a loop and *p* is the connectivity of the nodes. The networks shown in Figure 1.11 each have six nodes in each loop; therefore, *n* would be 6. And each node connects to three links; so *p* would be 3, meaning it is a Platonic uniform net given the Wells symbol (6,3).

If different nodes, links or multiple loop sizes exist, there is a need for a slightly different net classification, and it is the Schläfli notation that can be used to describe non-Platonic uniform nets.[148] This nomenclature accounts for loops of various sizes and the number of each type of loop at one chosen fragment. This symbol is determined by again choosing a link-node-link fragment and determining the shortest possible loop involving that fragment. In the (4,4) net shown in Figure 1.12, if only *cis*-linkages are considered, the shortest loop contains four nodes. Whereas, if *trans*-linkages are considered, the shortest loop contains six nodes. The way this is represented in Schläfli notation is $4^4.6^2$ (where n^m has n number of links in a loop and m number of loops of that size) and it is done for each loop size, typically starting from the shortest loop.

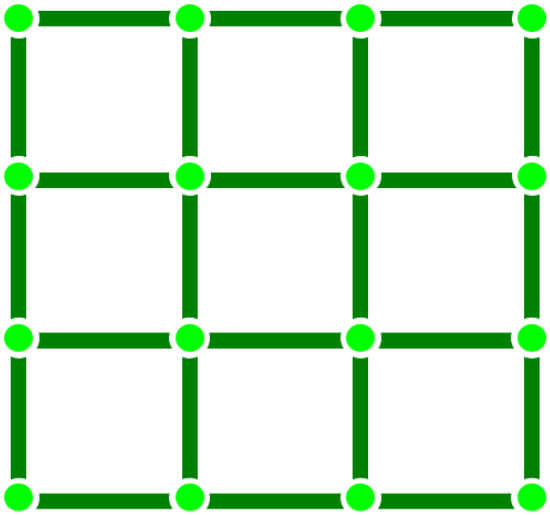

Figure 1.12. A net given the Wells symbol (4,4) and the Schläfli notation $4^4.6^2$, with light green spheres representing three-connecting nodes, and dark green bars representing links

Another common method of classifying non-platonic nets is the use of point symbols, which take the form $A^d.B^e.C^f$, in which A, B, and C are the lengths of each unique circuit and d, e, and f are the number of occurrences of each circuit length.

Three-dimensional nets are assigned in a similar way, however, as multiple types of networks can be assigned the same Schläfli symbol, and as the number of different circuits increases, the point symbol becomes increasingly more complex, additional classification is required to differentiate between them in a relatively straightforward way. This can be done using the Reticular Chemistry Structural Resource (RCSR) database,[149] which contains a large library (2940 3D nets, as of August 2022) of known structures and assigns each structure type a unique three-letter code, such as the primitive cubic topology (**pcu** topology) assigned to MOF-5. This classification is often inspired by structures that exist in minerals, such as diamondoid (RCSR code **dia**) and lonsdaleite (RCSR code **lon**) topologies (both shown in Figure 1.13) which have the same point symbol, and are now differentiable using this database. There is no analytical method of determining three-letter RCSR codes for a certain topology without comparison to the library of structure types in the database. This simplification can also be applied to hydrogen bonding networks in a material, however coordination bonds tend to be much more straightforward to identify unambiguously, whereas there is discourse on the exact definition of a hydrogen bond and therefore identification of hydrogen-bonded nets may complicate the understanding of a particular material. This assignment using the RCSR database is now commonly used throughout reporting of structures of coordination materials, where possible, and allows for efficient identification of known networks.

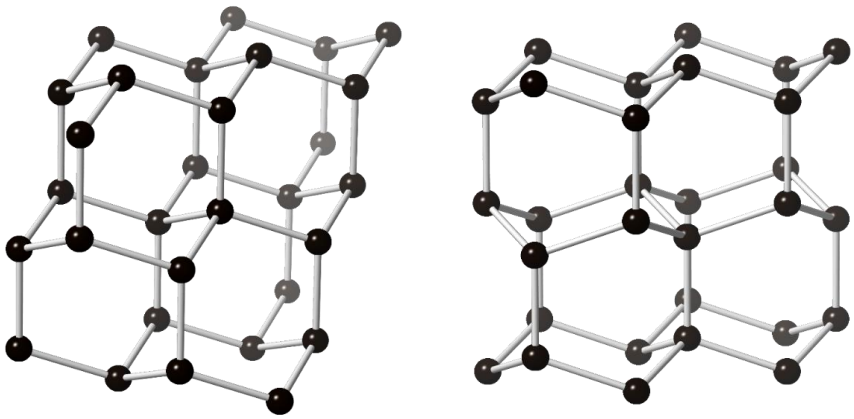

*Figure 1.13. Diamondoid topology (RCSR code **dia**) (left) and lonsdaleite topology (RCSR code **lon**) (right)*

1.8 Interpenetration

Interpenetration is a phenomenon that is frequently encountered in coordination polymers. This occurs when a network has one or more networks interlocking with it through its voids to maximise the density of the material and is aided by favourable interactions between neighbouring networks. These independent networks cannot be separated without breaking bonds, and in that way, they are polymeric analogues to molecular catenanes and rotaxanes. Interpenetration is often viewed as disadvantageous due to the reduction in porosity of a material, however some porosity can sometimes be maintained, and interpenetration often has a stabilizing effect, preventing the collapse of structures that likely would not survive solvent removal.[150] Due to the structural implications of interpenetration and the multitude of modes of interpenetration, it is also important to describe the topology of interpenetration. Generally speaking, interpenetrating networks often have the same topology, but interpenetration (or interweaving) of networks with different topologies does occur, however this is much rarer.[151,152]

There are several different modes of interpenetration, but they are referred to as *n*-fold interpenetrated, where *n* is the number of networks existing in the space of one network. The type of interpenetration takes the general form *m*D → *n*D, where *m*D is the dimensionality of the individual networks and *n*D is the dimensionality of the resulting interpenetrated structure.[153] The most straightforward mode of interpenetration to visualise is 1D → 1D interpenetration in which two one-dimensional chains are threaded through the holes within each other, again resulting in a one-dimensional chain.[154,155] Interpenetration of one-dimensional chains can also lead to structures of a higher dimension. This can occur when the chains extend in different directions (giving an *inclined* interpenetration) or when they are parallel, resulting in a 1D → 2D interpenetration, forming a two-dimensional sheet,[156,157] and this example is commonly encountered in literature, as is 1D → 3D interpenetration.[158,159]

Starting with a two-dimensional coordination net, these can also interpenetrate to form a structure with the same dimensionality, provided the nets are parallel to each other and this has been observed in a variety of

2D MOFs. This occurs between peaks and troughs of adjacent nets which lie slightly above and slightly below relative to each other.[160,161]

It is quite uncommon to observe parallel alignment of two-dimensional nets interpenetrating to give a three-dimensional structure, however *parallel* 2D → 3D interpenetration is occasionally encountered.[162,163] However, when the nets are not parallel to each other, this results in an overall higher dimensionality structure, or *inclined* 2D → 3D interpenetration which is much more common than *parallel* 2D → 3D interpenetration.[164,165] Finally, as expected 3D → 3D interpenetration is also a possibility and unfortunately occurs in many porous 3D MOFs and results in an overall loss of porosity.[166,167] An example of *parallel* 2D → 3D interpenetration and 3D → 3D interpenetration are shown in Figure 1.14.

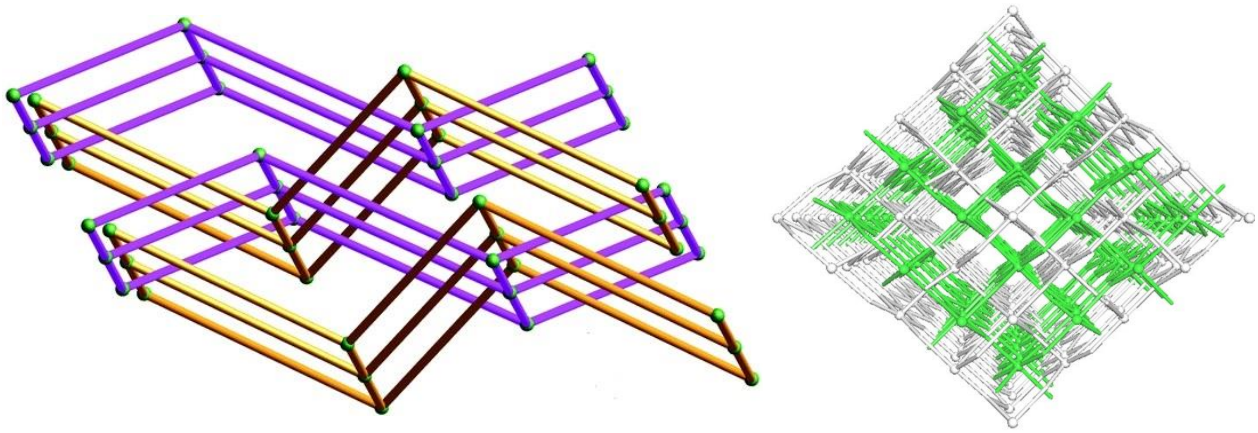

Figure 1.14. Three-fold parallel 1D → 3D interpenetration reported by Chen and co-workers.[158] *(left) and two-fold 3D → 3D interpenetration reported by Carpenter-Warren and co-workers,*[166] *(right). Independent networks are coloured separately and cannot be separated without breaking bonds.*

Interpenetration is generally promoted by favourable interactions between adjacent polymeric networks and is more likely in structures containing aromatic moieties in the ligands, as these can interact *via* π-π interactions which increase the likelihood of interpenetration. As there is no analogous aliphatic-aliphatic interaction, it is possible that by reducing the degree of aromaticity in coordinating ligands, the likelihood of interpenetration will also be reduced.

1.9 CO_2 Adsorption in MOFs

Perhaps the most significant challenge facing the modern world is climate change, with current CO_2 emissions reaching record highs, resulting in the global atmospheric concentration of CO_2 to reach above 419 parts per million (ppm) (in July 2022) as measured by the Mauna Loa Observatory in Hawaii, shown in Figure 1.15.[168] This figure has continued to grow since the onset of the industrial revolution in 1750 when the concentration was approximately at 277 ppm,[169] and has grown even during the economic slowdown in 2020/2021 due to the COVID-19 pandemic.

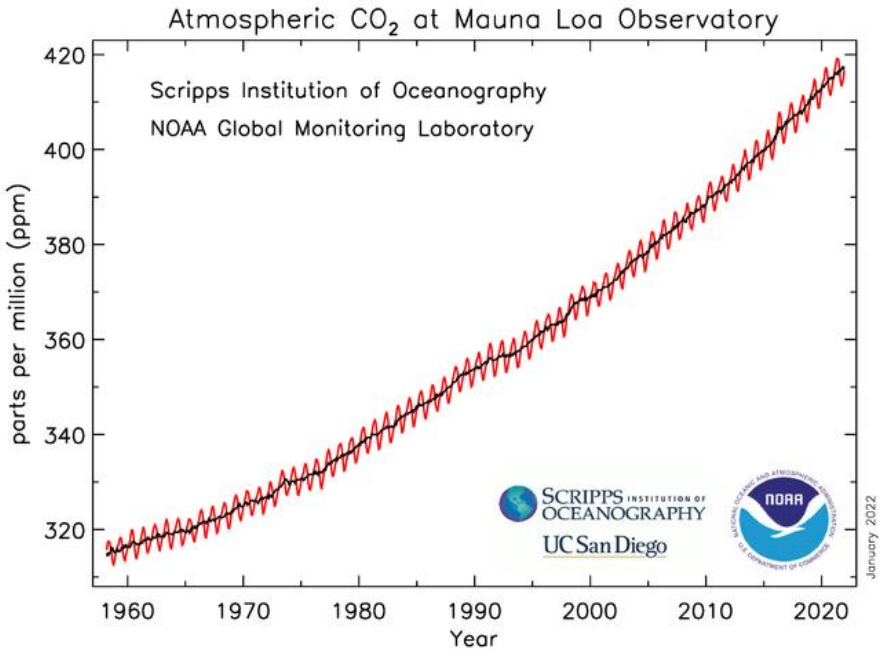

Figure 1.15. Atmospheric CO_2 concentration, as recorded from 1958 - 2022 at the Mauna Loa Observatory in Hawaii [168]

The levels are expected to rise to above 550 ppm in 2050.[170] It is well-known that anthropogenic CO_2 contributes largely to the greenhouse effect which has resulted in increasing global temperatures, a higher annual incidence of climate disasters and rising sea levels. Anthropogenic carbon dioxide is produced primarily by burning fossil fuels, and since the 1750s, nearly two-thirds of anthropogenic CO_2 emissions can be traced to 90 fossil fuel and cement producers.[171]

There have many attempts at reducing these emissions and mitigating the effects of climate change, mainly *via* carbon capture and sequestration (CCS) in which pure CO_2 is isolated and either stored in geological formations,[172] or used as a precursor to make more industrially practical chemicals, such as ureas, polymers and organic carbonates.[173] This can be done prior to burning fossil fuels (pre-combustion capture), by converting the fuel to "syngas" which is a mixture of CO (which is later converted to CO_2) and hydrogen gas that can be used for fuel. This can also be done by isolating pure CO_2 from flue gas, which is a mixture of gases produced by burning fossil fuels, *i.e.* in post-combustion capture. Oxyfuel combustion involves burning fossil fuels in an oxygen-rich environment resulting in fewer by-products which leads to a more straightforward separation of CO_2. From the perspective of separating CO_2 from the remaining components of flue gas, post-combustion capture is the most challenging of the three options due to the low concentration of CO_2 as well as other, potentially harmful components that need to be considered, such as the aforementioned issues associated with water and other by-products of fossil fuel combustion. The water content in flue gas produced by burning coal is between 5% and 7%,[174] and this can be higher for industrial processes that require more water. However, post-combustion capture is the most common method of carbon capture in pilot plants, as unlike pre-combustion and oxyfuel methods, this does not require any changes to the combustion steps prior to carbon capture and therefore, is the most straightforward to implement industrially.[175]

The current method employed for post-combustion capture is amine scrubbing (shown in Scheme 1.1), which involves the absorption of CO_2 from flue gas at ambient temperatures into an aqueous solution of an amine with low volatility (for example, monoethanolamine, piperazine and methylaminoethanol). This method utilises the partially positive carbon atom of CO_2 (arising from the molecular quadrupole imposed by the two electronegative oxygen atoms) and a lone pair of electrons of nitrogen, which act as a Lewis acid and base, respectively, and react reversibly to form an adduct. The water vapour from the aqueous solution is then removed at 100-120°C and condensed, and the amine is regenerated, leaving pure CO_2.[176] Unsurprisingly, this is a very energy-intensive process, and the energy required is provided by burning more

fossil fuels and generating more CO_2.[177] Furthermore, liquid amines regularly degrade following multiple cycles of high-temperature regeneration.[178]

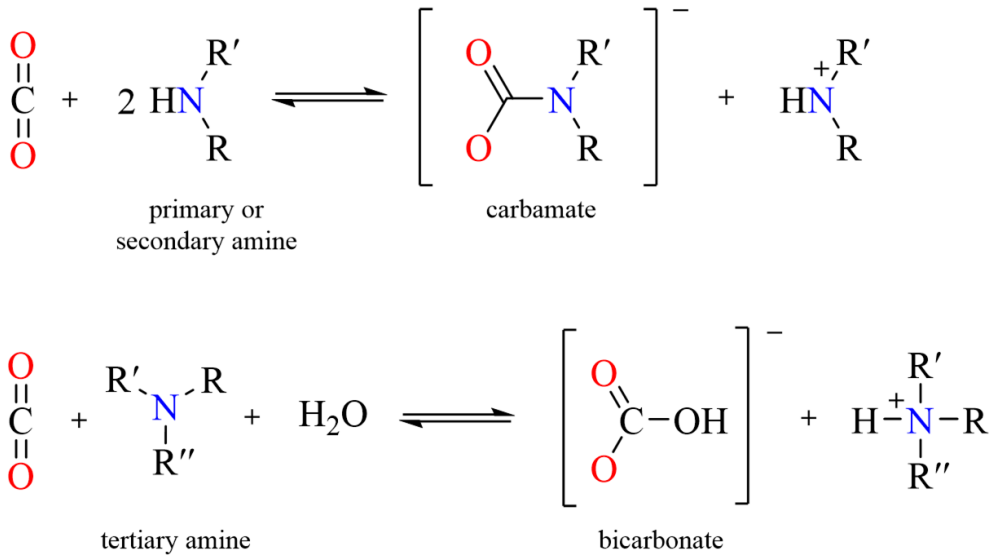

Scheme 1.1. Mechanism of amine scrubbing of CO_2 using amines

The problem with the aforementioned methods of carbon capture is that they either require a large amount of new infrastructure or changes to current infrastructure (pre-combustion and oxyfuel methods) or that they are incredibly resource and energy intensive (amine scrubbing). MOFs have frequently been considered as an alternative material for post-combustion carbon capture,[179] as they (relative to liquid amines) offer both a substantially higher volumetric capacity and lower material regeneration costs. This is the case because their interior surface chemistry is so finely tuneable, making them attractive potential subjects for such applications in which selectivity is an asset. There are several features to aid in a MOF selectively capturing CO_2 – open metal sites,[180,181] and nitrogen-rich ligand molecules (which importantly contain non-coordinating nitrogen atoms *i.e.* those having a lone pair of electrons).[182,183]

Similarly to amine scrubbing, the partially positive carbon atom of CO_2 can interact with the lone pairs of electrons of non-coordinating nitrogen atoms, therefore by increasing the number of non-coordinating

ligand nitrogen atoms will significantly improve the selectivity and uptake of a MOF towards CO_2 capture. This crucial role of accessible, uncoordinated nitrogen atoms in MOFs was highlighted in work presented by He and co-workers,[184] Three isostructural copper-based MOFs were constructed, ZJNU-43, ZJNU-44, and ZJNU-45, using ligands with different numbers of accessible, non-coordinating nitrogen atoms. Each MOF had similar porosities, yet it was ZJNU-44, the MOF with the highest number of uncoordinated nitrogen atoms that showed the best CO_2 uptake and highest CO_2/CH_4 and CO_2/N_2 selectivities.

The partially negative oxygen atoms of CO_2 on the other hand, can interact with open metal sites in a MOF, forming a weak coordination bond. This interaction tends to be stronger in metals with a higher "effective" charge, which is caused by the differences in 3d electron screening to the nucleus.[185] The likelihood of the appearance of open metal sites in a MOF can be improved by using sterically bulky ligands, which will reduce the coordination number of a metal cation, even if it prefers higher coordination numbers, leaving open metal sites in the place of coordinating ligands. As the CO_2 molecule is much smaller than coordinating ligands in MOFs, it will likely easily coordinate to those open metal sites, again improving the selectivity of the MOF towards CO_2 adsorption. This method of generating open metal sites in MOFs has been frequently utilised in the design of these materials for selective CO_2 adsorption, and in combination with *N*-functionalisation offer a promising approach to designing functional materials with high degrees of CO_2 uptake and adsorption selectivities.[186-188]

1.10 Aliphatic Ligands in Coordination Chemistry/MOFs

Aromatic ligands have largely dominated the field of metallosupramolecular chemistry and MOF chemistry and were instrumental in the initial development and current advancement of the field, as discussed in-depth in Section 1.6. There have also been examples of coordination polymers which contain aliphatic ligands such as succinic or malonic acid,[189-192] however due to issues associated with flexibility and a more complex synthetic procedure (relative to aromatic ligands), this class of ligands remains relatively unexplored. Aromatic ligands present many benefits to coordination materials such as rigidity, photophysical activity, and straightforward synthesis or commercial availability, which is why ligands such as terephthalic acid, or

benzene-1,4-dicarboxylic acid, are commonly encountered in MOFs such as MOF-5,[193] MIL-101[194] and UiO-66,[111] among others.

The same can be said for MOCs, with the literature showing a strong preference for largely aromatic ligands. The ligands are rarely fully aromatic, however, as they require some degree of flexibility in MOCs, which allows the cages to adapt their internal cavity for the encapsulation of various guests.[195] This often leads to the central part of the coordinating ligand being more flexible (and often partially aliphatic) while the coordinating ends of the ligands are often aromatic. An interesting example of this includes ursodeoxycholic acid-containing Pd_3L_6 cages reported by Rissanen and co-workers,[196] which incorporate a large, flexible aliphatic unit capped with coordinating aromatic pyridyl moieties. What is more typically observed, however, is a small aliphatic component close to the centre of the ligand, similar to what is seen in the series of cages based on bis(pyrazolylpyridine) ligands described by Ward and co-workers,[197] The incorporation of an aliphatic component to MOFs and MOCs has largely been limited to these components intended to add flexibility, however, the benefits of increasing the aliphatic character of coordination materials (and in particular porous coordination materials) is yet to be fully explored.[198]

The flexibility of linear aliphatic molecules tends to be the largest limiting factor to incorporating these ligands into porous coordination materials. The energy barrier for the rotation around carbon-carbon single bonds tends to be quite low (12 kJ mol^{-1} in disubstituted ethane),[199] leading to many stable conformations, which can often lead to an absence of reliable and permanent porosity, which is a crucial property in the design of porous coordination materials. However, where porosity is not the goal, these ligands have led to some interesting entangled coordination materials,[200,201] with phenomena such as polycatenation, polythreading and polyknotting,[202] in which the linker geometries are poorly defined.[203] However, by introducing a degree of rigidity into these ligands, they become comparable to traditional aromatic ligands and can act as alternative ligands for porous coordination materials. An approach to achieving coordination polymers with permanent porosity which incorporate aliphatic ligands, is the use of cyclic or fused-ring units to introduce rigidity into aliphatic coordinating ligands.

The rigidity of cyclic and fused-ring aliphatic molecules can be understood by comparing the energy barriers between possible isomers of increasingly more complex cyclic aliphatic molecules. As previously stated, the energy barrier between the three possible minima in disubstituted ethane is *ca*. 12 kJ mol^{-1}. Increasing the level of complexity to a substituted cyclohexane ring, the *cis* and *trans* isomers are not interconvertible without breaking bonds. The two conformers of substituted cyclohexane are separated by an energy barrier of >30 kJ mol^{-1} (51 kJ mol^{-1} for unsubstituted cyclohexane and 64 kJ mol^{-1} for permethyl cyclohexane), which is, as expected, significantly higher than the disubstituted ethane. Fusing two cyclohexane rings along one bond yields decalin, which essentially locks the conformation of one of the cyclohexane rings. This results in only the *cis*-isomer being able to undergo ring inversion, where this is not possible for the *trans*-isomer, again, without breaking bonds. This fusion of rings results in the increase in the rigidity of the molecule, as part of it is locked into one conformation. If this is complicated further, by adding a third fused cyclohexane ring, what results is adamantane, in which none of the rings are able to undergo ring inversion *i.e.* they are all locked into a certain conformation resulting in a complete absence of conformational freedom and flexibility. This lack of flexibility results in a rigidity of these fused-ring molecules that mimics the rigidity of aromatic ligands while introducing new and exciting properties such as unique geometries and improved hydrophobicity.

The non-planar geometry of aliphatic molecules arises from the absence of conjugation which is seen in two-dimensional aromatic molecules. While this atypical geometry of these ligands may appear disadvantageous from the perspective of the reticular design of coordination materials, their use in coordination complexes can provide access to new geometries that would otherwise be unachievable using two dimensional aromatic ligands. In aromatic ligands, the addition of coordinating functionalities is limited to one plane, however, in aliphatic (and in particular cyclic or fused-ring) systems, it is possible to functionalise at multiple faces of the molecule, leading to a unique relative orientation of coordinating moieties. This, in turn, can result in unique connectivity modes (beyond the typical linear bridging modes)

in coordination polymers that have not yet been encountered, due to the three-dimensional shape of the backbone.

This three-dimensional nature can result in new surface chemistry in porous materials. As is highlighted in examples of fused-ring aliphatic MOFs discussed further in this section, the $-CH_2$ moieties of these three-dimensional ligands can now point *into* the pores, whereas in aromatic MOFs these usually align *parallel to* the pores. One of the methods of improving the stability of MOFs to water (as discussed in Section 1.6) is by introducing aliphatic character to the ligand backbones. By that logic, the increase in aliphatic character of the internal pore surface area of the MOFs could also improve its water stability. The bulky hydrophobic fused-ring aliphatic units could prevent the approach of water to the sensitive coordination bonds in the MOF and subsequently prevent water displacement or hydrolysis. This has been illustrated to be successful by the addition of alkyl groups to IRMOF-3,[203] or the use of methyl-substituted BDC linkers in BDC-based MOFs.[204]

The rigidity provided by the addition of a cyclic or fused-ring unit to a coordinating ligand has been explored, with a large part of the early work focused on simple cyclohexane or adamantane derivatives. Cyclohexane-1,4-dicarboxylic acid is a popular choice as an aliphatic alternative to the similarly sized BDC linker and the reported MOFs highlight the fluxional behaviour ligands of this nature in solution. In one example, reported by Hong and co-workers,[205] the *cis* and *trans* isomers of the ligand were separated completely in the synthetic conditions, resulting in two unique cadmium(II) MOFs containing the two isomers. Similarly, the reaction of nickel(II) nitrate with a mixture of the two isomers again resulted in two unique MOFs containing one isomer each, reported by Takagi and co-workers.[206] Lanthanum(III) coordination polymers reported by Jung and co-workers,[207] controlled the conformation of the ligand in solution by changing the pH in the reaction conditions leading to three unique coordination polymers containing one conformation of the ligand each. More complex, adamantane-derived systems were then introduced, with the bulky aliphatic unit often contributing to the stability of the resultant coordination polymers due to its structural rigidity.[208,209]

Beyond the adamantane fused-ring system, the library of these aliphatic fused-ring ligands has been expanded by the introduction of cubane and bicyclo-[2.2.2]octane systems into non-aromatic MOFs. A series of CUB MOFs (containing cubane-1,4-dicarboxylic acid) has been reported by Hill and Macreadie and co-workers, starting with CUB-5 in 2019.[210] CUB-5 (Figure 1.16) is a homoleptic MOF which is isostructural to MOF-5, which demonstrates a complete reversal of guest selectivity, relative to MOF-5.[193] At low partial pressures, MOF-5 selectively adsorbs cyclohexane over benzene from a mixture of hydrocarbons, whereas the opposite is true for CUB-5. This is due to the protons associated with the BDC linker in MOF-5 aligning parallel to the pores in MOF-5 (due to the planar nature of BDC), however, in CUB-5. Due to the non-planar nature of the cubane core, the aliphatic protons of the linker point *into* the pores, having a marked effect on the internal pore chemistry. The expansion of this family of CUB MOFs then led to the incorporation of cubane-1,4-dicarboxylic acid into MOFs as a coligand, which was combined with aromatic carboxylate ligands of varying sizes yielding four new MOFs.[211] Similarly to CUB-5, these MOFs show remarkable hydrocarbon separation properties relative to their aromatic analogues, again due to the marked difference in pore chemistry. Finally, most recently, two homoleptic magnesium(II) MOFs, incorporating cubane-1,4-dicarboxylic acid and bicyclo[1.1.1]pentane-1,3-dicarboxylic acid have been reported by Macreadie and co-workers in 2022,[212] which they have termed 3DL-MOF-2 and 3DL-MOF-3 (in which 3DL = 3DLinker), respectively. While the pore volume of these coordination polymers was not accessible, this work again expanded the scope of rigid aliphatic units that can be introduced into the frameworks of porous coordination materials.

While the CUB series of MOFs demonstrated the effect of altering the pore chemistry to enhance guest selectivity, NU-403 (Figure 1.16) demonstrates how the unusual geometry of aliphatic ligands can be utilised to facilitate size and shape selective adsorption.[213] NU-403, reported by Farha and co-workers in 2020, is a fully aliphatic homoleptic MOF, which is isoreticular to UiO-66,[111] containing the fused-ring bicyclo-[2.2.2]octane-1,4-dicarboxylic acid. The novel geometries arising from the non-planar (and therefore bulkier) nature of the ligand molecules (which result in smaller pore openings) leads to an

improved selectivity towards xenon (Xe/Kr selectivity of ~9) relative to UiO-66 (Xe/Kr selectivity of ~8)[220] which is a challenge given the inert nature of the two gases. Their separation usually requires cryogenic distillation which is very energy-intensive,[214] but also industrially important.

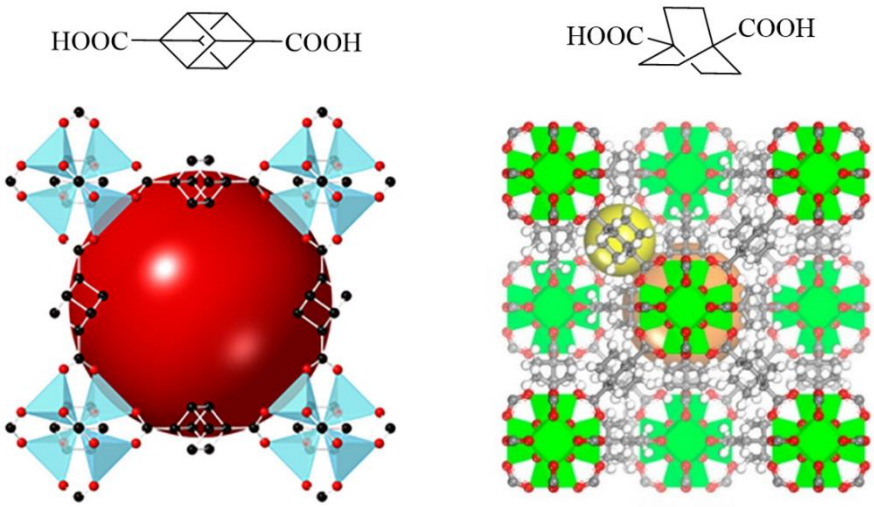

Figure 1.16. CUB-5 and corresponding cubane-1,4-dicarboxylic acid ligand (left)[210] and NU-403 and corresponding bicyclo-[2.2.2]octane-1,4-dicarboxylic acid ligand (right)[213]

These examples of aliphatic MOFs have demonstrated that these rigid, fused-ring units in the aliphatic backbones result in the ability of these MOFs to support pore volume, thus overcoming the problem associated with the flexibility of linear aliphatic ligands. However, the reported fused-ring ligands are so far limited to linear dicarboxylate ligands, resulting in similar coordination geometries to traditional aromatic dicarboxylates such as terephthalic acid. This creates a novel space for the exploration of fused-ring aliphatic cores that can be functionalised at multiple faces, leading to coordinating groups emerging in different directions from that core. This could yield some fascinating ligand geometries and unusual coordination modes, that are not accessible using linear dicarboxylate ligands or planar aromatic ligands. An attractive candidate for this could be the tropinone-derived 8-azabicyclo[3.2.1]octane core, which contains an apical

amine that points roughly 90° from the other heteroatomic component of the molecule, which could lead to a unique relative arrangement of coordinating functionalities, which is discussed further in Section 1.11.

1.11 Chemistry of Tropinone

Tropinone, shown in Figure 1.17, was first synthesised by Willstätter in 1901,[214] and was later optimised to a one-pot synthesis by Robinson in 1917.[215] It is a naturally occurring plant tropane alkaloid,[216] containing an 8-azabicyclo[3.2.1]octane core, which is comprised of a cycloheptane ring, spanned by a nitrogen atom, forming a second, fused five-membered ring. This bicyclic core is what defines this class of tropane alkaloids, which occur in high concentrations in the *Solanaceae* and *Erythroxylaceae* families.[217] Alkaloids are naturally occurring compounds that contain one or more nitrogen atoms, and their name is derived from the basic nature or "alkaline likeness" of many of the compounds. Though the structures of these tropane alkaloids are quite similar to each other, their pharmacological effects differ significantly.[218] Perhaps one of the most well-known tropane alkaloids, cocaine, occurring naturally in *Erythroxylum coca*, is commonly used as a recreational drug that causes psychoactive and hallucinogenic effects. On the other hand, scopolamine (marketed under the trade name Scopoderm TTS®), containing the same bicyclic core, was developed as a drug to treat motion sickness in 1981, and was used during World War II to treat shell shock.[219] Both cocaine and scopolamine are shown in Figure 1.17.

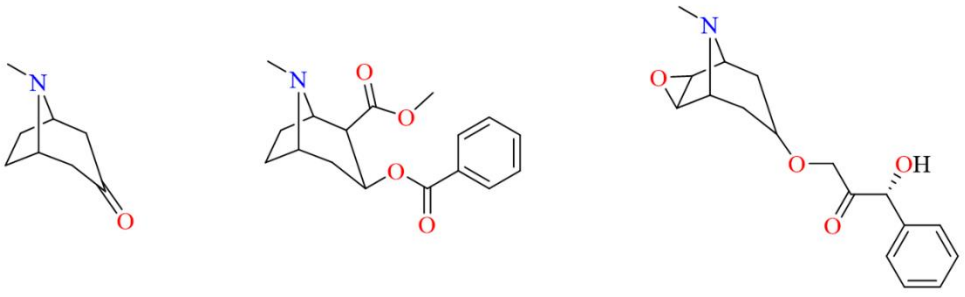

Tropinone Cocaine Scopolamine

Figure 1.17. (left to right) Structures of tropinone, cocaine and scopolamine, each containing the 8-azabicyclo[3.2.1]octane core

Tropinone itself is the first intermediate in the biosynthesis of several pharmacologically important tropane alkaloids and is used now as a precursor for atropine which is used to treat anticholinergic poisoning, bradycardia and as rapid sequence intubation (RSI) pre-treatment.[220,221] The one-pot synthesis presented by Robinson in 1917[215] demonstrates an elegant example of retrosynthesis and an in-depth mechanistic understanding of the chemistry of this compound, years ahead of its time, which earned him the Nobel Prize in Chemistry in 1947 "for his investigations on plant products of biological importance, especially the alkaloids".[222] The mechanism of the Robinson tropinone synthesis is shown in Scheme 1.2, and consists of a condensation reaction between methylamine and a dialdehyde to give a cyclic iminium ion, followed by a double Mannich reaction to form a bicyclic intermediate and a final double decarboxylation to give tropinone.

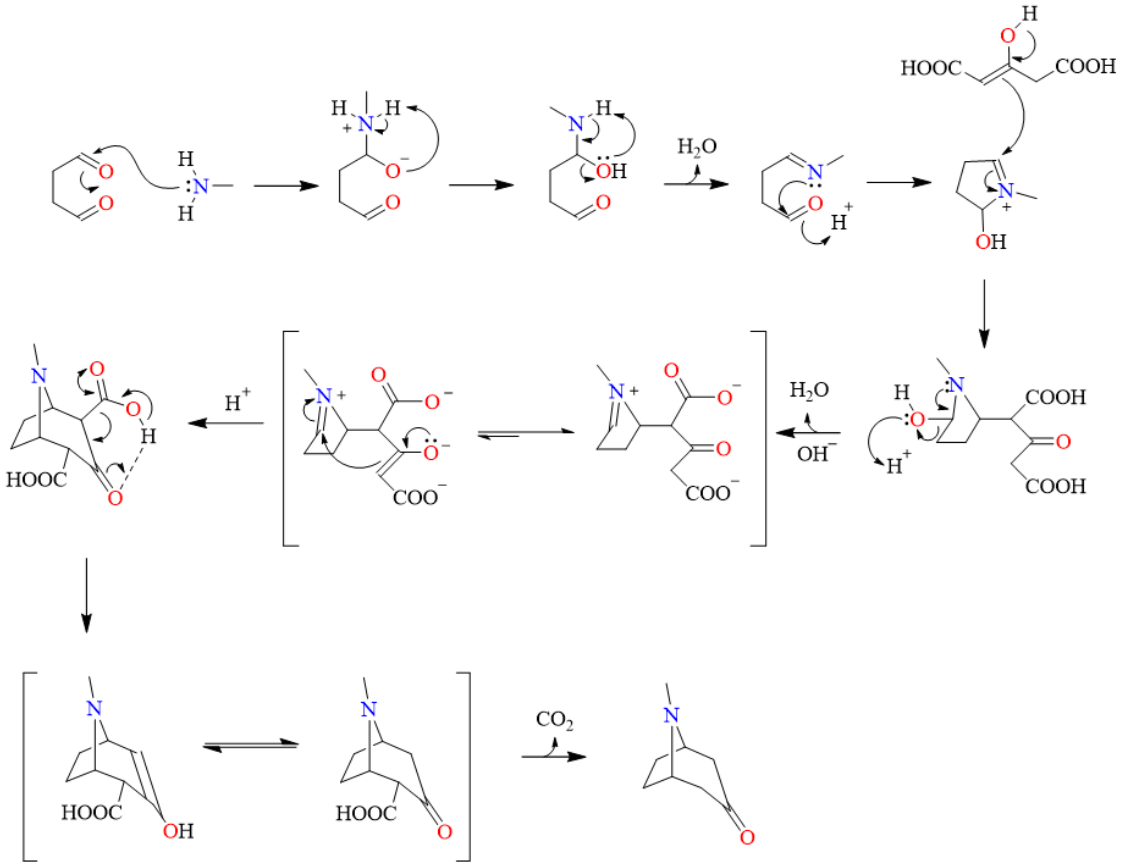

Scheme 1.2. Mechanism of Robinson's synthesis of tropinone[223]

The reaction is driven by the loss of water and carbon dioxide over the course of the cyclisation. This synthesis was inspired by Robinsons' hypothesis of how this synthesis occurs biologically, with simple starting materials that are more likely to be found in the sap of plants, than cycloheptanone, which is used as the starting material in Willstätters' synthesis.[215]

Tropinone is an attractive molecule for use in coordination compounds for a multitude of reasons. Firstly, with the goal of making hydrophobic or water-stable coordination polymers in mind, this bulky aliphatic moiety can potentially protect the interior of these materials from water degradation, by repelling any water as it approaches the sensitive areas of the materials. The molecule is also highly functionalisable, providing a wide scope for the potential ligands to be obtained from this bicyclic core. Starting from commercially available nortropinone hydrochloride, in which the *N*-methyl group is replaced by a proton to give a secondary amine, this molecule can be functionalised at three sites – the amine, the ketone and the alpha protons, as outlined in Figure 1.18. Each of these functionalisations, and frequently a combination of them, have been utilised in the design of the ligands for this project.

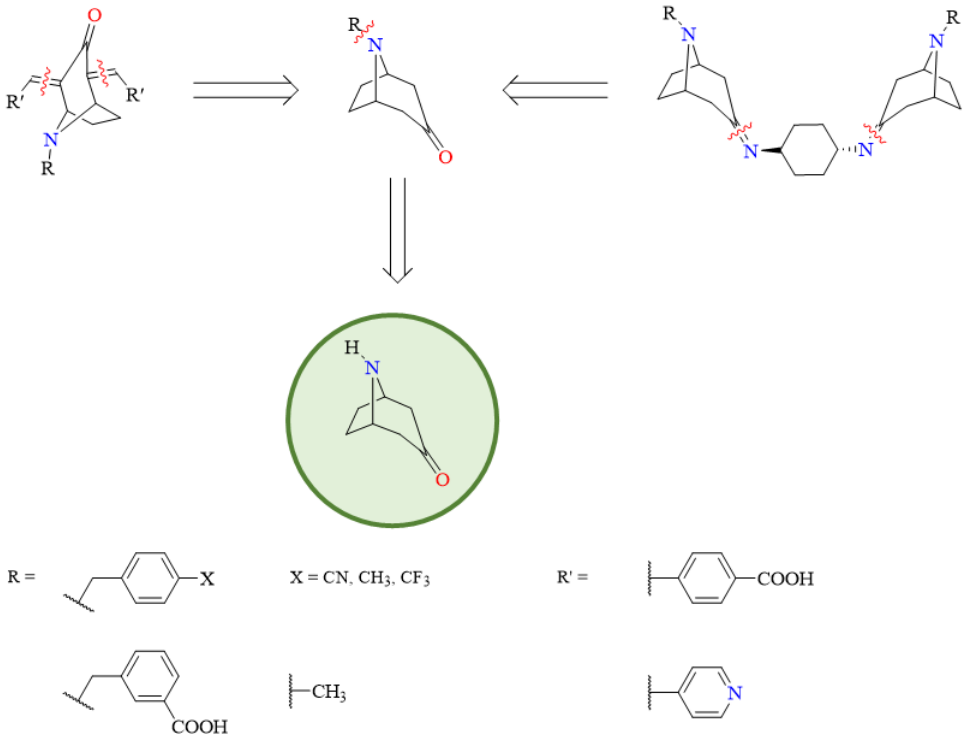

Figure 1.18. Functionalisations of nortropinone that have been utilised in this project

1.12 Present Study

This study examines ligands derived from tropinone and other aliphatic moieties as building blocks in metallosupramolecular assemblies, especially MOFs and MOCs. These species are studied with the aim of determining the influence of the non-planar cores on the local and extended structures, and guest uptake properties, of the resulting materials. We hypothesise that the rigid cyclic and fused-ring aliphatic cores can be used to generate porous materials of structural classes that are inaccessible from purely aromatic ligands. Particular attention was paid to the coordination of these ligands to first-row transition metals and some lanthanides, to investigate their behaviour when paired with metal ions with a range of coordination number and geometric preferences. The influence of the non-aromatic components on the network of close contacts and overall crystal packing was of great interest, in particular in polymeric porous materials. These close contacts could have a marked effect on not only the size and shape of the pores and pore openings, but also on the properties of the pore surfaces and therefore, the possible non-covalent host-guest interactions, potentially leading to some unusual guest selectivity tendencies.

Chapter 2 examines the coordination chemistry of three representative picolyl ligands containing an aliphatic component – piperidine, morpholine or a methyl amine group. Their preferred coordination modes to copper(II), cobalt(II) and silver(I) were examined and the trends in close contacts arising from the aliphatic components of the ligands were determined using a combination of SCXRD with Hirshfeld surface analysis. The observations were then used to design more structurally complex amine-containing cyclic aliphatic ligands based on the tropinone core, which are discussed in later chapters.

Chapter 3 describes the synthesis and coordination chemistry of tropinone-derived ligands produced by functionalising the core at the positions α- to the ketone, and at the amine. Using these ligands, a range of coordination polymers and MOFs are generated and the influence of the tropinone core is elucidated through structural analysis, guest exchange and gas adsorption studies. Following this, the water stability of the permanently porous materials was investigated by prolonged exposure to air, which in aromatic MOFs often leads to degradation by atmospheric water vapour.

Chapter 4 focuses on a series of tropinone-derived ligands, in which a cyclohexyl group bridges two *N*-functionalised nortropinone moieties *via* an imine formed at the ketone of each tropinone. The combination of these nitrogen-rich ligands with silver(I) salts resulted in a largely aliphatic MOF, and largely or fully aliphatic MOCs. NMR spectroscopy, in particular diffusion-ordered spectroscopy (DOSY) NMR, was used to support the crystallographic data, and provides insight into the dynamic assembly processes of these species in solution, as well as their anion binding preferences.

Chapter 5 describes the coordination chemistry of a spirocyclic aliphatic ligand, spiro[3.3]heptaine-2,6-dicarboxylic acid (Fecht's acid). Zinc(II) and ytterbium(III) complexes of this ligand are compared to analogous aromatic MOFs containing a similarly sized aromatic dicarboxylate ligand, terephthalic acid. As well as structural comparisons, the physical properties are compared between the aliphatic and aromatic MOFs, such as thermal stability and gas adsorption properties. This ligand offers an interesting comparison to tropinone-derived ligands discussed in previous chapters, as the significant decrease in heteroatoms in the ligand structure of Fecht's acid reduced the number of possible close contacts originating at the ligand molecule.

Chapter 6 contains a brief summary of the work presented in this thesis and possible routes for future work stemming from this research is also discussed.

Finally, Chapter 7 discusses the instrumental and synthetic details of each ligand and coordination complex discussed in earlier chapters. Additional data such as NMR and IR spectral details, melting points and powder XRD are reported also. Crystallographic tables, PXRD data, relevant TGA profiles and additional data and figures are included in the appendices (Appendix 1, 2, 3 and 4, respectively). A list of publications from the work presented in this thesis are also outlined in Appendix 4 (Section A4.3). All crystallographic data is included as electronic supplementary information in .cif format, available at https://bit.ly/3e4C8ev.

1.13 References

1. J. M. Lehn, *Angew. Chem., Int. Ed. Engl.*, 1990, **29**, 1304 – 1319.

2. A. Y. Robin and K. M. Fromm, *Coord. Chem. Rev.*, 2006, **250**, 2127 – 2157.

3. L. E. Bickerton, T. G. Johnson, A. Kerckhoffs and M. J. Langton, *Chem. Sci.*, 2021, **12**, 11252 – 11274.

4. W. Cao, X. Qin and T. Liu, *ChemBioChem*, 2021, **22**, 2914 – 2917.

5. C. J. Pedersen, *Angew. Chem., Int. Ed. Engl.*, 1988, **27**, 1021 – 1027.

6. H. E. Simmons and C. H. Park, *J. Am. Chem. Soc.*, 2002, **90**, 2428 – 2429.

7. J. M. Lehn, *Angew. Chem., Int. Ed. Engl.*, 1988, **27**, 89 – 112.

8. D. Wu, P. F. Zhang, G. P. Yang, L. Hou, W. Y. Zhang, Y. F. Han, P. Liu and Y. Y. Wang, *Coord. Chem. Rev.*, 2021, **434**, 213709.

9. S. Zhao, G. Wang, D. Poelman and P. Voort, *Materials*, 2018, **11**, 572.

10. P. J. Stang, *J. Am. Chem. Soc.*, 2012, **134**, 11829 – 11830.

11. S. Khalid, P. J. Bond, J. Holyoake, R. W. Hawtin and M. S. P. Sansom, *J. R. Soc. Interface*, 2008, **5**, 241 – 250.

12. L. Wågberg and J. Erlandsson, *Adv. Mater.*, 2020, **33**, 2001474.

13. Y. Sasaki, R. Kubota and T. Minami, *Coord. Chem. Rev.*, 2021, **429**, 213607.

14. S. Gupta, I. Singh, A. K. Sharma and P. Kumar, *Front. Bioeng. Biotechnol.*, 2020, **8**, 504.

15. The Nobel Prize in Chemistry 1987 - NobelPrize.org, https://www.nobelprize.org/prizes/chemistry/1987/summary/, (accessed December 29, 2021).

16. J. M. Harrowfield, *Comptes Rendus Chimie*, 2005, **8**, 199 – 210.

17. B. Kräutler, *Biochem. Soc. Trans.*, 2005, **33**, 806 – 810.

18. E. C. Constable and A. M. C. Thompson, *J. Chem. Soc., Dalton Trans.*, 1994, 1409 – 1418.

19. R. G. Pearson, *J. Am. Chem. Soc.*, 2002, **85**, 3533 – 3539.

20. X. L. Lv, S. Yuan, L. H. Xie, H. F. Darke, Y. Chen, T. He, C. Dong, B. Wang, Y. Z. Zhang, J. R. Li and H. C. Zhou, *J. Am. Chem. Soc.*, 2019, **141**, 10283 – 10293.

21. P. Atkins, T. Overton, J. Rourke, M. Weller, F. Armstrong and M. Hagerman, in *Shriver and Atkins' Inorganic Chemistry*, 5th edn., 2010, pp. 199–221.

22. S. K. Ghosh and S. Kitagawa, in *Metal Organic Frameworks: Design and Application*, ed. L. R. MacGillivray, 2010, pp. 165–192.

23. C. S. Hawes, *Dalton Trans.*, 2021, **50**, 6034 – 6049.

24. B. F. Abrahams, in *Frontiers in Crystal Engineering*, ed. E. R. T. Tiekink and J. J. Vittal, 1st edn., 2006, pp. 265 – 295.

25. H. L. Jiang, T. A. Makal and H. C. Zhou, *Coord. Chem. Rev.*, 2013, **257**, 2232 – 2249.

26. S. E. Wheeler, *J. Am. Chem. Soc.*, 2011, **133**, 10262 – 10274.

27. C. A. Hunter and J. K. M. Sanders, *J. Am. Chem. Soc.*, 2002, **112**, 5525 – 5534.

28. T. Steiner, *Angew. Chem. Int. Ed.*, 2002, **41**, 48 – 76.

29. M. Fourmigué, *Curr. Opin. Solid State Mater. Sci.*, 2009, **13**, 36 – 45.

30. H. T. Chifotides and K. R. Dunbar, *Acc. Chem. Res.*, 2013, **46**, 894 – 906.

31. J. C. Ma and D. A. Dougherty, *Chem. Rev.*, 1997, **97**, 1303 – 1324.

32. E. W. Dahl and N. K. Szymczak, *Angew. Chem. Int. Ed.*, 2016, **55**, 3101 – 3105.

33. Y. Shen, B. Shan, H. Cai, Y. Qin, A. Agarwal, D. B. Trivedi, B. Chen, L. Liu, H. Zhuang, B. Mu, and S. Tongay, *Adv. Mater.*, 2018, **30**, 1802497.

34. D. A. Leigh, J. J. Danon, S. D. P. Fielden, J. F. Lemonnier, G. F. S. Whitehead and S. L. Woltering, *Nature Chem.*, 2020, **13**, 117 – 122.

35. Y. Inomata, T. Sawada and M. Fujita, *J. Am. Chem. Soc.*, 2021, **143**, 16734 – 16739.

36. H. N. Zhang, Y. J. Lin and G. X. Jin, *Chem. Asian J.*, 2021, **16**, 1918 – 1924.

37. G. Baggi, B. H. Wilson, A. Dhara, C. A. O'Keefe, R. W. Schurko and S. J. Loeb, *Chem. Commun.*, 2021, **57**, 8210 – 8213.

38. Z. Yu, M. Centola, J. Valero, M. Matthies, P. Šulc and M. Famulok, *J. Am. Chem. Soc.*, 2021, **143**, 13292 – 13298.

39. M. Cirulli, E. Salvadori, Z. H. Zhang, M. Dommett, F. Tuna, H. Bamberger, J. E. M. Lewis, A. Kaur, G. J. Tizzard, J. van Slageren, R. Crespo-Otero, S. M. Goldup and M. M. Roessler, *Angew. Chem. Int. Ed.*, 2021, **60**, 16051 – 16058.

40. H. Han, J. Sha, C. Liu, Y. Wang, C. Dong, M. Li and T. Jiao, *J. Coord. Chem.*, 2021, **74**, 1781 – 1793.

41. A. W. H. Ng, S. K. M. Lai, C. C. Yee and H. Y. Au-Yeung, *Angew. Chem. Int. Ed.*, 2022, **61**, e202110200.

42. C. J. Serpell, A. Y. Park, C. V. Robinson and P. D. Beer, *Chem. Commun.*, 2021, **57**, 101 – 104.

43. Y. Li, Y. Zhou, Y. Yao, T. Gao, P. Yan and H. Li, *New J. Chem.*, 2021, **45**, 7196 – 7203.

44. L. Liang, B. Li, W. Zhang, A. Li, B. Zheng, X.-J. Yang, B. Wu, L. Liang, B. Li, W. Zhang, A. Li, B. Zheng, B. Wu and X. Yang, *Angew. Chem. Int. Ed.*, 2021, **60**, 9389 – 9394.

45. J. L. Do, H. M. Titi, L. A. Cuccia and T. Friščić, *Chem. Commun*, 2021, **57**, 5143 – 5146.

46. Q. Guo, Y. Jiao, Y. Feng and J. F. Stoddart, *CCS Chemistry*, 2021, **3**, 1542 – 1572.

47. R. Aksakal, C. Mertens, M. Soete, N. Badi and F. Du Prez, *Adv. Sci.*, 2021, **8**, 2004038.

48. B. S. Pilgrim and N. R. Champness, *Chempluschem*, 2020, **85**, 1842 – 1856.

49. Z. Ma and B. Moulton, *Coord. Chem. Rev.*, 2011, **255**, 1623 – 1641.

50. Y. Xue, X. Hang, J. Ding, B. Li, R. Zhu, H. Pang and Q. Xu, *Coord. Chem. Rev.*, 2021, **430**, 213656.

51. G. A. Taggart, A. M. Antonio, G. R. Lorzing, G. R. Lorzing, G. P. A. Yap and E. D. Bloch, *ACS Appl. Mater. Interfaces*, 2020, **12**, 24913 – 24919.

52. P. J. Stang, D. H. Cao, S. Saito and A. M. Arif, *J. Am. Chem. Soc.*, 1995, **117**, 6273 – 6283.

53. J. M. Lehn, A. Rigault, J. Siegel, J. Harrowfield, B. Chevrier and D. Moras, *Proc. Natl. Acad. Sci.*, 1987, **84**, 2565 – 2569.

54. J. Xu, T. D. P. Stack and K. N. Raymond, *Inorg. Chem.*, 1992, **31**, 4903–4905.

55. M. Fujita, J. Yazaki and K. Ogura, *J. Am. Chem. Soc.*, 2002, **112**, 5645 – 5647.

56. P. J. Stang, *Eur. J. Chem.*, 1998, **4**, 19 – 27.

57. H. Gildenast, F. Busse and U. Englert, *Cryst. Growth Des.*, 2021, **21**, 5807 – 5817.

58. M. R. Dworzak, M. M. Deegan, G. P. A. Yap and E. D. Bloch, *Inorg. Chem.*, 2021, **60**, 5607 – 5616.

59. M. D. Johnstone, E. K. Schwarze, G. H. Clever and F. M. Pfeffer, *Eur. J. Chem.*, 2015, **21**, 3948 – 3955.

60. G. Markiewicz, D. Pakulski, A. Galanti, V. Patroniak, A. Ciesielski, A. R. Stefankiewicz and P. Samorì, *Chem. Commun.*, 2017, **53**, 7278 – 7281.

61. G. Markiewicz, A. Walczak, F. Perlitius, M. Piasecka, J. M. Harrowfield and A. R. Stefankiewicz, *Dalton Trans.*, 2018, **47**, 14254 – 14262.

62. A. Walczak, G. Kurpik and A. R. Stefankiewicz, *Int. J. Mol. Sci.*, 2020, **21**, 6171.

63. R. A. A. Abdine, G. Kurpik, A. Walczak, S. A. A. Aeash, A. R. Stefankiewicz, F. Monnier and M. Taillefer, *J. Catal*, 2019, **376**, 119 – 122.

64. E. G. Percástegui, J. Mosquera and J. R. Nitschke, *Angew. Chem.*, 2017, **129**, 9264 – 9268.

65. T. R. Cook, Y. R. Zheng and P. J. Stang, *Chem. Rev.*, 2012, **113**, 734 – 777.

66. M. Konopka, P. Cecot, S. Ulrich and A. R. Stefankiewicz, *Front. Chem.*, 2019, **7**, 503.

67. A. Bavykina, A. Cadiau and J. Gascon, *Coord. Chem. Rev.*, 2019, **386**, 85 – 95.

68. N. Giri, M. G. del Pópolo, G. Melaugh, R. L. Greenaway, K. Rätzke, T. Koschine, L. Pison, M. F. C. Gomes, A. I. Cooper and S. L. James, *Nature*, 2015, **527**, 216 – 220.

69. P. F. Fulvio and S. Dai, *Chem*, 2020, **6**, 3263 – 3287.

70. D. Wang, Y. Xin, D. Yao, X. Li, H. Ning, H. Zhang, Y. Wang, X. Ju, Z. He, Z. Yang, W. Fan, P. Li and Y. Zheng, *Adv. Funct. Mater.*, 2021, **32**, 2104162.

71. P. M. Schoenecker, C. G. Carson, H. Jasuja, C. J. J. Flemming and K. S. Walton, *Ind. Eng. Chem. Res.*, 2012, **51**, 6513 – 6519.

72. L. N. McHugh, M. J. McPherson, L. J. McCormick, S. A. Morris, P. S. Wheatley, S. J. Teat, D. McKay, D. M. Dawson, C. E. F. Sansome, S. E. Ashbrook, C. A. Stone, M. W. Smith and R. E. Morris, *Nat. Chem.*, 2018, **10**, 1096 – 1102.

73. E. G. Percástegui, T. K. Ronson and J. R. Nitschke, *Chem. Rev.*, 2020, **120**, 13480 – 13544.

74. D. Zhang, T. K. Ronson, J. Mosquera, A. Martinez, L. Guy and J. R. Nitschke, *J. Am. Chem. Soc.*, 2017, **139**, 6574 – 6577.

75. A. Brzechwa-Chodzyńska, W. Drożdż, J. Harrowfield and A. R. Stefankiewicz, *Coord. Chem. Rev.*, 2021, **434**, 213820.

76. Y. Yao, Y. Zhou, T. Zhu, T. Gao, H. Li and P. Yan, *ACS Appl. Mater. Interfaces*, 2020, **12**, 15338 – 15347.

77. Z. Gao, J. Jia, W. Fan, T. Liao and X. Zhang, *Chin. Chem. Lett.*, 2022, **33**, 4415 – 4420.

78. Y. Yao, J. Li, Y. Zhou, T. Gao, H. Li and P. Yan, *Dyes and Pigments*, 2021, **192**, 109441.

79. M. Pan, K. Wu, J. H. Zhang and C. Y. Su, *Coord. Chem. Rev.*, 2019, **378**, 333 – 349.

80. L. Cheng, K. Liu, Y. Duan, H. Duan, Y. Li, M. Gao and L. Cao, *CCS Chemistry*, 2021, **3**, 2749 – 2763.

81. N. Judge, L. Wang, Y. Y. L. Ho and Y. Wang, *Macromol. Res.*, 2018, **26**, 1074 – 1084.

82. S. M. McNeill, D. Preston, J. E. M. Lewis, A. Robert, K. Knerr-Rupp, D. O. Graham, J. R. Wright, G. I. Giles and J. D. Crowley, *Dalton Trans.*, 2015, **44**, 11129 – 11136.

83. D. Preston, S. M. McNeill, J. E. M. Lewis, G. I. Giles and J. D. Crowley, *Dalton Trans.*, 2016, **45**, 8050 – 8060.

84. N. P. E. Barry, O. Zava, P. J. Dyson and B. Therrien, *Eur. J. Chem.*, 2011, **17**, 9669 – 9677.

85. D. Fujita, Y. Ueda, S. Sato, H. Yokoyama, N. Mizuno, T. Kumasaka and M. Fujita, *Chem.*, 2016, **1**, 91 – 101.

86. I. Eryazici, C. N. Moorefield and G. R. Newkome, *Chem. Rev.*, 2008, **108**, 1834 – 1895.

87. R. A. Petros and J. M. Desimone, *Nat. Rev. Drug Discov.*, 2010, **9**, 615 – 627.

88. G. Yu, M. Jiang, F. Huang and X. Chen, *Curr. Opin. Chem. Biol.*, 2021, **61**, 19–31.

89. I. V. Grishagin, J. B. Pollock, S. Kushal, T. R. Cook, P. J. Stang and B. Z. Olenyuk, *Proc. Natl. Acad. Sci.*, 2014, **111**, 18448 – 18453.

90. Y. Zhao, L. Zhang, X. Li, Y. Shi, R. Ding, M. Teng, P. Zhang, C. Cao and P. J. Stang, *Proc. Natl. Acad. Sci.*, 2019, **116**, 4090 – 4098.

91. Z. Yue, H. Wang, Y. Li, Y. Qin, L. Xu, D. J. Bowers, M. Gangoda, X. Li, H. B. Yang and Y. R. Zheng, *Chem. Commun.*, 2018, **54**, 731 – 734.

92. S. R. Batten, N. R. Champness, X. M. Chen, J. Garcia-Martinez, S. Kitagawa, L. Öhrström, M. O'Keeffe, M. P. Suh and J. Reedijk, *Pure Appl. Chem.*, 2013, **85**, 1715 – 1724

93. P. Hubberstey, X. Lin, N. R. Champness and M. Schroder, in *Metal-Organic Frameworks - Design and Applications*, ed. L. R. MacGillivray, 2010, pp. 131–164.

94. B. Chen, Z. Yang, Y. Zhu and Y. Xia, *J. Mater. Chem. A*, 2014, **2**, 16811 – 16831.

95. S. M. Moosavi, A. Nandy, K. M. Jablonka, D. Ongari, J. P. Janet, P. G. Boyd, Y. Lee, B. Smit and H. J. Kulik, *Nat. Comm.*, 2020, **11**, 1 – 10.

96. M. Ding, X. Cai and H. L. Jiang, *Chem. Sci.*, 2019, **10**, 10209 – 10230.

97. J. C. J. Bailer, in *Preparative Inorganic Reactions*, Interscience Publishers, New York, 1964, vol. 1, pp. 1 – 27.

98. H. J. Buser, A. Ludi, D. Schwarzenbach and W. Petter, *Inorg. Chem.*, 1977, **16**, 2704 – 2710.

99. J. Brown, *Phil. Trans. Roy. Soc. London*, 1724, **33**, 17 – 24.

100. B. F. Hoskins and R. Robson, *J Am Chem Soc*, 1990, **112**, 1546–1554.

101. O. M. Yaghi, G. Li and H. Li, *Nature 1995 378:6558*, 1995, **378**, 703–706.

102. H. Li, M. Eddaoudi, M. O'Keeffe and O. M. Yaghi, *Nature*, 1999, **402**, 276 – 279.

103. F. Millange, C. Serre and G. Férey, *Chem. Commun.*, 2002, **2**, 822 – 823.

104. S. S. Y. Chui, S. M. F. Lo, J. P. H. Charmant, A. G. Orpen and I. D. Williams, *Science*, 1999, **283**, 1148 – 1150.

105. W. Lu, Z. Wei, Z. Y. Gu, T. F. Liu, J. Park, J. Park, J. Tian, M. Zhang, Q. Zhang, T. Gentle, M. Bosch and H. C. Zhou, *Chem. Soc. Rev.*, 2014, **43**, 5561 – 5593.

106. Z. Wang and S. M. Cohen, *J. Am. Chem. Soc.*, 2007, **129**, 12368 – 12369.

107. M. Eddaoudi, J. Kim, N. Rosi, D. Vodak, J. Wachter, M. O'Keeffe and O. M. Yaghi, *Science*, 2002, **295**, 469 – 472.

108. H. J. Park, Y. E. Cheon and M. P. Suh, *Eur. J. Chem*, 2010, **16**, 11662 – 11669.

109. O. Karagiaridi, W. Bury, A. A. Sarjeant, C. L. Stern, O. K. Farha and J. T. Hupp, *Chem. Sci.*, 2012, **3**, 3256 – 3260.

110. Y. Tian, S. Yao, D. Gu, K. Cui, D. Guo, G. Zhang, Z. Chen, D. Zhao, Y. Tian, S. Yao, K. Cui, D. Guo, G. Zhang, Z. Chen and D. Zhao, *Eur. J. Chem.*, 2010, **16**, 1137 – 1141.

111. J. H. Cavka, S. Jakobsen, U. Olsbye, N. Guillou, C. Lamberti, S. Bordiga and K. P. Lillerud, *J. Am. Chem. Soc.*, 2008, **130**, 13850 – 13851.

112. T. Loiseau, C. Serre, C. Huguenard, G. Fink, F. Taulelle, M. Henry, T. Bataille and G. Férey, *Eur. J. Chem.*, 2004, **10**, 1373 – 1382.

113. K. Manna, P. Ji, Z. Lin, F. X. Greene, A. Urban, N. C. Thacker and W. Lin, *Nat. Commun.*, 2016, **7**, 1 – 11.

114. X. Ye and D. Liu, *Cryst. Growth Des.*, 2021, **21**, 4780 – 4804.

115. J. H. Lee, S. Jeoung, Y. G. Chung and H. R. Moon, *Coord. Chem. Rev.*, 2019, **389**, 161 – 188.

116. S. Wang, C. M. McGuirk, A. D'Aquino, J. A. Mason and C. A. Mirkin, *Adv. Mater.*, 2018, **30**, 1800202.

117. Q. Qian, P. A. Asinger, M. J. Lee, G. Han, K. M. Rodriguez, S. Lin, F. M. Benedetti, A. X. Wu, W. S. Chi and Z. P. Smith, *Chem. Rev.*, 2020, **120**, 8161 – 8266.

118. Y. Ming, N. Kumar and D. J. Siegel, *ACS Omega*, 2017, **2**, 4921 – 4928.

119. K. Tan, N. Nijem, Y. Gao, S. Zuluaga, J. Li, T. Thonhauser and Y. J. Chabal, *CrystEngComm*, 2014, **17**, 247 – 260.

120. J. B. Decoste, G. W. Peterson, B. J. Schindler, K. L. Killops, M. A. Browe and J. J. Mahle, *J. Mater. Chem. A*, 2013, **1**, 11922 – 11932.

121. J. Yang, A. Grzech, F. M. Mulder and T. J. Dingemans, *Chem. Commun.*, 2011, **47**, 5244 – 5246.

122. S. Xu, X. Guo, Z. Qiao, H. Huang and C. Zhong, *Ind. Eng. Chem. Res.*, 2020, **59**, 12451 – 12457.

123. D. Ma, Y. Li and Z. Li, *Chem. Commun.*, 2011, **47**, 7377 – 7379.

124. C. Serre, *Angew. Chem. Int. Ed.*, 2012, **51**, 6048 – 6050.

125. L. Kimberley, A. M. Sheveleva, J. Li, J. H. Carter, X. Kang, G. L. Smith, X. Han, S. J. Day, C. C. Tang, F. Tuna, E. J. L. McInnes, S. Yang and M. Schröder, *Angew. Chem.*, 2021, **133**, 15371 – 15375.

126. N. Sikdar, J. R. C. Junqueira, S. Dieckhöfer, T. Quast, M. Braun, Y. Song, H. B. Aiyappa, S. Seisel, J. Weidner, D. Öhl, C. Andronescu and W. Schuhmann, *Angew. Chem. Int. Ed.*, 2021, **60**, 23427 – 23434.

127. R. Cui, P. Zhao, Y. Yan, G. Bao, A. Damirin and Z. Liu, *Inorg. Chem.*, 2021, **60**, 1664 – 1671.

128. R. C. Alves, Z. M. Schulte, M. T. Luiz, P. B. D. Silva, R. C. G. Frem, N. L. Rosi and M. Chorilli, *Inorg. Chem.*, 2021, **60**, 11739 – 11744.

129. S. Okur, P. Qin, A. Chandresh, C. Li, Z. Zhang, U. Lemmer and L. Heinke, *Angew. Chem. Int. Ed.*, 2021, **60**, 3566 – 3571.

130. M. Lei, F. Ge, X. Gao, Z. Shi and H. Zheng, *Inorg. Chem.*, 2021, **60**, 10513 – 10521.

131. S. E. Henkelis, P. T. Judge, S. E. Hayes and T. M. Nenoff, *ACS Applied Mater. Interfaces*, 2021, **13**, 7278 – 7284.

132. P. Zhou, X. Wang, L. Yue, L. Fan and Y. He, *Inorg. Chem.*, 2021, **60**, 14969 – 14977.

133. Y. Wen, J. Zhang, Q. Xu, X. T. Wu and Q. L. Zhu, *Coord. Chem. Rev.*, 2018, **376**, 248 – 276.

134. S. L. Hou, J. Dong, X. L. Jiang, Z. H. Jiao and B. Zhao, *Angew. Chem. Int. Ed.*, 2019, **58**, 577 – 581.

135. E. D. Metzger, R. J. Comito, Z. Wu, G. Zhang, R. C. Dubey, W. Xu, J. T. Miller and M. Dinca, *ACS Sustain. Chem. Eng.*, 2019, **7**, 6654 – 6661.

136. S. Rojas-Buzo, P. Concepción, J. L. Olloqui-Sariego, M. Moliner and A. Corma, *ACS Appl. Mater. Interfaces*, 2021, **13**, 31021 – 31030.

137. Y. Li, *Polyhedron*, 2020, **179**, 114413.

138. X. Wu, L. K. Macreadie and P. A. Gale, *Coord. Chem. Rev*, 2021, **432**, 213708.

139. C. Lai, Z. Wang, L. Qin, Y. Fu, B. Li, M. Zhang, S. Liu, L. Li, H. Yi, X. Liu, X. Zhou, N. An, Z. An, X. Shi and C. Feng, *Coord. Chem. Rev.*, 2021, **427**, 213565.

140. P. Raja Lakshmi, P. Nanjan, S. Kannan and S. Shanmugaraju, *Coord. Chem. Rev.*, 2021, **435**, 213793.

141. J. C. G. Bünzli and C. Piguet, *Chem. Soc. Rev.*, 2005, **34**, 1048 – 1077.

142. T. Sun, Y. Gao, Y. Du, L. Zhou and X. Chen, *Front. Chem.*, 2021, **8**, 1291.

143. A. F. Wells, *Acta Crystallogr.*, 1954, **7**, 535 – 544.

144. A. F. Wells and R. R. Sharpe, *Acta Crystallogr.*, 1963, **16**, 857–871.

145. A. F. Wells, *Acta Crystallogr.*, 1954, **7**, 545–554.

146. A. F. Wells, *Acta Crystallogr.*, 1954, **7**, 842–848.

147. A. F. Wells, *Three-dimensional nets and polyhedra*, 1st ed., Wiley, New York, 1977.

148. V. A. Blatov, M. O'Keeffe and D. M. Proserpio, *CrystEngComm,*, 2009, **12**, 44 – 48.

149. M. O'Keeffe, M. A. Peskov, S. J. Ramsden and O. M. Yaghi, *Acc. Chem. Res.*, 2008, **41**, 1782 – 1789.

150. B. Chen, M. Eddaoudi, S. T. Hyde, M. O'Keeffe and O. M. Yaghi, *Science*, 2001, **291**, 1021 – 1023.

151. G. Mahmoudi and A. Morsali, *CrystEngComm*, 2009, **11**, 50 – 51.

152. J. J. Fu, J. G. Wo, Y. H. Luo, A. D. Xie, J. Wu, Y. Y. Zhang, Y. B. Zhao and D. E. Zhang, *J. Solid State Chem.*, 2021, **294**, 121839.

153. J. W. Steed and J. L. Atwood, *Supramolecular Chemistry*, 2nd edn., John Wiley and Sons, 2009.

154. S. W. Kelemu and P. J. Steel, *Eur. J. Inorg. Chem.*, 2014, **2014**, 434 – 436.

155. G. Truccolo, Z. Tessari, J. Tessarolo, S. Quici, L. Armelao and M. Rancan, *Dalton Trans.*, 2018, **47**, 12079 – 12084.

156. J. E. Mizzi and R. L. Laduca, *Inorganic Chem. Commun.*, 2016, **70**, 4 – 6.

157. S. Lee, D. Kim, J. Kim and O. S. Jung, *Cryst. Growth Des.*, 2020, **20**, 3601 – 3604.

158. G. Liu, Y. Li, Z. Lu, X. Li, X. Wang, X. Wang and X. Chen, *CrystEngComm*, 2019, **21**, 5344 – 5355.

159. J. Lin, H. Lin, Y. Liu, J. Lu and X. Wang, *J. Solid State Chem.*, 2021, **307**, 122869.

160. P. Thuéry and J. Harrowfield, *Inorg. Chem.*, 2021, **60**, 9074 – 9083.

161. H. Ju, M. Shin, I. H. Park, J. H. Jung, J. J. Vittal and S. S. Lee, *Inorg. Chem.*, 2021, **60**, 8285 – 8292.

162. H. Wu, H. Y. Liu, J. Yang, B. Liu, J. F. Ma, Y. Y. Liu and Y. Y. Liu, *Cryst. Growth Des.*, 2011, **11**, 2317 – 2324.

163. H. Guo, D. Qiu, X. Guo, S. R. Batten and H. Zhang, *CrystEngComm*, 2009, **11**, 2611 – 2614.

164. J. W. Yi, H. R. Fu, M. L. Han and D. S. Li, *Inorganic Chemistry Communications*, 2020, **112**, 107702.

165. L. P. Xue, Z. H. Li, T. Zhang, J. J. Cui, Y. Gao and J. X. Yao, *New J. Chem.*, 2018, **42**, 14203 – 14209.

166. R. Abazari, E. Yazdani, M. Nadafan, A. M. Kirillov, J. Gao, A. M. Z. Slawin and C. L. Carpenter-Warren, *Inorg. Chem.*, 2021, **60**, 9700 – 9708.

167. T. Liu, X. Shen, X. Shen, C. He, J. Liu and J. J. Liu, *CrystEngComm*, 2021, **23**, 4667 – 4673.

168. N. G. M. L. US Department of Commerce, Global Monitoring Laboratory - Carbon Cycle Greenhouse Gases, https://gml.noaa.gov/ccgg/trends/ (accessed January 14, 2022).

169. E. Monnin, A. Indermühle, A. Dällenbach, J. Flückiger, B. Stauffer, T. F. Stocker, D. Raynaud and J. M. Barnola, *Science*, 2001, **291**, 112 – 114.

170. C. Weyant, M. L. Brandeau, M. Burke, D. B. Lobell, E. Bendavid and S. Basu, *PLOS Med.*, 2018, **15**, e1002586.

171. R. Heede, *Clim. Change*, 2014, **122**, 229 – 241.

172. S. Bachu, *Prog. Energy Combust. Sci.*, 2008, **34**, 254 – 273.

173. A. D. N. Kamkeng, M. Wang, J. Hu, W. Du and F. Qian, *Chem. Eng. J.*, 2021, **409**, 128138.

174. E. J. Granite and H. W. Pennline, *Ind. Eng. Chem. Res.*, 2002, **41**, 5470 – 5476.

175. E. S. Rubin, H. Mantripragada, A. Marks, P. Versteeg and J. Kitchin, *Prog. Energy Combust. Sci.*, 2012, **38**, 630 – 671.

176. G. T. Rochelle, *Science*, 2009, **325**, 1652 – 1654.

177. R. S. Haszeldine, *Science*, 2009, **325**, 1647 – 1652.

178. G. T. Rochelle, *Curr. Opin. Chem. Eng.*, 2012, **1**, 183 – 190.

179. J. R. Li, R. J. Kuppler and H. C. Zhou, *Chem. Soc. Rev.*, 2009, **38**, 1477 – 1504.

180. R. Poloni, K. Lee, R. F. Berger, B. Smit and J. B. Neaton, *J. Phys. Chem. Lett.*, 2014, **5**, 861 – 865.

181. R. A. Maia, B. Louis, W. Gao and Q. Wang, *React. Chem. Eng.*, 2021, **6**, 1118 – 1133.

182. S. Kazemi and V. Safarifard, *Polyhedron*, 2018, **154**, 236 – 251.

183. P. Z. Li and Y. Zhao, *Chem. Asian J.*, 2013, **8**, 1680 – 1691.

184. C. Song, J. Hu, Y. Ling, Y. Feng, R. Krishna, D. L. Chen and Y. He, *J. Mater. Chem. A*, 2015, **3**, 19417 – 19426.

185. D. Yu, A. O. Yazaydin, J. R. Lane, P. D. C. Dietzel and R. Q. Snurr, *Chem. Sci.*, 2013, **4**, 3544 – 3556.

186. X. L. Yang, Y. T. Yan, W. J. Wang, Z. Z. Hao, W. Y. Zhang, W. Huang and Y. Y. Wang, *Inorg. Chem.*, 2021, **60**, 3156 – 3164.

187. Y. Zhao, J. Liu, M. le Han, G. P. Yang, L. F. Ma and Y. Y. Wang, *Rare Metals*, 2021, **40**, 499 – 504.

188. R. Goswami, N. Seal, S. R. Dash, A. Tyagi and S. Neogi, *ACS Appl. Mater. Interfaces*, 2019, **11**, 40134 – 40150.

189. S. G. Gizer and N. Sahiner, *Inorg. Chim. Acta*, 2021, **528**, 120611.

190. J. Wang, Z. Wei, F. Guo, C. Li, P. Zhu and W. Zhu, *Dalton Trans.*, 2015, **44**, 13809 – 13813.

191. D. Sun, Y. H. Li, S. T. Wu, H. J. Hao, F. J. Liu, R. B. Huang and L. S. Zheng, *CrystEngComm*, 2011, **13**, 7311 – 7315.

192. M. S. Deshpande, A. S. Kumbhar and C. Näther, *Dalton Trans.*, 2010, **39**, 9146 – 9152.

193. H. Li, M. Eddaoudi, T. L. Groy and O. M. Yaghi, *J. Am. Chem. Soc.*, 1998, **120**, 8571 – 8572.

194. C. Férey, C. Mellot-Draznieks, C. Serre, F. Millange, J. Dutour, S. Surblé and I. Margiolaki, *Science*, 2005, **309**, 2040 – 2042.

195. A. E. M. Díaz and J. E. M. Lewis, *Front. Chem.*, 2021, **9**, 456.

196. O. Jurček, Nonappa, E. Kalenius, P. Jurček, J. M. Linnanto, R. Puttreddy, H. Valkenier, N. Houbenov, M. Babiak, M. Peterek, A. P. Davis, R. Marek and K. Rissanen, *Cell Rep. Phys. Sci.*, 2021, **2**, 100303.

197. M. D. Ward, C. A. Hunter and N. H. Williams, *Acc. Chem. Res.*, 2018, **51**, 2073 – 2082.

198. A. P . Katsoulidis, D. Antypov, G. F. S. Whitehead, E. J. Carrington, D. J. Adams, N. G. Berry, G. R. Darling, M. S. Dyer and M. J. Rosseinsky, *Nature*, 2019, **565**, 213 – 217.

199. J. Clayden, N. Greeves and S. Warren, in *Organic Chemistry*, 2012, vol. 2, pp. 360–381.

200. S. L. Wang, F. L. Hu, J. Y. Zhou, Y. Zhou, Q. Huang and J. P. Lang, *Cryst. Growth Des.*, 2015, **15**, 4087 – 4097.

201. F. H. Zhao, L. W. Huang, Y. C. He, X. Q. Yan, Z. L. Li, X. M. Jia, R. Feng, J. X. Li and J. M. You, *Inorg. Chim. Acta.*, 2020, **499**, 119184.

202. L. Carlucci, G. Ciani and D. M. Proserpio, *Coord. Chem. Rev.*, 2003, **246**, 247 – 289.

203. J. G. Nguyen and S. M. Cohen, *J. Am. Chem. Soc.*, 2010, **132**, 4560 – 4561.

204. H. Jasuja, Y. Huang and K. S. Walton, *Langmuir*, 2012, **28**, 16874 – 16880.

205. W. Bi, R. Cao, D. Sun, D. Yuan, X. Li, Y. Wang, X. Li and M. Hong, *Chem. Commun.*, 2004, 2104 – 2105.

206. M. Kurmoo, H. Kumagai, M. Akita-Tanaka, K. Inoue and S. Takagi, *Inorg. Chem*, 2006, **45**, 1627 – 1637.

207. Y. J. Kim and D. Y. Jung, *Chem. Commun.*, 2002, **2**, 908 – 909.

208. J. C. C. Houlihan, S. C. Moratti and L. R. Hanton, *Dalton Trans.*, 2020, **49**, 12009 – 12017.

209. G. A. Senchyk, A. B. Lysenko, H. Krautscheid, E. B. Rusanov, A. N. Chernega, K. W. Krämer, S. X. Liu, S. Decurtins and K. V. Domasevitch, *Inorg. Chem.*, 2013, **52**, 863 – 872.

210. L. K. Macreadie, E. J. Mensforth, R. Babarao, K. Konstas, S. G. Telfer, C. M. Doherty, J. Tsanaktsidis, S. R. Batten and M. R. Hill, *J. Am. Chem. Soc.*, 2019, **141**, 3828 – 3832.

211. L. K. Macreadie, R. Babarao, C. J. Setter, S. J. Lee, O. T. Qazvini, A. J. Seeber, J. Tsanaktsidis, S. G. Telfer, S. R. Batten and M. R. Hill, *Angew. Chem. Int. Ed.*, 2020, **59**, 6090 – 6098.

212. A. D. Dharma, C. Chen and L. K. Macreadie, *Aus. J. Chem.*, 2022, **75**, 155 – 159.

213. K. B. Idrees, Z. Chen, X. Zhang, M. R. Mian, R. J. Drout, T. Islamoglu and O. K. Farha, *Chem. Mater.*, 2020, **32**, 3776 – 3782.

214. R. Willstätter, *Justus Liebigs Ann. Chem.*, 1901, **317**, 204 – 265.

215. R. R. Robinson, *J. Chem. Soc., Trans.*, 1917, **111**, 762 – 768.

216. K. L. Kohnen-Johannsen and O. Kayser, *Molecules*, 2019, **24**, 796.

217. J. Jirschitzka, G. W. Schmidt, M. Reichelt, B. Schneider, J. Gershenzon and J. C. D'Auria, *Proc Nat. Acad. Sci.*, 2012, **109**, 10304 – 10309.

218. K. L. Kohnen-Johannsen and O. Kayser, *Molecules*, 2019, **24**, 796.

219. M. Heinrich and A. K. Jäger, *Ethnopharmacology*, 2015.

220. S. E. Avetisov, V. P. Fisenko, A. S. Zhuravlev and K. S. Avetisov, *Vestn. Oftalmol*, 2018, **134**, 84 – 90.

221. H. Smulyan, *Am. J. Med. Sci.*, 2018, **356**, 441 – 450.

222. Sir Robert Robinson - Biographical - NobelPrize.org, https://www.nobelprize.org/prizes/chemistry/1947/robinson/biographical/, (accessed December 29, 2021).

223. J. W. Medley and M. Movassaghi, *Chem. Commun.*, 2013, **49**, 10775 – 10777.

224. D. Fujita, Y. Ueda, S. Sato, N. Mizuno, T. Kumasaka and M. Fujita, *Nature*, 2016, **540**, 563 – 566.

225. M. Shöâeè, J. R. Agger, M. W. Anderson and M. P. Attfield, *CrystEngComm*, 2008, **10**, 646 – 648.

Chapter 2

· Complexes of 4-Picolyl Ligands ·

2.1 Introduction

Aromatic ligands are ubiquitous in coordination chemistry and their behaviour is well-known, which has allowed for the advancement of structure prediction technology,[1,2] of these materials in metallosupramolecular systems. The ligands possess a level of rigidity, which in turn simplifies the structure prediction process. They also tend to absorb visible or near-UV radiation, allowing the formation of complexes to be monitored in real time *via* various spectroscopic techniques such as UV-Vis and fluorescence spectroscopy,[3] providing insight into the mechanism of the formation of these complexes in solution. Knowledge of certain properties of these complexes can then be inferred from their behaviour in solution, which may be beneficial for future application-driven design of coordination materials.

Aliphatic ligands are much less studied than their aromatic counterparts, due to their relatively higher flexibility (which makes structure prediction more challenging) and absence of chromophores, making the mechanism of assembly of their complexes more difficult to monitor. The influence of aliphatic moieties on the non-covalent interactions and subsequent crystal packing of their coordination complexes is therefore less understood. As the geometry of these compounds is much more diverse than their aromatic counterparts, the range of possible short contacts such as hydrogen bonding is much more varied.

Piperidine and morpholine functionalities (such as those containing the picolyl moieties in **L2.1** and **L2.2** in Figure 2.1, respectively) have commonly been incorporated into coordinating ligands to impart some specific function on the ligand, rather than to examine their effect on the crystal packing. Lovitt *et. al.*[4] reported two morpholino-substituted naphthalimide ligands, in which the morpholino functionality is used to enhance the photophysical and pH-responsive properties of the ligand for use in fluorescent manganese(II) and cobalt(II) materials. Lee *et. al.*[5] reported a morpholine-derived fluorescent probe for the detection of zinc(II) ions, again incorporating the morpholino functionality to enhance the electronic properties, which is a common practice when designing fluorescent materials.[6,7] Similarly, a piperidine-containing naphthalimide ligand, reported by Szakács *et. al.*[8] show that the incorporation of piperidine into the ligand also improved its fluorescent properties.

Alternatively, Miller *et. al.* reported a library of morpholino-containing salen-type ligands in which the morpholino component acts as a proton acceptor in materials that recover metal ions from aqueous solutions.[9] Piperidine, on the other hand, has been incorporated into ligands to add rigidity, for example, to a manganese(II) complex as an MRI contrast agent, reported by Martinelli *et. al.*[10] Despite this wide range of piperidine- and morpholine-containing ligands, systematic investigations of the specific intermolecular contacts involving these groups are not common.

L2.1 and **L2.2** (Figure 2.1) were synthesised, as representative simplified amine-containing alicycles, to gain some initial insight into the behaviour of these types of ligand molecules in coordination complexes, to then apply this understanding to the prediction of complexes incorporating more structurally complex ligands, such as those presented in subsequent chapters. **L2.1** and **L2.2** are ligands that contain both an aliphatic amine and an aromatic component, which serve as simplified analogues to tropinone-containing ligands, discussed in Chapters 3 and 4. Close attention was paid to the behaviour of both the aromatic and aliphatic components of the ligands and the weaker interactions that affect the crystal packing of the complexes.

`

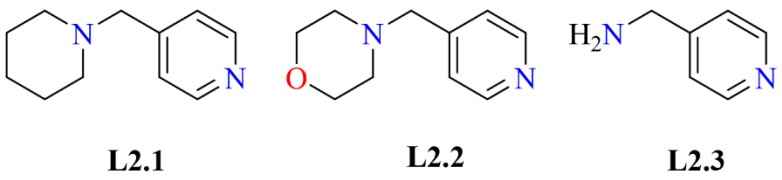

*Figure 2.1. Structures of piperidine-derived **L2.1**, morpholine-derived **L2.2** and **L2.3***

These ligands were combined with late third row transition metal ions – copper(II) and cobalt(II) to study the geometric constraints imparted by the metal ion. On the other hand, complexes of a softer acid metal ion, silver(I), allow for the geometric constraints of the ligand to have a larger influence over the resulting coordination complexes, due to the more geometrically flexible nature of the d^{10} metal ion. The single-atom difference between the piperidine- and morpholine-containing ligands drew attention to the weaker interactions in the coordination complexes and their effects on the overall crystal packing. The morpholine oxygen atom (which is absent in **L2.1**) introduces an added hydrogen-bond acceptor into the complexes, resulting in a significantly different hydrogen bonding network in each case, as when the ligand nitrogen atoms are coordinating there are no hydrogen bond acceptors in the molecule. This difference between **L2.1** and **L2.2** also result in a significant difference between their pKa values – piperidine has a pKa of ≈ 11, whereas the pKa of morpholine is much lower (≈ 8). The difference in pKa values between the two ligand precursors likely will have a marked effect on the likelihood of the formation of a coordination complex, which may justify the higher success rate of the formation of coordination complexes of **L2.1**, relative to **L2.2**.[11] Finally, **L2.3** was introduced into this study to observe the effect of a much less sterically hindered amine on the coordination observed in the metal complexes. Again, comparisons were made between complexes of different metal ions, however, this ligand served as an important contrast to the larger ligands **L2.1** and **L2.2.**

The solvents used for the syntheses were chosen based on several factors.[12] Firstly, solubility of the reagents was important to consider, and as both the ligand and metal ion are reasonably polar materials, polar solvents

such as methanol and acetonitrile were frequently used throughout the syntheses. Secondly, the coordinating ability of the solvents was an important factor, as they could compete with the ligands for coordination to the metal ion, possibly resulting in no desired ligand coordination. In particular in the synthesis of porous materials, solvent choice can also play a vital templating role, and therefore solvents of a certain size or property can be carefully selected to impart certain properties on the material. An elegant example of this was reported by Zuo *et. al.*,[13] in which two magnesium-based MOFs were synthesised in two different solvent systems (DMF/H_2O and DMSO/DMF/H_2O) resulting in the templating of two different magnesium-containing nodes. A low boiling point solvent may also be desirable as it would be easily removed from the pores for guest adsorption applications.

2.2 Hirshfeld Surface Analysis

Hirshfeld surface analysis[14] was used throughout the study of these complexes, to visualise and examine the variety in surface interactions between neighbouring moieties in the crystal structure. Most of the complexes of ligands **L2.1 – L2.3** are discrete, and their interaction with neighbouring discrete complexes could be easily observed and simplified to interactions between certain atoms near the surface. The Hirshfeld surface is described by Spackman *et. al.* as a shape that "defines the volume of space where the promolecule electron density exceeds that from all neighbouring molecules".[14]

The mapping onto this surface (in this chapter), is done so based on a normalised contact distance, d_{norm}, which is given in terms of the distance from the surface to the nearest atom inside the surface, d_i, and the distance from the surface to the nearest atom outside the surface, d_e, and is determined using Equation 2.1,

Equation 2.1

$$d_{norm} = \frac{d_i - {r_i}^{vdw}}{{r_i}^{vdw}} + \frac{d_e - {r_e}^{vdw}}{{r_e}^{vdw}}$$

where r^{vdw} are the van der Waals radii of the atoms inside (i) and outside (e) of the Hirshfeld surface. The

`

result is that d_{norm} is a positive or negative value indicating that intermolecular contacts are, respectively, shorter or longer than the van der Waals separations. The visualisation of this on the Hirshfeld surface results in a red area on the surface map where contacts are shorter than the van der Waals separations (i.e., d_{norm} is positive), indicating the presence of some interactions with a neighbouring crystallographic fragment. A two-dimensional fingerprint plot of d_e vs. d_i, summarises all of the intermolecular contacts present in the system and can be narrowed down to interactions between specific elements inside and/or outside of the surface.

This large variety of interactions and effects even in complexes of relatively simple ligand molecules is indicative of the complexity of interactions present in more structurally elaborate ligands (such as those in Chapters **3** and **4**) and their complexes. The knowledge gained from studies of the complexes of **L2.1**, **L2.2** and **L2.3** demonstrate the importance of the more subtle interactions in these complexes and will assist in the design and prediction of complexes of similar tropinone-containing ligands.

2.3 Ligand Synthesis

N-alkylation was the chosen method for the synthesis of tertiary amine-containing ligands **L2.1** and **L2.2**, starting from the corresponding secondary amines – piperidine and morpholine, respectively, and an alkyl halide – 4-(chloromethyl)pyridine, outlined in Scheme 2.1.

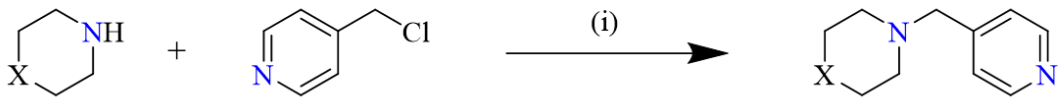

L2.1 X = CH_2
L2.2 X = O

*Scheme 2.1. General synthetic scheme for the synthesis of ligands **L2.1** and **L2.2**, (i) K_2CO_3, KI, MeCN*

For the synthesis of secondary amines, other methods such as reductive amination of an aldehyde or ketone, or reduction of an amide, are preferable, as *N*-alkylation could result in a mixture of mono- and di-alkylated products, as well as a quaternary salt, subsequently requiring more complex purification.[15] However, the synthesis of tertiary amines *via N*-alkylation is much more straightforward, as over-alkylation is less likely,[16] but also easier to separate, as the resulting product would contain a charged quaternary nitrogen atom, and would therefore be water-soluble, requiring a simple liquid-liquid extraction in order to obtain the product in high purity. Both piperidine[17] and morpholine[18] are used as precursors for pharmaceuticals and both are occasionally used as a solvent or a base, making them both accessible commercially available precursors for the syntheses of **L2.1** and **L2.2**, respectively.

The *N*-alkylation was carried out using excess potassium carbonate and a catalytic amount of potassium iodide in a Finkelstein reaction.[19] In the reaction, a small quantity of 4-(chloromethyl)pyridine is converted to the alkyl iodide, and iodide is a much better leaving group than chloride, which results in the formation of the product and regeneration of the KI catalyst. This is promoted by the formation of potassium chloride, which has very low solubility in acetonitrile and precipitates, driving the equilibrium towards the alkyl iodide, which then reacts to irreversibly form the products, **L2.1** and **L2.2**.

2.4 Copper(II) Chloride Complexes of L2.1 and L2.2

Combination of **L2.1** and **L2.2** with $CuCl_2 \cdot 2H_2O$ in each case yielded a tetranuclear copper(II) cluster, Cu_4OCl_6, which varied slightly depending on the ligand and the solvent used. [Cu_4OCl_6(**L2.1**)$_4$] (complex **2.1**) formed the same complex in both methanol and acetonitrile, and the crystal structure was solved and refined in the tetragonal space group $I4_1/a$. The asymmetric unit (shown in Figure 2.2) was found to contain one copper(II) ion, coordinated by one ligand molecule *via* the pyridyl nitrogen atom, an oxygen atom and two chlorido ligands.

`

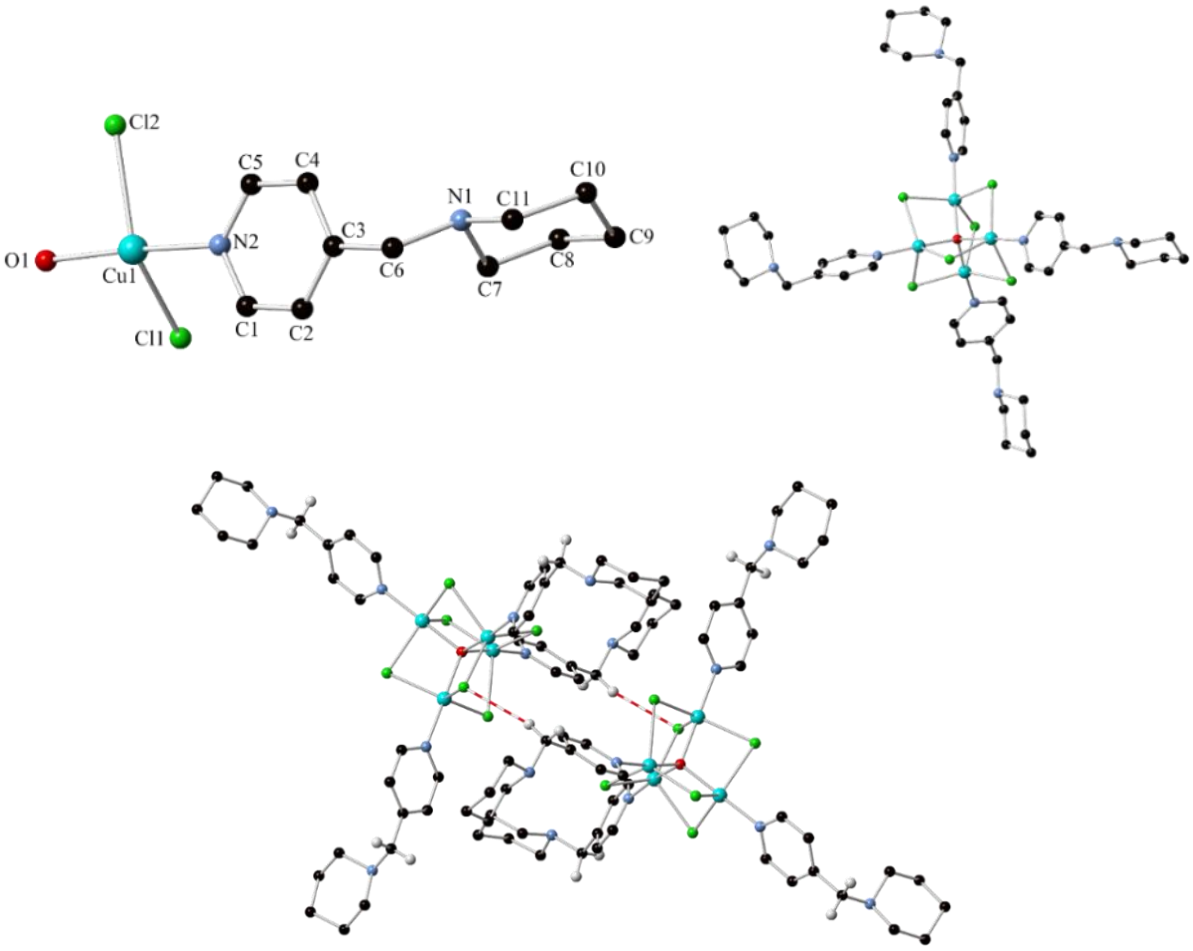

*Figure 2.2. Asymmetric unit (top, left), discrete cluster (top, right) and C-H···Cl contacts (bottom) in [Cu_4OCl_6(**L2.1**)$_4$] (complex **2.1**) (some hydrogen atoms were omitted for clarity)*

The structure grows into a discrete tetranuclear complex, containing four ligand molecules, coordinated to one copper(II) ion each, which form an internal tetrahedral Cu_4OCl_6 cluster, with the Cu1···Cu1′ distances measuring at 3.1245(6) Å. The resulting geometry of the copper(II) is trigonal bipyramidal, and the equatorial Cu1-Cl bond lengths are significantly longer (2.3844(9), 2.3500(9) and 2.4999(9) Å for Cl1, Cl2 and Cl2′ respectively) than the axial Cu1-O1 (1.9072(4)Å) and Cu1-N2 (1.981(3)Å) bonds. The coordination geometry of the copper(II) deviates slightly from a perfect trigonal bipyramid – the equatorial angles varying from 107.747(2)° to 131.950(2)°, while the axial angles are all within 90±8° (τ_5 = 0.711).[20] While the τ_5 parameter is indicative of a trigonal bipyramidal coordination geometry, the Cu1-Cl2′ bond length is substantially longer than the remaining Cu1-Cl bond lengths, possibly suggesting some distorted

square planar character in the metal coordination sphere. The intermolecular interactions between the discrete complexes are dominated by C-H···Cl weak interactions, with the bridging CH_2 involved in the interaction (with a C-Cl distance of 3.784(4) Å and a C-H···Cl angle of 165.5(2)°, shown in Figure 2.2.

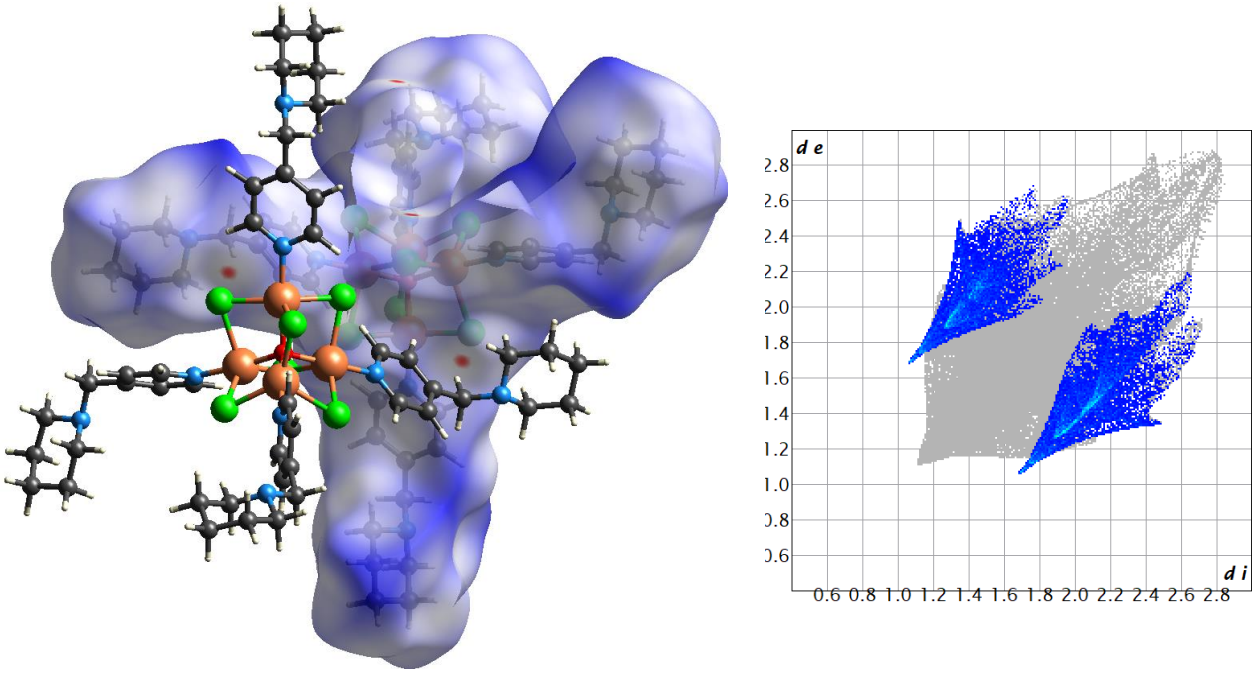

*Figure 2.3. d_{norm} mapping of the Hirshfeld surface (left) and 2D fingerprint plot of Cl···O interactions in $[Cu_4OCl_6(\mathbf{L2.1})_4]$ (complex **2.1**)*

d_{norm} mapping of the Hirshfeld surface and the associated 2D fingerprint plot (Figure 2.3 above) confirm that these are the dominating intermolecular interactions. This is surprising, given that as the piperidine nitrogen atom is not coordinating, it would therefore be assumed to be a better hydrogen bond acceptor than a doubly bridging chlorido ligand. This interaction results in the respective orientation of the ligand pyridyl moieties to not allow for π-π interactions between adjacent discrete complexes.

`

Complexes of **L2.2** offer an interesting comparison to complex **2.1**, with the tetranuclear complex present in all three complexes (**2.1**, **2.2** and **2.3**), however in the case of **L2.2**, the chosen solvent participates in the formation of the resulting coordination complexes. The protic nature of methanol and the added hydrogen bond acceptor in the morpholine oxygen atom introduces new potential interactions, that are not possible with an aprotic solvent such as acetonitrile or in complexes of **L2.1**, leading to different resulting coordination complexes.

The crystallographic data of $[Cu_4OCl_6(\mathbf{L2.2})_4]\cdot 2MeOH$ (complex **2.2**) were solved and refined in the triclinic space group $P\bar{1}$ and the asymmetric unit (shown in Figure 2.4) consists of a similar Cu_4OCl_6 cluster as seen in the previous complex, with four ligand molecules, each coordinating to a copper(II) ion *via* the pyridyl nitrogen atom, but in this case the entire discrete complex makes up the asymmetric unit, with two slightly disordered methanol solvent molecules. The inequivalence of the four ligand molecules is exemplified by the solvent methanol molecules interacting with a pyridyl C-H group and a morpholine oxygen atom in the discrete complex, and the slightly distorted nature of the interior Cu_4OCl_6 cluster.

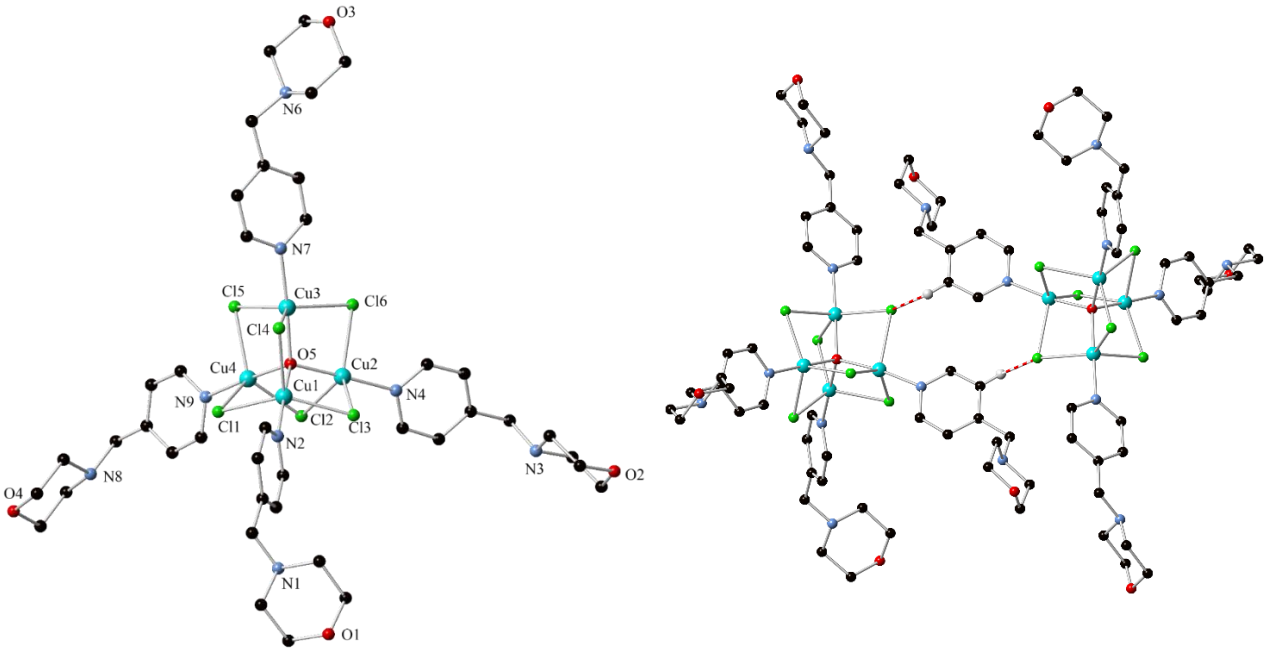

*Figure 2.4. Asymmetric unit of $[Cu_4OCl_6(\mathbf{L2.2})_4]\cdot 2MeOH$ (complex **2.2**) (left) and CH···Cl contacts between discrete complex **2.2** clusters (right) (some hydrogen atoms and solvent molecules were omitted for clarity)*

The coordination geometry of each copper(II) ion is again trigonal bipyramidal, however the τ_5 parameter of Cu1 (0.529) differs significantly to that of Cu2, Cu3 and Cu4 (0.865, 0.826 and 0.818, respectively). The bond lengths, however, remain consistent for each copper(II) ion, with the equatorial Cu1-Cl bond lengths (2.427(1), 2.3726(10) and 2.4063(10) Å for Cl1, Cl2 and Cl3, respectively) being significantly longer than the axial Cu1-O5 (1.896(2)Å) and Cu1-N2 (1.980(3)Å) bonds. The Cu···Cu distances range from 3.0652(3) to 3.1410(3) Å.

The weak C-H···Cl interactions are again present between neighbouring discrete complexes, and this time it is the 3-pyridyl CH that is involved in this interaction, with a C···Cl distance of 3.6841(19) Å and a C-H···Cl angle of 173.41(12)°, visualised in Figure 2.4. This is confirmed to be the dominant interaction between adjacent discrete units by analysis of the d_{norm} mapping of the Hirshfeld surface in Figure 2.5.

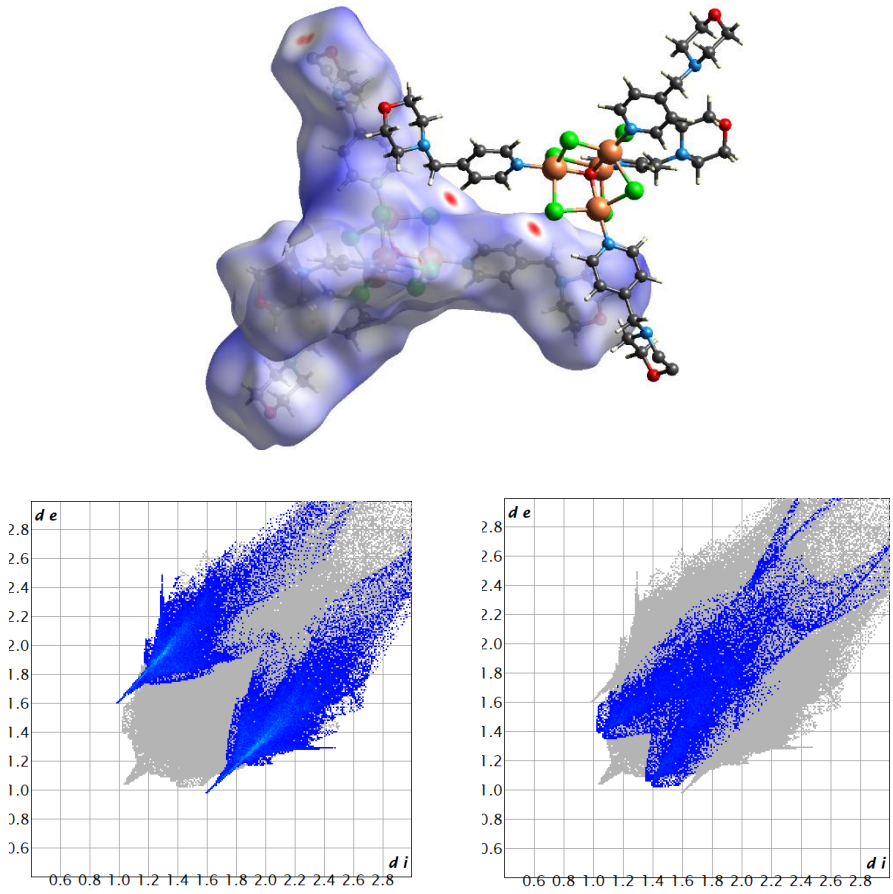

*Figure 2.5. d_{norm} mapping of the Hirshfeld surface (top) and 2D fingerprint plots of Cl···H interactions (bottom, left) and O···H interactions (bottom, right) in $[Cu_4OCl_6(\mathbf{L2.2})_4]\cdot 2MeOH$ (complex **2.2**)*

`

There are also some short contacts between the morpholine oxygen atom and a neighbouring morpholine CH_2 moiety, with a C···O distance of 3.745(4) Å and a C-H···O angle of 136.74(15)°. This added interaction, that is not present in complex **2.1** results in a closer interaction between neighbouring discrete complexes. The ligands are therefore oriented differently and offset face-to-face π-π interactions are now also observed between ligand molecules of neighbouring complexes (with an interplanar distance of 3.728(3) Å and a shift of 1.369(4) Å). There are also some solvent accessible voids present in the structure, that are 121 $Å^3$ in volume, which are occupied by the aforementioned disordered methanol molecules, and this is reflected in the 2D fingerprint plot of Hirshfeld surface analysis, with a lot of data points being concentrated in the upper right-hand corner, where d_e and d_i are large.

Interestingly, when the synthetic conditions are repeated in an aprotic solvent, acetonitrile, this has a significant effect on the resulting complex **2.3**, whereas the complex **2.1** forms in both solvents. In complex **2.2**, the interaction that associates adjacent discrete units is the hydrogen bonding provided by the solvent molecule and the four morpholine oxygen atoms, whereas these interactions are absent in complex **2.3**, as are the π-π interactions, resulting in a significantly different network of short contacts. $[Cu_4OCl_7(\mathbf{L2.2})_2(\mathbf{L2.2H})]\cdot 2MeCN\cdot 3H_2O$ (complex **2.3**, shown in Figure 2.6), again contains a tetranuclear copper(II) cluster, however, in this case one of the ligand molecules is replaced by a terminal chlorido ligand.

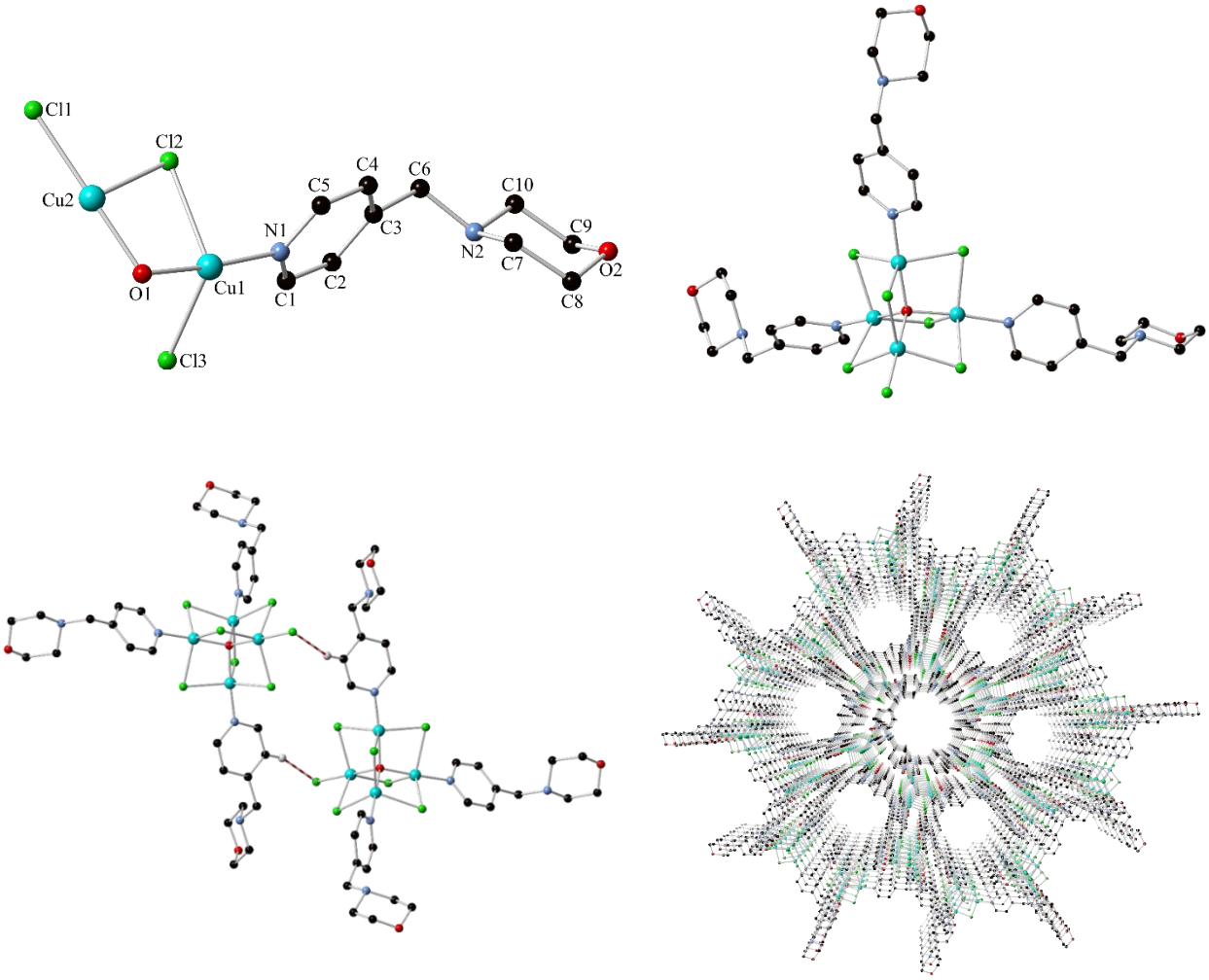

*Figure 2.6. Asymmetric unit (top, left), discrete cluster (top, right), C-H···Cl contacts (bottom, left) and solvent channels (bottom, right) in [Cu_4OCl_7(**L2.2**)$_2$(**L2.2H**)]·2MeCN·3H_2O (complex **2.3**) (some hydrogen atoms and solvent molecules were omitted for clarity)*

The crystallographic data were solved and refined in the trigonal space group $P\bar{3}$, and the asymmetric unit consists of one ligand molecule coordinated to a copper(II) ion which is linked to a second copper(II) ion *via* an oxygen atom and a chlorine atom, each copper(II) ion is bonded to a second chlorido ligand. The cluster exhibits an overall 1− charge arising from the additional chlorido ligand, and this charge is balanced by the protonation at the morpholine nitrogen atom at a **L2.2** ligand molecule. As each ligand molecule is crystallographically equivalent, each morpholine nitrogen atom was modelled with protonation at one-third occupancy. This protonation was verified using IR spectroscopy data, with a peak observed at 3340 cm^{-1} to

`

represent the N-H stretch. There is a water molecule interacting with the morpholine nitrogen atom of the ligand molecule, either with the protonated nitrogen atom or a lone pair of a deprotonated nitrogen atom, acting as a hydrogen bond acceptor or donor, respectively, with an N···O distance of 2.911(7) Å and a N-H···O angle of 169.2(3)°. Again, the geometry around each copper(II) ion is trigonal bipyramidal, with slightly higher τ_5 parameters of 0.842 and 1.012 for Cu1 and Cu2, respectively. The geometry surrounding Cu2 is likely much closer to a perfect trigonal bipyramid due to the significantly reduced steric bulk in its coordination geometry, as this copper(II) ion bears the terminal chlorido ligand. The Cu···Cu distances range from 3.0935(9) to 3.1202(9) Å, which are consistent with the distances observed in complexes **2.1** and **2.2**. Despite the terminal chlorido ligand replacing a ligand molecule in complex **2.3**, leading to the complex appearing to be the least symmetric, the wide range of Cu···Cu distances and τ_5 parameters indicate that complex **2.2** is the most distorted.

As in complexes **2.1** and **2.2**, the bond lengths surrounding Cu1 in complex **2.3** follow the same trends, with the Cu1-N2 and Cu1-O2 being significantly shorter (1.967(4) and 1.9005(14) Å, respectively) than the Cu1-Cl bond lengths, which range from 2.3794(11) to 2.4257(14) Å. The same is almost the case for the bond lengths surrounding Cu2. The Cu2-Cl2 bond lengths are 2.4076(12) Å, and the Cu2-O2 bond length is 1.909(4), which is consistent with what has been observed in previous complexes **2.1** and **2.2**.

Adjacent discrete complexes interact through the terminal chlorido ligand, with a pyridyl CH moiety (with a C···Cl distance of 3.650(4) Å and a C-H···Cl angle of 157.6(3)°) and a morpholine CH_2 (with a C···Cl distance of 3.686(5) Å and a C-H···Cl angle of 155.5(3)°). The interaction originating at the pyridyl CH moiety, interestingly originates at the 3-position, similarly to what is observed in complex **2.2**, but not complex **2.1**. This is unusual, given that this proton at the 3-position would be less acidic than the proton at the 2-position, which occurs in all three complexes **2.1**, **2.2** and **2.3**. This interaction likely occurs due to the intramolecular C-H···Cl contacts occurring between the proton at the 2-position with the closest bridging chlorido ligand in that same complex.

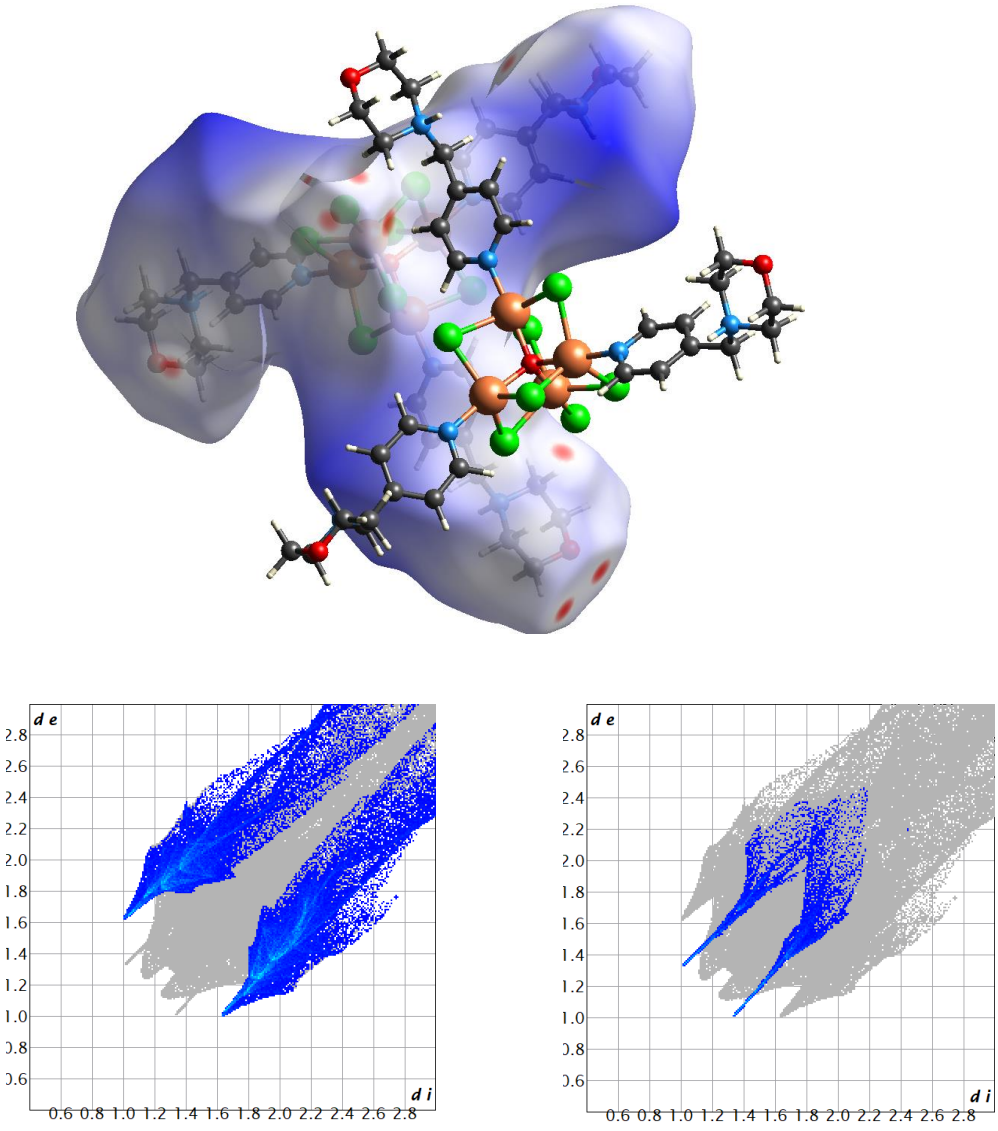

*Figure 2.7. d_{norm} mapping of the Hirshfeld surface (top) and 2D fingerprint plots of Cl···H interactions (bottom, left) and O···H interactions (bottom, right) in [Cu_4OCl_7(**L2.2**)$_2$(**L2.2H**)]·2MeCN·3H_2O (complex **2.3**)*

These interactions are reflected in the d_{norm} mapping of the Hirshfeld surface, and 2D fingerprint plot of Cl···H interactions, shown in Figure 2.7 above. As the network of short contacts in complex **2.3** significantly differs from that of complexes **2.1** and **2.2**, this results in a different crystal packing mode in which solvent channels are observed parallel to the crystallographic *c* axis (shown in Figure 2.6). These are roughly 10.6 Å in diameter and they are occupied by acetonitrile solvent molecules. The presence of these voids is reflected

`

in the 2D fingerprint plot of the Hirshfeld surface analysis, with a large quantity of data points in the upper right-hand corner of the plot, indicating a larger interatomic separation than their corresponding van der Waals radii, giving both a large d_e and d_i.

Attempts to investigate the gas adsorption properties of this material were unsuccessful and first analysed using thermogravimetric analysis. The TGA profile (Appendix 3, Figure A3.1) revealed that the loss of solvent was complete at 65 °C and the onset of decomposition occurred at 210 °C. However, when the material was heated to 80 °C under vacuum overnight to remove the solvent from the channels in order to activate it for gas adsorption measurements, the sample decomposed resulting in the collapse of the solvent channels. This implies that the complex was not stable to solvent removal *i.e.* the short contacts between adjacent discrete clusters were not strong enough to sustain the framework upon solvent removal.

2.4.1 Tetranuclear Copper(II) Cluster, Cu_4OCl_6

This tetranuclear copper(II) cluster, Cu_4OX_n (X = Cl, Br, n = 6,7), the structure of which was first reported in 1966 by Bertrand *et. al.*,[21] has been encountered in literature since, most commonly with *N*- or *O*-donor ligands and has been a source of crystallographic and magnetochemical interest. In some cases, the cluster is arranged in a perfect tetrahedron, in which each copper(II) ion is crystallographically and chemically equivalent,[22] as is seen in this chapter in complex **2.1**. In other cases, there is a significant distortion from a perfect tetrahedron, in which case, the copper(II) ions are not equivalent (either chemically and/or crystallographically), and that distortion is regular throughout the crystal.[23] This is seen in this chapter in complex **2.3** where there are two chemically and crystallographically unique copper(II) ions, and complex **2.2** where each copper(II) ion in the cluster is crystallographically unique (both types of copper(II) cluster are shown in Figure 2.8). In each of these clusters, the interactions between neighbouring paramagnetic copper(II) ions will differ, due to the difference in geometries in each cluster reported in this chapter.

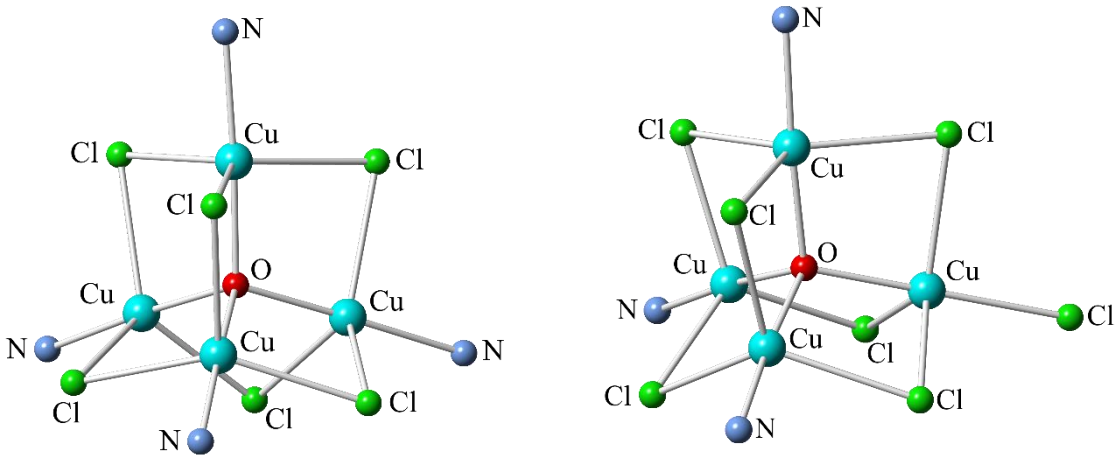

*Figure 2.8. Copper(II) clusters encountered in Chapter 2, a cluster in which all copper(II) ions are crystallographically equivalent (complex **2.1**, left) and a cluster in which there are multiple unique copper(II) ions (complex **2.3**, right)*

The magnetic properties of these materials would be of interest to investigate, as the different types of interior copper(II) clusters would result in different magnetic properties that could then be correlated to the subtle structural differences. The unpaired copper(II) $d_{x^2-y^2}$ electrons can interact with each other *via* the chlorido bridge and/or the central oxygen atom orbitals in the cluster through superexchange, and the degree of this interaction depends on orbital overlap and therefore the structure of the cluster. As each cluster is unique, the magnetic properties could be attributed to these slight structural variations.

The presence of a chlorido ligand in complex **2.3** strongly affects the geometry and symmetry of the complex, resulting in the copper(II) ions in the cluster no longer being crystallographically (or chemically) equivalent (as they are in complex **2.1**) which will have a marked effect on the magnetic susceptibilities of the complex. The magnetic measurements are beyond the scope of this research, however, limited magnetic measurements have been carried out on similar complexes containing the same types of clusters, both with four ligand molecules and with three ligand molecules and an extra chlorido ligand.

In their study, Cortes *et. al.*[24] report antiferromagnetic interactions between discrete units of $[Cu_4OCl_7(PhIm)_3](HPhIm)\cdot H_2O$ (where PhIm is 4-phenylimidazole), in which a chlorido ligand replaces a ligand molecule, like in complex **2.3**, has a Weiss constant of -16.94K, with quite a low Curie constant of

`

0.25 cm^3 mol^{-1}. They report two other complexes in which the cluster has four ligand molecules coordinated to it, in which all copper(II) ions are unique,[25] and yet the interactions are ferromagnetic in one complex and antiferromagnetic in the other. This suggests that the magnetic properties of these complexes are not straightforward to predict, and therefore the measurement of the magnetic properties of the complexes discussed in this chapter would be of interest, in order to possibly predict the magnetic behaviour of similar complexes in future studies.

2.5 Copper(II) Acetate Complex of L2.1

Introducing a counterion with a different coordination mode, such as acetate, into the copper(II) complexes of **L2.1** in similar synthetic conditions again resulted in a discrete complex, however, its structure differs significantly to the previously discussed complexes **2.1**, **2.2** and **2.3**. $[Cu_2(OAc)_4(\mathbf{L2.1})_2]$ (complex **2.4**, shown in Figure 2.9) forms a dinuclear linear complex and crystallises in the monoclinic space group $P2_1/n$. The anion effect is clearly identifiable, by comparison of this structure to complex **2.1**, as both were synthesised under equivalent synthetic conditions.

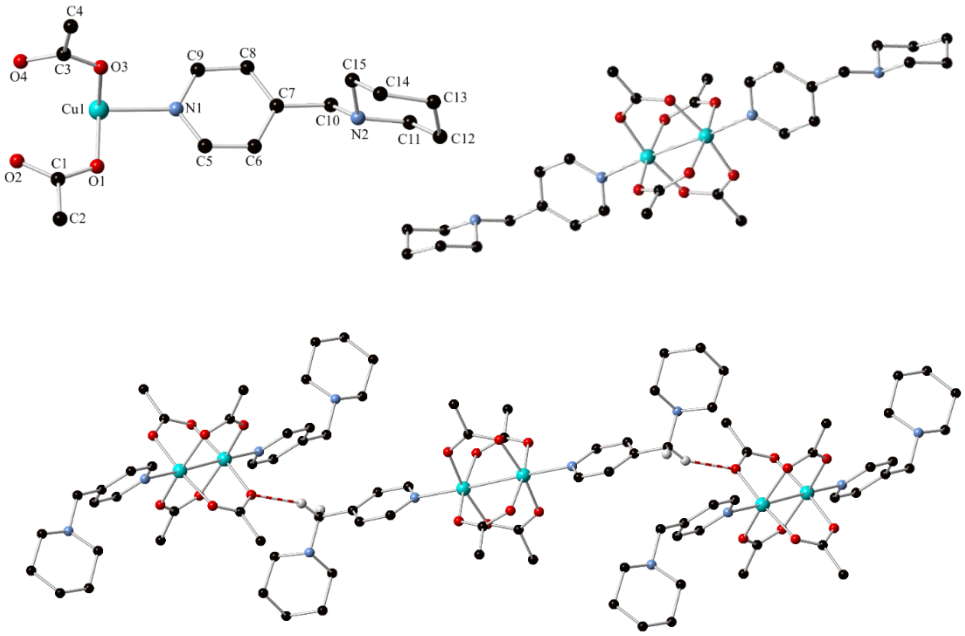

*Figure 2.9. Asymmetric unit (top, left), discrete complex (top, right) and C-H···O contacts in $[Cu_2(OAc)_4(\mathbf{L2.1})_2]$ (complex **2.4**) (some hydrogen atoms were omitted for clarity)*

The asymmetric unit of complex **2.4** (shown in Figure 2.9 above) consists of one ligand molecule coordinated to a copper(II) ion via the pyridyl nitrogen atom and two acetato ligands coordinating to the copper(II) *via* an oxygen atom each. The overall discrete complex (shown in Figure 2.9) is a copper(II) acetate paddlewheel structure with two **L2.1** ligand molecules coordinating at the axial copper(II) sites.

A square pyramidal geometry is observed at each copper(II) metal centre, with a τ_5 parameter of 0.153. The Cu1-O bond lengths are all significantly shorter (ranging from 1.968(3) to 1.980(3) Å), than the axial Cu1-N1 bond length (2.156(4) Å. Neighbouring complexes interact through C-H···O interactions, (shown in Figure 2.9), originating at one out of the four acetato oxygen atoms to an acetato CH_3 moiety of an adjacent complex, with a C···O distance of 3.567(3)Å and a C-H···O angle of 168.2(3)°. There are also C-H···O contacts between a bridging CH_2 moiety and an adjacent acetato oxygen atom, with a C···O distance of 3.480(6) Å and a C-H···O angle of 153.6(3)°. The d_{norm} mapping of the Hirshfeld surface (shown in Figure 2.10) confirms that these C-H···O contacts are easily the most dominant interactions within the complex that govern the crystal packing of this material, and the size and shape of the red regions of the d_{norm} mapping of the Hirshfeld surface (Figure 2.10) indicate that these interactions are strong and highly directional.

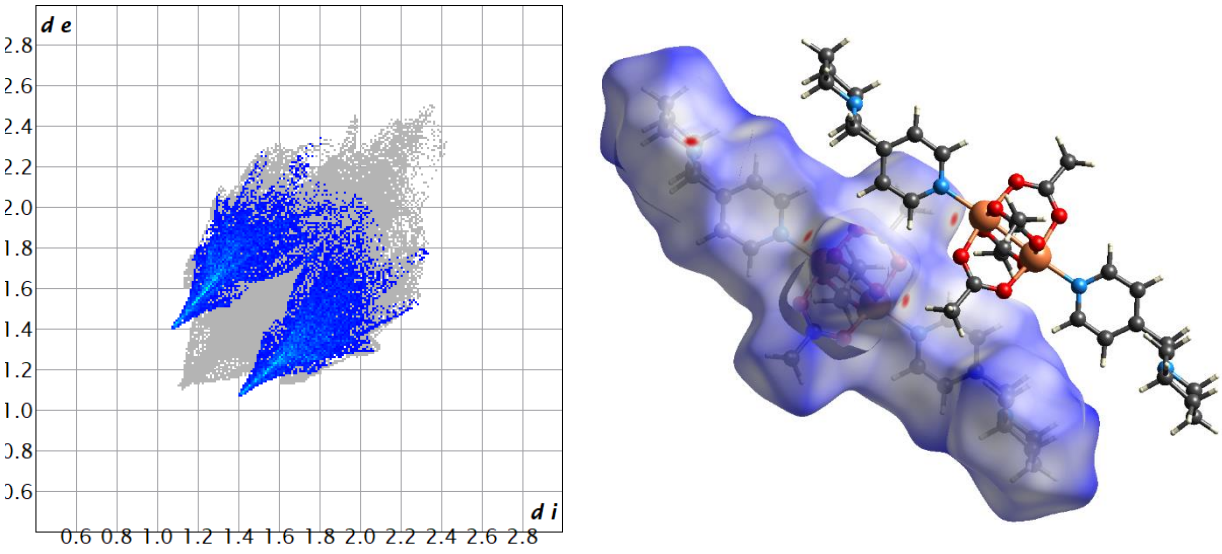

*Figure 2.10. 2D fingerprint plot of O···H contacts (left) and d_{norm} mapping of the Hirshfeld surface (right) of $[Cu_2(OAc)_4(\mathbf{L2.1})_2]$ (complex **2.4**)*

`

2.6 Cobalt(II) Complexes of L2.1, L2.2 and L2.3

Similarly to copper(II) complexes of **L2.1** and **L2.2**, in cobalt(II) complexes of these ligands it is only the pyridyl nitrogen atom of the ligand that is coordinating, and the complexes are also discrete. In the case of both **L2.1** and **L2.2**, a discrete trichlorocobaltate complex of each ligand is observed (Figure 2.11), with the piperidine/morpholine nitrogen atom being protonated in order to charge balance the discrete complex, and in both cases the presence of an N-H moiety was confirmed by IR spectroscopy. [$CoCl_3$(**L2.1H**)]·MeCN (complex **2.5**) crystallises in the monoclinic space group $P2_1/c$, with a protonated ligand molecule coordinated to a cobalt(II) ion *via* the pyridyl nitrogen atom, and three coordinating chlorido ligands, giving the cobalt(II) a tetrahedral geometry, and a noncoordinating solvent acetonitrile molecule in the asymmetric unit (shown in Figure 2.11).

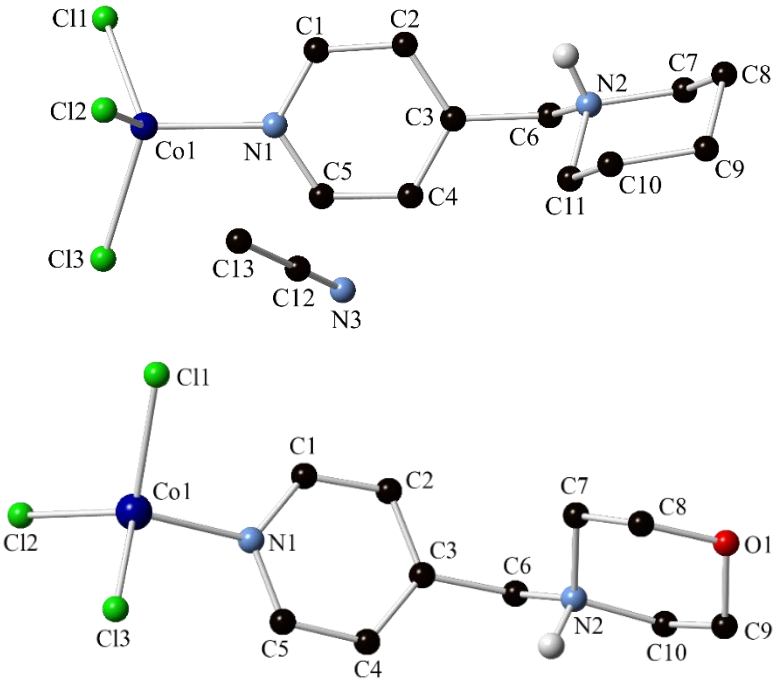

*Figure 2.11. Asymmetric unit of [$CoCl_3$(**L2.1H**)]·MeCN (complex **2.5**) (top) and asymmetric unit of [$CoCl_3$(**L2.2H**)] (complex **2.6**) (bottom) (some hydrogen atoms were omitted for clarity)*

The discrete complexes form one-dimensional chains through hydrogen bonding (shown in Figure 2.12) occurring between one of the chlorido ligands of one complex and an N-H of a protonated ligand molecule of a neighbouring complex, with an N···Cl distance of 3.2007(17) Å and a N-H···Cl bond angle of

171.0(3)°. This was confirmed to be the dominant interaction by the d_{norm} mapping of the Hirshfeld surface (Figure 2.13). A much weaker halogen-hydrogen interaction is present between another chlorido ligand of one complex and a bridging CH_2 moiety of a neighbouring discrete complex, with a C···Cl distance of 3.669(2) Å and a C-H···Cl bond angle of 148.59(11)°. Almost half of the close contacts comprising the Hirshfeld surface coverage in this complex are due to Cl···H interactions.

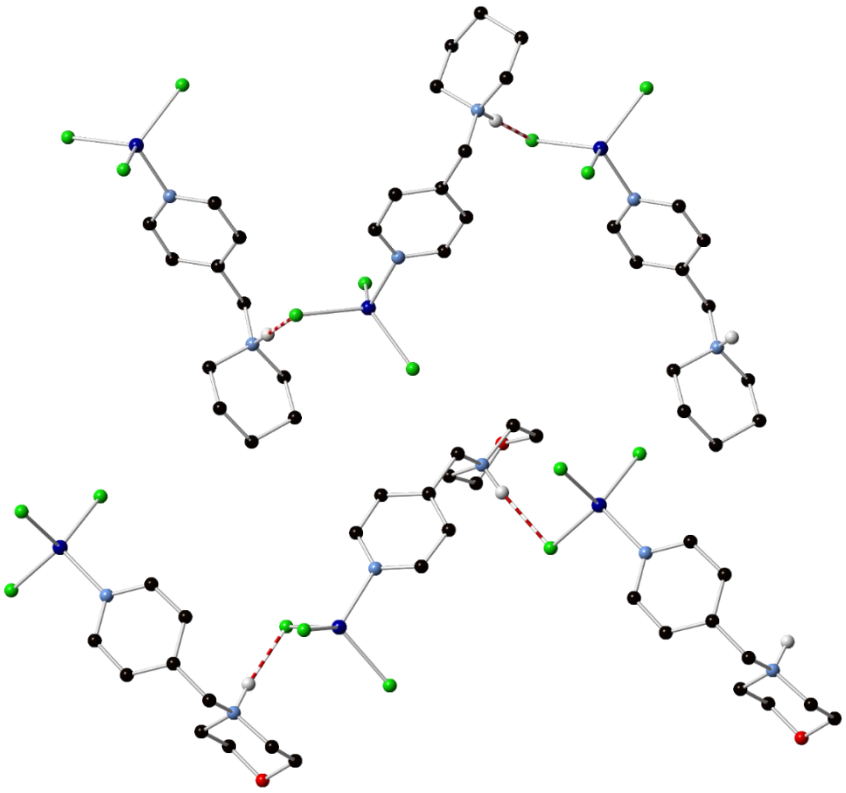

*Figure 2.12. Hydrogen bonding in [$CoCl_3$(**L2.1H**)]·MeCN (complex **2.5**) (top) and hydrogen bonding in [$CoCl_3$(**L2.2H**)] (complex **2.6**) (bottom) (some hydrogen atoms and solvent molecules were omitted for clarity)*

[$CoCl_3$(**L2.2H**)] (complex **2.6**) bears a lot of similarities to complex **2.5**, with similar interactions governing the crystal packing, however due to the subtle influence of the morpholine oxygen atom, there are some interesting differences observed also. The crystallographic data were solved and refined in a related monoclinic space group, $P2_1/n$, and the asymmetric unit (shown in Figure 2.11) consists of a protonated ligand molecule coordinating to a cobalt(II) ion, with three chlorido ligands completing the tetrahedral coordination sphere of the cobalt(II) ion. In this case however, the solvent is not present in the asymmetric unit or in the crystal structure. Again, the dominant interaction within the complex, as confirmed by the d_{norm} mapping of the Hirshfeld surface (Figure 2.13) is the hydrogen bonding of a chlorido ligand of one discrete unit with an N-H moiety of a neighbouring unit, with an N···Cl distance of 3.1366(11) Å and an N-H···Cl angle of 175.6(17)°.

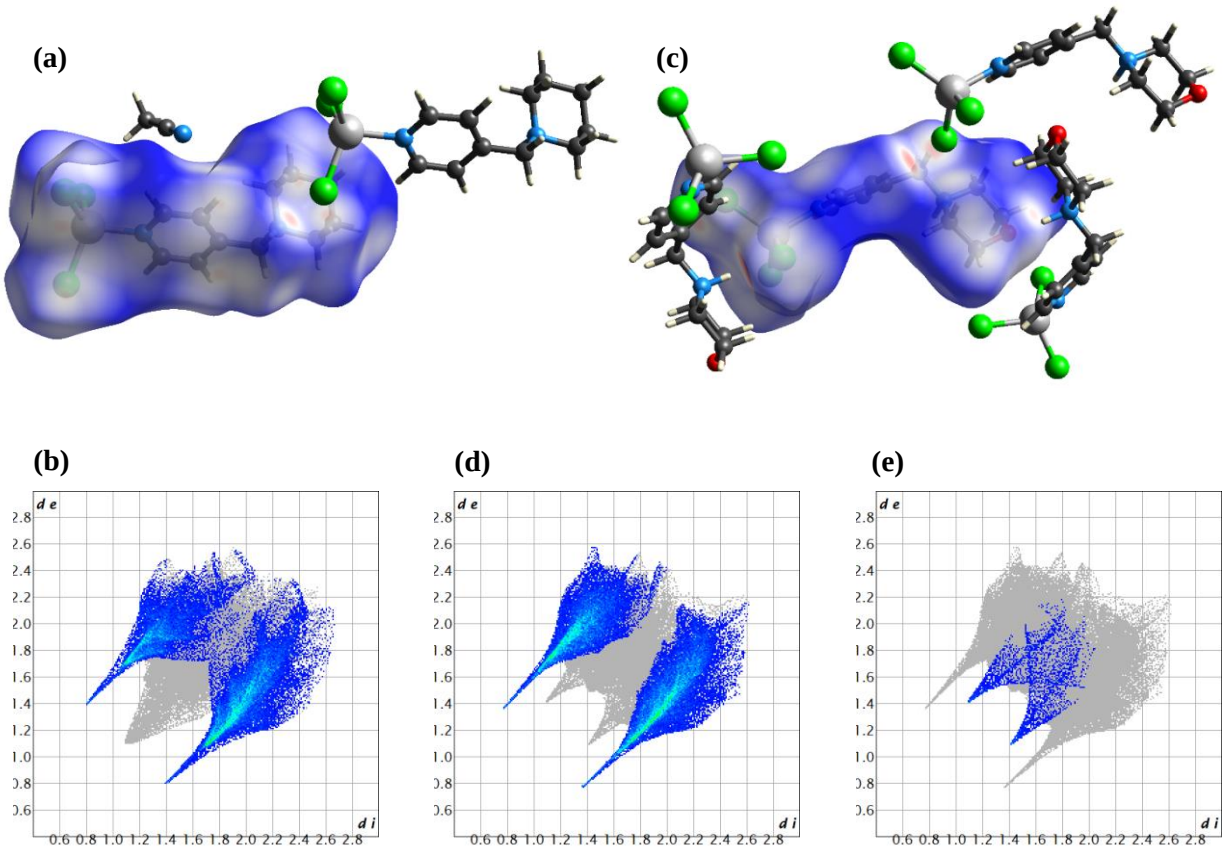

*Figure 2.13. (**a**) d_{norm} mapping of the Hirshfeld surface, (**b**) 2D fingerprint plot of Cl···H contacts in [$CoCl_3$(**L2.1H**)]·MeCN (complex **2.5**) and (**c**) d_{norm} mapping of the Hirshfeld surface, (**d**) 2D fingerprint plot of Cl···H contacts & (**e**) 2D fingerprint plot of O···H contacts in [$CoCl_3$(**L2.2H**)] (complex **2.6**)*

The key difference in the 2D fingerprint plots of the two complexes is seen between the two Cl···H "spikes" in the profiles, where there are two smaller spikes between them in the plot of complex **2.6**, where it is absent in that of complex **2.5**. There two smaller spikes represent the O···H short contacts (Figure 2.13) and account for only a small proportion of surface interactions, however, they do represent a significant fraction of the remainder of short contacts. These interactions are, of course, absent in complex **2.5**, as the morpholine oxygen atom is replaced by a piperidine CH_2 unit.

The presence of an added hydrogen bond acceptor in the form of a morpholine oxygen atom promotes weak C-H···O interactions between adjacent morpholine groups, originating at the CH_2 moiety adjacent to the morpholine nitrogen atom, with a C···O distance of 3.5184(18) Å and a C-H···O angle of 155.39(8)° (Figure 2.14).

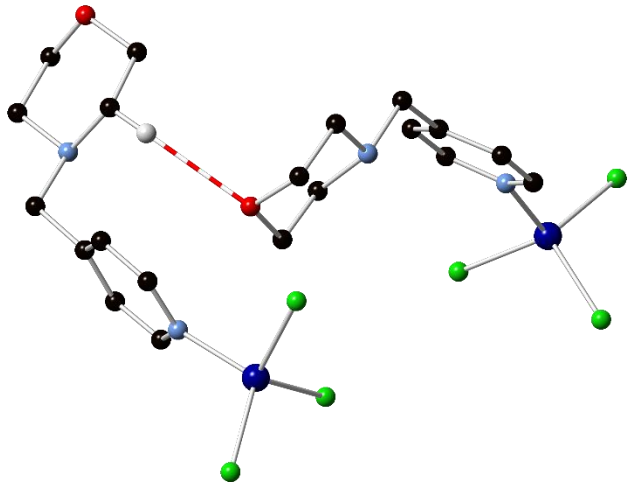

*Figure 2.14. C-H···O contacts associating adjacent discrete units of [$CoCl_3$(**L2.2H**)] (complex **2.6**)*

This is accompanied by a shift in the C-H···Cl interaction mode between the two complexes, which involves the neighbouring pyridyl C-H group in complex **2.6** but is shifted towards the piperidine methylene groups in complex **2.5**. Due to this shift, the relative orientation between discrete complexes differs between the two complexes, even though the interactions themselves are very similar. This slight difference allows for π-π interactions to take place in complex **2.6** (with an interplanar distance of 3.747 Å and a shift of 1.644 Å), where they are absent in complex **2.5**. This results in a significantly different d_{norm} mapping of the

`

Hirshfeld surface, with a higher quantity of short contacts observed in the form of red/pink areas on the surface of the diagram and a different overall shape to the 2D fingerprint plot (Figure 2.13).

In contrast to **L2.1** and **L2.2**, **L2.3** replaces the sterically hindered tertiary amines of the former two ligands with a much less bulky primary amine. The cobalt(II) complex of **L2.3** is analogous to that of cobalt(II) complexes **2.5** and **2.6**, producing a discrete trichlorocobaltate complex, [$CoCl_3$(**L2.3H**)], complex **2.7**. The structure is very similar to cobalt(II) complexes of **L2.1** and **L2.2**, with the ligand being triply protonated at the primary amine. The crystallographic data were solved and refined in the monoclinic space group $P2_1/n$. The asymmetric unit (Figure 2.15) consists of one triply protonated ligand molecule coordinating to a cobalt(II) ion *via* the pyridyl nitrogen atom, with three chlorido ligands completing the tetrahedral coordination sphere of the cobalt(II) ion.

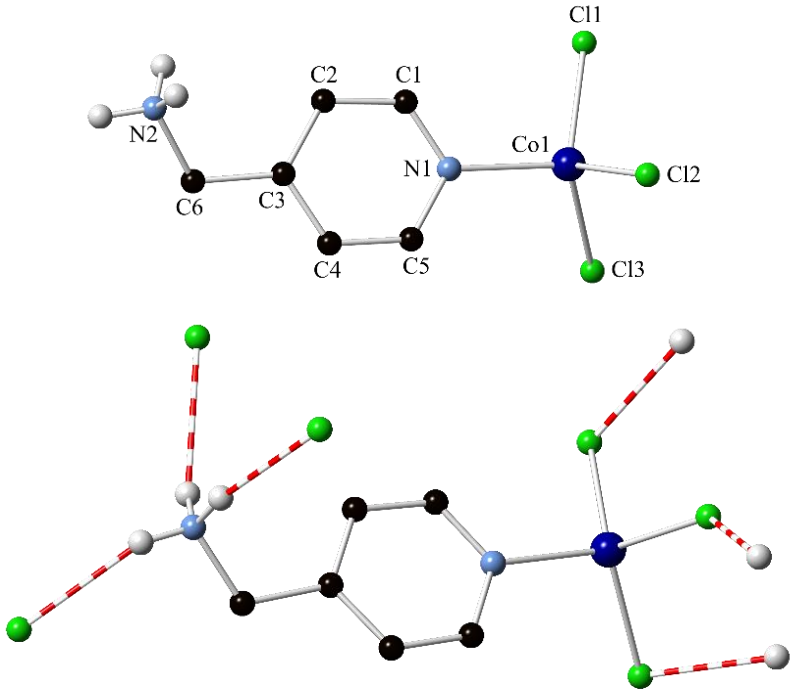

*Figure 2.15. Asymmetric unit (top) and hydrogen bonding network (bottom) of [$CoCl_3$(**L2.3H**)] (complex **2.7**) (some hydrogen atoms were omitted for clarity)*

The crystal packing is largely governed by hydrogen bonding originating at the protonated amine N-H moieties to the chlorido ligands of neighbouring discrete complexes, with N···Cl distances of 3.202(5), 3.214(5) and 3.253(6) Å, with corresponding N-H···Cl angles of 153.1(3), 134.0(3) and 166.9(3),

respectively (Figure 2.15). Each of the three amine protons and each of the three chlorido ligands of the discrete complex participates in this reciprocated hydrogen bonding, resulting in each discrete complex forming short contacts with six other discrete complexes (outlined in Figure 2.15). There are also some C···Cl contacts originating at the pyridyl CH moiety (at the 3-position, similar to what is observed in the copper(II) chloride complexes of **L2.2**), with a C···Cl distance of 3.687(6) Å and a C-H···Cl angle of 169.7(4)°. Both of these interactions are reflected in the d_{norm} mapping of the Hirshfeld surface (Figure 2.16). Interestingly, despite the high degree of aromaticity of **L2.3** (and subsequently complex **2.7**), there are surprisingly no π-π interactions, indicating that the hydrogen bonding network is much more favoured by the crystal packing of this complex.

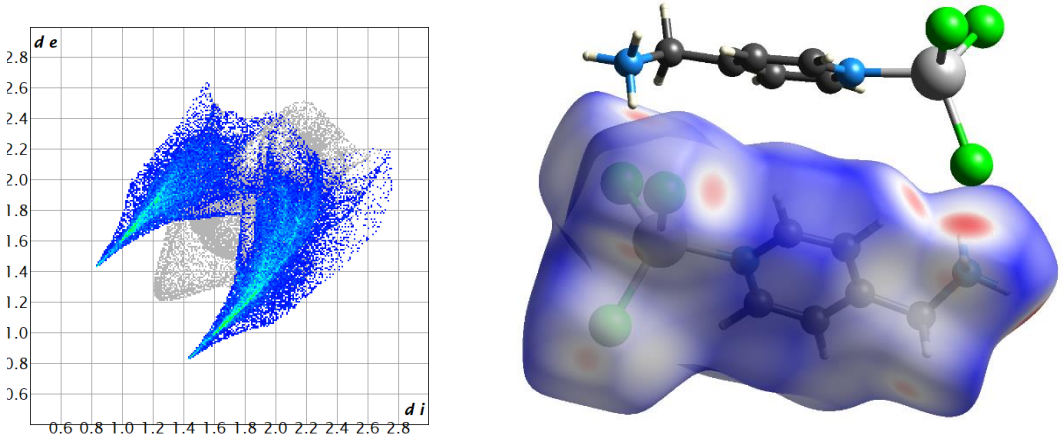

*Figure 2.16. 2D fingerprint plot of Cl···H contacts (left) and d_{norm} mapping of the Hirshfeld surface (right) of [$CoCl_3$(**L2.3H**)] (complex **2.7**)*

2.7 Silver(I) Complexes of L2.1 and L2.2

Incorporating a more geometrically flexible, d^{10} metal ion, silver(I), into the synthesis results in coordination of both ligand nitrogen atoms to a metal ion, providing insight into the influence of the ligand on the resulting crystal packing. These structures offer an interesting contrast to copper(II) and cobalt(II) complexes of these ligands, in which the geometric restraints of the metal ion had a more restrictive influence on the ligand coordination modes. The structures of *poly*-[Ag**L2.1**]SbF_6·0.5THF (complex **2.8**) and *poly*-[Ag(**L2.2**)]SbF_6·0.5THF (complex **2.9**) allow for direct comparison of the piperidine and

`

morpholine substituents and their influence on the crystal packing tendencies, with all other variables held constant.

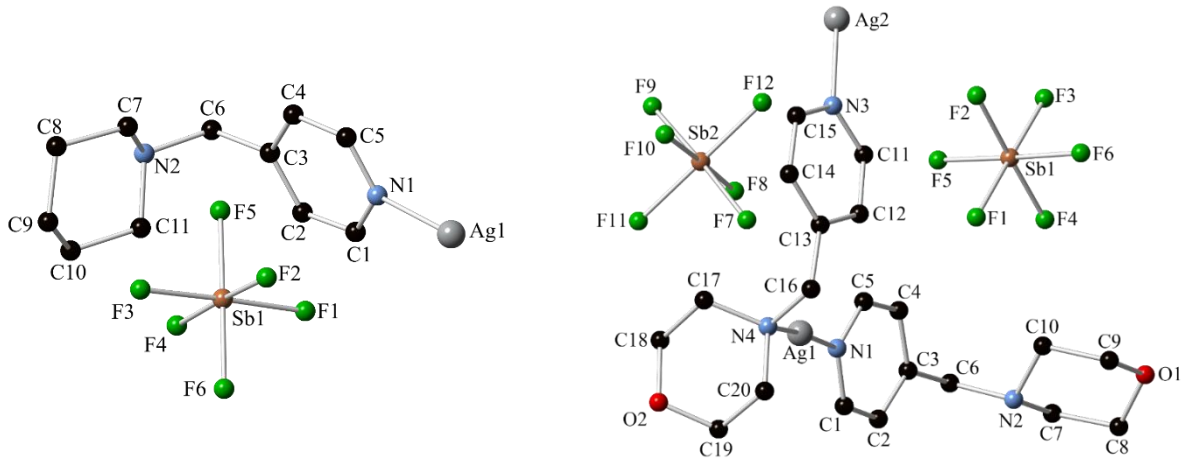

*Figure 2.17. Asymmetric unit of poly-[Ag**L2.1**]SbF_6·0.5THF (complex **2.8**) (left) and asymmetric unit of poly-[Ag(**L2.2**)]SbF_6·0.5THF (complex **2.9**) (right) (hydrogen atoms and solvent molecules were omitted for clarity)*

Complex **2.8** crystallises in the monoclinic space group $P2_1/n$, and the asymmetric unit (shown in Figure 2.17 above) consists of one ligand molecule coordinated to a silver(I) ion *via* the pyridyl nitrogen atom, a disordered THF solvent molecule and an SbF_6^- anion. The polymer extends in one direction in a linear fashion, with the aromatic region providing the linearity, with the Ag1-N2-C6-C3 torsion angle measuring at 179.0(2)°. There are face-to-face π-π interactions between adjacent chains (with an interplanar distance of 3.641 Å and a shift of 0.605 Å).

Complex **2.9** crystallises in a related monoclinic space group $P2_1/c$, however the asymmetric unit consists of two ligand molecules coordinated to two silver(I) ions, two SbF_6^- anions and a disordered THF solvent molecule (Figure 2.17). Like in complex **2.8**, the geometry of the silver(I) ions is linear with N-Ag-N angles of 173.59(14)° and 177.63(11), which is similar to the angle observed in complex **2.9** (177.75(11)°). Both complexes **2.8** and **2.9** are one-dimensional coordination polymers with very similar coordination geometries but with a substantial difference in the extended structures, as shown in Figure 2.18. Examining the extended structure of complex **2.9** reveals a much more twisted motif than is seen in complex **2.8**,

highlighted by a much smaller Ag1-N4-C16-C13 torsion angle of 56.8(2)°. The difference in asymmetric units results in the morpholine moieties facing outward at each apex of the zig-zag motif and forming reciprocated C-H···O interactions with neighbouring chains (with a C···O distance of 3.330(4) Å, and C-H···O angle of 155.0(3)°).

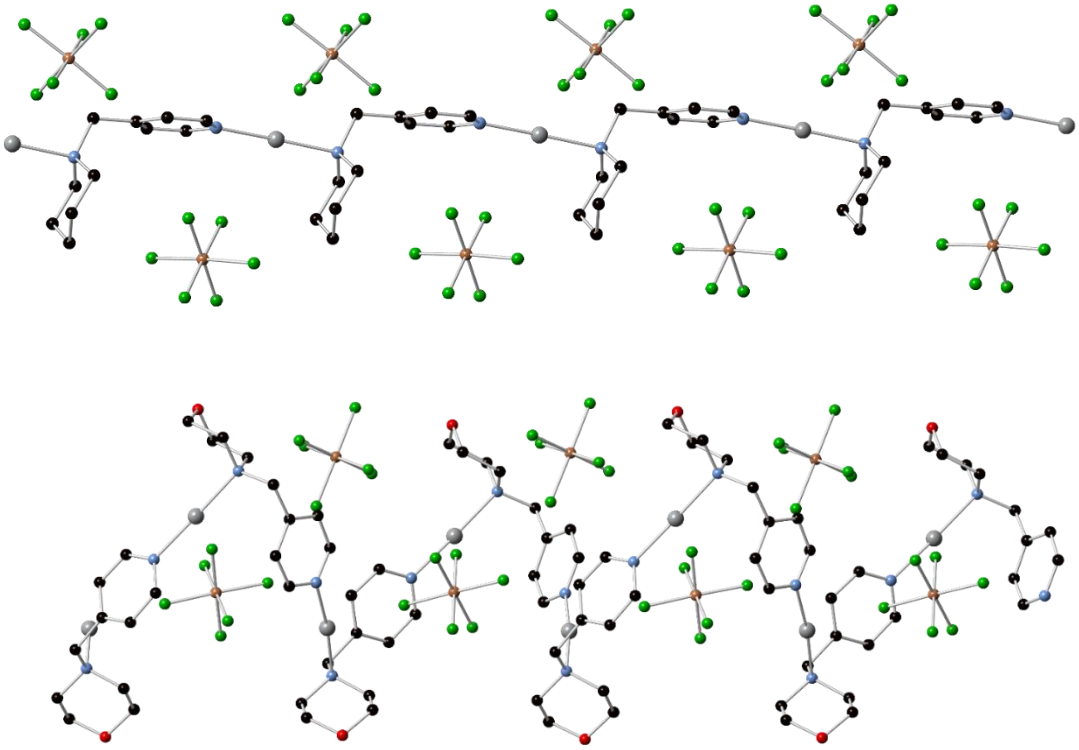

*Figure 2.18. Extended 1D chain of poly-[Ag**L2.1**]SbF_6·0.5THF (complex **2.8**) (top) and extended 1D chain of poly-[Ag(**L2.2**)]SbF_6·0.5THF (complex **2.9**) (bottom) (hydrogen atoms and solvent molecules were omitted for clarity)*

The anion interactions also differ between the two complexes, though the anions are the same. In complex **2.8**, anion association is largely governed by C-H···F contacts originating at a piperidine CH_2, with a C···F distance of 3.458(5) Å, and C-H···F angle of 151.3(3)°. In the case of complex **2.9**, the anions are encapsulated by Ag···F contacts (2.815(6) Å) and anion···π interactions (with an F···π distance of 3.329(5) Å). The C-H···F contacts account for a large majority of surface interactions which are observed in the d_{norm} mapping of the Hirshfeld surface and subsequent 2D fingerprint plot (Figure 2.19), highlighting the

`

C-H···F interactions in complex **2.8**. The pink regions on the surface map indicate that the F···Ag interactions are the strongest interactions on the surface, and account for a large proportion of short contacts.

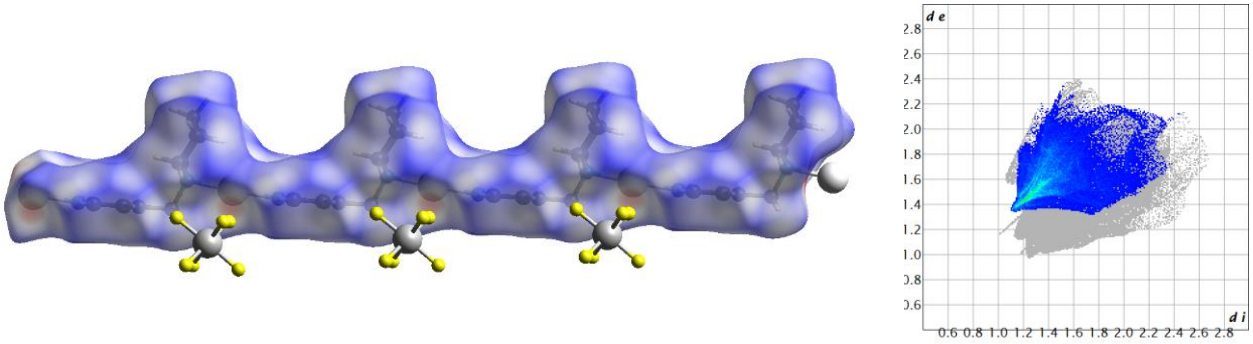

*Figure 2.19. d_{norm} mapping of the Hirshfeld surface (left) and 2D fingerprint plot of H···F contacts (right) in poly-[Ag**L2.1**]SbF_6·0.5THF (complex **2.8**)*

The d_{norm} mapping of the Hirshfeld surface of complex **2.9** on the other hand (shown in Figure 2.20), clearly reveals that C-H···F contacts, originating at the CH moiety adjacent to the pyridyl nitrogen atom (with a C11···F2 distance of 3.359(5) Å and a C11-H···F2 angle of 152.6(2)°) are the dominant interaction on the surface, with multiple regions of red/pink on the surface map highlighting these interactions. The subsequent 2D fingerprint plot highlights these contacts and reveals that they comprise a large portion of the surface interactions, similar to complex **2.8**.

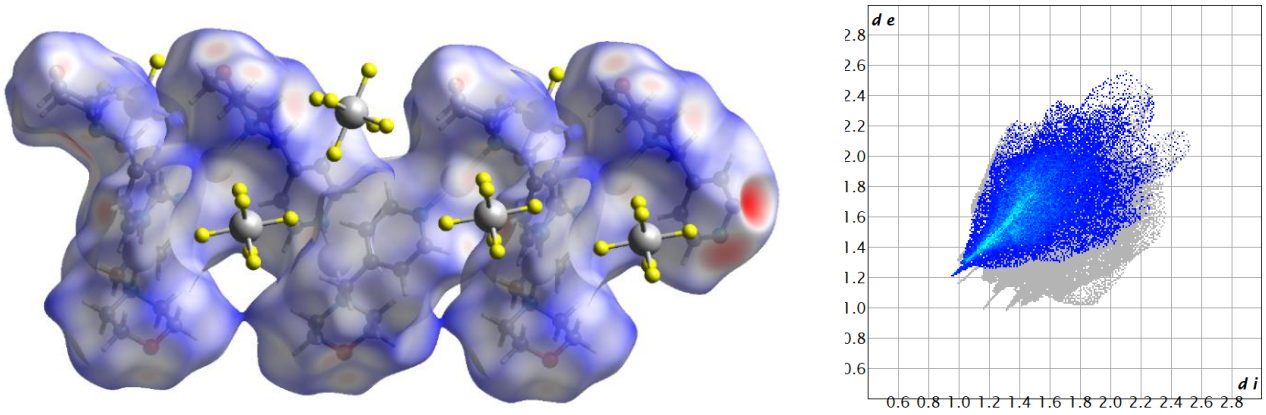

*Figure 2.20. d_{norm} mapping of the Hirshfeld surface (left) and 2D fingerprint plot of F···H interactions in -[Ag(**L2.2**)]SbF_6·0.5THF (complex **2.9**)*

In the case of these two complexes, the similarities of the synthetic procedures allow for direct comparison of the crystallographic properties. The morpholine oxygen atom has had a substantial difference on the geometry of the ligand molecule and on the overall crystal packing and coordination mode of these complexes, likely due to the reciprocated C··O contacts between adjacent one-dimensional chains, resulting in the anion association no longer governing the interaction between neighbouring 1D polymeric chains.

Interestingly, upon closer inspection of the PXRD pattern of the bulk sample of complex **2.9**, it was determined that the pattern did not match the simulated pattern of the SCXRD data for the complex. The SCXRD data were recollected on a second crystal, and it was determined that complex **2.9** was a minor product, and the major product, $[Ag_2(\mathbf{L2.2})_2(THF)_4(SbF_6)_2$ (complex **2.9a**), was a discrete dinuclear complex of the formula $[Ag_2(\mathbf{L2.2})_2(THF)_4]\cdot(SbF_6)_2$. The crystallographic data were solved and refined in the triclinic space group $P\bar{1}$. The asymmetric unit (shown in Figure 2.21 below) consists of one silver(I) ion coordinated by one **L2.2** ligand molecule *via* its pyridyl nitrogen atom, and two THF solvent molecules *via* their respective oxygen atoms and one non-coordinating SbF_6^- anion.

`

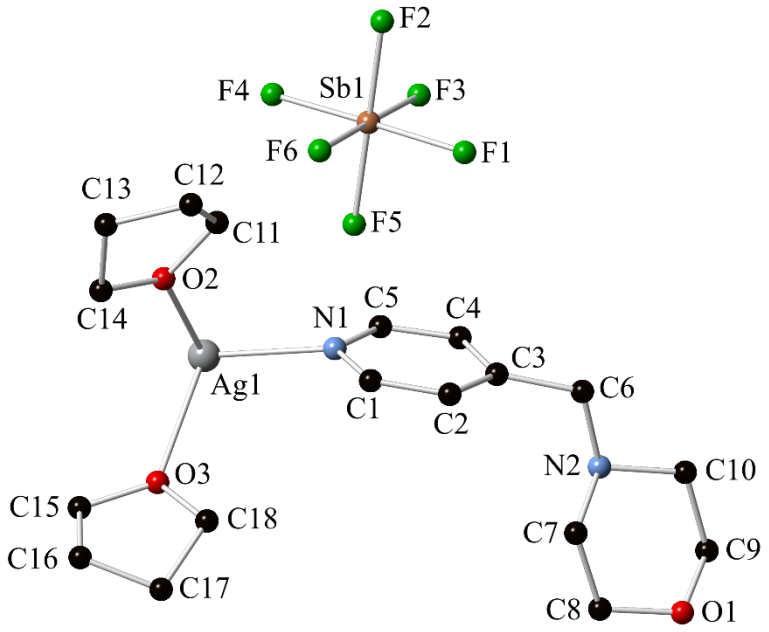

*Figure 2.21. Asymmetric unit of $[Ag_2(\mathbf{L2.2})_2(THF)_4(SbF_6)_2$ (complex **2.9a**)*

As with all previous silver(I) complexes, both nitrogen atoms are coordinating to a silver(I) ion. The silver(I) ion has a distorted tetrahedral geometry, with a τ_4 parameter of 0.739,[26] with a large variation in the bond angles surrounding Ag1 (94.181(2) – 129.8030(17)°). The bond angles also reflect this distortion, with the Ag1-N bonds being shorter (2.28357(6) and 2.29761(6) Å for Ag1-N1 and Ag1-N2, respectively) than the Ag1-O bond lengths (2.36973(6) and 2.52479(7) Å for Ag1-O2 and Ag1-O3, respectively). The Ag-N bond lengths are longer than those observed in complexes **2.8** and **2.9**, but this is to be expected with a higher coordination number. In the discrete dinuclear complex (shown in Figure 2.22) the ligand molecules run antiparallel to one another, and the offset between the pyridyl moieties results in no face-to-face π-π interactions.

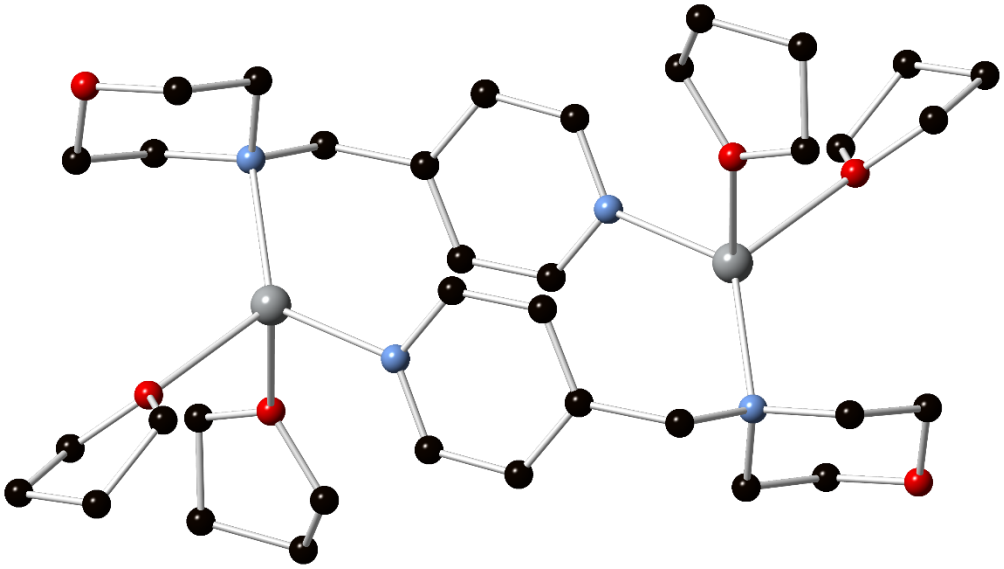

*Figure 2.22. Discrete complex [Ag_2(**L2.2**)$_2$(THF)$_4$(SbF_6)$_2$ (complex **2.9a**)*

Adjacent discrete complexes associate *via* reciprocated C-H···O contacts, similar to what is observed in complex **2.9**, originating at a morpholine oxygen atom and a THF CH_2 moiety, with a C···O distance of 3.370(4) Å and a C-H···O angle of 145.40(17)°, (Figure 2.23).

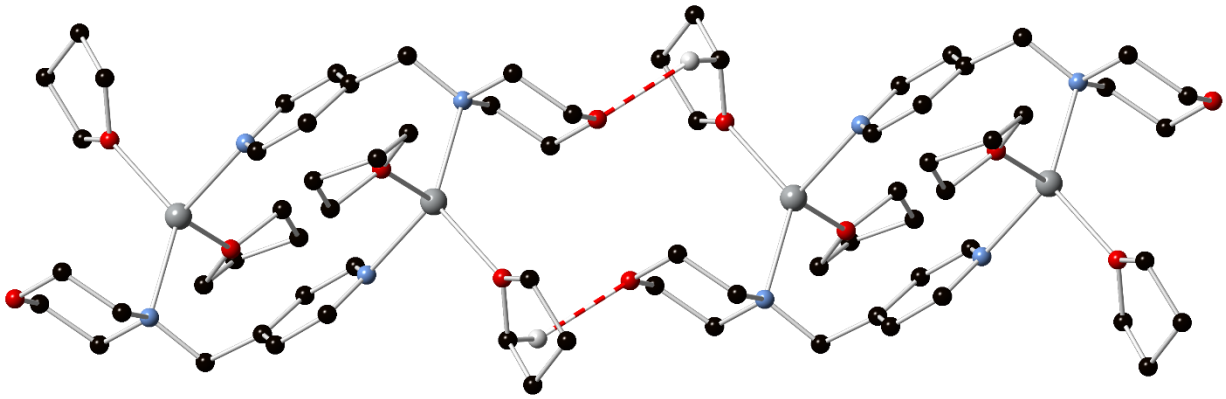

*Figure 2.23. Association of adjacent discrete complexes **2.9a** via reciprocated C-H···O contacts*

These reciprocated C-H···O contacts are also reflected in the d_{norm} mapping of the Hirshfeld surface (Figure 2.24). The surface also highlights short contacts between the 2-CH moiety of the pyridyl moiety and an SbF_6^- fluorine atom, with a C···F distance 3.404(3) Å and a C-H···F angle of 155.54(15)°.

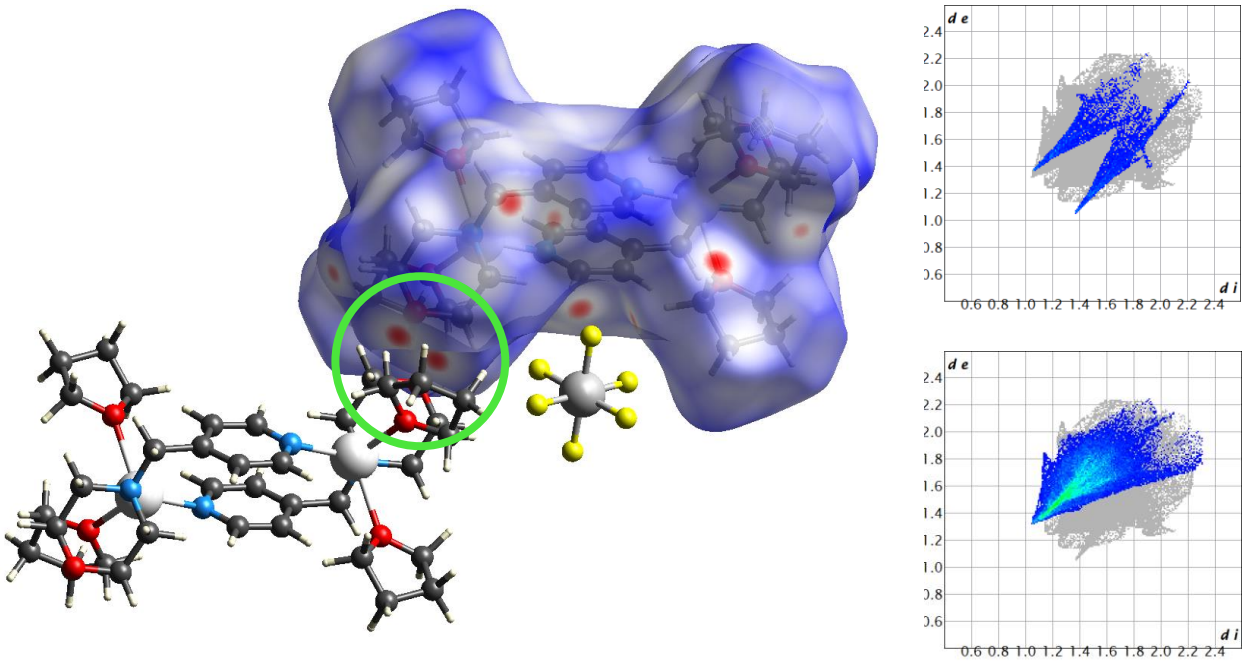

*Figure 2.24. d_{norm} mapping of the Hirshfeld surface highlighting close contacts in green circles (left) and 2D fingerprint plot highlighting O···H contacts (right, top) and 2D fingerprint plot highlighting F···H contacts (right, bottom) in poly-[Ag**L2.1(**CO_2CF_3)] (complex **2.10**)*

Finally, *poly*-[Ag**L2.1(**CO_2CF_3)] (complex **2.10**) closely resembles complexes that form from **L2.3** and silver (discussed in Section 2.8 below), in which a dinuclear "box" (which is also present in complex **2.9a**) is observed in a polymeric structure. This complex was used to investigate the geometric influence of a coordinating anion, trifluoroacetate. In this case, a one-dimensional chain is formed that crystallises in the monoclinic space group $P2_1/n$, and the asymmetric unit (Figure 2.25) consists of one ligand molecule, coordinated to a silver(I) ion *via* the piperidine nitrogen atom, and a trifluoroacetato ligand is also coordinated to the silver(I) ion *via* one of the oxygen atoms (O1).

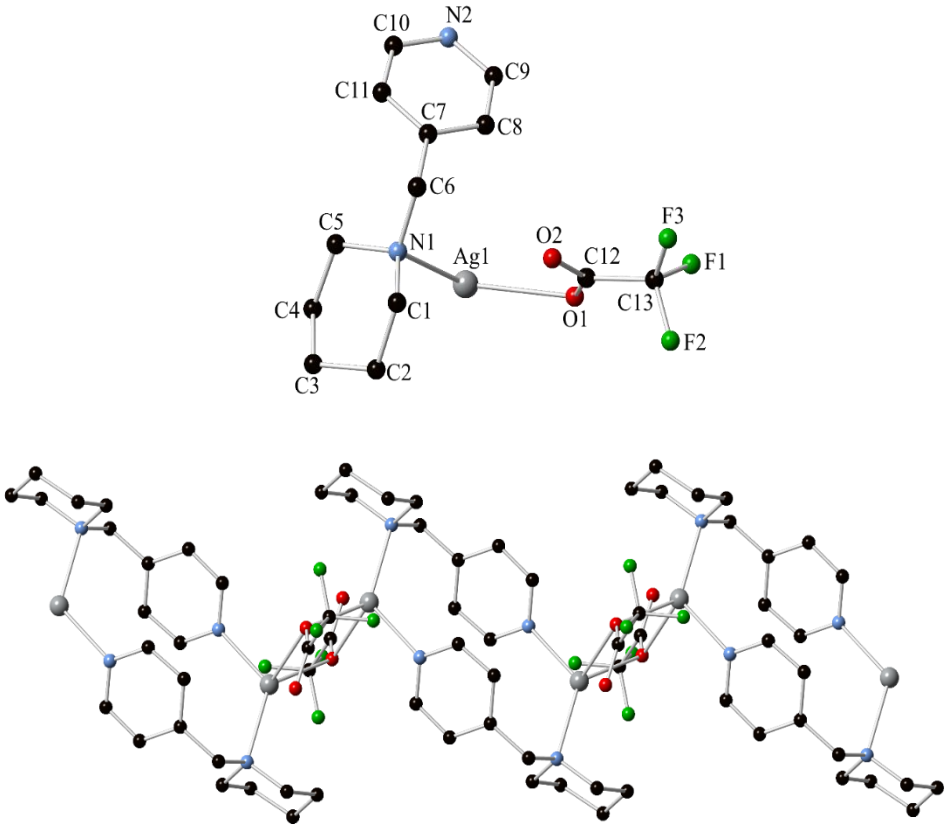

*Figure 2.25. Asymmetric unit (top) and extended 1D chain of poly-[Ag**L2.1**(CO_2CF_3)] (complex **2.10**) (hydrogen atoms were omitted for clarity)*

Upon examination of the extended structure (Figure 2.25), it is observed that the one-dimensional chain consists of alternating units – a dinuclear [Ag_2(**L2.1**)$_2$] box of antiparallel ligand molecules and a smaller four-membered ring in which two silver(I) ions are bridged by two trifluoroacetato ligands *via* an oxygen atom each (Figure 2.26 below). Each silver(I) ion has a tetrahedral geometry, with a τ_4 parameter of 0.753, which is lower than those observed in complex **2.9a** and complexes of **L2.3** when the ratio of metal to ligand is 2:1. The bond angles surrounding the silver(I) ion stray significantly from a perfect tetrahedron, ranging from 96-128° and this (along with the lower τ_4 parameter) is likely due to the restraints of the strained four-membered Ag_2O_2 ring, combined with some steric clash with the ligand piperidine moiety. Like in the bond angles, this steric clash is reflected in the Ag1-O bond lengths with one bond length (Ag1-O1′ - 2.43578(9) Å) being significantly longer than the other (Ag1-O1 - 2.29248(8) Å), while the Ag1-N bond lengths are

`

quite congruent with one another, with the Ag1-N1 and Ag1-N2 bond lengths measuring at 2.30258(9) and 2.31019(8) Å, respectively. The relative orientation of the two aromatic systems within the box is slightly less offset (relative to complex **2.9a**), leading to face-to-face π-π interactions within each [Ag_2(**L2.1**)$_2$] "box", with an interplanar distance of 3.32862(10) Å and a shift of 1.9051(2) Å.

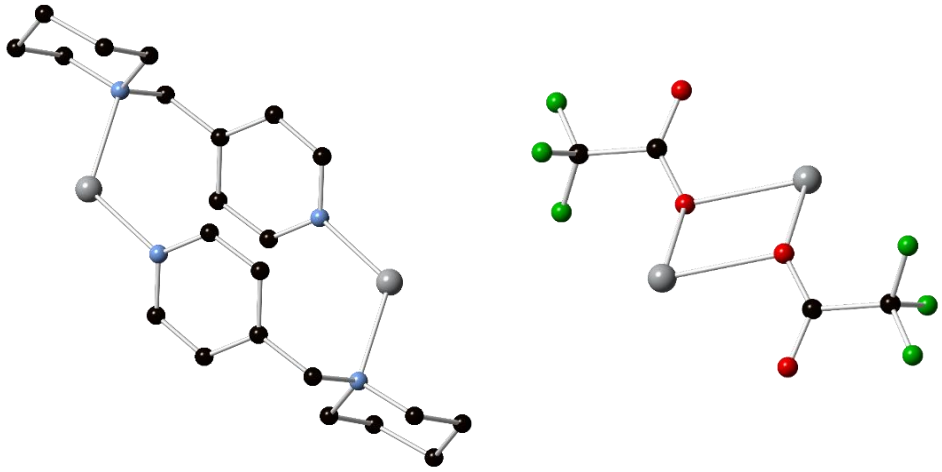

*Figure 2.26. [Ag_2(**L2.1**)$_2$] "box"(left) and silver(I) trifluoroacetato coordination (right) in poly-[Ag**L2.1**(CO_2CF_3)] (complex **2.10**) (hydrogen atoms were omitted for clarity)*

Complex **2.10** (provides an interesting comparison to complexes **2.8** and **2.9**, in which the metal anion is not coordinating. As the anion is significantly less sterically bulky than another ligand molecule, this allows the silver(I) to adopt a tetrahedral geometry, similar to what is observed in complex **2.9a**. This of course has a marked effect on the interactions that are observed in the complex, however, in the case of all three complexes, it is the anion that governs the interactions between neighbouring polymers. In complex **2.10**, C-H···O contacts between a bridging CH_2 group and an anion oxygen atom of a neighbouring chain (with a C···O distance of 3.775(3) Å and a C-H···O angle of 158.78(12)°) are observed, and this is the dominant interaction between neighbouring chains, which is represented by pale pink regions on the d_{norm} mapping of the Hirshfeld surface and the corresponding 2D fingerprint plot, highlighting the O···H contacts in the complex, shown in Figure 2.27. There are also some weaker reciprocated C-H···F contacts between neighbouring chains (with a C···F distance of 3.491(2) Å and a C-H···F angle of 128.20(12)°), similar to

what is seen in complex **2.8**, also shown in Figure 2.27. The Ag1-N1-C6-C7 torsion angle in this case (53.306(3)°), closely resembles the torsion angle observed in the twisted complex **2.9 (**56.8(2)°), as the dinuclear "box" itself requires a somewhat twisted ligand arrangement.

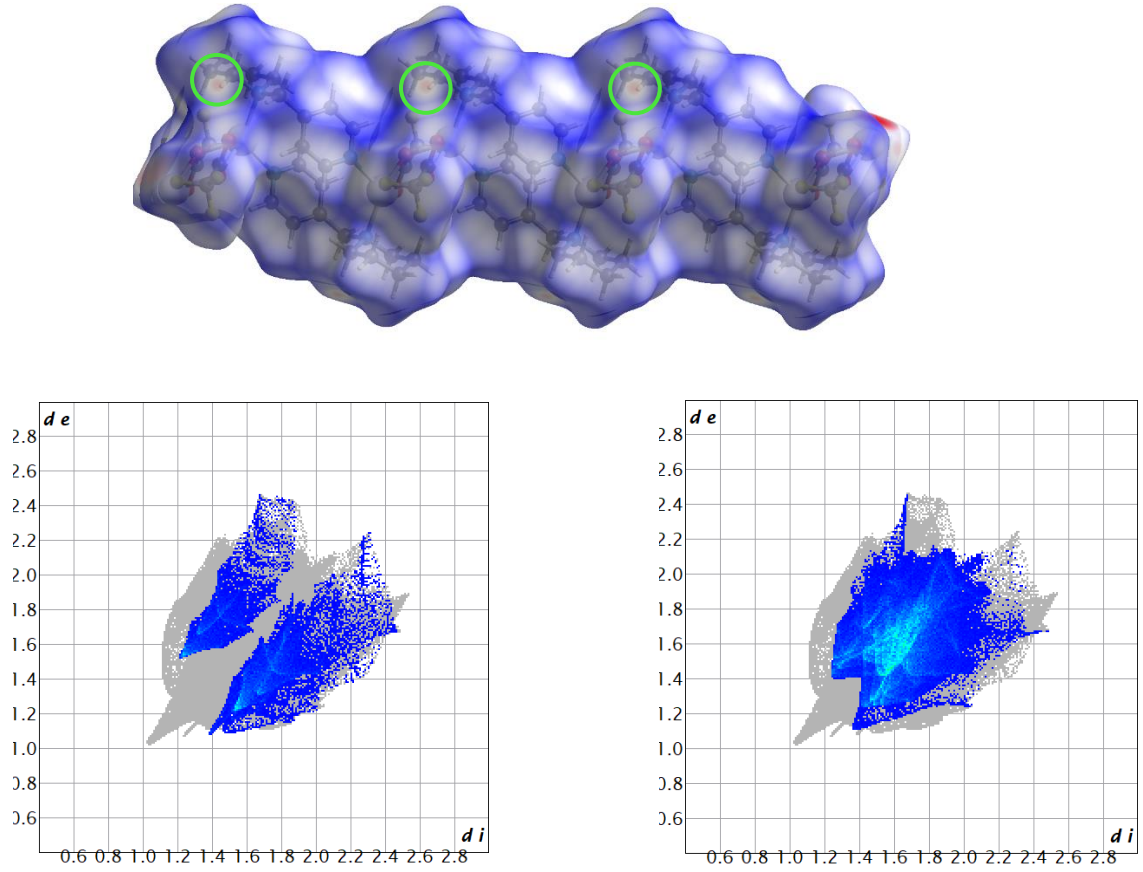

*Figure 2.27. d_{norm} mapping of the Hirshfeld surface highlighting close contacts in green circles (top) and 2D fingerprint plot highlighting O···H contacts (bottom, left) and 2D fingerprint plot highlighting F···H contacts (bottom, right) in poly-[Ag**L2.1(**CO_2CF_3)] (complex **2.10**)*

2.8 Literature Complexes of Silver(I) and L2.3

Complexes of silver(I) trifluoromethanesulfonate, silver(I) tetrafluoroborate and silver(I) trifluoroacetate and **L2.3**, reported by Feazell *et. al.*[27] and Sailaja *et. al.*,[28] offer an interesting set of examples in which neither the ligand nor the metal ion imparts rigid geometric constraints on the resulting crystal packing. The ratios of metal salt to ligand were varied after which some interesting patterns emerged in the formation of the resulting coordination complexes. In each case, when the quantities of metal and ligand are equimolar, each coordination complex is one-dimensional and relatively linear. Once the quantity of ligand is doubled,

`

the geometry of the silver(I) changes to tetrahedral, as it is forced to accept an additional two *N*-donors, and a [**L2.3**$_2$Ag$_2$] dinuclear "box" is present in each of the 2:1 L:M complexes, similar to what is seen in complexes **2.9a** and **2.10**. This "box" again contains two antiparallel **L2.3** ligand molecules, coordinated to two symmetrically equivalent silver(I) ions *via* both nitrogen atoms. The complexes were all synthesised in acetonitrile, allowing for direct comparison of the complexes as the only variables were the molar ratio or the silver salt that was used.

The silver(I) ions in all 1:1 M:L complexes are two-coordinate and have a linear geometry (Figure 2.28 below). The Ag-N-C-C torsion (which proceeds *via* the amine nitrogen atom) and N-Ag-N bond angles for all 1:1 M:L complexes are outlined in Table 2.1, and closely resemble those angles seen in complex **2.8**, which has a high degree of linearity.

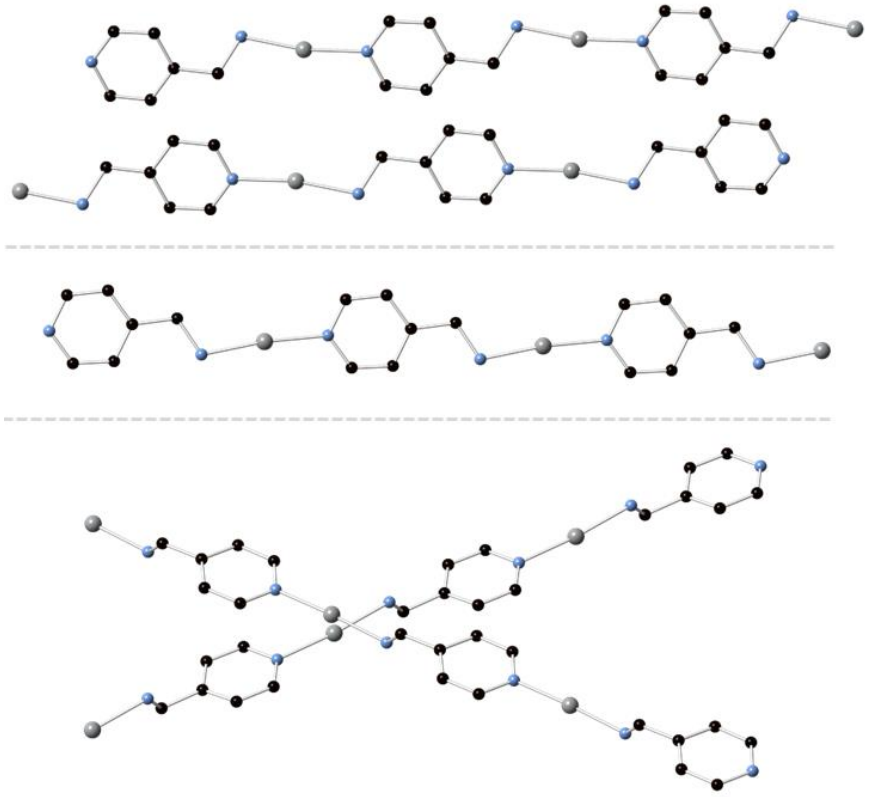

*Figure 2.28 (top to bottom) 1:1 M:L $AgCO_2CF_3$, AgOTf and $AgBF_4$ complexes of **L2.3***

The angles are, as expected, all significantly larger than those seen in complexes **2.9**, **2.9a** and **2.10**, which are either a twisted motif (complex **2.9**) or contain the Ag_2L_2 box (complexes **2.9a** and **2.10**). The Ag-N bond lengths are also all consistent throughout the 1:1 M:L complexes, irrespective of the metal salt used, with all bond lengths ranging from 2.12 to 2.18 Å.

*Table 2.1. N-Ag-N bond angles and Ag-N-C-C torsion angles in 1:1 M:L silver(I) complexes of **L2.3***

Metal salt	N-Ag-N angle(s)	Ag-N-C-C torsion angle(s)
$AgCO_2CF_3$	176.01(10) & 176.68(9)°	178.29(17) &179.80(15)°
AgOTf	172.73(7)°	179.52(14)°
$AgBF_4$	175.0303(13) & 176.8636(12)°	174.568(4) & 176.0603(6)°

`

The presence of a dinuclear [**L2.3**$_2$Ag$_2$] box in the 1:2 M:L complexes of **L2.3** (Figure 2.29) results in the silver(I) ion to obtain a tetrahedral geometry, and this change is also reflected in the Ag-C-C-N torsion angles (again, involving the amine nitrogen atom) in the ligand molecules in each complex (summarised along with the τ_4 parameters in Table 2.2).

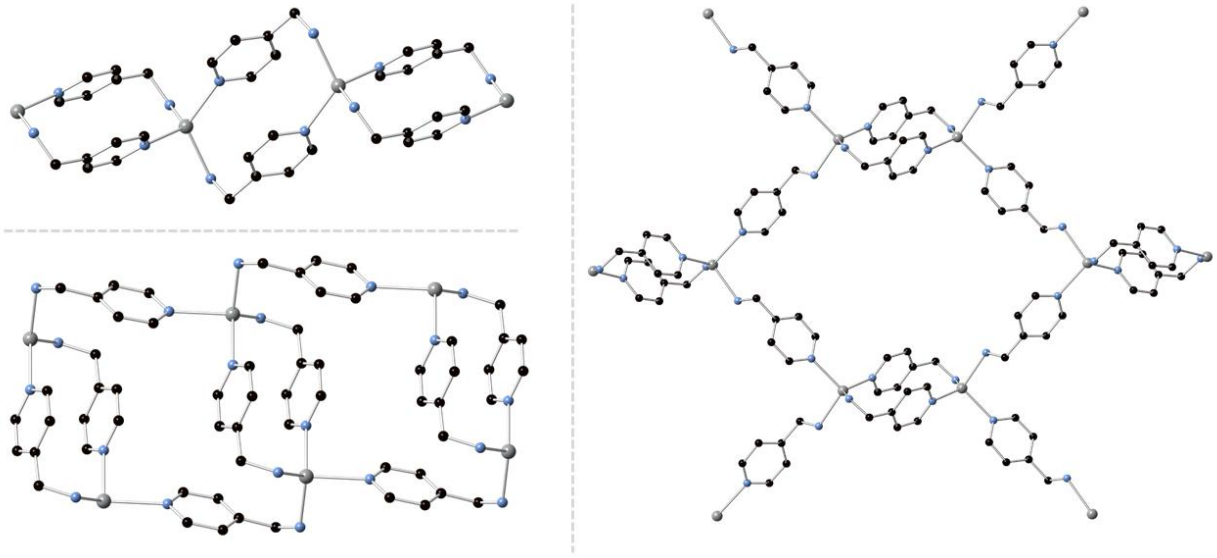

*Figure 2.29. 1:2 M:L complexes of $AgCO_2CF_3$ (left, top), AgOTf (left, bottom) and $AgBF_4$ (right) of **L2.3***

The angles overall become smaller than those in the 1:1 M:L complexes, which is reasonable due to the new geometric constraints likely imparted by the geometry of the silver(I) ion and the favourable π-π interactions present in the "boxes". None of the anions are coordinating, however, likely due to the smaller size and minimal coordinating ability of BF_4^-, relative to the other anions, a two-dimensional polymer forms resulting in the larger variation in torsion angles, in order to accommodate for the presence of the Ag_2L_2 boxes (Figure 2.29).

Table 2.2. Ag τ_4 parameters and Ag-N-C-C torsion angles in 1:1 M:L silver(I) complexes of L2.3

Metal salt	Ag(I) τ_4	Ag-N-C-C torsion angle(s)
$AgCO_2CF_3$	0.833	53.6(3)°
AgOTf	0.865	51.51(10)°
$AgBF_4$	0.826	168.79(17) & 43.19(15)°

The τ_4 parameters are all congruent with one another, likely due to the elongation of some bonds to accommodate for the higher coordination number of the silver(I) ions, with bond lengths now ranging from 2.27 to 2.44 Å, which is significantly longer than those in 1:1 M:L complexes. The τ_4 parameters are all larger than that of complex **2.10**, as none of the anions are coordinating.

2.9 Discussion

The goal of the synthesis and analysis of the 4-picolyl derived ligands **L2.1** and **L2.2** and their coordination chemistries was to gain an understanding of the trends observed in the short contacts arising from the non-aromatic components of the ligands, and their influence on the subsequent crystal packing of their complexes. **L2.3** was then introduced as the equivalent primary amine to study the effects of a much less sterically hindered amine on the network of close contacts. The most significant close contacts in each complex are outlined in Table 2.3.

`

*Table 2.3. Most significant short contacts in complexes **2.1** to **2.10** (inclusive)*

Complex	Metal	CN	Donor Type	Acceptor Type	D···A Distance (Å)	D-H···A Angle (°)
2.1	Cu	5	Picolyl CH_2	Chlorido ligand	3.784(4)	165.5(2)
2.2	Cu	5	3-Pyridyl CH	Chlorido ligand	3.6841(19)	173.41(12)
			Picolyl CH_2	Morpholine O	3.745(4)	136.74(15)
2.3	Cu	5	3-Pyridyl CH	Chlorido ligand	3.650(4)	157.6(3)
			Morpholine NH	Water O	2.911(7)	169.2(3)
			Morpholine N-CH_2	Chlorido ligand	3.686(5)	155.5(3)
2.4	Cu	5	Acetato CH_3	Acetato O	3.567(3)	168.2(3)
			Picolyl CH_2	Acetato O	3.480(6)	153.6(3)
2.5	Co	4	Piperidine NH	Chlorido ligand	3.2007(17)	171.0(3)
			Picolyl CH_2	Chlorido ligand	3.669(2)	148.59(11)
2.6	Co	4	Morpholine NH	Chlorido ligand	3.1366(11)	175.6(17)
			Morpholine N-CH_2	Morpholine O	3.5184(8)	155.39(8)
2.7	Co	4	Amine NH_3	Chlorido ligands	3.202(5), 3.214(5), 3.253(6)	153.1(3), 134.0(3), 166.9(3)
			3-Pyridyl CH	Chlorido ligand	3.687(6)	169.7(4)
2.8	Ag	2	Piperidine N-CH_2	SbF_6^- F	3.458(5)	151.3(3)
2.9	Ag	2	Morpholine N-CH_2	Morpholine O	3.330(4)	155.0(3)
			2-Pyridyl CH	SbF_6^- F	3.359(5)	152.6(2)
2.9a	Ag	4	THF O-CH_2	Morpholine O	3.370(4)	145.40(17)
			2-Pyridyl CH	SbF_6^- F	3.404(3)	155.54(15)
2.10	Ag	4	Picolyl CH_2	$CO_2CF_3^-$ O	3.775(3)	158.78(12)

The shortest close contacts appear to originate at protonated amine donors, provided these are sterically accessible. In complexes **2.3**, **2.5**, **2.6** and **2.7**, these interactions originate at a chorido ligand within the complex and in each case are significantly shorter than the remaining short contacts in the complex, as well as being significantly shorter than the short contacts in the remaining complexes discussed in this chapter. The D-H···A angles in most cases also measure relatively close to 180°. These contacts are classified as

classical hydrogen bonding as the donor atom is nitrogen, resulting in a much more electron-deficient hydrogen atom (relative to a carbon donor atom), resulting in stronger and shorter close contacts. Of these aliphatic CH_2 moieties, the bridging picolyl CH_2 moiety was more likely than the CH_2 in the piperidine ring to form short contacts in complexes of **L2.1**, while in complexes of **L2.2**, the CH_2 moiety in the morpholine ring was much more likely than the picolyl CH_2 moiety to form short contacts.

If there was no protonated heteroatom, *i.e.* strong hydrogen bond donor, in the complex, the most polarised aliphatic CH_2 moieties were most likely to form short contacts. Interestingly, despite the slightly higher electronegativity of oxygen, the aliphatic CH_2 moieties that formed significant close contacts were adjacent to the morpholine or piperidine nitrogen atoms in ligands **L2.1** and **L2.2**, and no significant short contacts were observed to originate at a CH_2 moiety adjacent to the morpholino oxygen atom. In the events where no polarised aliphatic CH_2 moiety is accessible, the most accessible proton/protons are the most likely to partake in close contacts, as some weaker interactions are observed to originate at aromatic protons, such as those in complexes **2.2**, **2.3**, **2.9** and **2.9a**.

The effects of the morpholine oxygen on the crystal packing is observable by comparison of cobalt(II) complexes and silver(I) complexes of both ligands **L2.1** and **L2.2**. Direct comparison of the copper(II) complexes of these ligands was difficult, given the significant structural differences between the complexes. In cobalt(II) and silver(I) complexes of **L2.2**, the morpholine oxygen atom has a tendency to form reciprocated short contacts with an adjacent complex. This, in turn, leads to an observable change to the ligand conformation and subsequent crystal packing, relative to analogous complexes of **L2.1**. In silver(I) hexafluoroantimonate complexes of **L2.1** and **L2.2** (complexes **2.8** and **2.9**) the introduction of a morpholine oxygen atom results in a change to the mode of interaction of the ligand and the anion. This highlights the strong influence of the morpholine oxygen atom on the short contacts and therefore, relative orientation of adjacent complexes within the crystal packing.

In the case of all complexes discussed in this chapter, the crystal packing shows a strong preference for short contacts arising from the most polarised CH_2 moieties adjacent to an amine nitrogen atom or protonated

`

amine nitrogen atoms, where available, assuming they are sterically accessible. Some weaker interactions are present which originate at aromatic CH moieties, if no polarised aliphatic protons are accessible. The trends in short contacts observed in these complexes of relatively simple representative ligands provide a strong basis for designing more complex, aliphatic amine-containing coordinating ligands, such as those derived from tropinone, discussed in Chapters 3 and 4.

2.10 References

1. D. Kim, H. Ha, Y. Kim, Y. Son, J. Choi, M. H. Park, Y. Kim, M. Yoon, H. Kim, D. Kim and M. Kim, *Cryst. Growth. Des.*, 2020, **20**, 5338 – 5345.

2. M. A. Addicoat in *Computer Simulation of Porous Materials: Current Approaches and Future Opportunities*, ed. K. Jelfs, Roy. Soc. Chem., London, 1st edn, 2022, vol. 1, ch. 2, pp. 27 – 78.

3. R. J. Weekes and C. S. Hawes, *CrystEngComm*, 2019, **21**, 5152 – 5163.

4. J. I. Lovitt, T. Gorai, E. Cappello, J. M. Delente, S. T. Barwich, M. E. Möbius, T. Gunnlaugsson and C. S. Hawes, *Mater. Chem. Front.*, 2021, **5**, 3458 – 3469.

5. H. Lee, C. Cho, H. Seo, S. Singha, Y. W. Jun, K. Lee, Y. Jung, K. Kim, S. Park, S. C. Bae and K. H. Ahn, *Chem. Commun*., 2016, **52**, 124 – 127.

6. Y. Tang, Y. Ma, J. Yin and W. Lin, *Chem. Soc. Rev.*, 2019, **48**, 4036 – 4048.

7. S. Park, N. Kwon, J. Lee, J. Yoon and I. Shin, *Chem. Soc. Rev*., 2020, **49**, 143 – 179.

8. Z. Szakács, S. Rousseva, M. Bojtár, D. Hessz, I. Bitter, M. Kállay, M. Hilbers, H. Zhang and M. Kubinyi, *Phys. Chem. Chem. Phys.*, 2018, **20**, 10155 – 10164.

9. H. A. Miller, N. Laing, S. Parsons, A. Parkin, P. A. Tasker and D. J. White, *J. Chem. Soc., Dalton Trans.*, 2000, 3773 – 3782.

10. J. Martinelli, E. Callegari, Z. Baranyai, A. Fraccarollo, M. Cossi and L. Tei, *Molecules*, 2021, **26**, 5993.

11. S. V. F. Beddoe, R. F. Lonergan, M. B. Pitak, J. R. Price, S. J. Coles, J. A. Kitchen and T. D. Keene, *Dalton Trans.*, 2019, **48**, 15553 – 15559.

12. R. Seetharaj, P. V. Vandana, P. Arya and S. Mathew, *Arab. J. Chem.*, 2019, **12**, 295 – 315.

13. C. Zuo, Z. Lu and M. Zhang, *Inorg. Chem. Comm.*, 2015, **52**, 41 – 45.

14. M. A. Spackman and D. Jayatilaka, *CrystEngComm*, 2009, **11**, 19 – 32.

15. R. N. Salvatore, C. H. Yoon and K. W. Jung, *Tetrahedron*, 2001, **57**, 7785 – 7811.

16. O. I. Afanasyev, E. A. Kuchuk, K. M. Muratov, G. L. Denisov and D. Chusov, *Eur. J. Org. Chem.*, **2021**, 543 – 586.

17. R. Vardanyan, *Piperidine-Based Drug Discovery*, Elsevier, Amsterdam, 2017.

18. A. Kumari and R. K. Singh, *Bioorg. Chem.*, 2020, **96**, 103578.

19. J. A. Miller and M. J. Nunn, *J. Chem. Soc., Perkin Trans.*, **1**, 1976, 416 – 420.

20. A. W. Addison, T. N. Rao, J. Reedijk, J. van Rijn and G. C. Verschoor, *J. Chem. Soc., Dalton Trans.*, 1984, 1349 – 1356.

21. J. A. Bertrand and J. A. Kelley, *J. Am. Chem. Soc.*, 1966, **20**, 4746 – 4747.

22. G. Ondrejovič, M. Koman and A. Kotočová, *Chem. Papers*, 2008, **62**, 480 – 486.

23. N. S. Gill and M. Sterns, *Inorg. Chem.*, 1970, **9**, 1619 – 1625.

24. P. Cortes, A. M. Atria, M. Contreras, M. T. Garland, O. Peña and G. Corsini, *J. Chil. Chem. Soc.*, 2006, **51**, 957 – 960.

25. P. Cortes, A. M. Atria, M. T. Garland and R. Baggio, *Acta Crystallogr. C*, 2006, **62**, 311 – 314.

`

26. L. Yang, D. R. Powell and R. P. Houser, *Dalton Trans.*, 2007, 955 – 964.

27. R. P. Feazell, C. E. Carson and K. K. Klausmeyer, *Inorg. Chem.*, 2006, **45**, 935 – 944.

28. S. Sailaja and M. V. Rajasekharan, *Inorg. Chem.*, 2003, **42**, 5675 – 5684.

Chapter 3

· Complexes of Conjugated Tropinone Ligands ·

3.1 Introduction

The observations gained from coordination complexes of **L2.1** and **L2.2**, discussed in Chapter 2 have provided a basis for predictions to be made about more complex aliphatic amine-containing ligands. The conclusion drawn from these representative ligands was that the most polarised CH_2 moiety (adjacent to a protonated or coordinating heteroatom) in the aliphatic backbone is favoured in short contacts that contribute to the crystal packing of the complexes unless this is inaccessible due to steric constraints. This is predicted to also be the case in the complexes of tropinone-derived ligands discussed in this chapter. Similarly to ligands **L2.1** and **L2.2**, these contain a cyclic aliphatic amine functionality, and aromatic coordinating functionalities, with heteroatoms in both the aliphatic and aromatic components of the ligands, which will similarly lead to polarised aliphatic CH_2 moieties that can partake in short contacts.

As discussed in Section 1.11, tropinone, which contains the 8-azabicyclo[3.2.1]octane core, is an attractive starting point for the synthesis of geometrically diverse ligands for metallosupramolecular assemblies. This is due to its rigidity, which arises from the fused-ring moiety, and the versatility of modifications that can be made, as there are multiple sites on the core which can be functionalized using established and relatively straightforward chemistry. The possible functionalisation sites of nortropinone (*i.e.* tropinone without the

methyl moiety at the apical amine) are highlighted in Figure 3.1, and consist of functionalisation of the apical amine, the α-positions and the carbonyl moiety of the ketone itself.

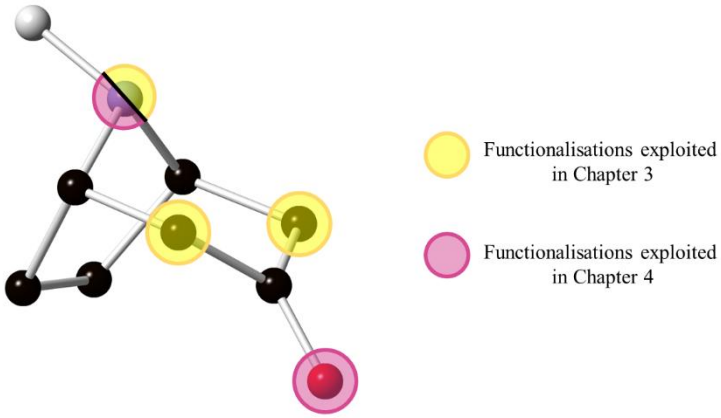

Figure 3.1. Possible functionalisation sites on the nortropinone core (with carbon atoms shown in black, oxygen atoms in red, nitrogen atoms in blue and hydrogen atoms in white)

The modifications of this tropinone-derived core have been previously exploited in the design of pharmaceutically active compounds, as tropane alkaloids have been shown to demonstrate promising biological activity, in particular in the treatment of some cancers and other illnesses,[1-4] which is further discussed in Section 1.11. Tropinone-derived compounds have also been investigated as light-switchable adhesives[5] and catalyst ligands,[6] however, they have not yet been employed as building blocks in metal-organic assemblies.

The modifications that will be discussed in this chapter will be limited to functionalisation at the α-protons and at the apical amine. Ligands resulting from modifications to the ketone functionality combined with *N*-functionalisations, and their coordination chemistries will be discussed further in Chapter 4. The addition of two equivalent coordinating groups onto the tropinone α-positions results in ligands that are structurally similar to traditional ditopic ligands, with coordinating groups approximately 180° from each other (if the coordinating moieties are on the 4-positions of the aromatic ring). However, due to the three-dimensional bicyclic core, these are not quite coplanar and provide an interesting comparison to the planar aromatic ligands that are more commonly encountered in coordination chemistry. The central bulky aliphatic core

will also, in theory, prohibit π-π interactions across the full length of the molecule, and instead restrict these interactions to the outer ends of ligands. The easily functionalised apical amine is the functionality that most significantly distinguishes this family of ligands from others, in some cases leading to coordinating functionalities which are perpendicular to the remaining coordinating moieties at the α-positions.

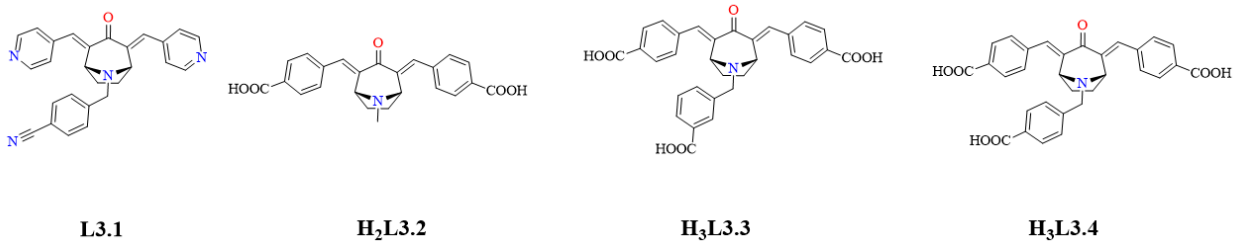

Figure 3.2. Conjugated tropinone ligands discussed in this chapter (left to right) ***L3.1****,* ***H2L3.2****,* ***H3L3.3*** *and* ***H3L3.4***

Four novel ligands, **L3.1**, **L3.2**, **L3.3** and **L3.4** are presented in this chapter, which contain coordinating functionalities consisting largely of pyridyl or carboxylate moieties (Figure 3.2). Therefore, the resulting ligands were mostly combined with first-row transition metals such as cobalt(II) and zinc(II), and lanthanides such as ytterbium(III) and gadolinium(III).

What results is a library of novel coordination complexes (including some MOFs) which are the first to incorporate the fused-ring 8-azabicyclo[3.2.1]octane core, expanding the limited library of rigid aliphatic-containing metallosupramolecular assemblies.

3.2 Ligand Synthesis

A general scheme for the synthesis of the ligands discussed in this chapter is outlined in Scheme 3.1.

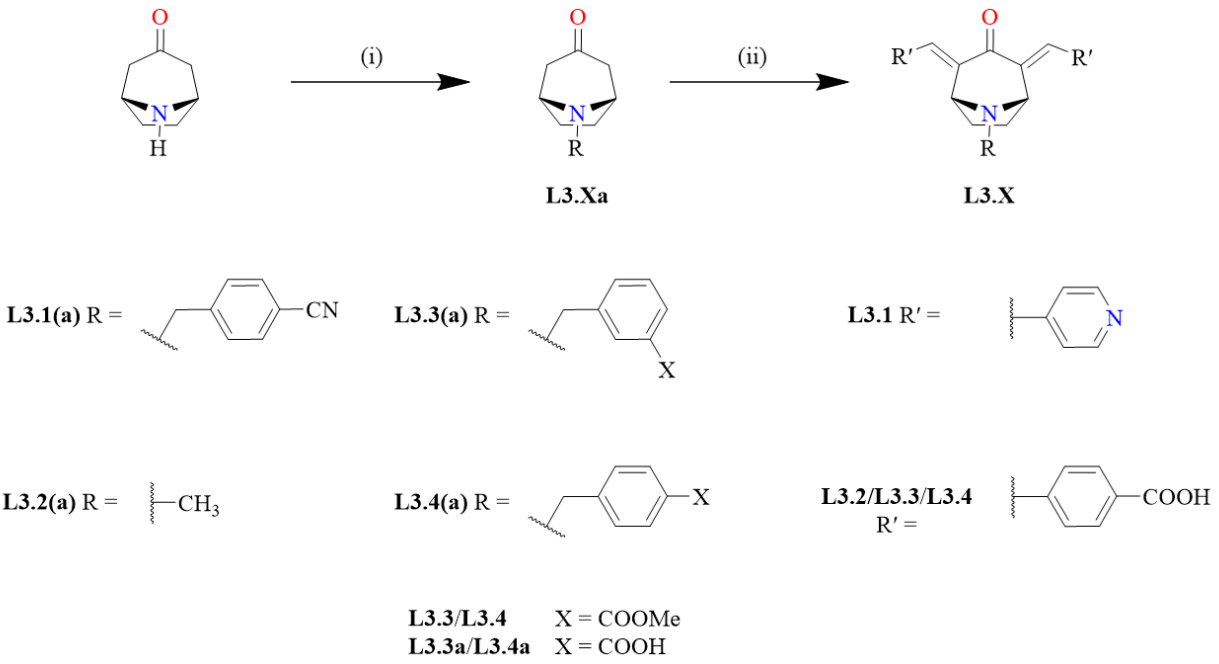

Scheme 3.1. General synthetic scheme for the synthesis of conjugated tropinone ligands discussed in this chapter, (i) R-Br, K_2CO_3, KI, MeCN, (ii) R'-CHO, NaOH, EtOH, N_2

Similarly to the synthesis of ligands **L2.1** and **L2.2**, the functionalisation of the secondary amine of nortropinone proceeds *via N*-alkylation, and is the first step in the synthetic route, leading to intermediates **L3.1a**, **L3.3a** and **L3.4a**. This was chosen as the first step, as *N*-alkylation is frequently a high-yielding transformation, often requiring little to no purification, with little risk of over-alkylation in sterically hindered systems. Addition of coordinating groups to the α-positions of the ketone proceeds *via* a base-catalysed double Claisen-Schmidt condensation. These are commonly used conditions for the modification of tropinone to achieve α-functionalised tropinone derivatives.[7-9]

The synthesis of ligands **H_3L3.3** and **H_3L3.4** demonstrate a convenient one-pot reaction in which an excess of a strong base such as KOH or NaOH is used to simultaneously hydrolyse the ester substituent at the *N*-position to the corresponding carboxylic acid, while also catalysing the condensation reactions at the tropinone α-positions to add the 4-carboxybenzylidene moieties. In the case of **H_2L3.2**, the acidification (to

protonate the carboxylate moieties) after the condensation reaction was carried out with HCl(aq), however, with ligands **H_3L3.3** and **H_3L3.4**, a weaker, non-aqueous acid, HOAc was used. Acidification with HCl(aq) resulted in difficulty in isolation of a solid product due to the protonation of the amine nitrogen atoms, which would cause the ligands to be soluble in the reaction solution, due to the aqueous nature of the acid. This over-acidification likely occurs because the pK_a of the conjugate acid of the amine nitrogen atom is higher than that of the remaining carboxylate functionalities, resulting in complex equilibria which largely involve zwitterionic species in aqueous conditions. Isolation of any solid from the reactions was the hydrochloride salt of the ligands, **H_3L3.3·HCl** and **H_3L3.4·HCl**, which would interfere with future syntheses of metal complexes. Acidification with HOAc, however, resulted in a lower risk of over-acidification, as well as no further addition of water into the system, thus improving the probability of isolating a solid product. As the risk of over-acidification is significantly lowered, so is the risk of isolating the ligands in the form of a salt. Unlike the hydrochloride salt, the acetate salt of the ligands would be easily detected by ^{1}H NMR *via* the acetate peak, which is not observed.

3.3 Complexes of L3.1

Ligand **L3.1** was combined with cobalt(II) and zinc(II) salts in combination with **H_2BDC** or **H_3BTC** in hopes of synthesising porous coordination polymers. The nitrile functionality of **L3.1** was unlikely to coordinate to either cobalt(II) or zinc(II), as it is a soft base which prefers to coordinate to soft acids such as silver(I) or copper(I). In theory, assuming a successful synthesis of a porous material, the lone pair of electrons of the nitrile nitrogen atoms would be available to interact with CO_2, to improve the materials' selectivity towards its adsorption, or act as a site for post-synthetic metallation.[10]

Poly-[Zn(L3.1)$_2$(BDC)$_2$]·2H$_2$O, complex 3.1

Poly-[Zn(**L3.1**)$_2$(**BDC**)$_2$]·2H$_2$O, complex **3.1** forms upon the combination of zinc(II) nitrate with **H$_2$BDC** and **L3.1** in DMF. Although the crystal displayed poor diffraction characteristics, diffraction data of sufficient resolution (*ca*. 1 Å) for an approximate connectivity could be collected. The crystallographic data were solved and refined in the triclinic space group, $P\bar{1}$. The asymmetric unit consists of two zinc(II) ions coordinated by one **L3.1** ligand molecule each, *via* one pyridyl nitrogen atom. There are also two **BDC** molecules, one of which is bridging the two zinc(II) ions, by coordinating *via* one carboxylate oxygen atom on either side, with a second **BDC** molecule coordinating to one of the zinc(II) ions *via* a carboxylate oxygen atom, as well as three lattice water molecules (Figure 3.3).

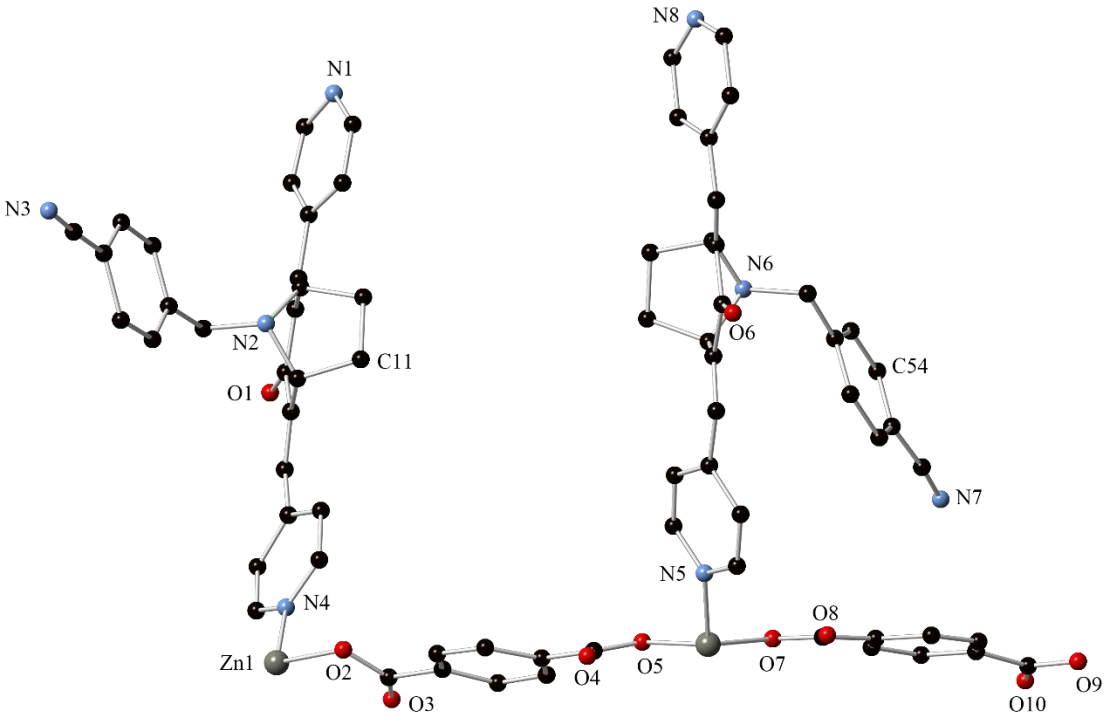

*Figure 3.3. Asymmetric unit of poly-[Zn(**L3.1**)$_2$(**BDC**)$_2$]·2H$_2$O (complex **3.1**), with hydrogen atoms and solvent molecules omitted for clarity*

The geometry of each zinc(II) ion is tetrahedral, and both are coordinated by two **L3.1** pyridyl nitrogen atoms and two **BDC** oxygen atoms. The geometry of both zinc(II) ions does not deviate significantly from that of a perfect tetrahedron, with τ_4 parameters of 0.879 and 0.867 for Zn1 and Zn2, respectively.[11] There is a small variation in bond lengths involving the zinc(II) ions, with the Zn-N bonds being marginally longer than the Zn-O bonds in both the Zn1 and Zn2 coordination spheres, with Zn-N bond lengths ranging from 2.000(17) to 2.031(16) Å and Zn-O bond lengths ranging from 1.979(15) to 1.996(14) Å.

The complex is a three-dimensional polymer, in which **L3.1** ligand molecules are extending parallel to the crystallographic *a*-axis, and **BDC** molecules are extending parallel to the crystallographic *c*-axis. There appear to be square-shaped pores parallel to the crystallographic *b*-axis, however, upon closer inspection of the crystal packing, it was determined that the structure is two-fold interpenetrated with a **cds** topology, with a second three-dimensional network occupying the pores of the first (shown in Figure 3.4).

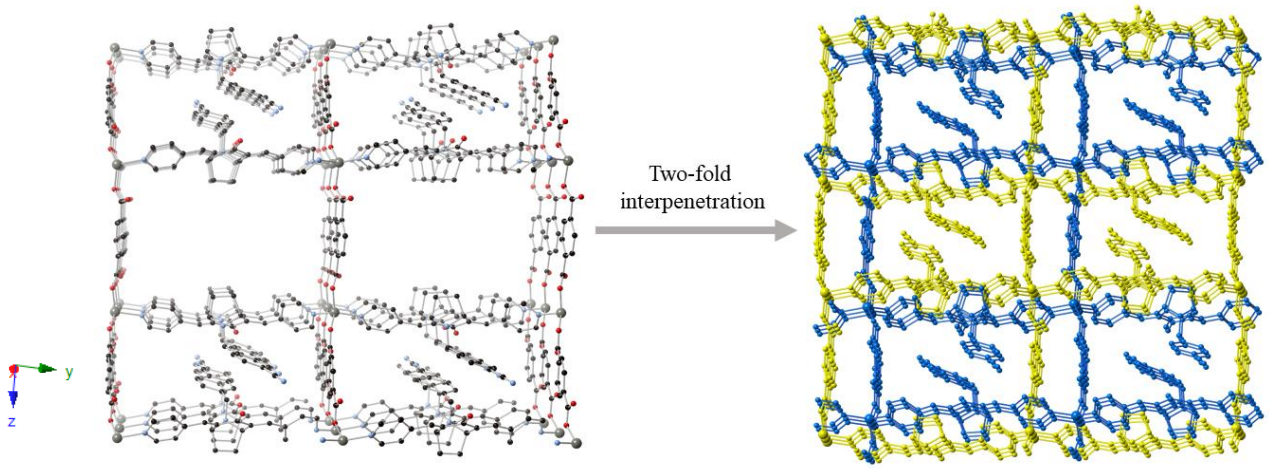

*Figure 3.4. Two-fold interpenetration in poly-[Zn(**L3.1**)$_2$(**BDC**)$_2$]·2H$_2$O (complex **3.1**), with hydrogen atoms and solvent molecules omitted for clarity, individual networks are coloured separately*

There are significant face-to-face π-π interactions between adjacent networks, between the two aromatic systems of **BDC** ligands, with a C34···plane distance of 3.44(3) Å. There is also some hydrogen bonding originating at the lattice water molecule which aids in the association between adjacent networks, though these are not particularly strong due to the significant apparent deviation of the D-H···A angles from 180°. One water molecule forms hydrogen bonds with non-coordinating carboxylate **BDC** oxygen atoms of two different networks with O11···O8/O10 distances of 2.82(2) and 2.75(2) Å, respectively, with a second water molecule interacting with the first, with an O12···O11 distance of 2.89(4) Å. The close contacts which are not involving the water molecule primarily occur between both of the **L3.1** tropinone oxygen atoms of one network and the tropinone CH_2 moieties of another network, with a C11···O1 distance of 3.21(3) Å and a C47···O6 distance of 3.36(2) Å, and these are reciprocated in the other direction. Of the aliphatic tropinone protons, the CH_2 protons are the most accessible, sterically speaking, as they point into the pores of one network. Similarly, the tropinone oxygen atom is relatively unhindered, again making it accessible to participate in close contacts with guests, solvent molecules or other interpenetrated networks.

***Poly*-[Zn(L3.1)(HBTC)]·2H$_2$O·DMF, complex 3.2**

Poly-[Zn(**L3.1**)(**HBTC**)]·2H_2O·DMF, complex **3.2** forms upon the combination of zinc(II) nitrate with **H_3BTC** and **L3.1** in DMF. The crystallographic data were solved and refined in the triclinic space group, $P\bar{1}$, and the asymmetric unit (Figure 3.5) contains one zinc(II) ion coordinated by an **L3.1** ligand molecule *via* a pyridyl nitrogen atom and a **HBTC** molecule *via* one of its carboxylate oxygen atoms. There is also a water molecule forming a hydrogen bond to one of the other **HBTC** carboxylate oxygen atoms.

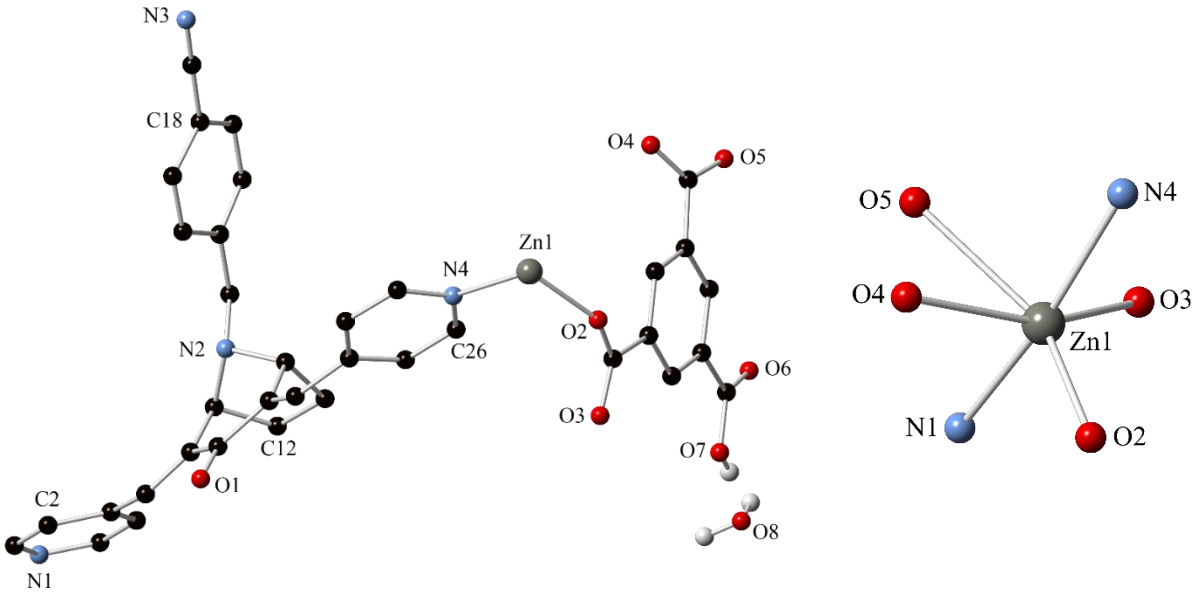

*Figure 3.5. Asymmetric unit of poly-[Zn(**L3.1**)(**HBTC**)]·2H₂O·DMF (complex **3.2**), with selected hydrogen atoms omitted for clarity (left) and coordination geometry of Zn1 in complex **3.2** (right)*

The zinc(II) ions have an octahedral geometry (Figure 3.5) – coordinated by two **L3.1** pyridyl nitrogen atoms *trans* to one another. The remainder of the coordination sphere is completed by **HBTC** carboxylate oxygen atoms, two of which are chelating and two of which are bridging one zinc(II) ion to an adjacent ion. The coordination geometry is significantly distorted from a perfect octahedron, with *cis* angles ranging from 57.95(6)° to 114.54(6)°, with the smaller angle arising due to the geometric constraints of a chelating carboxylate moiety, resulting in a Σ parameter of 96.09°.[12] The bond lengths surrounding Zn1 also reflect this geometric distortion, and range from 2.09 to 2.36 Å, which are longer and encompass a much wider range of bond lengths than those in complex **3.1**, accommodating for the higher coordination number of the zinc(II) ions. Two of the three **HBTC** carboxylate moieties are coordinating (one is chelating and one is bridging, with a μ_2-κO;κO′ bridging mode), while the third is non-coordinating and protonated, and forms a hydrogen bond to an oxygen atom of a water molecule, with an O7···O8 distance of 2.688(3) Å and an O7-H···O8 angle of 172.08(15)°.

The complex is a two-dimensional polymer (Figure 3.6), with zinc(II) carboxylate dimers joined by bridging **HBTC** molecules extending parallel to the crystallographic *a*-axis. If the dinuclear zinc(II) units are assigned as nodes, the complex is assigned a (4,4) Wells symbol. The **L3.1** ligand molecules extend perpendicular to the **HBTC** molecules, with the *N*-(4-methyl)benzonitrile moieties extending at roughly 90° to the remainder of the ligand molecule, parallel to the crystallographic *b*-axis. Adjacent networks associate *via* a combination of hydrogen bonding originating at the water molecule and face-to-face π-π interactions.

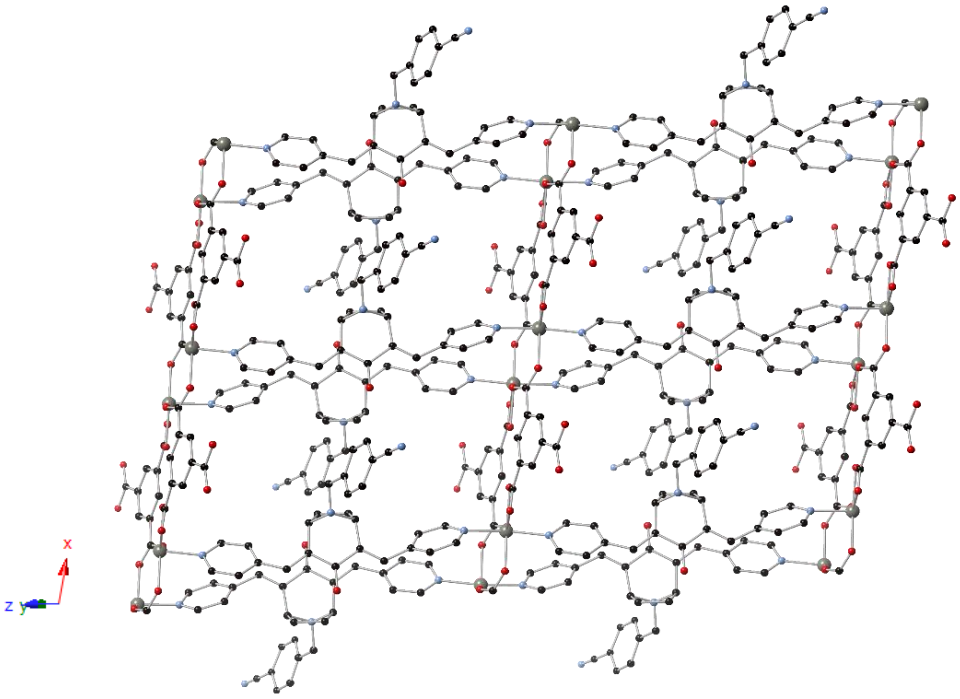

*Figure 3.6. Extended structure of poly-[Zn(**L3.1**)(**HBTC**)]·2H_2O·DMF (complex **3.2**), with hydrogen atoms and solvent molecules omitted for clarity*

The water molecules form a hydrogen bond with a protonated non-coordinating carboxylate OH moiety of a **HBTC** molecule. It also forms a hydrogen bond from its hydrogen atom to a chelating carboxylate oxygen atom of a **HBTC** molecule of an adjacent network, with an O8···O4 distance of 2.787(3) Å and an O8-H···O4 angle of 173.82(14)°. There is also a weaker hydrogen bond from the other water hydrogen atom to a chelating oxygen atom of a **HBTC** molecule in the same network, with an O8···O4′ distance of 3.008(3) Å and an O8-H···O4′ angle of 130.15(13)°. As is evident from the multiple and highly directional hydrogen bonds, the water molecule plays a central role in establishing a strong hydrogen bonding network throughout

the structure (Figure 3.7), having a large influence over the crystal packing of the complex, much more so than is seen in complex **3.1**.

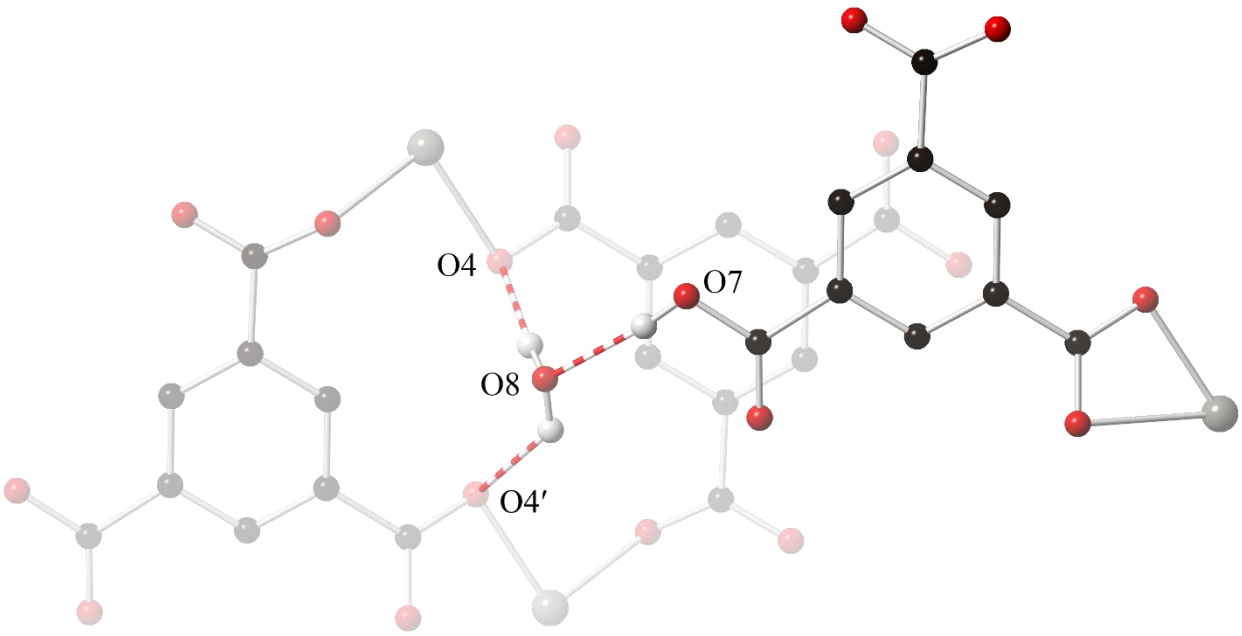

*Figure 3.7. Hydrogen bonding in poly-[Zn(**L3.1**)(**HBTC**)]·2H$_2$O·DMF (complex **3.2**) originating at the lattice water molecule, with one network shown in the foreground and the second associated network shown in the background, with selected hydrogen atoms omitted for clarity*

There are some offset face-to-face π-π interactions, however, none of these are particularly strong with relatively large interplanar distances and large offsets, suggesting that the system favours the stronger hydrogen bonding network in the crystal packing system. The π-π interactions are present between benzonitrile moieties of adjacent networks (with a C18⋯plane distance of 3.656(5) Å) and between a benzonitrile moiety of one network and a **HBTC** benzene ring of an adjacent network (with a C15⋯plane distance of 3.783(3) Å).

Similarly to complex **3.1**, there are some reciprocated C⋯O contacts between the tropinone CH$_2$ moieties and a tropinone oxygen atom of an adjacent network, with a C12⋯O1 distance of 3.34(2) Å and a C12-H⋯O1 angle of 160.3(10)°. Besides these interactions, there are also short contacts originating at both the 2- and 3-pyridyl CH moieties of **L3.1**, to coordinating carboxylate oxygen atom of an adjacent network,

which are not observed in complex **3.1**. The contact originating at the 3-pyridyl CH moiety (C2···O5 distance of 3.212(3) Å), has a D-H···A angle much closer to 180° (C2-H···O5 angle of 170.85(16)°), than the contact originating at the 2-pyridyl CH (with a C26···O6 distance of 3.198(3) Å and a C26-H···O6 angle of 134.09(15)°). A similar phenomenon occurs in complexes discussed in Chapter 2, where the most polarised CH moiety of the pyridyl ring is expected to be at the 2-position of the ring (*i.e.* adjacent to the pyridyl nitrogen atom) and therefore expected to participate in the stronger short contacts. However, this again is not the case, suggested by the D-H···A angle that is significantly smaller than 180°, suggesting this CH moiety is much less accessible than the CH moiety at the 3-position, again resulting in the stronger C-H···O contacts originating at the 3-position.

***Poly*-[Co(L3.1)(HBTC)]·2.5H$_2$O, complex 3.3**

Poly-[Co(**L3.1**)(**HBTC**)]·2.5H$_2$O, complex **3.3** is isostructural to complex **3.2**, despite incorporating a different transition metal ion with different electronic properties. The complex again crystallises in the triclinic space group, $P\bar{1}$. The asymmetric unit (Figure 3.8) contains one cobalt(II) ion, an **L3.1** ligand molecule coordinated to the cobalt(II) ion *via* a pyridyl nitrogen atom, a **HBTC** molecule coordinating *via* an oxygen atom and a water molecule forming a hydrogen bond to the protonated carboxylate oxygen atom of a **HBTC** molecule.

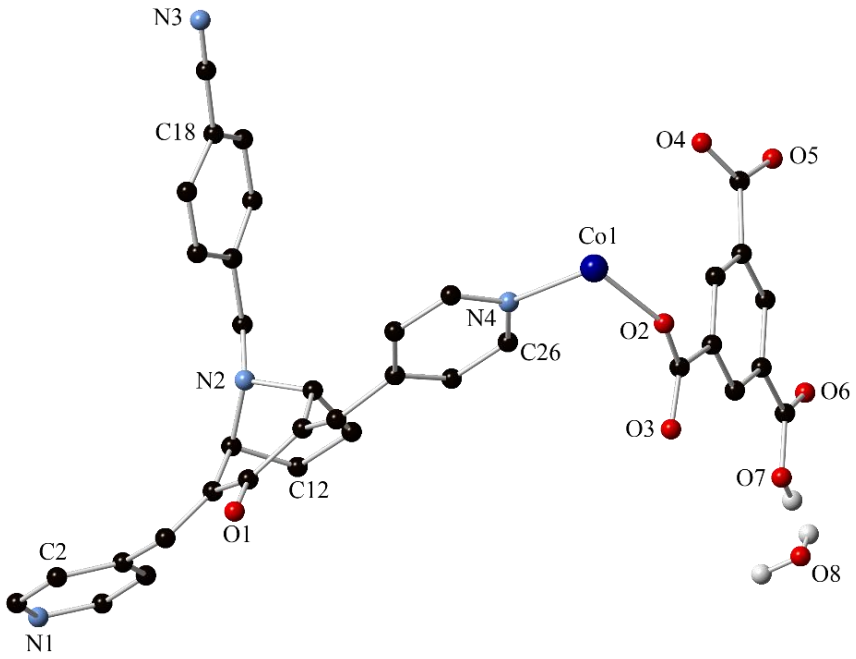

*Figure 3.8. Asymmetric unit of poly-[Co(**L3.1**)(**HBTC**)]·2.5H$_2$O (complex **3.3**), with selected hydrogen atoms omitted for clarity*

Complex **3.3** is again a two-dimensional polymer, and the cobalt(II) ion has an octahedral geometry coordinated by two **L3.1** pyridyl nitrogen atoms *trans* to one another, and four carboxylate oxygen atoms – two are chelating and two are bridging (Figure 3.9).

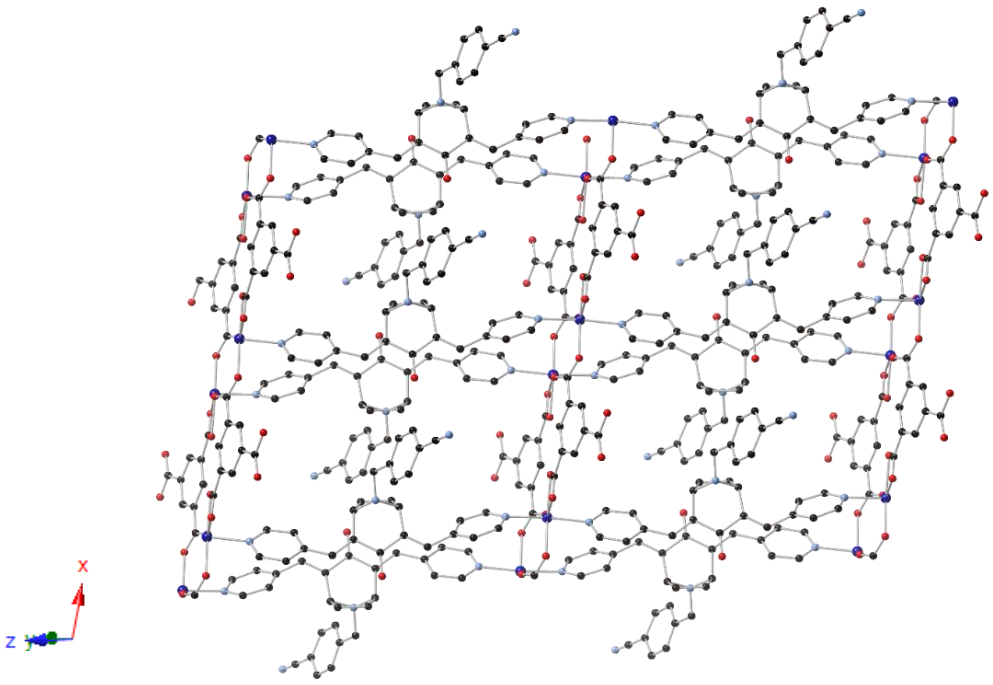

*Figure 3.9. Extended structure of poly-[Co(**L3.1**)(**HBTC**)]·2.5H_2O (complex **3.3**), with hydrogen atoms and solvent molecules omitted for clarity*

The geometry surrounding the cobalt(II) ion is only slightly less distorted than its zinc(II) analogue, with *cis* angles ranging from 59.50(6)° to 112.32(7)°, with a Σ parameter of 91.9°. This lower Σ parameter (relative to complex **3.2**) is likely due to the ligand field stabilisation energy (LFSE) experienced by cobalt(II) (which has an [Ar]$3d^7$ electron configuration), which is not experienced by zinc(II) (which has an [Ar]$3d^{10}$ electron configuration), and therefore has no preference for any coordination geometry. The range of bond lengths surrounding the cobalt(II) ion is interestingly narrower than in complex **3.2**, ranging from 2.02 to 2.25 Å, which appears to be a common trend in isostructural zinc(II) and cobalt(II) complexes, irrespective of coordination number or geometry.[13-16]

***Poly*-[Zn_3(**L3.1**)$_2$(**BTC**)$_2$(H_2O)$_2$]·4H_2O·DMF, complex 3.4**

Poly-[Zn_3(**L3.1**)$_2$(**BTC**)$_2$(H_2O)$_2$]·4H_2O·DMF, complex **3.4** is a two-dimensional polymer which forms upon the combination of **L3.1**, **H_3BTC** and $ZnCl_2$·H_2O in DMF. This complex serves as an interesting comparison

to complex **3.2**, in which all synthetic conditions were kept consistent except for the chosen metal salt. Although the crystal displayed poor diffraction characteristics, diffraction data of sufficient resolution (*ca.* 1 Å) for an approximate connectivity could be collected. The crystallographic data for complex **3.4** was solved and refined in the orthorhombic space group *Pcca*. The asymmetric unit (Figure 3.10) consists of a zinc(II) ion coordinated by one **L3.1** ligand molecule *via* a pyridyl nitrogen atom, and a **BTC** molecule *via* one of the carboxylate oxygen atoms. The **BTC** molecule is also coordinating to a second zinc(II) ion *via* an oxygen atom of an adjacent carboxylate moiety. The zinc(II) ion is also coordinated by a water molecule *via* its oxygen atom. There are also two lattice water molecules present.

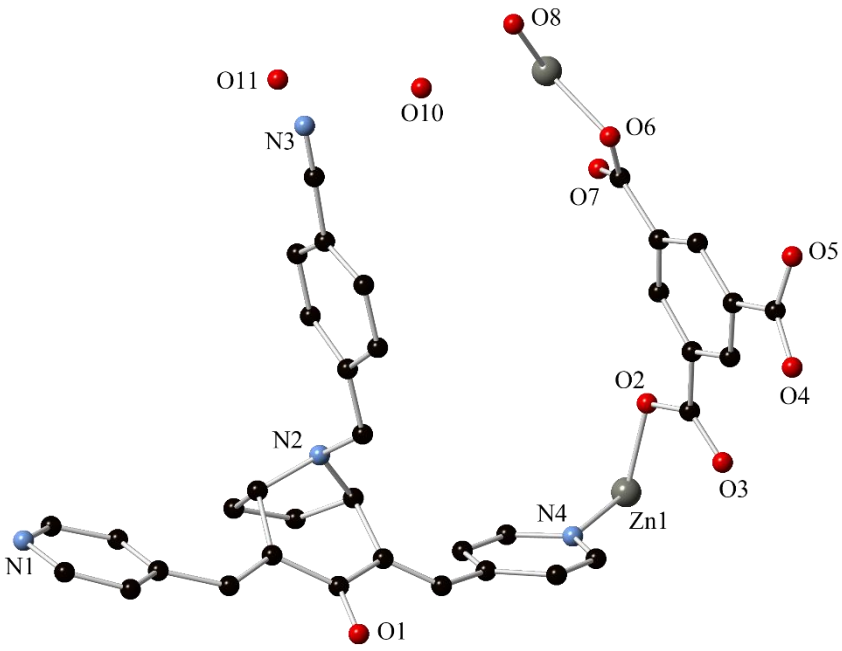

*Figure 3.10. Asymmetric unit of poly-[Zn_3(**L3.1**)$_2$(**BTC**)$_2$(H_2O)$_2$]·4H_2O·DMF (complex **3.4**), with hydrogen atoms omitted for clarity*

Each zinc(II) ion has a tetrahedral geometry, with Zn1 being coordinated by two **L3.1** molecules *via* their respective pyridyl nitrogen atoms and two **BTC** molecules *via* a carboxylate oxygen atom each. Zn2, on the other hand, is coordinated by two **BTC** molecules, again *via* a carboxylate oxygen atom each and two water

molecules, *via* their respective oxygen atoms. Due to the large quantity of both coordinating and non-coordinating water molecules, there appears to be a significant hydrogen bonding network throughout this material, originating at a coordinating water molecule, to one lattice water molecule (O8···O9 distance of *ca*. 2.655(16) Å) and then from that water molecule to a second lattice water molecule (O9···O10 distance of *ca*. 2.82(3) Å), however no meaningful D-H···A angles can be reported due to the low quality of the SCXRD data obtained. As in complexes **3.2** and **3.3**, there appear to be short contacts originating at the 3-pyridyl CH moiety of one network to a **BTC** oxygen atom. Also, similarly to all of the complexes discussed thus far, there appear to be reciprocated contacts between a tropinone oxygen atom and the tropinone CH_2 moieties of an adjacent network.

The extended structure, shown in Figure 3.11, is a two-fold interpenetrated (2D → 2D) two-dimensional polymer. In one network, the **L3.1** ligand molecules extend parallel to the crystallographic *c*-axis, while the **BTC** molecules extend parallel to the crystallographic *a*-axis, joined by zinc(II) ions between two **BTC** molecules. The benzonitrile moieties of the **L3.1** molecules also extend parallel to the crystallographic *a*-axis. The association of adjacent networks occurs *via* a combination of hydrogen bonding and π-π interactions between **BTC** molecules of adjacent networks, as has been observed in complexes **3.2** and **3.3**.

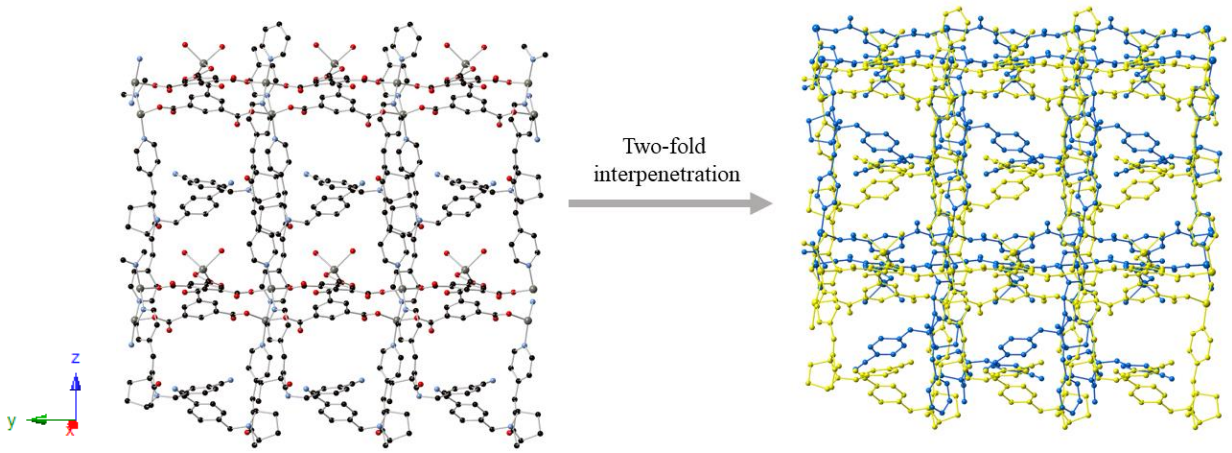

*Figure 3.11. Two-fold interpenetration in poly-[Zn_3(**L3.1**)$_2$(**BTC**)$_2$(H_2O)$_2$]·4H_2O·DMF (complex **3.4**), with hydrogen atoms and solvent molecules omitted for clarity, individual networks are coloured separately*

It is interesting to observe the differences between complex **3.2** and **3.4**, as the only difference was the choice of metal salt (zinc(II) nitrate and zinc(II) chloride, respectively). In both complexes, there are lattice water molecules, which largely govern the network of short contacts in the crystal packing. In both cases, the hydrogen bonding appears to be relatively strong, with the D···A distances being relatively short, and the D-H···A angles appearing close to 180°. Both complexes are also two-dimensional, however, only complex **3.4** is two-fold interpenetrated. Neither anion appears in the crystal structure of either complex, however the modes of interactions that these anions can offer differ significantly, and thus affect the dimensionality and structural properties of each respective complex. More direct comparisons of hydrogen bonding and other short contacts would be made if better structural data were available for complex **3.4**, however it is interesting to observe the fundamental differences in connectivity between the two complexes that arise from simply using different zinc(II) salts in the synthetic procedure. If each Zn_2 is considered as a link and the BTC molecules that are coordinating *via* all three of their carboxylate functionalities are considered three-connecting nodes, the connectivity can be considered to be analogous to that of complex **3.2**, if half of the original links (two-coordinate HBTC molecules) are now three-connecting nodes.

3.4 Complexes of Carboxylate Ligands

Carboxylate ligands **L3.2** and **L3.3** were synthesised to offer a comparison to the aromatic dicarboxylate ligands traditionally encountered in MOF chemistry. In particular, the two α-carboxylic acid moieties that point approximately 180° from each other in both ligands resemble ditopic aromatic dicarboxylates such as terephthalic acid, however as previously discussed, they are typically not within the same plane and have a bulky non-planar component separating them. **L3.3** has an added coordinating functionality at the apical amine, which further diversifies the coordination modes of these ligands. These ligands formed exclusively porous coordination polymers, which is not observed in complexes of **L3.1**.

Poly-[Yb_3(L3.2)$_4$(HL3.2)]·4H_2O·6DMF, complex 3.5

Poly-[Yb_3(**L3.2**)$_4$(**HL3.2**)]·4H_2O·6DMF, complex **3.5** is a three-dimensional MOF forming from the combination of $YbCl_3$·6H_2O and **H_2L3.2** in DMF. The crystallographic data were solved and refined in the monoclinic space group _C_2/_m_ and the asymmetric unit (Figure 3.12) consists of two ytterbium(III) ions and one full and three half **L3.2** ligand molecules. One of the nitrogen atoms in the complex is protonated, as evidenced by the N-H stretch at 3408 cm^{-1} in the IR spectrum, which charge balances the complex. As there are no ordered hydrogen bond acceptors observed near any of the nitrogen atoms, it is not possible to determine which of the nitrogen atoms in the complex is protonated, and as such, a protonated tropinone nitrogen atom is treated as the most likely formulation. While the framework of the complex itself could be well-modelled from the diffraction data, due to the large voids present within the structure there was a large quantity of disordered solvent molecules within the lattice, and so, the SQUEEZE routine was applied to the model.[17]

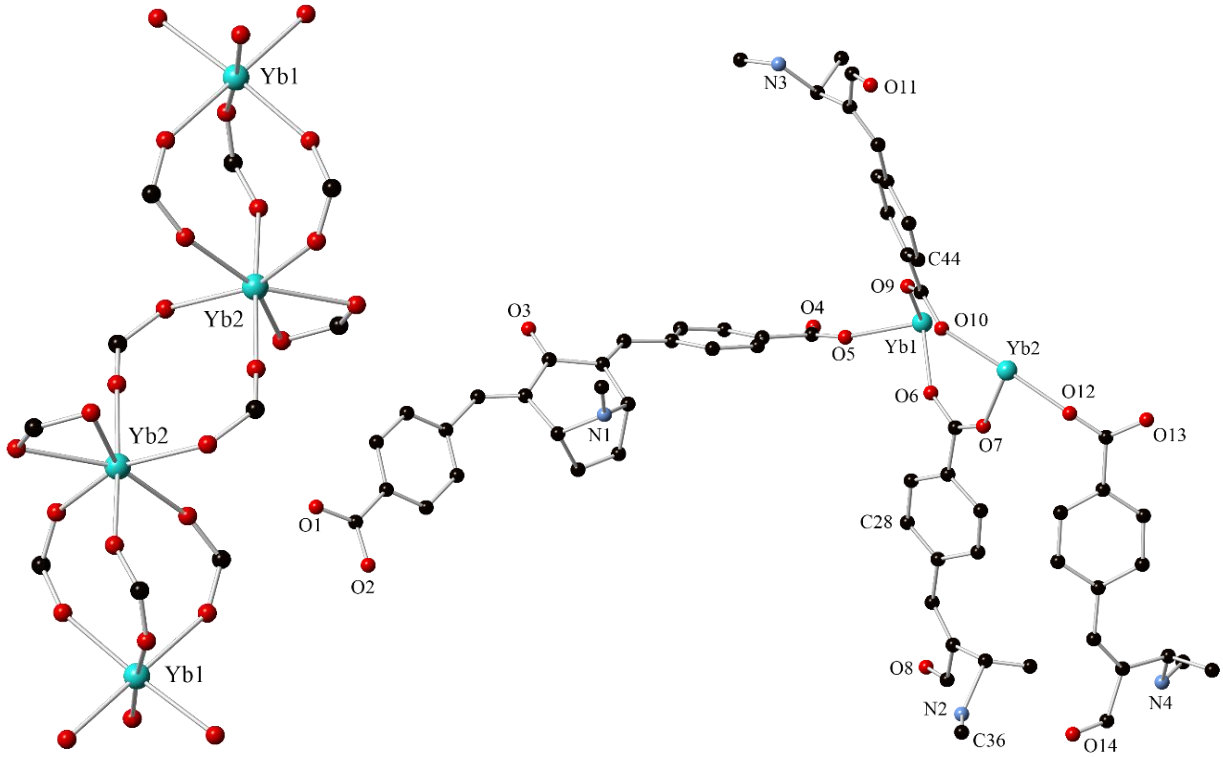

*Figure 3.12. Ytterbium(III) carboxylate chains (left) and asymmetric unit (right) of poly-[Yb_3(**L3.2**)$_4$(**HL3.2**)]·4H_2O·6DMF (complex **3.5**), with hydrogen atoms omitted for clarity*

As is common with lanthanide coordination complexes, the ytterbium(III) ions form one-dimensional ytterbium(III) carboxylate chains along the crystallographic *a*-axis (Figure 3.12). These chains are linked to neighbouring chains *via* ligand molecules which run along the crystallographic *b*- and *c*-axes. The ligand molecules have two coordination modes; in some cases, the two carboxylate oxygen atoms are chelating to one ytterbium(III) ion, and in other cases, the two oxygen atoms of one carboxylate moiety are coordinating to two different ytterbium(III) ions, leading to μ_3 and μ_4 ligand coordination modes. The two metal ions also differ slightly in their coordination geometries, Yb1 is six-coordinate with an octahedral geometry (which is only slightly distorted, with a Σ parameter of 36.7°), whereas Yb2 is seven-coordinate with a pentagonal bipyramidal geometry. The largest pore channels run along the crystallographic *a*-axis (Figure 3.13) and they are lined with ligand molecules along each side with the ytterbium(III) carboxylate chains at each corner. These pores are approximately 12.5 Å in width, which corresponds to the distance between two opposing tropinone methyl groups which point into the pores, and the calculated pore volume per unit cell is 13458 $Å^3$, which accounts for *ca*. 62.2% of the total unit cell volume.

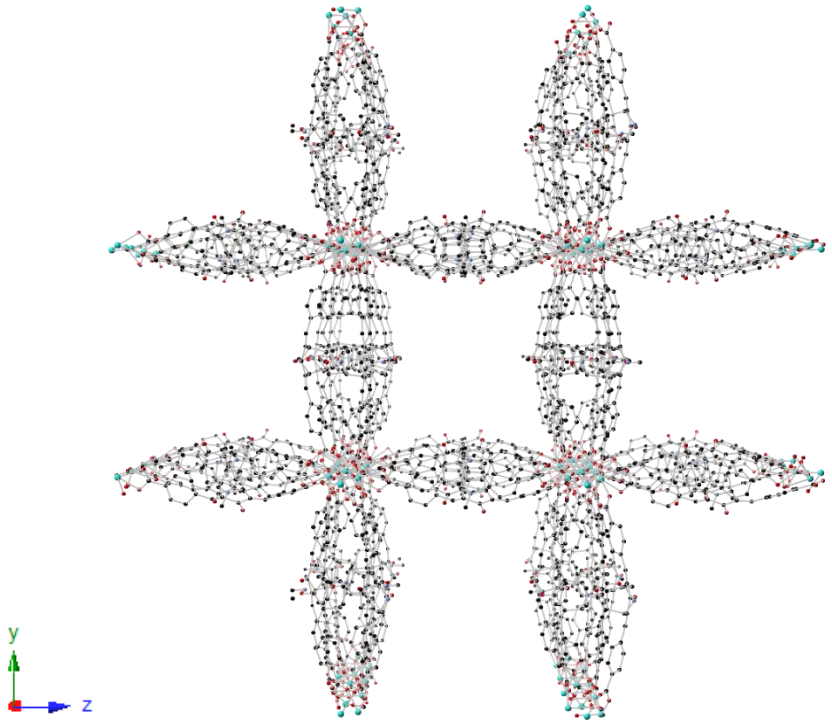

*Figure 3.13. Extended structure of poly-[Yb_3(**L3.2**)$_4$(**HL3.2**)]·4H_2O·6DMF (complex **3.5**), with hydrogen atoms omitted for clarity*

The internal pore chemistry appears to have significant aliphatic character, as the tropinone methyl moieties and the remainder of the tropinone core line the surface of the pores. Interestingly, despite the large size of the pores, there is no interpenetration of networks. This could be due to the aromatic components of the ligands being less accessible for significant π-π interactions as they are surrounding the sterically crowded metal ions, while the more accessible components of the ligands are the aliphatic tropinone core, which itself is bulky, likely hindering the ability to form short contacts with adjacent networks. There are some offset π-π interactions between adjacent benzene rings, with a C28···plane distance of 3.534(15) Å. The **L3.2** molecules align in pairs between the ytterbium(III) carboxylate chains (Figure 3.14), and there are some offset face-to-face π-π interactions between the aromatic components of the ligands, with an interplanar distance of 3.520(11) Å and an offset of 1.690(18) Å. The complex has a **pcu** rod packing topology,[18] if the ytterbium(III) carboxylate chains are assigned as one-dimensional rods.

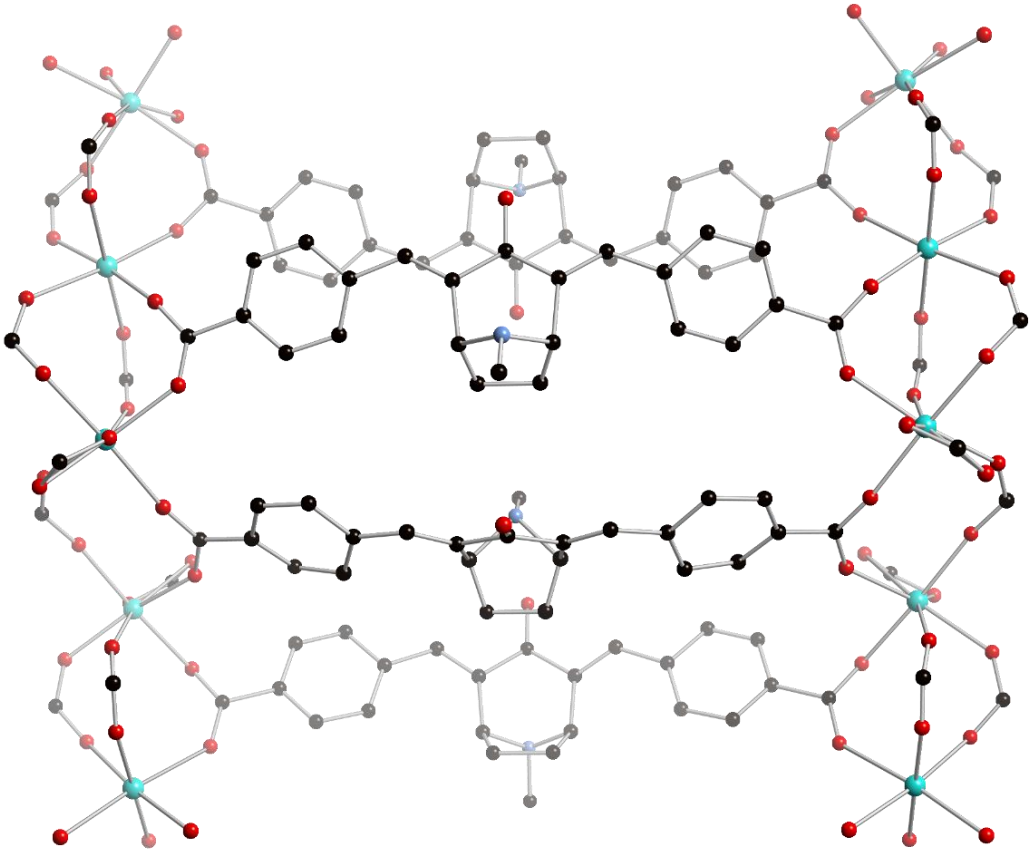

*Figure 3.14. Linking of adjacent ytterbium(III) carboxylate chains via **L3.2** ligand molecules in poly-[Yb_3(**L3.2**)$_4$(**HL3.2**)]·4H_2O·6DMF (complex **3.5**), with hydrogen atoms omitted for clarity*

Interestingly, similar to complexes of **L3.1**, there are again reciprocated short contacts that originate at the tropinone oxygen atom, however in this case it is associated with the tropinone *N*-CH_3 of an adjacent **L3.2** ligand molecule, with a C36···O14 distance of 3.55(4) Å, and a C36-H···O14 angle of 148.0(10)°. There are also C···O contacts between a chelating carboxylate oxygen atom and the 2-CH benzyl moiety of an adjacent ligand molecule, with a C44···O1 distance of 3.575(10) Å, and a C44-H···O1 angle of 163.1(5)°. These interactions are understandably, significantly weaker than those observed in complexes of **L3.1**, as there is no lattice water molecule to participate in any significant hydrogen bonding. This complex is also not interpenetrated, as opposed to complexes **3.1** and **3.4**, resulting in less opportunity for ligands to associate with one another due to the larger separation between them.

Poly-[Gd(L3.3)(DMF)$_2$]·2DMF·H$_2$O, complex 3.6

Poly-[Gd(**L3.3**)(DMF)$_2$]·2DMF·H$_2$O, complex **3.6**, is also a three-dimensional MOF, which crystallises in the monoclinic space group *C*2/*c*. The asymmetric unit (Figure 3.15) consists of one **L3.3** ligand molecule, which coordinates to a gadolinium(III) ion *via* one of its carboxylate oxygen atoms. There are also two DMF solvent molecules coordinating to that gadolinium(III) ion *via* their respective oxygen atoms. While the main framework of complex **3.6** could be well established, there was again a large amount of disordered solvent present within the lattice. In order to provide the best representation of the complex itself, the SQUEEZE routine was applied to the model.[17]

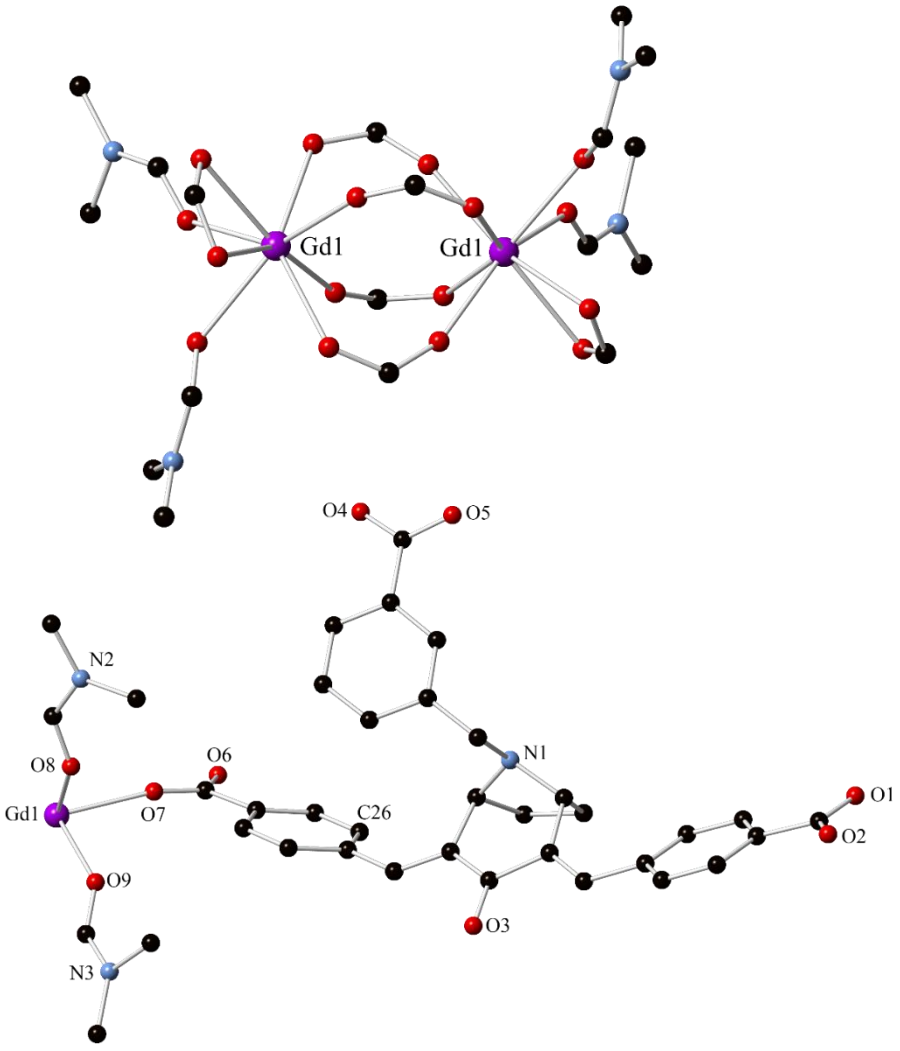

*Figure 3.15. Gadolinium(III) carboxylate dimers (top) and asymmetric unit of poly-[Gd(**L3.3**)(DMF)$_2$]·2DMF·H$_2$O (complex **3.6**), with hydrogen atoms omitted for clarity*

Unlike complex **3.5**, and many other lanthanide coordination complexes, there is an absence of a one-dimensional lanthanide carboxylate chain in this complex. Instead, there are dinuclear gadolinium(III) carboxylate cluster nodes (Figure 3.15), in which the two gadolinium(III) ions are bridged *via* four separate ligand carboxylate moieties, each with a μ^2-κO:κO′ bridging mode. Each gadolinium(III) ion is equivalent, and the remainder of the eight-coordinate geometry is completed by chelation of another ligand carboxylate moiety and two solvent DMF molecules, leading to a dodecahedral geometry. The bridging occurs only *via* the α-carboxylate moieties, while chelation occurs only *via* the carboxylate moiety that is at the apical amine of the tropinone core. Despite the large aromatic proportion of the ligand molecule, there appear to be no π-π interactions present in the structure.

Upon examination of the extended structure, there are several observable pores that all run along the crystallographic *c*-axis (Figure 3.16). The largest of these is approximately 12.0 Å in diameter and the internal volume is calculated to be 1428 $Å^3$ per unit cell, which accounts for *ca*. 15.2% of the total unit cell volume. The smaller pore channels are approximately 6.9 and 9.8 Å in diameter and account for 806 Å (8.5%) and 1088 $Å^3$ (11.4%) in volume per unit cell.

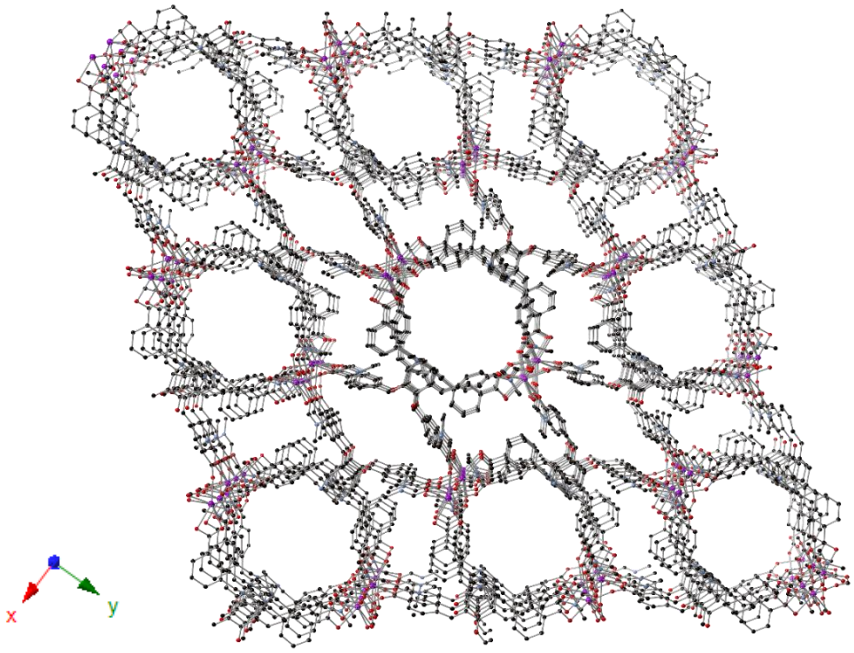

*Figure 3.16. Extended structure of poly-[Gd(**L3.3**)(DMF)$_2$]·2DMF·H_2O (complex **3.6**), with hydrogen atoms omitted for clarity*

Assigning the tropinone core as a three-connecting node and the gadolinium(III) carboxylate dimers as six-connecting nodes, an **ant** topology results, of which there are sixty examples in the Inorganic Crystal Structural Database (ICSD),[19] and 139 reported coordination compounds/MOFs. The complex has the same connectivity as the anatase form of TiO_2.[20]

Again, the short contacts in this complex are significantly weaker than in complexes of **L3.1**, due to the larger separation between adjacent ligand molecules and absence of interpenetration. However, as with previously reported complexes, there are short contacts from the tropinone oxygen atom, yet this is the first complex in which the contacts do not originate at an aliphatic CH_2/CH_3 moiety. Instead, the contacts originate at a 3-benzyl CH moiety of an α-carboxylate functionality, with a C26···O3 distance of 3.428(9) Å and a C26-H···O3 angle of 130.7(4)°, which is quite weak, given the significant deviation of the D-H···A angle from 180°. Aside from this, a coordinating DMF CH_3 moiety forms a short contact with a coordinating carboxylate oxygen atom of a **L3.3** moiety, with a C33···O5 distance of 3.534(13) Å and a C33-H···O5 angle of 174.5(10).

Interestingly, the synthesis of complex **3.6** was only successful in the presence of **dpe** as a weak base (with a pK_a range of *ca*. 4.8 to 5.9),[21] and does not form satisfactory crystals for SCXRD analysis *via* the standard route of carboxylic acid deprotonation by heating the solution in DMF to generate a strong base, dimethylamine (with a pK_a of *ca.* 10.7).[22]

***Poly*-[Co_3(L3.4)$_2$(dpe)$_2$(H_2O)]·8H_2O·2DMF, complex 3.7**

Finally, *poly*-[Co_3(**L3.4**)$_2$(**dpe**)$_2$(H_2O)]·8H_2O·2DMF, complex **3.7**, crystallises in the triclinic space group $P\bar{1}$. The asymmetric unit (Figure 3.17) consists of one ligand molecule coordinated to two cobalt(II) ions *via* an oxygen atom of one of the α-carboxylate moieties and one of the oxygen atoms of the *N*-carboxylate moiety of **L3.4**. There is also one half of a **dpe** molecule coordinating to the Co2 *via* the pyridyl nitrogen atom, and a water molecule coordinating *via* its oxygen atom. There is also a non-coordinating lattice water molecule in the asymmetric unit. As with complexes **3.5** and **3.6**, the SQUEEZE routine was applied to the

crystallographic data in order to obtain a representative model of the framework, due to the large amount of disordered solvent molecules in the pore channels.[17]

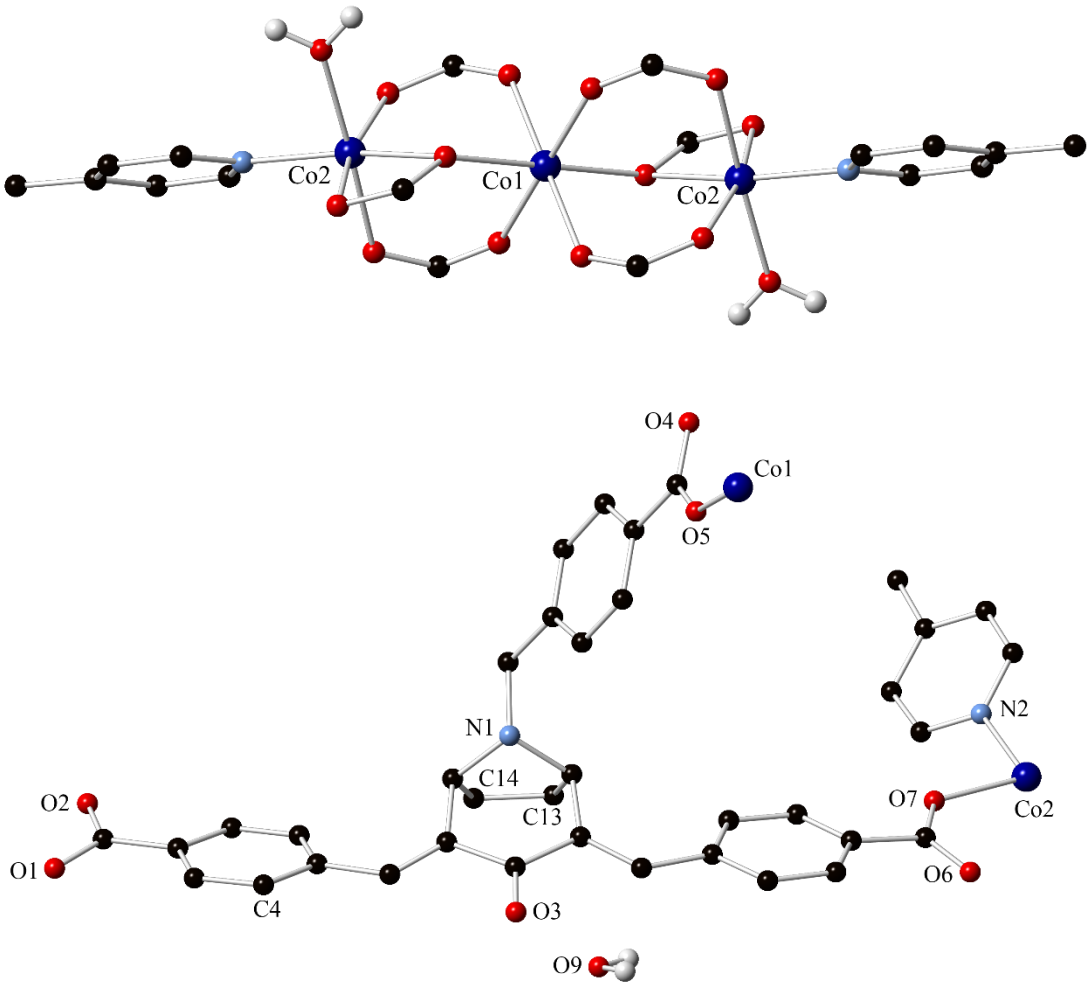

*Figure 3.17. Cobalt(II) trimers (top) and asymmetric unit (bottom) of poly-[Co_3(**L3.4**)$_2$(**dpe**)$_2$(H_2O)]·8H_2O·2DMF (complex **3.7**), with selected hydrogen atoms omitted for clarity*

Each cobalt(II) ion has an octahedral geometry, with a Σ parameter of 20.24° and 77.66°, for Co1 and Co2, respectively. The coordination sphere of Co1 consists entirely of carboxylate oxygen atoms, four from the α-carboxylate moieties of four ligand molecules, and two from the *N*-carboxylate moieties, none of which are chelating, leading to the relatively small Σ parameter. The bonds surrounding Co1 range from 2.043(3)

Å (Co1- O2) to 2.124(3) Å (Co1-O5). The coordination environment surrounding Co2 is also octahedral with two *trans* sites being occupied by a DMF/H_2O oxygen atom and an *N*-carboxylate oxygen atom. The remaining equatorial sites are occupied by a chelating α-carboxylate moiety, an α-carboxylate oxygen atom of another ligand molecule and a nitrogen atom of a **dpe** coligand molecule (Figure 3.17). It is the chelating carboxylate moiety that distorts the octahedral geometry surrounding Co2, leading to a much larger Σ parameter than is seen in Co1. Two adjacent bond lengths are significantly longer than the remainder, with Co2-O4 and Co2-O5 (2.148(3) and 2.144(3) Å, respectively), with the remainder of the Co-O bond lengths ranging from 2.021(3) Å (Co2-O6) to 2.097(4) Å (Co2-O8). This results in cobalt(II) carboxylate trimers of Co2-Co1-Co2 parallel to the crystallographic *a*-axis, which are capped with **dpe** molecules which connect adjacent trimers (Figure 3.17). There are also one-dimensional rectangular-shaped pore channels that extend parallel to the crystallographic *b*-axis, which are approximately 12.0 × 8.4 Å in size, and the pore volume was calculated to be 437 $Å^3$ per unit cell, which accounts for *ca.* 21.0% of the total unit cell volume (Figure 3.18). In one direction, the ligand molecules align in pairs, with face-to-face π-π interactions between the aromatic components at the α-positions of both ligands (with a C4···plane distance of 3.329(9) Å), with the carboxylate moieties of both ligand molecules coordinating to adjacent cobalt(II) ions, Co1 and Co2, at either end. The ligand *N*-functionalities extend in an almost perpendicular direction to the remainder of the ligand and act as connecting units for adjacent π-π connected ligand dimer chains.

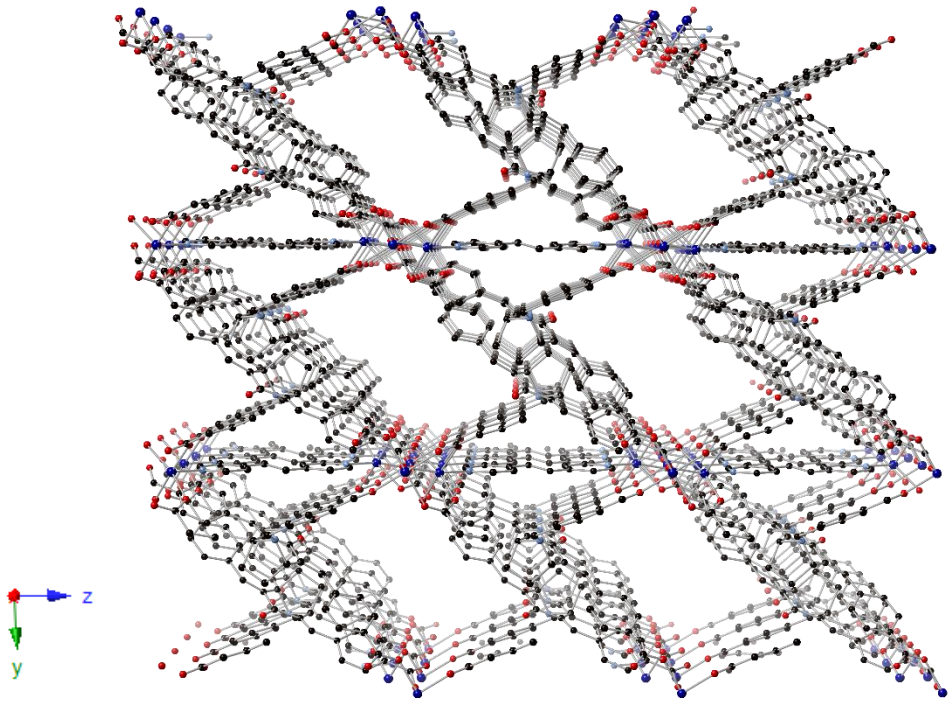

*Figure 3.18. Extended structure of poly-[Co_3(**L3.4**)$_2$(**dpe**)$_2$(H_2O)]·8H_2O·2DMF (complex **3.7**), with hydrogen atoms omitted for clarity*

Assigning the tropinone core as a three-connecting node and the cobalt(II) carboxylate trimers as eight-connecting nodes results in a **tfz-d** topology, of which there are only five examples in the ICSD. The connectivity is analogous to what is seen in α-UO_3,[23] and there are only two other reported coordination polymers with the same connectivity, both of which contain a benzene *n*-carboxylate ligand.[24,25]

The short contacts in this complex closely resemble those seen in complexes **3.1** to **3.4** (inclusive), with reciprocated C···O contacts from the tropinone oxygen atom to a tropinone CH_2 moiety of an adjacent **L3.3** tropinone core, with a C13···O3 distance of 3.506(11) Å and a C13-H···O3 angle of 149.7(5)°. The protons of the lattice water molecule are pointing into the pores, and do not appear to form any significant short contacts with the MOF framework. However, as the SQUEEZE routine was applied to crystallographic data, it is likely that these protons are forming short contacts with other lattice solvent molecules, that were too disordered to model.

The oxygen atom of the water molecule forms weak short contacts with the tropinone CH_2 moiety that is not forming short contacts with the tropinone oxygen atom, with a C14···O9 distance of 3.649(17) Å and a C14-H···O9 angle of 127.4(6)°.

3.5 Gas Adsorption

Gas sorption measurements were carried out for all three complexes that appeared porous – complexes **3.**5, **3.6** and **3.7**. Complexes **3.5** and **3.7**, however, did not display any significant gas uptake, and the PXRD analysis following evacuation (Appendix 2, Figures A2.14 and A2.15, respectively) suggested that the complexes lost their crystallinity. Therefore the remainder of the gas sorption discussion is focused exclusively on the gadolinium(III) MOF (complex **3.6**) as this was the only complex to demonstrate any notable gas uptake. Thermogravimetric analysis (TGA) was first carried out to in order to analyse both the thermal stability and potential porosity of this complex. The TGA profile (Figure 3.19) revealed that the loss of lattice DMF molecules is complete by *ca*. 135 °C, which accounts for 25.2 wt%, however soaking the material in methanol appeared to easily displace these, resulting in the removal of solvent to occur at only *ca*. 67 °C. Both the freshly synthesised and MeOH soaked materials appear to have an exceptionally high thermal stability, with no mass loss due to ligand decomposition observable below 500 °C.

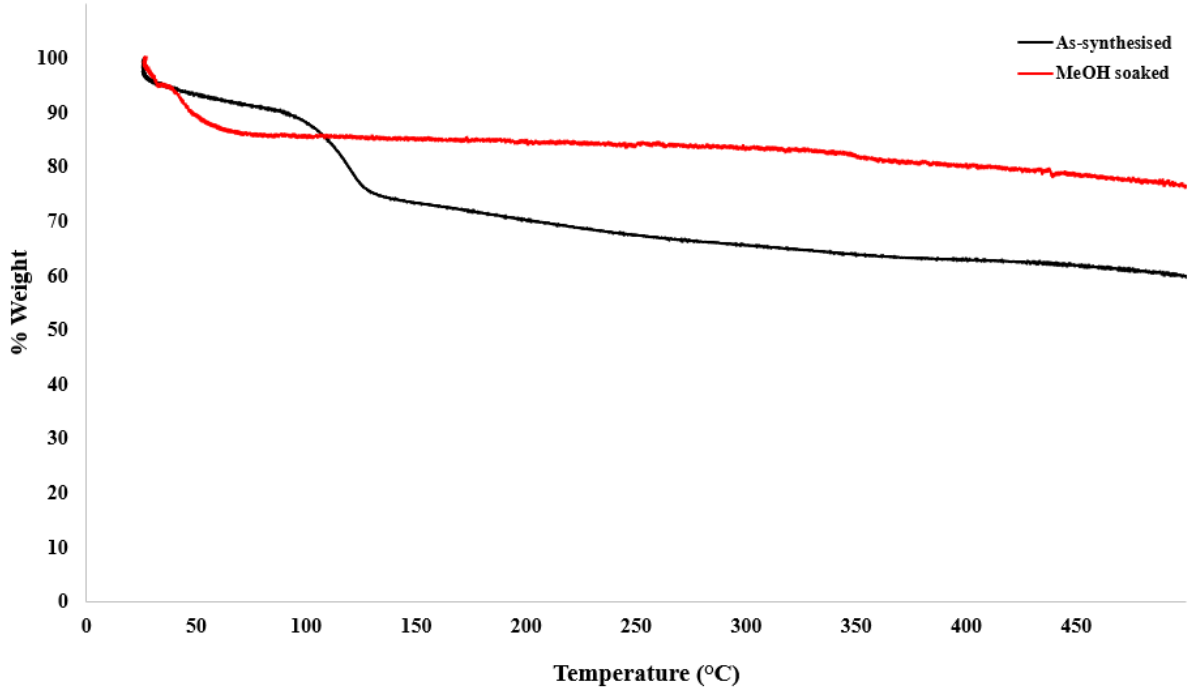

*Figure 3.19. TGA profile of as-synthesised complex **3.6** (black) and complex **3.6** post-MeOH soaking (red)*

The complex exhibits a type IV N_2 adsorption isotherm (Figure 3.20) with an abnormally wide hysteresis loop, suggesting a wide distribution of pore sizes in the material. The material adsorbs *ca*. 90 cc(STP) g^{-1} in the micropore region below $P/P_0 = 0.05$ with a small secondary adsorption step at $P/P_0 = 0.7$. The desorption branch remains near-linear in the range $0.99 > P/P_0 > 0.25$ before rejoining the adsorption branch only below $P/P_0 = 0.1$. The N_2 sorption measurements were repeated a second time, with added desorption data points in the lower pressure range, to ensure the hysteresis loop closed. Features in this region of the adsorption and desorption traces are indicative of structuring within the 50 – 100 nm diameter range, which is much larger than the typical pores in MOFs and larger than the defects that are seen in the UiO MOF series,[26] however, it is too small to be condensation between individual particles of the MOF. If this hysteresis were sharper, it may be indicative of monodisperse defects within the MOF, which is not observed in the adsorption isotherm for complex **3.6**. Desorption hysteresis continuing with wide loops well below $P/P_0 = 0.42$ may indicate some complexity in mesoporous features within the material, such as non-linear

slit pores, irregular mosaicity of the individual crystallites, or "ink-bottle" shaped mesopores. Alternatively, the hysteresis may relate to a semi-reversible structural transformation occurring along the adsorption branch which is only reversed at very low partial pressures. The BET surface area of the material was calculated to be 383 m^2 g^{-1} (Table 3.1).

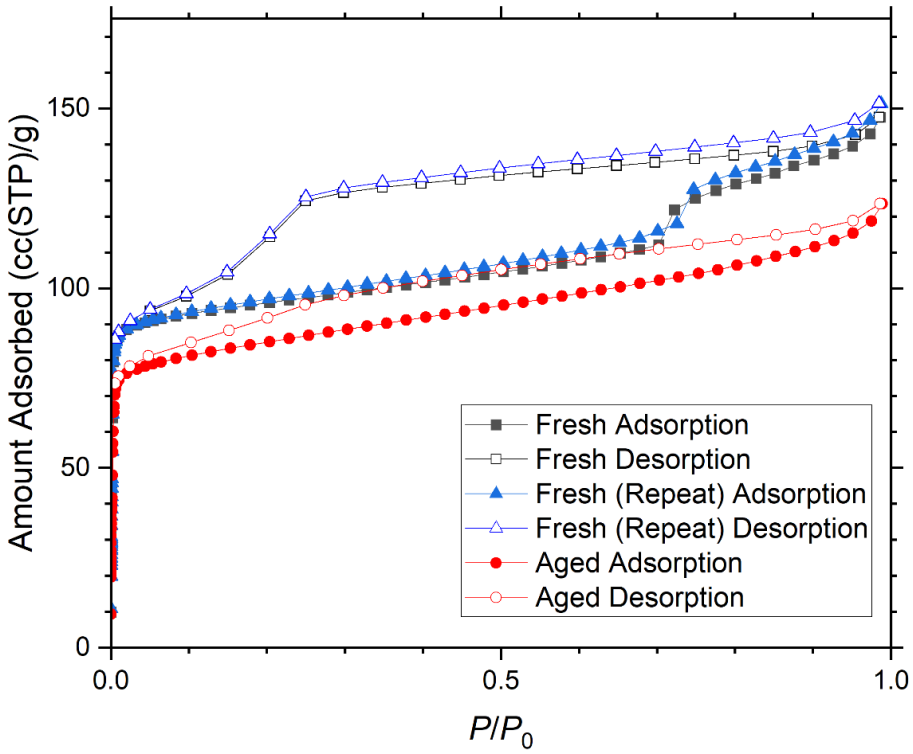

*Figure 3.20. N_2 adsorption isotherms of the fresh complex **3.6** (black filled, blue filled) and aged complex **3.6** (red filled), and desorption isotherms of the fresh complex **3.6** (black hollow, blue hollow) and aged complex **3.6** (red hollow)*

After aging for three weeks in air, the N_2 sorption measurements were repeated, and the BET surface area was calculated to be 330 m^2 g^{-1}, which amounts to a 13.8% loss in porosity. The BET summary parameters are outlined in Table 3.1.

*Table 3.1. BET summary of the fresh (left) and aged (right) complex **3.6***

	Fresh complex 3.6	**Aged complex 3.6**
Slope	9.090 g^{-1}	10.544 g^{-1}
Intercept	2.238×10^{-3} g^{-1}	4.062×10^{-3} g^{-1}
Correlation coefficient, r	0.999997	0.999964
C constant	4063.624	2596.912
BET surface area	383 m^2 g^{-1}	330 m^2 g^{-1}

In the N_2 isotherm of the aged sample, the sharp increase in the volume of gas adsorbed in the low P/P_0 values (between *ca*. 0.0 and 0.1) represents the filling of micropores, which are mostly retained after the sample was exposed to air (90 cc(STP) g^{-1} *vs.* 78 cc(STP) g^{-1} for the fresh and aged complex **3.6**, respectively). The pore size distribution (shown in Figure 3.21), was calculated from the N_2 adsorption isotherm using an NLDFT model from the adsorption branch, and shows calculated micropore widths in the range 7 – 12 Å which closely matches those observed crystallographically. In this calculation, the additional adsorption step at $P/P_0 = 0.7$ manifests as an additional series of pores of *ca*. 100 Å in diameter. It must be noted, however, that any potential structural flexibility is not accounted for in this model.

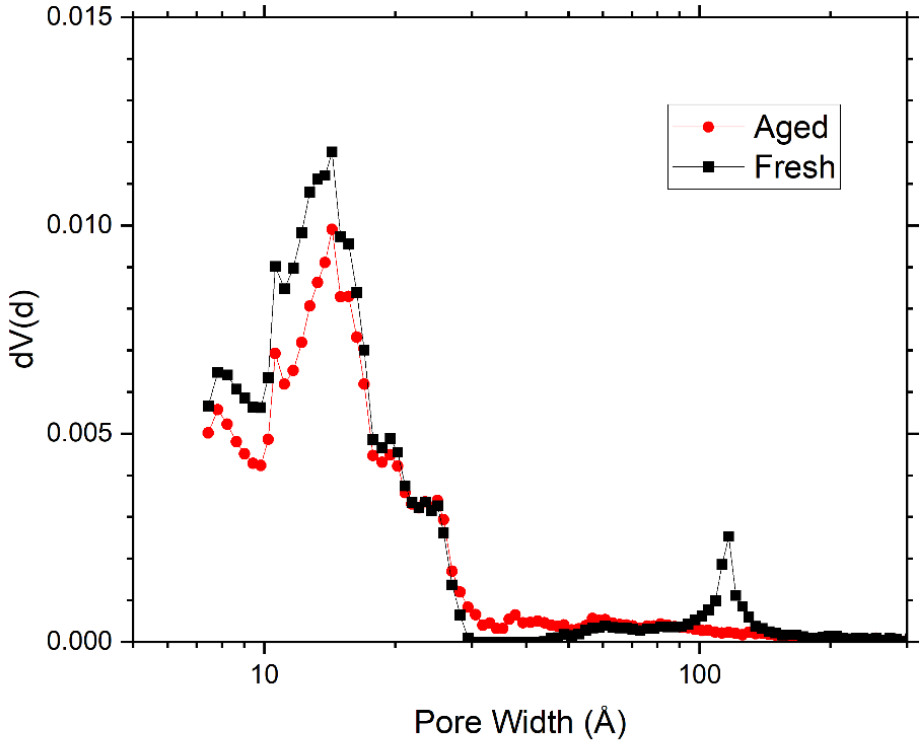

*Figure 3.21. Pore width distribution in the fresh complex **3.6** (black) and the aged complex **3.6** (red)*

After ageing, the apparent pores that are *ca*. 100 Å in diameter are lost. However, the presence of the wide hysteresis loop in the N_2 adsorption measurements of the aged samples, imply that a wide distribution of pore sizes remains. This suggests that the largest voids *i.e.* those that account for the space between individual components of a crystal remain after exposure to ambient air, however the mid-sized pores in the 100 Å range are lost. The micropores (*ca.* 10 Å in diameter) remain relatively unchanged after exposure.

During this exposure to ambient air, the sample adsorbed 4.2 mg of water, which accounted for 7.2 wt%, which is significantly less than the wt% of lattice DMF which is lost during TGA (25.2 wt%). As DMF and water have similar densities (0.944 g cm^{-3} and 0.997 g cm^{-3} for DMF and water, respectively), this implies that the water is not fully occupying the sites which were occupied by the lattice DMF molecules, prior to activation of the sample for gas sorption measurements. This, in combination with the relatively small loss

in adsorption capacity post exposure to atmospheric water vapour, suggests some resistance to degradation by atmospheric water.

At 278 K, the CO_2 adsorption isotherm shows steep uptake below 200 mmHg before tapering to a shallower gradient for the remainder of the trace reaching a maximum value of 29 cc(STP) g^{-1} (Figure 3.22). This is consistent with monolayer adsorption at low partial pressures and incomplete micropore filling in this pressure range, giving similar loading values to other medium-pore MOFs such as MOF-5,[27,28] and UiO-66,[29,30] in contrast to narrower-pore MOFs which tend to completely fill at these pressures. The maximum value of 29 cc(STP) g^{-1} corresponds to *ca*. 5.32 wt% and the enthalpy of adsorption at zero loading (Appendix 4, Figure A4.2) was calculated to be −33 kJ mol^{-1}.

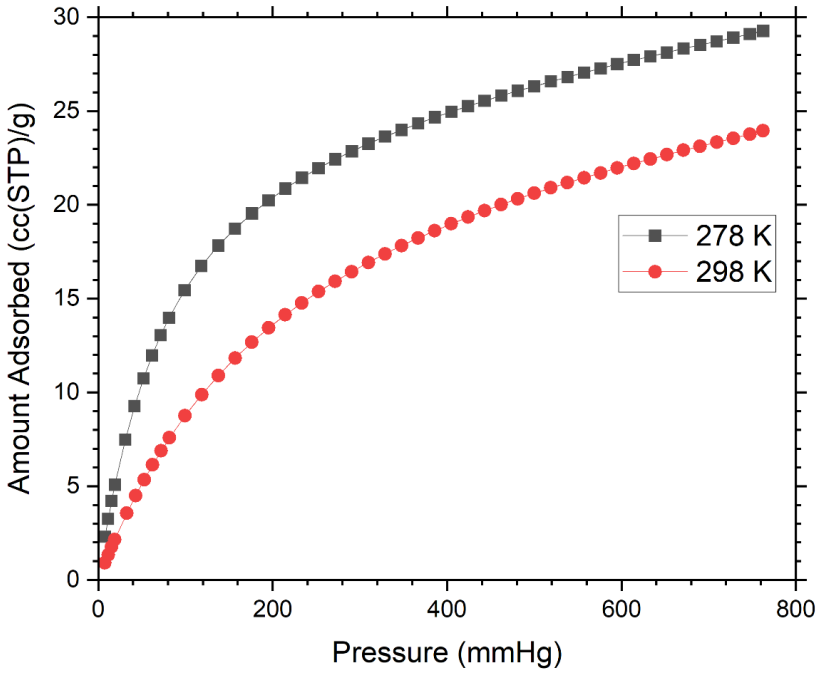

*Figure 3.22. CO_2 adsorption isotherms of complex **3.6** at 278 K (black) and 298 K (red)*

The PXRD pattern of the material after the gas sorption measurements showed that there was a change to the material, however, the peaks were still relatively sharp and well-resolved and most reflections retain their original positions, indicating a retention of crystallinity (Figure 3.23), and this pattern remained unchanged after aging for three weeks.

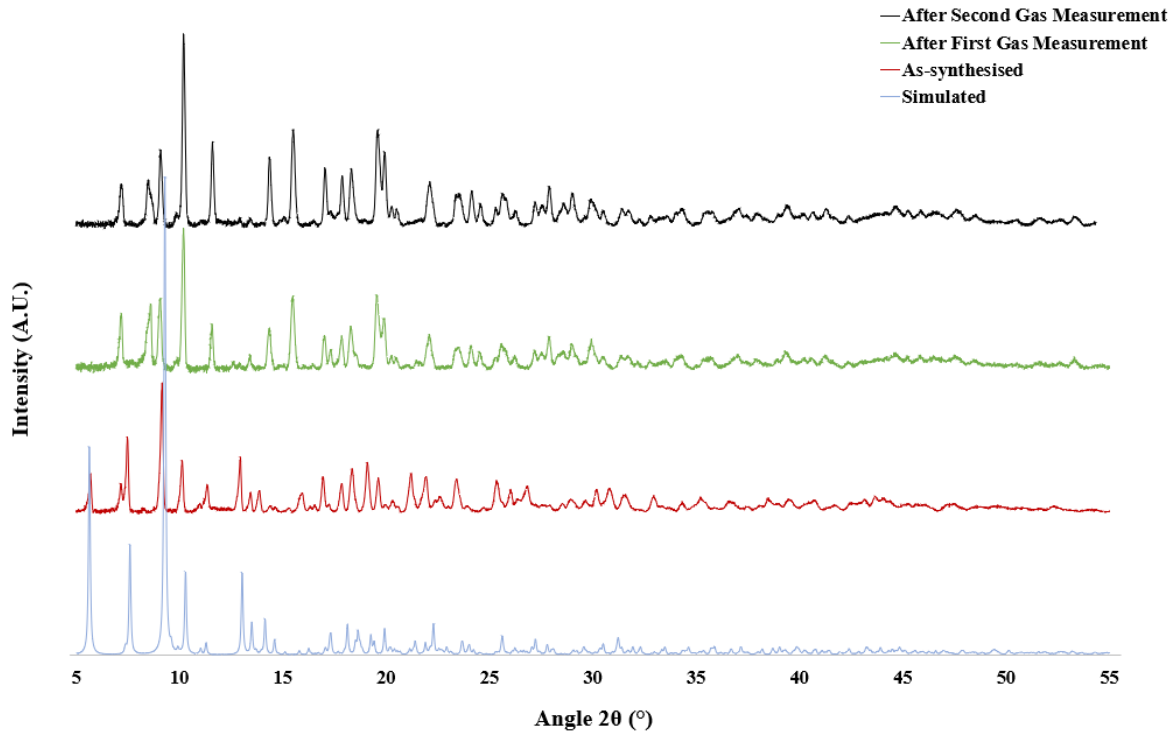

*Figure 3.23. X-ray powder diffraction data for complex **3.6** showing pattern simulated from single crystal data at 150K (blue), measured as synthesised (red, room temperature), measured after first gas adsorption measurement (green, room temperature/capillary) and measured after aging and a second gas adsorption measurements (black, room temperature)*

3.6 Discussion

Following the predictions made from the analysis of the ligands discussed in Chapter 2, it was concluded that the most likely aliphatic protons to form short contacts would be those adjacent to heteroatoms in the aliphatic core, as these would be the most polarised aliphatic protons in the core, provided they were sterically accessible. The most polarised protons in the tropinone core would be those adjacent to either the carbonyl carbon atom or those adjacent to the apical amine, and the functionalisation of the tropinone core resulted in no protons α- to the carbonyl, leaving the tertiary tropinone CH and the CH_2 or CH_3 in **L3.2**. No short contacts were observed to originate at the tertiary CH moiety, which is reasonable considering the relatively sterically hindered surrounding environment. The same can be said for the bridging CH_2 moiety in *N*-functionalised ligands **L3.1**, **L3.3** and **L3.4**, in which the large aromatic moiety hinders the formation

of any significant short contacts in the resulting complexes. The only complex in which a polarised aliphatic proton forms any notable close contacts is in complex **3.5**, in which the apical *N*-CH_3 moiety is relatively unhindered *and* polarised, resulting in close contacts to the tropinone oxygen atom. It is important to note that an accurate representation of all the short contacts could not be identified given either poor diffraction data or the implementation of the SQUEEZE routine in the data refinement process, however, those that could be identified were compared and tentative conclusions were drawn from the available data.

*Table 3.2. Representative **L3.X** short contact D···A distances and D-H···A angles in relevant complexes (complex **3.4** is not included due to the low quality of crystallographic data obtained)*

Complex	***Empirical formula***	***D···A distance***	***D-H···A angle***	***Type of donor***
3.1	*poly*-[Zn(**L3.1**)$_2$(**BDC**)$_2$]·2H_2O	3.21(3) & 3.36(2) Å	n/a	Tropinone CH_2
3.2	*poly*-[Zn(**L3.1**)(**HBTC**)]·2H_2O·DMF	3.34(2) Å	160.3(10)°	Tropinone CH_2
3.3	*poly*-[Co(**L3.1**)(**HBTC**)]·2.5H_2O	3.440(4) Å	153.73(17)°	Tropinone CH_2
3.5	*poly*-[Yb_3(**L3.2**)$_4$(**HL3.2**)]·4H_2O·6DMF	3.55(4) Å	148.0(10)°	Tropinone *N*-CH_3
3.6	*poly*-[Gd(**L3.3**)(DMF)$_2$]·2DMF·H_2O	3.428(9) Å	130.7(4)°	α-Tropinone 3-Ar-CH
3.7	*poly*-[Co_3(**L3.4**)$_2$(**dpe**)$_2$(H_2O)]·8H_2O·2DMF	3.506(11) Å	149.7(5)°	Tropinone CH_2

In complexes of **L3.1** and complex **3.7**, these contacts to the tropinone oxygen atom all originate at the tropinone CH_2 moieties, which are less polarised than those adjacent to the apical amine, however, they are much less sterically hindered (with the D···A distances and D-H···A angles summarised in Table 3.2). These interactions appear to be strongest in complexes of **L3.1** and **BTC** (**3.2** and **3.3**), which is likely due the higher quantity of hydrogen bonding acceptors in these complexes relative to complex **3.1** (with a **BDC** coligand) leading to a slightly more versatile hydrogen bonding network allowing for the crystal packing to optimise both types of short contacts in the complex. In complex **3.1**, however, the crystal packing evidently favours the much stronger hydrogen bonding network with the lattice water molecule, than the contacts originating at the tropinone oxygen atoms, resulting in one of these contacts originating at the tropinone core being slightly weaker. Complexes **3.5**, **3.6** and **3.7** are all porous, resulting in an overall larger

separation between adjacent ligand/coligand molecules, and this is reflected in the interactions originating at the tropinone oxygen atom. In complexes **3.5** and **3.7**, the D···A distances tend to be larger than in complexes **3.2** and **3.3**, and the D-H···A angles stay further from 180°. In complex **3.6**, this logic stands, in which the distance between the tropinone oxygen atom to the closest tropinone CH_2 is too far, thus resulting in the most significant short contact from the tropinone oxygen atom, originating at an aromatic CH moiety, with a significant deviation from 180°.

Interestingly, a similar trend is observed in the π-π interactions present (if any) in the reported complexes, which are summarised in Table 3.3.

*Table 3.3. Shortest C···π distances of π-π interactions in relevant complexes (complex **3.4** is not included due to the low quality of crystallographic data obtained)*

Complex	***C···plane distance***
3.1	3.44(3) Å
3.2	3.656(5) Å
3.3	3.658(6) Å
3.5	3.534(15) Å
3.6	-
3.7	3.329(9) Å

In complexes of **L3.1**, the lattice water molecule(s) play a significant role in the network of hydrogen bonding in the association of their respective adjacent networks, therefore it is reasonable to assume that the crystal packing would favour the formation of this integral interaction. However, the high quantity of oxygen atoms (*i.e.* hydrogen bond acceptors/donors if protonated) allows for both the hydrogen bonding and π-π interactions to be favoured by the crystal packing. As the coligands are relatively small, it is more straightforward to reorient them to allow for π-π interactions, relative to the larger **L3.1** ligand molecules. Complex **3.5** is the only homoleptic complex that forms π-π interactions because of the relative orientation of ligand molecules. There are no significant π-π interactions in complex **3.6**, in which the similar preference of the metal ion for higher coordination numbers cannot accommodate for an equivalent relative ligand orientation, due to the *N*-substituent of ligand **L3.3**, which is much larger than the *N*-methyl group of **L3.2**. This is similar to what is observed in the short contacts originating at the tropinone oxygen atom, in which

the high coordination number preference of gadolinium(III) dominates over the network of short contacts in the crystal packing, leading to a relative orientation of the ligand molecules that does not lead to short contacts originating at the least sterically hindered aliphatic proton. Similar face-to-face π-π interactions of the tropinone α-substituents is present in complex **3.7** as it is in complex **3.5**. The lower coordination number preference of cobalt(II), relative to ytterbium(III) and gadolinium(III) allows for the closer association of adjacent tropinone-containing ligand molecules, leading to notable face-to-face π-π interactions. In complexes of **L3.1** (which contains the same number of aromatic systems to **L3.4**), the small aromatic coligands are always involved in the π-π interactions in the system, however, this does not occur in complex **3.7** with the **dpe** ligand. The π-π interactions occur only between **L3.4** ligand molecules, despite the ease with which it would be to orient the **dpe** molecule to partake in these interactions, as this would not disturb any network of short contacts.

The porous coordination polymers only formed when the tropinone-containing ligand was the *O*-donor in the complexes, *i.e.* there was no porosity observed in complexes of **L3.1**, only **L3.2**, **L3.3** and **L3.4**. Complex **3.6** was the only complex to demonstrate any significant gas uptake, and retained porosity after exposure to ambient air for over three weeks (with only a 13.8% reduction in BET surface area, following the adsorption of 7.2 wt% of water) and some retention of crystallinity after ageing, suggesting some resistance to degradation by atmospheric water, which could be imposed by the bulky aliphatic core of the **L3.3** ligand molecule. While complexes **3.5** and **3.7** likely collapsed upon activation for sorption measurements (Appendix 2, Figures A2.14 and A2.15, respectively), these complexes demonstrate that the predictions made from the complexes of **L2.1** and **L2.2** are true for more complex systems. The complexes also highlight the feasibility of incorporating ligands of this nature into porous coordination polymers, and that this porosity is permanent and possibly less sensitive to water degradation, as demonstrated by complex **3.6**, which shows that these aliphatic cores do indeed provide rigidity comparable to aromatic molecules, and importantly are capable of maintaining that porosity after solvent removal.

The observations of the short contacts originating from the aliphatic components of the representative ligands **L2.1** and **L2.2** in complexes discussed in Chapter 2, provided a strong basis for predictions to be made about the close contacts that were observed in the more complex ligands discussed in this chapter. Where sterically accessible, the short contacts arising from the aliphatic components of the ligands originated at the most *polarised* aliphatic protons and the remainder originated at the most *accessible* protons, which were most often the tropinone CH_2 moieties.

3.7 References

1. B. Yadav, S. Taurin, R. J. Rosengren, M. Schumacher, M. Diederich, T. J. Somers-Edgar and L. Larsen, *Bioorg. Med. Chem.*, 2010, **18**, 6701 – 6707.

2. N. Samir, R. F. George, E. Z. Elrazaz, I. M. Ayoub, E. M. Shalaby, J. R. Plaisier, N. Demitri and M. Wink, *Future Med. Chem.*, 2020, **12**, 2123 – 2140.

3. X. Yin, C. Geng, X. Chen, C. Sun, T. Yang, T. Li, J. Zhou, X. Zhang and J. Chen, *Nat. Prod. Bioprospect.*, 2017, **7**, 215 – 223.

4. K. Piechowska, M. Mizerska-Kowalska, B. Zdzisińska, J. Cytarska, A. Baranowska-Łączkowska, K. Jaroch, K. Łuczykowski, W. Płaziński, B. Bojko, S. Kruszewski, K. Misiura and K. Z. Łączkowski, *Int. J. Mol. Sci.*, 2020, **21**, 9050.

5. T. Xue, H. Yuan, J. Sun, G. Lu, Z. Si, B. Huang, R. Tang, J. Nie and X. Zhu, *Dyes and Pigments*, 2022, **201**, 110241.

6. A. Armstrong, G. Ahmed, B. Dominguez-Fernandez, B. R. Hayter and J. S. Wailes, *j. Org. Chem.*, 2002, **67**, 8610 – 8617.

7. A. F. Mabied, A. S. Girgis, E. M. Shalaby, R. F. George, B. E. M. El-Gendy and F. N. Baselious, *J. Heterocycl. Chem.*, 2015, **53**, 1074 – 1080.

8. D. Pawelski, A. Walewska, S. Ksiezak, D. Sredzinski, P. Radziwon, M. Moniuszko, R. Gandusekar, A. Eljaszewicz, R. Lazny, K. Brzezinski and M. E. Plonska-Brzezinska, *Int. J. Mol. Sci.*, 2021, **22**, 11384.

9. R. F. George, N. Samir, I. M. Ayoub, E. M. Shalaby, N. Demitri and M. Wink, *Future Med. Chem.*, 2018, **10**, 2815 – 2833.

10. W. M. Bloch, A. Burgun, C. J. Coghlan, R. Lee, M. L. Coote, C. J. Doonan and C. J. Sumby, *Nat. Chem.*, 2014, **6**, 906 – 912.

11. L. Yang, D. R. Powell and R. P. Houser, *Dalton trans.*, 2007, 955 – 964.

12. M. G. B. Drew, C. J. Harding, V. McKee, G. G. Morgan and J. Nelson, *J. Chem. Soc., Chem. Commun.*, 1995, 1035 – 1038.

13. S. Chetry, P. Sharma, A. Frontera, U. Saha, A. K. Verma, B. Sarma, P. J. Kalita and M. K. Bhattacharyya, *New J. Chem.*, 2021, **45**, 3699 – 3715.

14. R. Murugavel, M. Sathiyendiran and M. G. Walawalkar, *Inorg. Chem.*, 2001, **40**, 427 – 434.

15. H. Arora, S. K. Barman, F. Lloret and R. Mukherjee, *Inorg. Chem.*, 2012, **51**, 5539 – 5553.

16. P. Goszczycki, K. M. Stadnicka, B. Musielak and K. Ostrowska, *Polyhedron*, 2019, **159**, 400 – 407.

17. A. L. Spek, *Acta Crystallogr. C*, 2015, **71**, 9 – 18.

18. N. L. Rosi, J. Kim, M. Eddaoudi, B. Chen, M. O'Keeffe and O. M. Yaghi, *J. Am. Chem. Soc.*, 2005, **127**, 1504 – 1518.

19. Inorganic Crystal Structure Database (ICSD) | Physical Sciences Data Science Service, https://www.psds.ac.uk/icsd, (accessed 10 August 2022).

20. L. Vegard, *The London, Edinburgh and Dublin Philosophical Journal of Science*, 1916, **32**, 505 – 518.

21. A. Vallat, R. Meunier-Prest and E. Laviron, *J. Electroanal. Chem.*, 1997, **428**, 11 – 17.

22. S. Calmels, H. Ohshima, P. Vincent. A. Gounot and H. Bartsch, *Carcinogenesis*, 1985, **6**, 911 – 915.

23. B. O. Loopstra and E. H. P. Cordfunke, *Recueil des Travaux Chimiques des Pays-Bas*, 1966, **85**, 135 – 142.

24. C. Falaise, J. Delille, C. Volkringer, H. Vezin, P. Rabu and T. Loiseau, *Inorg Chem*, 2016, **55**, 10453 – 10466.

25. S. Chen, E. Yang and J. Zhang, *Chin. J. Struct. Chem.*, 2019, **32**, 149.

26. X. Feng, H. S. Jena, C. Krishnaraj, K. Leus, G. Wang, H. Chen, C. Jia and P. van der Voort, *ACS Appl Mater Interfaces*, 2021, **13**, 60715 – 60735.

27. H. Li, M. Eddaoudi, M. O'Keeffe and O. M. Yaghi, *Nature*, 1999, **402**, 276 – 279.

28. J. A. Botas, G. Calleja, M. Sánchez-Sánchez and M. G. Orcajo, *Langmuir*, 2010, **26**, 5300 – 5303.

29. J. H. Cavka, S. Jakobsen, U. Olsbye, N. Guillou, C. Lamberti, S. Bordiga and K. P. Lillerud, *J. Am. Chem. Soc.*, 2008, **130**, 13850 – 13851.

30. A. D. Wiersum, E. Soubeyrand-Lenoir, Q. Yang, B. Moulin, V. Guillerm, M. B. Yahia, S. Bourrelly, A. Vimont, S. Miller, C. Vagner, M. Daturi, G. Clet, C. Serre, G. Maurin and P. L. Llewellyn, *Chem. Asian J.*, 2011, **6**, 3270 – 3280.

Chapter 4

· Silver(I) Coordination Cages ·

4.1 Introduction

4.1.1 Metal-Organic Cages (MOCs)

Metal-organic cages (MOCs), also known as metal-organic polyhedra (MOPs), are discrete coordination materials that offer the benefits of tuneability akin to that of metal-organic frameworks, while providing improved solubility, widening the scope of their applications to the solution phase. As with MOFs, a large part of tuning the properties of MOCs lies in ligand design. As discussed in more detail in Section 1.5, the size and shape of the ligands can determine the size and shape of the resultant MOC, and the design of heteroleptic cages has become of particular interest, to improve their selectivity towards guest encapsulation or adsorption.[1] Largely aliphatic coordination cages are still a relatively unexplored area within the field, and if the trend that is observed in some recently published aliphatic MOFs[2,3] is also true for MOCs, the introduction of aliphatic character to MOCs could significantly alter their adsorption selectivity towards guests. The added aliphatic character will also likely affect the solubility of the resultant MOCs, which in turn will have an effect on its potential applications.

The goal of the design of the coordinating ligands discussed in this chapter, and throughout this thesis, was to create largely aliphatic, rigid molecules, whereas traditionally, as discussed in Section 1.5, the ligands employed in coordination materials, and therefore coordination cages are largely aromatic in nature. For most aromatic ligands, the self-assembly processes of their coordination materials is much more straightforward to observe using not only NMR spectroscopy, but also UV-Vis and fluorescence spectroscopy. Aliphatic (or largely aliphatic) ligands have little to no chromophores or contain functional groups whose absorbance is outside the solvent window, meaning UV-Vis and fluorescence techniques are of little use in the study of their coordination materials, and therefore NMR was the chosen method for their analysis.

4.2 Characterisation Techniques

NMR can also provide more specific information about the system, where peaks responsible for particular protons (or other nuclei) in the ligand (or anion) structure can be monitored throughout the self-assembly process. There are several key features in the NMR spectra of metal-organic cages that provide valuable information about the assembly and behaviour of the species in solution, particularly through the use of a titration experiment. Firstly, the nuclei experience different chemical shifts dependent on the local environment in the complex, which is different to that of the free ligand, and this will change as more of a metal ion is added to the ligand, and the way in which the NMR spectra evolve can provide a lot of information about the species in solution. Secondly, information about the symmetry of the material in solution can also be gained using NMR spectroscopy, by observing the number of peaks in the spectra. Finally, the width of the peaks in the spectra provide information about the number of species in solution and their relationship to one another. If there are multiple species present in solution and the ^{1}H NMR peaks are broad, this can mean that, relative to the NMR timescale (which is within the order of 0.1 – 10 seconds) the species are in fast exchange, resulting in an average signal between the signals of the individual species. On the other hand, narrow and well-resolved peaks in the ^{1}H NMR spectrum could be indicative of either multiple species in slow exchange with each other (relative to the NMR timescale), or multiple species

which co-exist in solution, which would be determined using diffusion ordered spectroscopy, (DOSY) NMR. This technique can also provide an indication of the size of the species in solution, by using the diffusion coefficient (D) to calculate the hydrodynamic radius (r_s), using the Stokes-Einstein equation (Equation 4.1),[4]

Equation 4.1

$$r_S = \frac{k_B T}{6\pi\eta D}$$

in which, k_B represents the Boltzmann constant (J K^{-1}) , T is temperature (K) and η is the viscosity of the solvent (Pa s), resulting in the hydrodynamic radius in metres. This value is not definitive, however, as the Stokes-Einstein equation assumes the material is perfectly spherical, which is rarely the case. For non-spherical entities, there is a modified Stokes-Einstein equation which takes the shape and size factors into consideration (Equation 4.2).[5]

Equation 4.2

$$r_h = \frac{k_B T}{c\pi\eta D f_h}$$

In this modified equation, *c* is the size factor and relates the ratio of the size of the diffusing species to the solvent in which it is diffusing. The value f_h is the shape factor, which is always greater than one. Neither of these equations, however, provide any information regarding the charge of the species. Mass spectrometry provides more definitive information for the determination of the size and charge of the species present in solution, and for highly charged species containing silver(I) for example, the pattern in the mass spectra would be very distinctive. There are several difficulties associated with mass spectrometric analysis of coordination cages, and in particular, silver(I) coordination cages. Firstly, a cage containing multiple metal ions could lead to a dense mass spectrum which is challenging to interpret, leading to multiple

possibilities for fragmentation given the high quantity of labile coordination bonds, in particular the silver(I)-nitrogen bonds present in the cages discussed in this chapter. Secondly, if the ligand molecules within the cage are prone to hydrolysis, this increases the number of possible fragmentation patterns, further complicating the mass spectra. The ligands discussed in this chapter, for example, contain a sensitive imine bond which make them highly prone to hydrolysis. The concentrations of complexes in solution for mass spectrometric analysis are also much lower than the solutions used for NMR analysis, and therefore, it is possible that the same complexes will not form at the lower concentrations,[6,7] and a simple proof of this is provided in Appendix 4, Proof A4.1.

4.3 Ligand Design

The ligands typically encountered in polymeric coordination materials tend to be divergent *i.e.* functionalised in a way to ensure that the donors are pointing *outward* (such as the α-functionalised ligands described in Chapter 3) to encourage the formation of a polymeric species. The ligands designed for MOPs on the other hand, tend to be convergent, *i.e.* functionalised in a way to ensure the donors are pointing *inward*, to discourage the formation of a polymeric species. Further to the ligands discussed in Chapter 3, that contain the fused-ring bicyclic 8-azabicyclo[3.2.1]octane core, varying the chemical modifications carried out on this core results in a different library of coordinating ligands. Functionalising the tropinone-derived core at the apical amine, and the carbonyl oxygen atom (instead of the α-positions, as in Chapter 3), results in a family of convergent ligands in which all of the *N*-donors are pointing inward, which are outlined in Figure 4.1, whose coordination chemistry is described in this chapter.

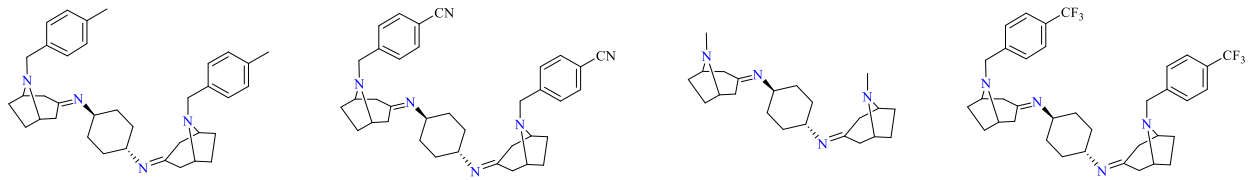

L4.1 **L4.2** **L4.3** **L4.4**

Figure 4.1. Tropinone-derived ligands (left to right) ***L4.1****,* ***L4.2****,* ***L4.3*** *and* ***L4.4****, described in this chapter*

L4.1, **L4.2** and **L4.3** were designed as largely aliphatic, nitrogen-rich coordinating ligands, which when combined with silver(I) salts, yielded the first coordination cages to incorporate the 8-azabicyclo[3.2.1]octane core. In order to better understand the properties of the coordination cages which incorporate these ligands in multiple media, their structures in the solid state were first determined crystallographically. Following this, the solubility of the discrete cages was exploited in order to analyse their complex self-assembly process, using a combination of one- and two-dimensional NMR techniques. This was firstly used to determine if the structures observed in the solid state persisted in solution, and secondly if there were species that exist in solution *besides* what is observed crystallographically. **L4.4** was designed as a representative ligand for structurally similar ligands **L4.1** and **L4.2**, in order to monitor the process both *via* ^{1}H NMR and ^{19}F NMR. Following this, provided the cages persist in solution, it was of interest to determine if what persists in solution is the thermodynamically stable product or if it is a kinetically trapped species. Lastly, the behaviour of these cages in solution was investigated, with respect to various anions – for example, if the cages preferentially bind certain anions or if the presence of an anion in the solution results in the templating or transformation to a different cage.

4.4 Ligand Synthesis

Trans-1,4-diaminocyclohexane was chosen as the bridging component of two tropinone moieties, due to the presence of a relatively structurally simple cyclic aliphatic unit, which, due to its cyclic nature, would act as an added rigid component in the ligand structures. Much like the ligands discussed in Chapter 3, the first step of the synthesis of ligands **L4.1**, **L4.2**, and **L4.4** was the functionalisation of the secondary amine of the nortropinone starting material. This, again, proceeds *via* an S_N2 *N*-alkylation reaction, which proceeds *via* an intermediate from a Finkelstein reaction, which in each case resulted in a high-yielding reaction requiring no purification, resulting in intermediates **L4.1a**, **L3.2a**, and **L4.4a**. Following this, the intermediates, or tropinone (**L4.3a**) in the case of **L4.3**, underwent an imine condensation reaction with *trans*-1,4-diaminocyclohexane to give ligands **L4.1**, **L4.2**, **L4.3** and **L4.4**. The synthetic scheme is outlined in Scheme 4.1.

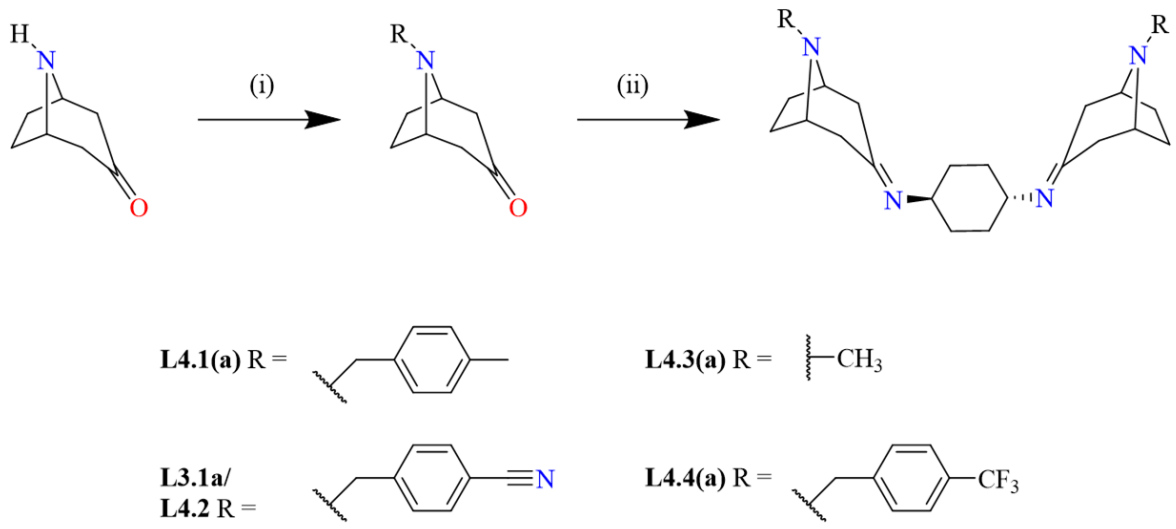

*Scheme 4.1. Synthetic scheme for the preparation of ligands **L4.1** to **L4.4**, (i) R-Br, K_2CO_3, KI, MeCN, (ii) trans-1,4-diaminocyclohexane, p-TsOH, toluene*

The condensation of the tropinone precursor with *trans*-1,4-diaminocyclohexane was first carried out by heating the two precursors to reflux in EtOH, however, the majority of the product, as determined by ^{1}H NMR was the asymmetric condensation product, *i.e.* with only one amine of the *trans*-1,4-diaminocyclohexane forming an imine, and the desired condensation product was only present in small quantities which were difficult to isolate. Instead, the condensation reactions with *trans*-1,4-diaminocyclohexane (catalysed by *p*-TsOH), were then carried out under harsher conditions using a Dean-Stark apparatus,[8] to ensure that the reaction was driven towards the product by removing water from the reaction vessel. The crude ^{1}H NMR spectra of the products again contained the asymmetric condensation products, however, under these conditions there was a much larger quantity of the desired product, which in each case was isolated by trituration with MeCN, causing the pure desired product to precipitate as a white solid. Acetone was the chosen solvent for the subsequent complex crystallisations, as it is a weakly coordinating polar aprotic solvent, which will not compete with the ligand functionalities for coordination to silver(I).

As outlined in the coordination compounds discussed earlier in Chapter 2, silver(I) is a soft acid metal ion with a much more flexible coordination geometry, relative to copper(II), cobalt(II) and zinc(II). This is due to the d^{10} electronic configuration of silver(I), resulting in an absence of ligand field stabilisation energy (LFSE). This absence means that silver(I) has no firm geometric preference, likely making it more sensitive to the geometric preferences of the ligand, in particular for similar ligands with minor changes to the backbones, such as those discussed in this chapter.

4.5 Crystallographic Data

4.5.1 Cage C4.1

Combination of **L4.1** with AgOTf in acetone afforded the discrete and highly symmetric $M_{12}L_6$ cage, **C4.1**. The crystallographic data were solved and refined in the cubic space group *I*23. The asymmetric unit, shown in Figure 4.2, consists of one half of an **L4.1** ligand molecule, coordinating to a silver(I) ion, and one whole triflate anion, as well as one-third of a second triflate anion, which lies on a threefold rotation axis. The silver(I) ion is modelled with an occupancy of one, while the full triflate anion is modelled with an occupancy of two-thirds.

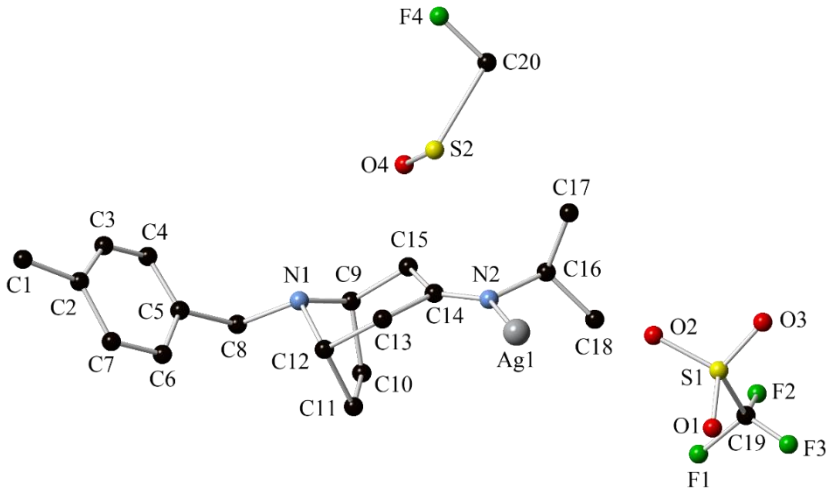

*Figure 4.2. Asymmetric unit of [Ag_{12}(**L4.1**)$_6$$(OTf)_{12}$] (cage **C4.1**) (hydrogen atoms omitted for clarity)*

Each ligand imine and amine nitrogen atom is coordinating to a silver(I) ion, which has a near-linear geometry, with an N1-Ag1-N2 angle of 162.7(5)° (Figure 4.3). The resultant discrete $M_{12}L_6$ cage that forms takes the form of a truncated tetrahedron, when assigning the silver(I) ions as the vertices of the cage. This is outlined in a wireframe representation of the cage showing the silver(I) ions as the shape vertices in Figure 4.3, The distance between each Ag_3 centroid is approximately 10.8 Å, which corresponds to an internal cage volume of 148 $Å^3$. The arrangement of individual ligand molecules within the cage is visualised in Figure 4.4.

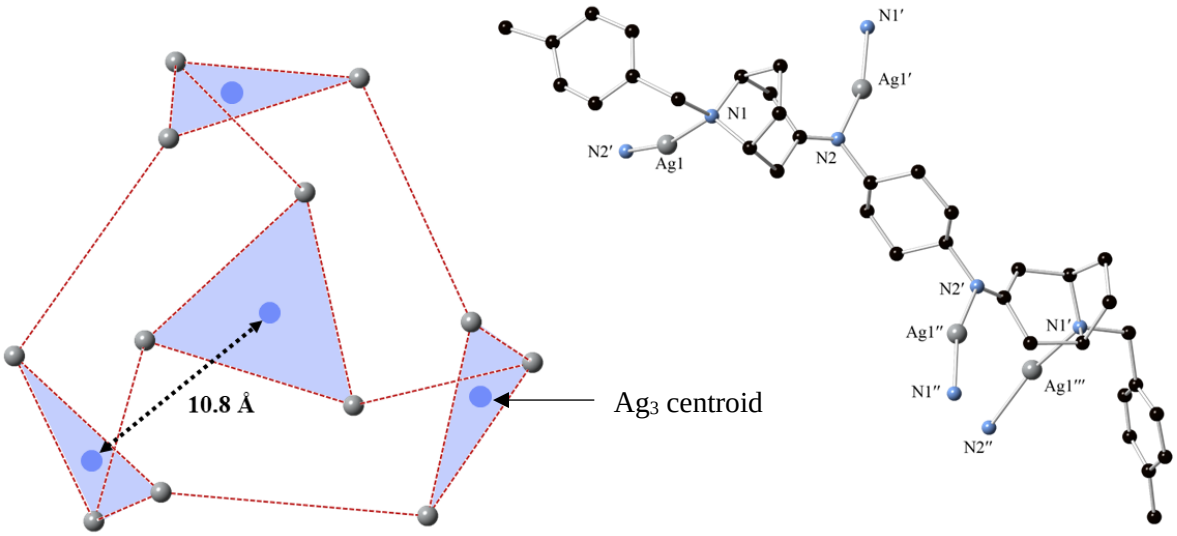

*Figure 4.3. Wireframe representation of [Ag_{12}(**L4.1**)$_6$(OTf)$_{12}$] (cage **C4.1**) (truncated tetrahedron), highlighting a Ag_3 centroid (purple) and the distance between the centroids (left), **L4.1** coordination mode (right) (hydrogen atoms and anions were omitted for clarity)*

There are four triflate anions encapsulated within each cage, with the oxygen atoms of the anions pointing at a silver(I) ion each (visible in the wireframe depiction of cage **C4.1** in Figure 4.4), with an Ag1···O4 distance of 2.98(3) Å.

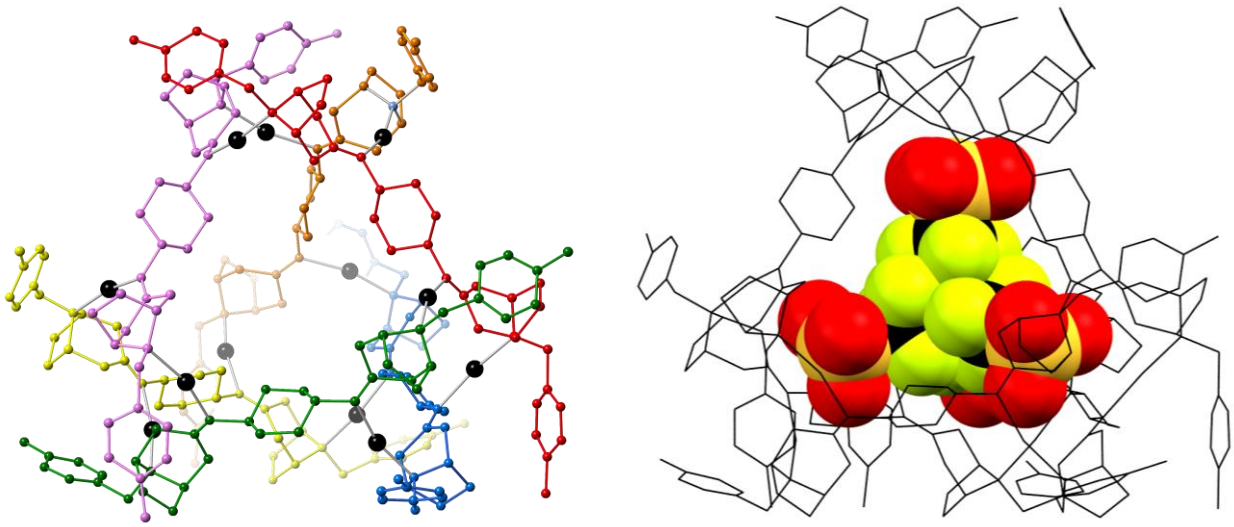

*Figure 4.4. [Ag_{12}(**L4.1**)$_6$$(OTf)_{12}$] (cage **C4.1**) highlighting individual **L4.1** ligand molecules in different colours and silver(I) ions in black (right), wireframe representation of cage **C4.1**, showing encapsulated triflate anions (hydrogen atoms and some anions were omitted for clarity)*

As well as Ag···O contacts originating at the encapsulated anions, there are also short C-H···O contacts, with a C15···O4 distance of 3.19(3) Å, and a C15-H···O4 angle of 124.0(12)°) and C-H···F contacts (with a C17···F4 distance of 3.28(5) Å and a C17-H···F4 angle of 146.7(17)°), both originating at cyclohexyl -CH_2 moieties. This is due to these protons being the most sterically accessible aliphatic protons which point into the cage, as the most polarised protons (the CH_2 moieties α-to the imine in the tropinone core, or the CH moieties adjacent to the cyclohexyl nitrogen atom) are both sterically encumbered by the surrounding non-planar aliphatic bulk, which is similar to the trends observed in the tropinone-derived ligands, discussed in Chapter 3. The -CF_3 moieties of the encapsulated triflate anions point towards the -CF_3 moieties of the remaining three triflate anions within the cage, with F···F distances of 2.49(11) and 2.44(8) Å, which is significantly shorter than the sum of their van der Waals radii (1.33 Å each, *i.e.* a sum of 2.66 Å)[9] indicating that they are quite tightly bound. Intermolecular F···F distances that are this short are a rare phenomenon, with a slightly longer distance of 2.563 Å reported between fluorine atoms of adjacent triflate anions in a linear ruthenium(II) [3]catenane by Singh *et. al.*[10]

Adjacent cages associate with one another, as expected, *via* anion interactions. The triflate anion that is not encapsulated, associates with the cage *via* C-H···O contacts originating at a cyclohexyl -CH_2 moiety (with a C18···O2 distance of 3.56(3) Å and a C18-H···O2 angle of 149.3(11)°) and at tropinone -CH_2 moieties (with a C11···O1 distance of 3.71(3) Å and a C11-H···O1 angle of 161.5(18)°, and a C15···O3 distance of 3.59(4) Å and a C15-H···O3 angle of 149.3(11)°). Due to the large pore openings, it was difficult to calculate the pore volume within each cage (using Olex2) separately from the remainder of the pore volume of the complex, as the pore openings in the cage are an integral part of the overall pore network. Instead, the distance between the Ag_3 centroids of the truncated tetrahedron (10.8 Å) was used as an indicative measurement of the cage size, of which there are two in the unit cell. If the internal volume of the cage is considered to have a tetrahedral shape, the volume can be calculated using the edge length, 10.8 Å, giving an approximate volume of 148 $Å^3$ (visualised in Figure 4.5). The overall pore volume was calculated to be 4451 $Å^3$ per unit cell (with individual pore components of 2571 and 1880 $Å^3$ per unit cell, accounting for 15.8% and 11.6% of the unit cell volume, respectively).

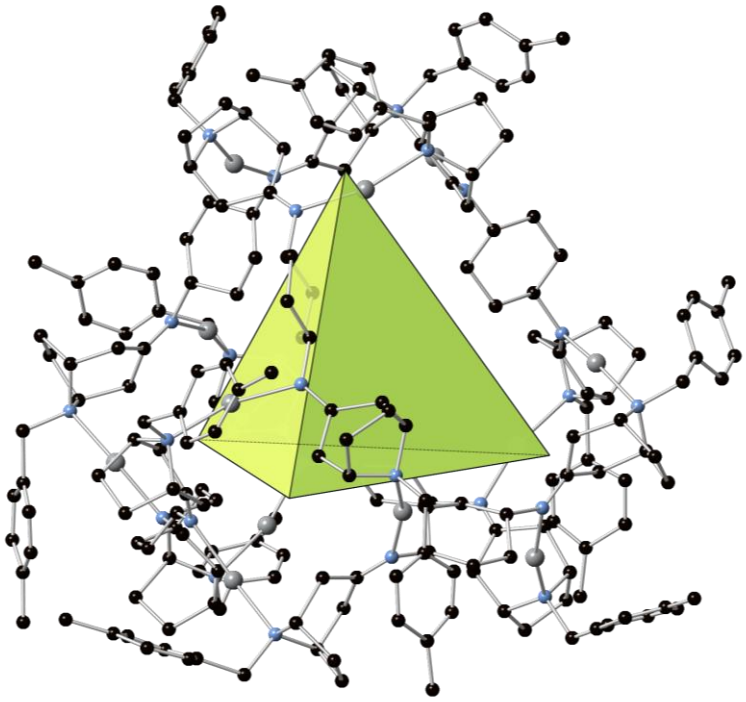

*Figure 4.5. Visual representation of the tetrahedral pore shape (shown in green) inside the discrete $[Ag_{12}(\mathbf{L4.1})_6(OTf)_{12}]$ (cage **C4.1**), with hydrogen atoms and anions omitted for clarity*

4.5.2 Cage C4.2 & C4.2a

In cage **C4.1**, the pendant tolyl groups of the **L4.1** ligand molecules do not contribute to the connectivity of the resultant cage, and therefore adding a coordinating functionality to that position would allow the cage to be linked to neighbouring discrete cages, forming a polymeric species. As silver(I) was the chosen metal ion for these assemblies, the coordinating functionality that replaced the methyl groups of the tolyl functionalities were nitrile groups, resulting in ligand **L4.2**. Combination of this ligand with $AgBF_4$ in acetone yielded cage **C4.2**, consisting, again, of a truncated tetrahedral $M_{12}L_6$ cage analogous to the discrete cage **C4.1**, however in this case adjacent cages were connected to form a three-dimensional network.

The crystallographic data were solved and refined in the cubic space group $P\bar{4}3n$. Similarly to cage **C4.1**, the asymmetric unit (Figure 4.6) consists of one half ligand molecule, coordinated to two silver (I) ions, *via* the nitrile nitrogen atom and an amine nitrogen atom, as well as one-third of a BF_4^- anion that lies on a threefold rotation axis. The remainder of the BF_4^- anions could not be located crystallographically, as the crystals did not diffract strongly and the BF_4^- anions (which were likely significantly disordered) do not contain heavy atoms.

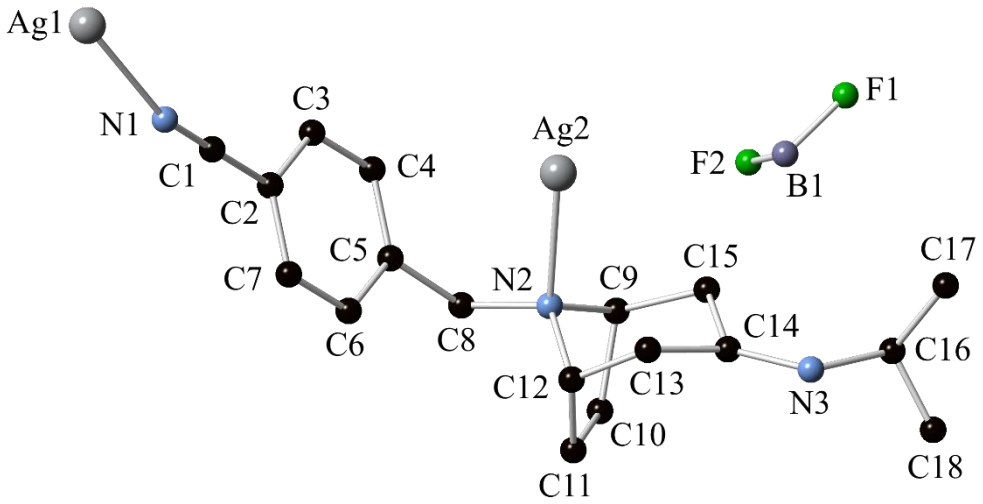

*Figure 4.6. Asymmetric unit of poly-[Ag_{15}(**L4.2**)$_6$(BF_4)$_{12}$] (cage **C4.2**) (hydrogen atoms omitted for clarity)*

Again, all imine and amine nitrogen atoms are coordinating to a linear silver(I) ion (with an N2-Ag2-N3 angle of 160.5736(6)°) to form the $M_{12}L_6$ cage. The ligand nitrile nitrogen atoms are coordinating to a tetrahedral silver(I) ion which connects neighbouring $M_{12}L_6$ cages. The N1-Ag1-N1′ angles range from 100.6322(14)° to 129.1233(14)°, leading to a τ_4 of 0.72.[11] To better visualise the connectivity between neighbouring cages, in Figure 4.7 below, the internal $M_{12}L_6$ cage is represented by a purple sphere which is connected to twelve tetrahedral silver(I) ions (coloured in yellow), which are coordinated by the ligand nitrile nitrogen atoms. Each of these yellow silver(I) ions acts as a tetrahedral node, which connects four $M_{12}L_6$ cages. The cages themselves are a twelve-connecting node, with respect to the tetrahedral silver(I) ions, with an icosahedral geometry. By assigning these two nodes, an **ith** topology is assigned to the complex, which has the same connectivity as Yaghi's MOF-812,[12] which consists of the $[Zr_6(OH)_4(O)_4(RCOO)_{12}]$ cluster linked by tetrahedral linkers.

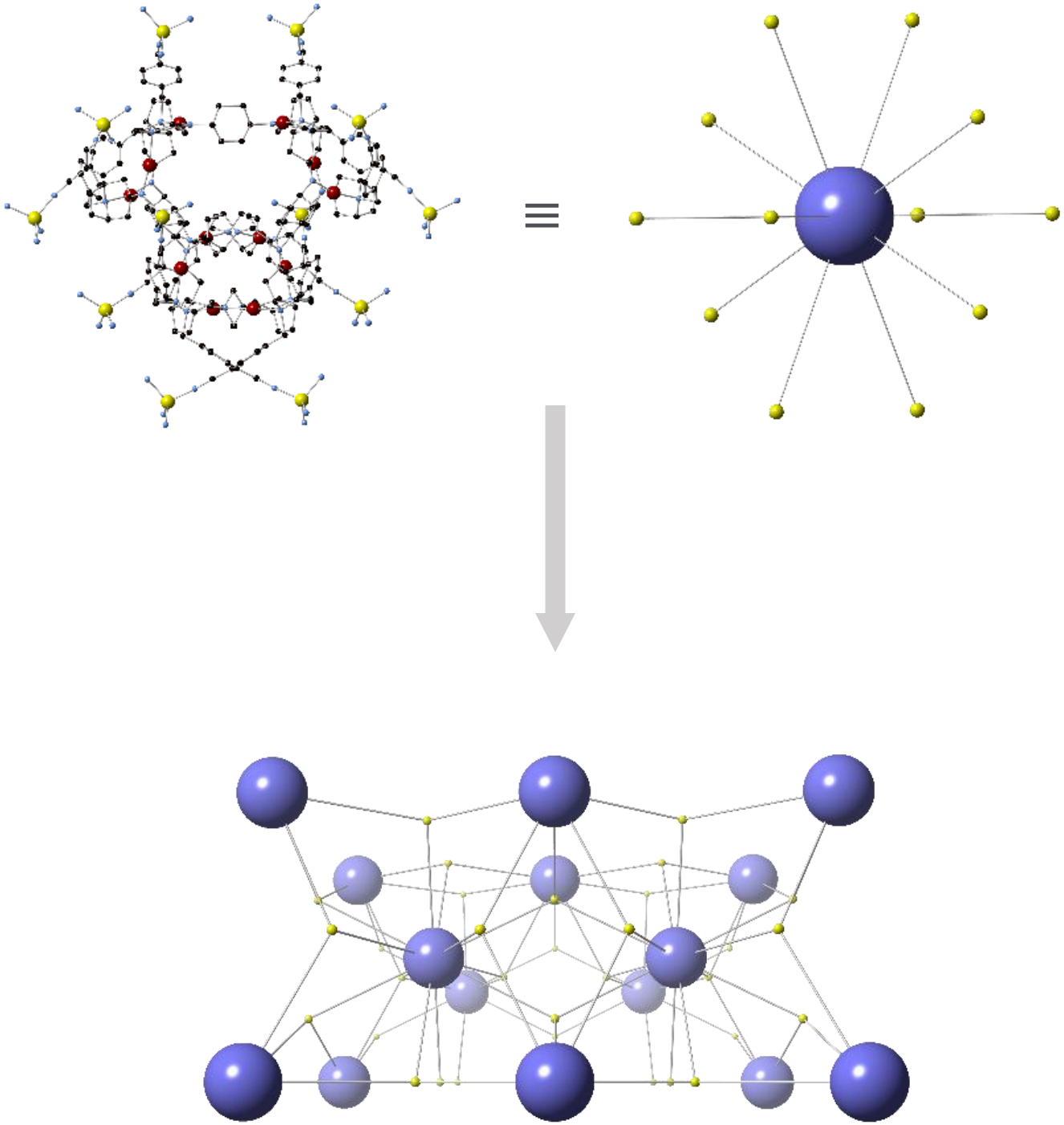

*Figure 4.7. $M_{12}L_6$ cage - poly-[Ag_{15}(**L4.2**)$_6$(BF_4)$_{12}$] (cage **C4.2**) with linear silver(I) ions (red) and bridging tetrahedral silver(I) ions (yellow) (top, left), connectivity of $M_{12}L_6$ cage (purple sphere) to twelve tetrahedral silver(I) ions (yellow) (top, right), extended 3D MOF of connected cages (bottom)*

Similarly to cages **C4.1**, there are four anions encapsulated within each cage, however, as the BF_4^- anions are much smaller, they are much less tightly bound. The association of the anions occurs *via* C-H···F contacts originating at both sets of the tropinone α-protons, with C···F distances of 3.24(3) Å (C13···F2) and 3.24(3) Å (C15···F2) and C-H···F angles of 134.1(16)° (C13-H···F2) and 133.2(17)° (C15-H···F2), respectively. The anions are now much further away from one another within the cage, than what was seen in previous $M_{12}L_6$ cages, with the shortest F···F distances at 4.89688(8) Å. The distance between the Ag_3 centroids is similar to cage **C4.1**, at 10.7 Å. Similarly to cage **C4.1**, there are two cages per unit cell. The internal pore volume was calculated to be 7569 $Å^3$ per unit cell, accounting for 47.5% of the cell volume, which is significantly higher than what is observed in cages **C4.1**, which is due to the difference in connectivity between the cages having an effect on the overall crystal packing.

We noted that when left undisturbed in a capped vial for two days, a second crystalline phase emerged, **C4.2a**, which was a discrete $M_{12}L_6$ cage analogous to **C4.1**, in which none of the nitrile nitrogen atoms are coordinating. This is easily monitored by visually inspecting the crystals under cross-polarised light, as crystals with a cubic symmetry (**C4.2**) are not visible under this light, however, once the cage begins to transform to the lower symmetry discrete cage, it is no longer cubic and can be seen under cross-polarised light.[13] This is because the cubic crystal system is *optically isotropic*, as the crystallographic axes are indistinguishable from one another and therefore the refractive indices are all equivalent, leading to an absence of birefringence. However, in crystal systems where the axes are inequivalent, there is a distinguishable refractive index, *i.e.* they are *optically anisotropic*, leading to the rotation of polarised light by that crystal, and its subsequent visualisation using cross-polarised light.[14]

At first, this transformation was speculated to be a silver(I) to **L4.2** stoichiometry issue, after which a range of stoichiometries were trialled (ranging from an excess of silver(I) tetrafluoroborate to an excess of **L4.2**), which in each case produced the same polymeric phase which later transformed to the discrete second phase, **C4.2a**. A range of concentrations and temperatures were also investigated, which yielded the same results. Finally, it was determined that the solvent water content determined the speed and occurrence of this

transformation, as when the synthesis was repeated in dry acetone, this led exclusively to the formation of the polymeric species. The water in the solvent likely disturbs the coordination of the least sterically hindered and most weakly coordination nitrogen atoms (*i.e.* the nitrile nitrogen atoms) to the tetrahedral silver(I) ions, forming the discrete species.

Following this, in order to gain some control over the formation of the second phase, different quantities of water were added to the crystallisation vials with dry solvent, at different stages of crystal formation to determine the optimal time for the addition and the optimal quantity. The formation of crystals was monitored using an optical microscope and the addition of 20 μL of water upon the observation of visible crystals in the vial was the optimal time for the addition, leading exclusively to the second phase of the cage **C4.2a** within 24 hours of the addition.

The resultant cage **C4.2a**, crystallises in the orthorhombic space group $P2_12_12$. The asymmetric unit comprises one half of a complete cage, containing two full ligand molecules, and two half ligand molecules which are coordinating to six linear silver(I) ions, with the N-Ag-N bond angles ranging from 161.7(8) to 169.6(8)°. As the connectivity of the internal cage is very similar to cage **C4.2**, with regards to the imine and amine nitrogen atoms, the main observable difference is in the orientation of the ligand nitrile functionalities, in relation to the remainder of the cage (Figure 4.8). Interestingly, the positions of these aromatic moieties are very similar in the discrete cage **C4.1** and the polymeric cage **C4.2**, and it is the discrete cage **C4.2a** that differs significantly from the remaining two, whereas the expectation might be that the two discrete cages would be more alike, as the aromatic components are non-coordinating.

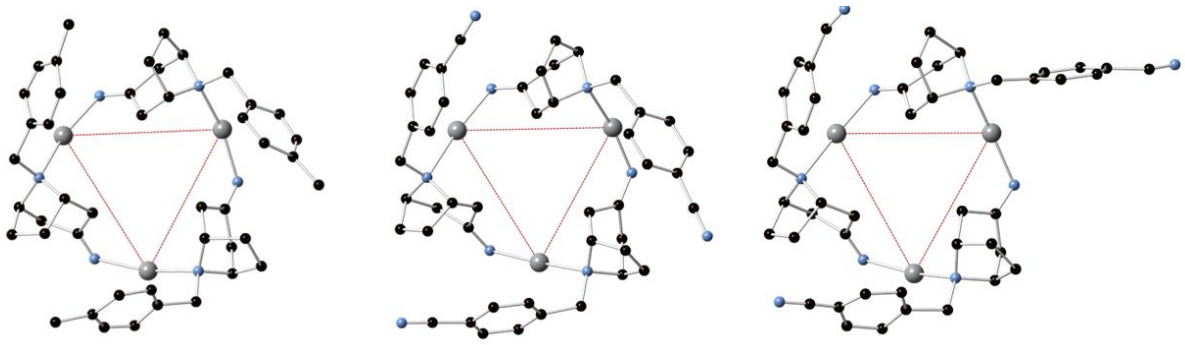

*Figure 4.8. Ligand environment surrounding Ag_3 centroid in cage **C4.1**, **C4.2** and **C4.2a** (left to right) (hydrogen atoms have been omitted for clarity)*

As is seen in Figure 4.8, one of the three ligand benzonitrile components of **C4.2a** is in a significantly different position to the remaining aromatic functionalities both in that same cage, and all the aromatic components in the other two cages, **C4.1** and **C4.2**. The other two aromatic functionalities of **C4.2a** appear to be in very similar positions as they are in its precursor, **C4.2**, suggesting that to go from the polymeric phase to the discrete cage, does not require a large amount of reordering of the ligand components. This is indicative of the connecting tetrahedral silver(I) ions of cage **C4.2**, being leached out of the crystal to form the discrete, lower symmetry cage **C4.2a**, with a slight reordering of ligand components – which would be easy to reorder given that they are no longer coordinating, *i.e.* a solid-to-solid phase change within the crystals, rather than a dissolution-crystallisation. This is observable under the microscope, as crystals of the second phase appear to be replacing segments of crystals of the first, polymeric phase.

4.5.3 Cage C4.3

Each cage discussed thus far has incorporated a ligand with an aromatic functionality into its structure (**L4.1** and **L4.2**), however, the aromatic component only appears to be involved in the connectivity of the $M_{12}L_6$ cages to adjacent cages. It is the amine and imine nitrogen atoms which coordinate to silver(I) ions to form the core $M_{12}L_6$ cages. Therefore, it was of interest to obtain a cage containing **L4.3**, to investigate the effect of removing the large aromatic component, present in **L4.1** and **L4.2**, from the ligand structure. The ligand contains no aromatic component, and instead it is replaced with a methyl group, while still containing the core cyclohexyl-bridged tropinone structure which contains amine and imine nitrogen atoms to form the

expected $M_{12}L_6$ cage. Interestingly, however, the cage that forms differs from previously reported cages, in that it is now of the M_8L_6 stoichiometry, giving the cage a near-cubic form, if the silver(I) ions are again considered as vertices, highlighted in the wireframe representation of the cage in Figure 4.9. The figure also offers a simplified visualisation of the ligand arrangement within the cage, by colouring each individual ligand a different colour.

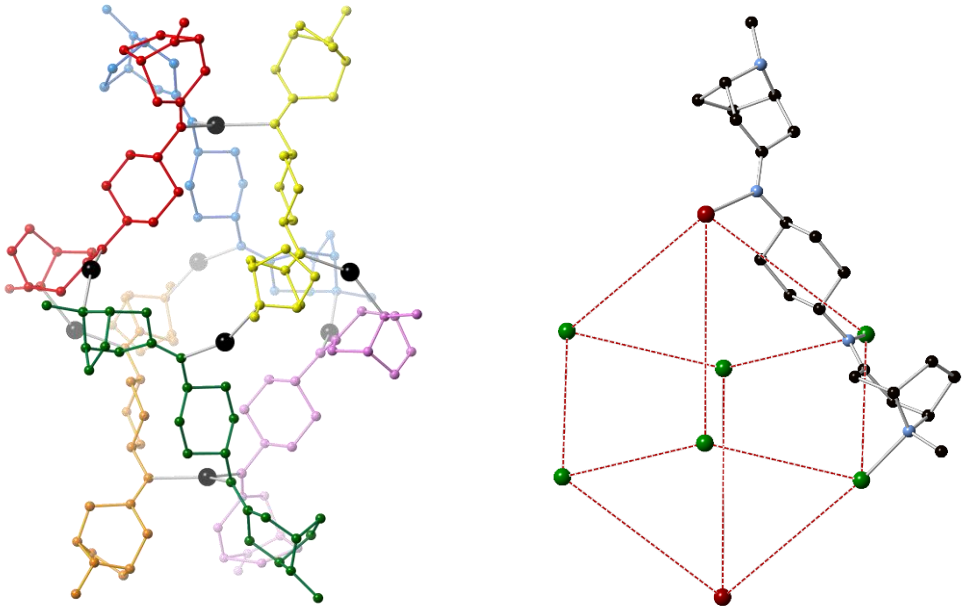

*Figure 4.9. Discrete M_8L_6 - $[Ag_8(\mathbf{L4.3})_5(\mathbf{L4.3'})^*(OTf)_8]\cdot 5H_2O$ (cage **C4.3**) showing the individual **L4.3** ligand molecules in different colours and silver(I) ions in black (left), wireframe representation of **C4.3** showing ligand coordination, with apical silver(I) ions (red) and equatorial silver(I) ions (green) (right) (hydrogen atoms and some anions were omitted for clarity)*

The crystallographic data were solved and refined in the monoclinic space group $P2_1/n$. The asymmetric unit (Figure 4.10) consists of half of one M_8L_6 cage – three ligand molecules, coordinating to four silver(I) ions *via* some of the amine and imine nitrogen atoms (note that not every ligand nitrogen atom is coordinating), as well as three whole and one half of a triflate anion. The remaining one-half of a triflate anion could not be located crystallographically, as it was likely too disordered to be modelled. In each of the three crystallographically unique ligand molecules, three of the four nitrogen atoms are coordinating, and it is always one amine nitrogen atom that is non-coordinating. One of the triflate anions is coordinating

to a silver(I) ion, giving it a T-shaped geometry and one water molecule is coordinating to a different silver(I) ion, also leading to a T-shaped geometry.

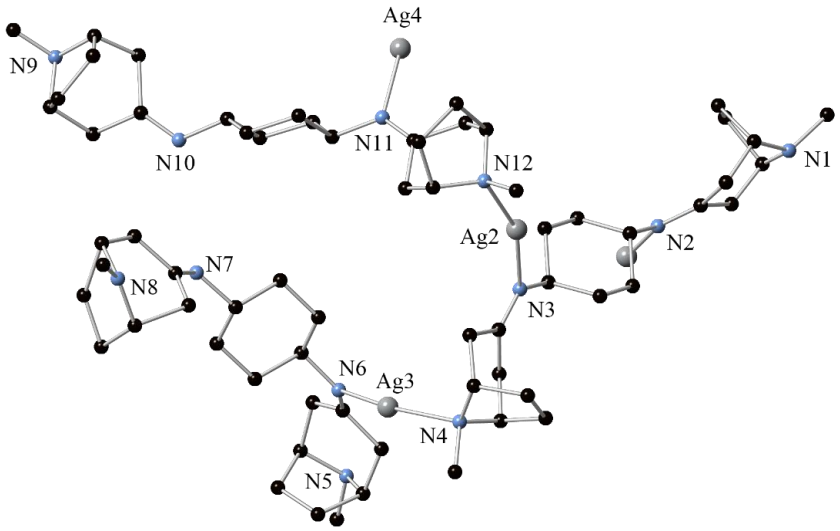

*Figure 4.10. Asymmetric unit of [Ag_8(**L4.3**)$_5$(**L4.3'**)*$(OTf)_8$]·5H_2O (cage **C4.3**) (hydrogen atoms and anions omitted for clarity)*

Within the cage (shown in Figure 4.9), the "apical" silver(I) ions are three-coordinate with a trigonal planar geometry, with N-Ag1-N angles measuring at 120.8(4)° (N7-Ag1-N2), 117.7(4)° (N2-Ag1-N10) and 121.5(4)° (N10-Ag1-N7). These apical silver(I) ions are coordinated by three ligand imine nitrogen atoms, and the amine nitrogen atoms of these ligands that are closest to the coordinating imine nitrogen atoms are non-coordinating. The remaining amine and imine nitrogen atoms of these ligand molecules are coordinating to the "equatorial" silver(I) ions. Each of these equatorial silver(I) ions are coordinated by one amine and one imine nitrogen atom each. Four of the six equatorial silver(I) ions are coordinated by a triflate ion *via* one of its oxygen atoms, with Ag···O distances of 2.555(12) Å (Ag4···O4) and 2.44(2) Å (Ag3···O7), leading to a T-shaped coordination geometry surrounding each silver(I) ion. The remaining two

equatorial silver(I) ions within the cage are coordinated by a water molecule *via* its oxygen atom (with an Ag2···O13 distance of 2.471(12) Å), again leading to a T-shaped coordination geometry of Ag2.

Due to the smaller size of the M_8L_6 cage, relative to previous $M_{12}L_6$ cages, there is only one triflate anion encapsulated within each cage (Figure 4.11). The anion interacts with the core cage *via* C-H···O and C-H···F contacts, both originating at ligand cyclohexyl -CH_2 moieties, with a C13···O10 distance of 3.442(10) Å and a C13-H···O10 angle of 160.6(5)°, and a C56···F12 distance of 3.034(12) Å and a C56-H···F12 angle of 128.8(6)°.

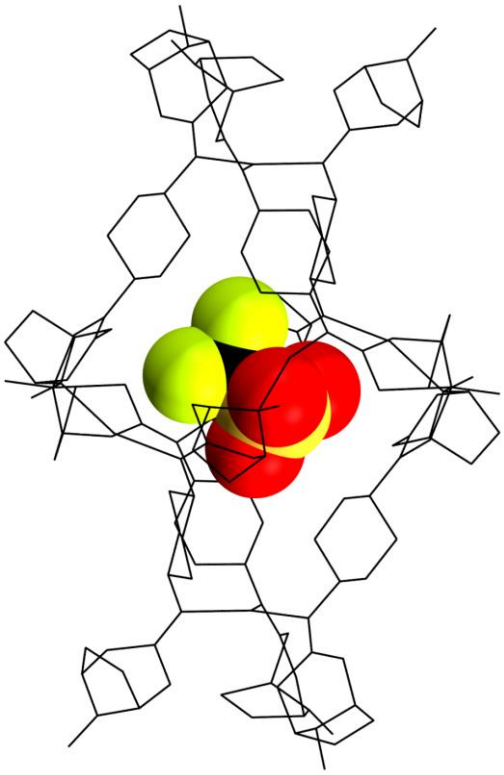

*Figure 4.11. Wireframe representation of $[Ag_8(\mathbf{L4.3})_5(\mathbf{L4.3'})^*(OTf)_8]\cdot 5H_2O$ (cage **C4.3**), showing encapsulated triflate anion*

The collection of the diffraction data for this cage was repeated a second time, as in the first measurement it appeared that one tropinone moiety had substantially larger ADPs than its neighbours, with the exception of the three carbon atoms of the tropinone ring that were adjacent to the imine bond (Figure 4.12), and this was observed in both data collections.

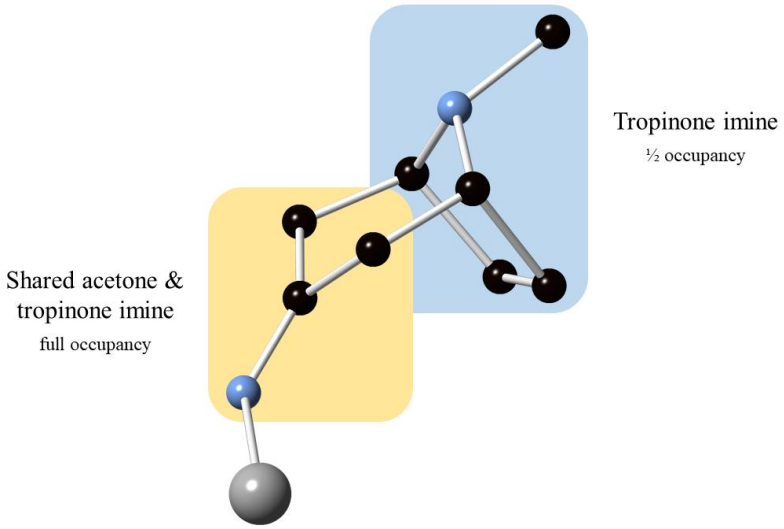

*Figure 4.12. Imine component of **L4.3** in [Ag_8(**L4.3**)$_5$(**L4.3'**)*$(OTf)_8$]·5H_2O (cage **C4.3**), showing acetone and tropinone imine modelling in crystallographic mode (hydrogen atoms have been omitted for clarity)*

Modelling the remaining large tropinone carbon atoms at half occupancy resulted in a much more reasonable model showing half occupancy acetone and tropinone. This is reasonable given the dynamic nature of imine bonds in solution, in particular in the presence of an excess of another ketone, resulting in the gradual displacement, in particular due to the nitrogen of that tropinone moiety not coordinating to a silver(I) ion.[15,16] This implies that this forms readily and relatively quickly in solution, as only two of the six ligands in the cage experience this partial displacement, whereas if the free ligand remained uncoordinated in solution for a significant length of time, this displacement (*i.e.* hydrolysis) would be much more widespread throughout the complex. Following the same assumptions, this does not occur in the $M_{12}L_6$ complexes, as each ligand nitrogen atom is coordinating in the complex, which implies that it must form and persist in solution, as again, hydrolysis and displacement of the tropinone ketone would also be apparent.

The triflate anions in cage **C4.3** which are not encapsulated, form contacts with adjacent cages, which govern the crystal packing of the discrete cages. The coordinating triflate anions of one cage form reciprocated C-H···O contacts with a cyclohexyl -CH_2 moiety of an adjacent cage (with a C63···O6 distance of 3.462(18) Å and a C63-H···O6 angle of 163.6(7)°). Again, similar to cage **C4.1**, **C4.2** and **C4.2a**, there are two cages in the unit cell, and the internal pore volume of the complex was calculated to be 2294 $Å^3$ per unit cell, which accounts for 23.7% of the total unit cell volume. This likely accounts largely for the space between adjacent cages, as the internal volume of the cages is quite small, in particular when considering the encapsulated triflate anion.

4.6 NMR Studies

Based on the fascinating connectivity of the cages and the potential for both the aromatic and non-aromatic ligand classes to form either of the two cages, the focus was then turned to NMR spectroscopy to probe the behaviour of these systems in solution. The ^{1}H NMR spectrum of ligand **L4.2** is shown in Figure 4.13 along with the assignments of the signals, which are consistent throughout the ligands described in this chapter, with the exception of the aromatic protons, which are not present in **L4.3**.

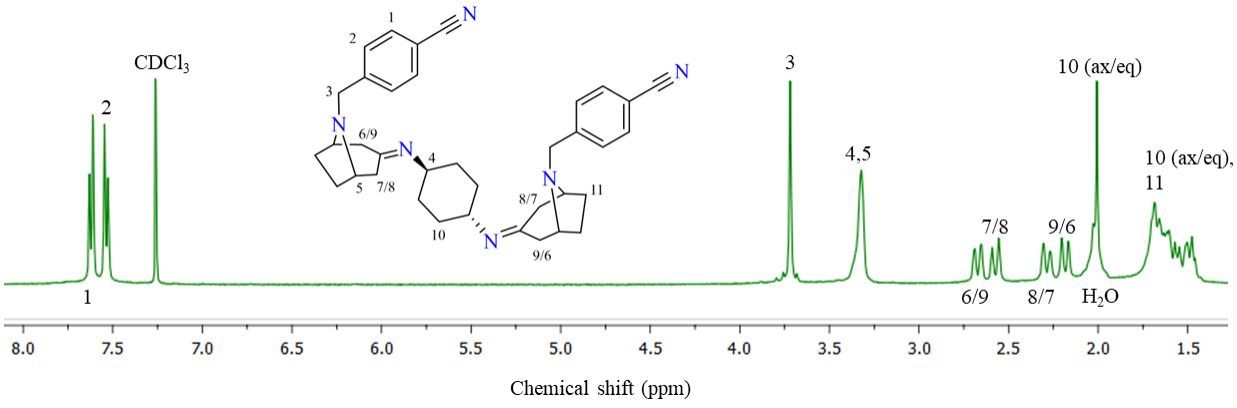

*Figure 4.13. ^{1}H NMR spectrum of **L4.2** with the associated labelling scheme*

Initially, as the coordination cages were all formed in acetone, that was the chosen solvent for the solution studies. The **L4.2** ligand combined with $AgBF_4$ was the chosen system, as both a discrete and polymeric

species were observed crystallographically and it was of interest to understand this assembly process *in-situ*. The **L4.2** ligand was dissolved in acetone-d_6 and small quantities of a solution of $AgBF_4$ was added to this solution. The chemical shift of each ligand proton was recorded after each addition and the difference of the shift relative to that of the free ligand was plotted against the equivalents of the metal solution added. This resulted in some solubility issues as firstly, the free ligand was not entirely soluble in pure acetone-d_6, and then the formation of the polymeric cage **C4.2** species also resulted in some precipitation of this complex, leading to ^{1}H NMR spectra that were not entirely representative of the system.

Attempts were made to isolate **C4.2a** *in-situ*, *via* titration of TBACl into the **L4.2**/$AgBF_4$ system, in hopes of mimicking the behaviour in the solid state upon addition of water, which disrupts the coordination between the nitrile nitrogen atoms and the bridging tetrahedral silver(I) ions. In theory, this would result in the precipitation of silver(I) chloride, which would first leach out the most accessible silver(I) ions in the polymer, which would be the tetrahedral connecting silver(I) ions that are coordinated by the nitrile nitrogen atoms, leaving the discrete cage **C4.2a** in solution. The resulting spectra were very difficult to interpret, as a large majority of the species in solution was the TBA^+ cation, and any complex was hidden in the baseline of the ^{1}H NMR spectra, which were of very poor resolution, and therefore, impossible to identify with any certainty.

Following this, the decision was made to change the solvent from acetone-d_6 to CD_3CN for the metal titration experiments, as the acetonitrile molecules would prevent the ligand nitrile nitrogen atoms from coordinating, and therefore, forming a polymeric species. Unfortunately, however, the free ligand was not soluble in CD_3CN, therefore the ligand was then dissolved in CD_3CN with the smallest volume of $CDCl_3$ that would ensure complete dissolution of the ligand, and the resulting solvent was an 11:5 ratio of CD_3CN to $CDCl_3$, respectively, though this also led to a small amount of precipitation after the final few additions of silver(I). Firstly, it was noted that the signals representing the α-protons, the tertiary tropinone CH proton and the bridging *N*-CH_2 were the signals that shifted upon subsequent additions of equivalents of $AgBF_4$.

The change in chemical shift of these signals was recorded after each subsequent addition and plotted against the equivalents of silver(I) added (Figure 4.14).

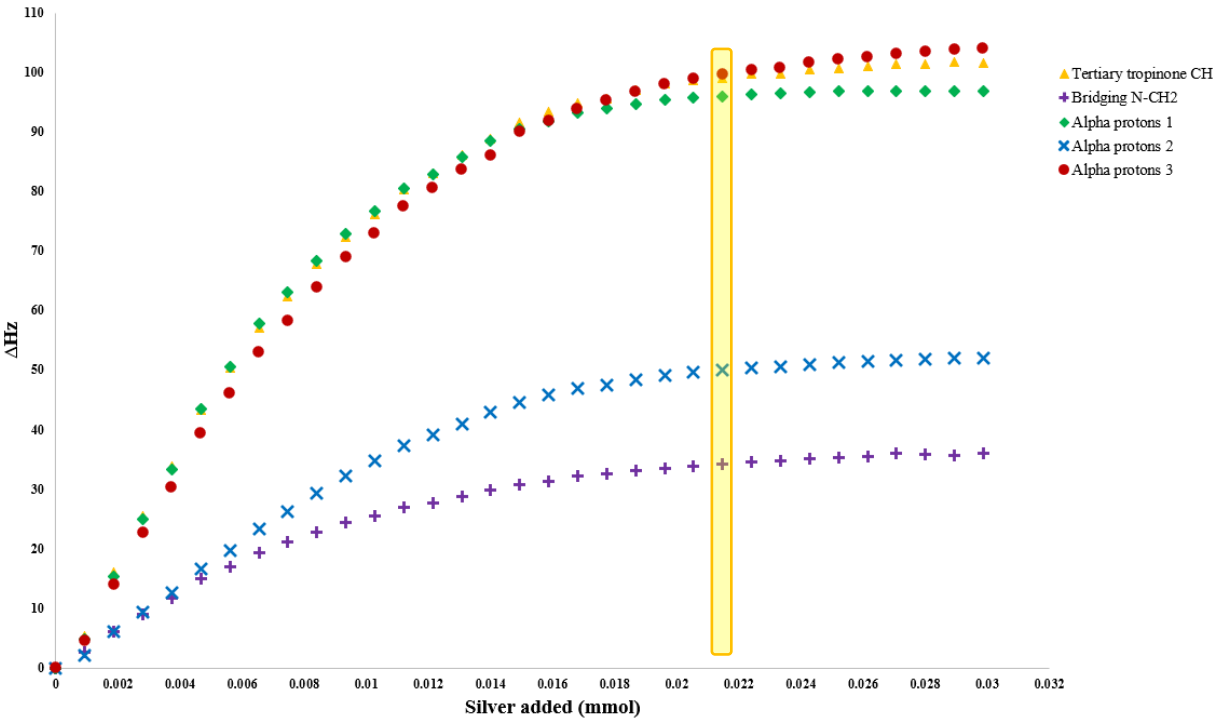

*Figure 4.14. Titration curves of $AgBF_4$ addition to **L4.2** in $CD_3CN/CDCl_3$, with the change in chemical shift plotted on the y-axis (Hz) and the quantity of silver added on the x-axis (mmol), with the titration curves for individual peaks labelled in different colours. The starting concentration of **L4.2** in the solution was 1.375 μM. The point at which the solution M:L ratio reaches 2:1 is highlighted in yellow.*

As is evident from Figure 4.14, the change in chemical shift of these protons followed the same trend. However, the point at which the M:L ratio in solution reaches 2:1 (the expected stoichiometry of the $M_{12}L_6$ cage), the change in chemical shifts upon addition of further silver(I) equivalents has decreased substantially, and the titration curves have tapered off. The curve never fully tapers off, however, due to the equilibrium between the formed complex and the free silver(I) ions in solution. Each addition of silver(I) will affect the equilibrium and therefore the positions of the signals, and the minimal change in chemical shifts after a certain M:L ratio is reached suggests that the ideal M:L ratio for the forming complex has been achieved. The point at which these titration curves begin to plateau, more strongly suggests a 2:3 M:L ratio

in the forming complex. This was attributed to the high quantity of $CDCl_3$, which likely has a marked effect on both the behaviour of the ligand in solution and the formation of any subsequent complexes. The attempted growth of crystals of any complex in the same mixture of chloroform and acetonitrile was unsuccessful, however, the titrations provided provisional data about the coordination of the ligand to silver(I) in solution, and in particular which parts of the ligand are most affected by this coordination. The remainder of the solution studies were carried out in pure CD_3CN, which would, in theory, not interfere with the formation of these complexes as $CDCl_3$, given the different polarity and behaviour of this solvent relative to the crystallisation solvent, acetone, whereas CD_3CN is chemically much more similar. While CD_3CN will outcompete ligand nitrile functionalities in coordination to silver(I), the stronger coordinating ligand imine and amine nitrogen atoms are still likely to coordinate in the presence of CD_3CN, whereas this could have been affected by the presence of $CDCl_3$. As well as this, the residual chloride ions present in $CDCl_3$ can affect the free silver(I) ion concentration, by precipitation of AgCl.

The resultant spectra in pure CD_3CN were well-resolved, and the complexes remained in solution throughout the analyses. Some initial studies of the $M_{12}L_6$ stoichiometry were first carried out using **L4.1**, as in the solid state, this ligand produced a discrete complex upon combination with silver(I). The self-assembly solutions were prepared by combination of the ligand and the relevant silver(I) salt in the NMR tube. The resultant spectra could also be compared to the dissolved cage **C4.1**. After these initial studies using **L4.1**, **L4.4** was chosen as a representative ligand for systems containing **L4.1** and **L4.2**. In the case of both of those ligands, the resultant complexes are also of the form $M_{12}L_6$ in the solid state, and **L4.4** gave the most well-resolved spectra, as well as allowing for the monitoring of the behaviour of the species *in-situ* using both ^{1}H and ^{19}F NMR.

4.6.1 $M_{12}L_6$ System

L4.1 Systems

In order to obtain a self-assembly solution directly comparable to the solid state data, AgOTf and **L4.1** were combined in a 12:6 M:L ratio in CD_3CN, and the resultant ^1H NMR spectrum was compared to that of the redissolved crystals of cage **C4.1**, also in CD_3CN (Figure 4.15). It is important to note that the free ligand **L4.1**, and all subsequent ligands are not soluble in CD_3CN, and any soluble species derived from these ligands imply at least dynamic metal coordination, if not the persistent formation of coordination compounds in solution. The NMR spectra of the redissolved cage and the self-assembly solution were in good agreement with each other, indicating that the complex(es) that form in solution, form both from the dissolution of crystals and the combination of the metal and the ligand. The self-assembly solution (containing the individual components) was then heated to 50 °C and ^1H NMR and ^{19}F NMR spectra were measured at regular time intervals. The ^1H NMR was monitored to observe any changes to the chemical shifts, quantity and multiplicity of the signals signifying a change in symmetry of the species in solution, or the formation of a new species after a period of heating. In the decoupled ^{19}F NMR, the number of signals represented the number of anion environments, as this ligand was not fluorinated. This was done in order to determine the nature of the material in solution, more specifically, if it was the thermodynamically stable product or a kinetically trapped intermediate, that over a period of heating would transform into the thermodynamically favoured product, which would be observable *via* the various spectra (Figure 4.15).

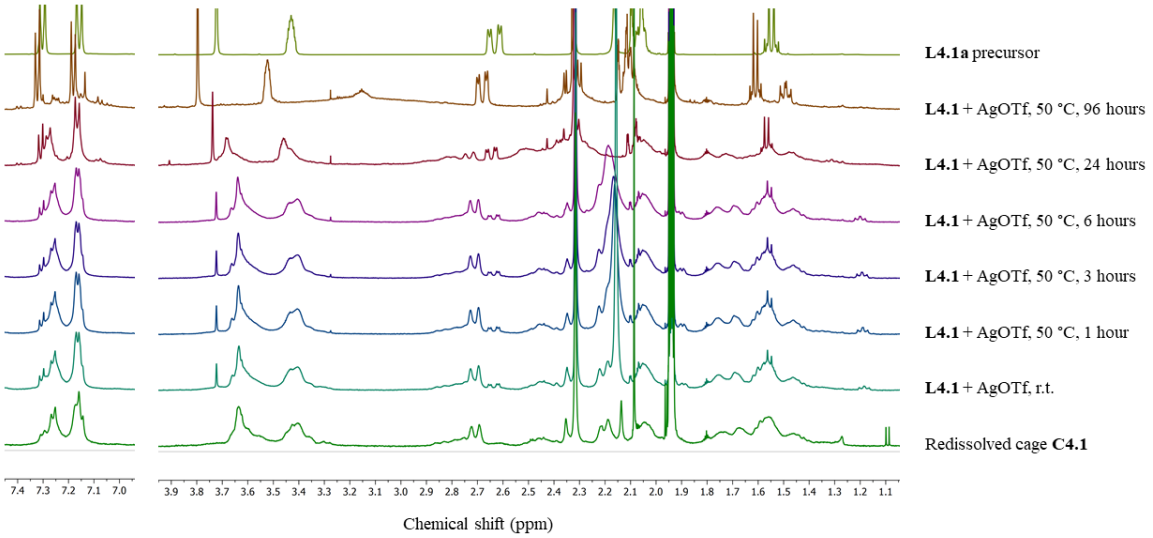

*Figure 4.15. ^{1}H NMR spectra of **L4.1**/AgOTf self-assembly system (50 °C in CD_3CN) compared to redissolved cage **C4.1** (bottom) and ligand precursor **L4.1a** (top)*

As becomes apparent after 24 hours of heating at 50 °C, the ligand begins to decompose to the tropinone-containing ligand precursor, which is even more clear at 96 hours. This is evidenced by the appearance of a doublet of doublets at 2.68 ppm, (with a second set hidden under the water signal), which become dominant after 96 hours of heating. These signals represent the two sets of tropinone α-protons in the ligand precursor. The signals at 1.48 and 3.15 ppm are likely representing further decomposition products, though these could not be identified. It is assumed that the hydrolysis of the imine bond occurs, resulting in the symmetry of the molecule being restored, leading to only two signals for the α-protons, rather than the expected four in **L4.1**. These signals are slightly downfield of those in the ligand precursor **L4.1a**, likely due to some coordination of the decomposition product to the silver(I) ions in solution. The ^{19}F NMR spectra throughout this titration suggest only one anion environment as there is only ever one signal present. The presence of only one peak, which is also relatively narrow is indicative of the presence of only the free anion in solution, and not the exchange of encapsulated and free anions, which would lead to multiple signals or peak broadening, respectively.

As there are no significant changes to the ^{1}H and ^{19}F NMR spectra prior to ligand decomposition, it is assumed that the complex present in solution at room temperature is indeed the thermodynamically stable product. The poor resolution of the resulting ^{1}H NMR spectra of the self-assembly solution and the

redissolved cage resulted in difficulty in obtaining 2D NMR characterisation, however the similarity in the ^{1}H NMR spectra of the self-assembly solution and redissolved cage **C4.1** is indicative of the possible presence of cage **C4.1** in solution.

In order to compare to the **L4.1**/AgOTf system, **L4.1** was combined with $AgBF_4$ in CD_3CN, which resulted in a much more resolved ^{1}H NMR spectrum at room temperature, which remained consistent throughout the heating process (at 50 °C) until the onset of ligand decomposition was observed at 24 hours (Figure 4.16).

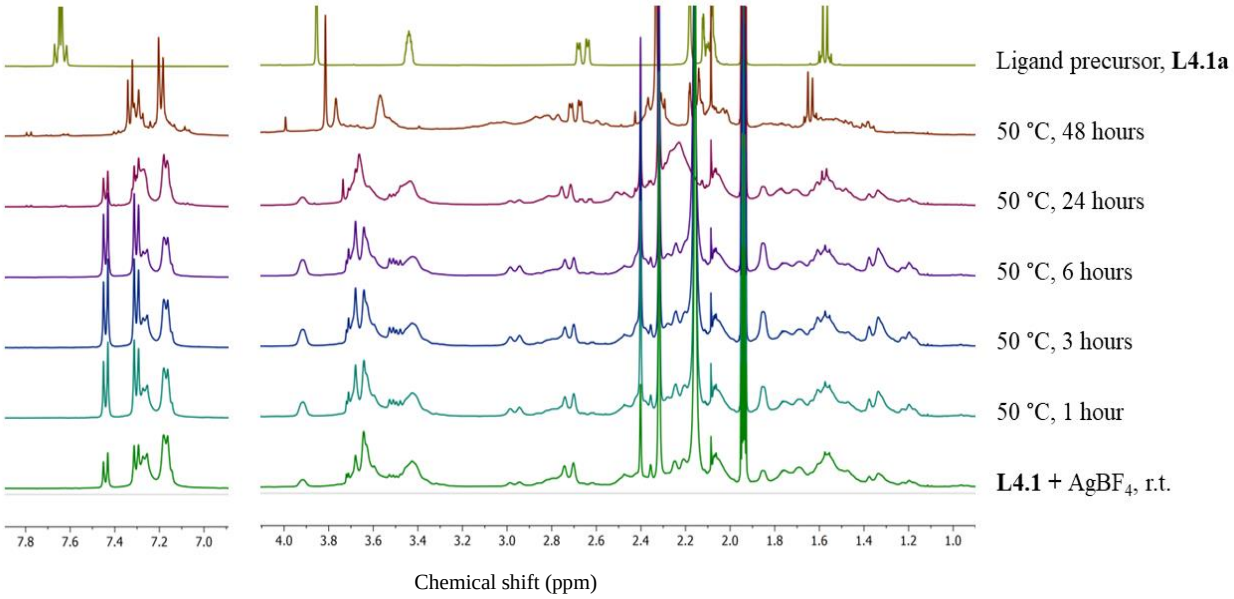

*Figure 4.16. ^{1}H NMR spectra of **L4.1**/$AgBF_4$ self-assembly system (50 °C in CD_3CN) compared to the ligand precursor **L4.1a** (top)*

The signals representing the ligand precursor **L4.1a** upon decomposition vary slightly from the free ligand precursor in the ^{1}H NMR spectra, likely due to some coordination of this precursor to the silver(I) ions in solution, resulting in each peak being shifted downfield, which is typical of the deshielding of ligand peaks upon metal coordination.[17] The multiplicity and appearance of the **L4.1a** signals are clearly analogous to those seen in the self-assembly solution post-decomposition, and therefore, it can be said with reasonable confidence that imine hydrolysis of **L4.1** occurs and results in the formation in **L4.1a** *in-situ*.

The study of systems containing **L4.1** provided provisional data about the $M_{12}L_6$ system *in-situ*, which was significantly aided by the comparison of the self-assembly solutions to the available crystals of cage **C4.1**.

The ^{1}H NMR spectra containing **L4.1** were relatively poorly resolved, and therefore the remainder of the analysis of the $M_{12}L_6$ system was carried out using the **L4.4** ligand, as the initial analyses demonstrated the behaviour was very similar to that of **L4.1** systems. **L4.4** provided an overall improved resolution of the ^{1}H NMR spectra, which significantly simplified the analysis of the system.

Unfortunately, due to the aforementioned issues of mass spectrometric analysis of complex coordination materials, it was not possible to observe the presence of any M_8L_6 and $M_{12}L_6$ complexes in the resulting spectra of the redissolved cages **C4.1** and **C4.3**, and any relevant NMR self-assembly solutions that contained only one complex. Only very small M + L and 2M + L fragments were observed by electrospray mass spectrometry. Therefore, all analyses and speculation of the composition of the self-assembly solutions will be strictly derived from the NMR data obtained only.

L4.4 Systems

As with systems containing **L4.1**, **L4.4** was first combined with AgOTf in both 12:6 and 8:6 M:L ratios in CD_3CN and heated to 50 °C to monitor the self-assembly process and determine the thermodynamically stable product. There was a noticeable difference between the room temperature self-assembly solutions (prior to heating) for the two different ratios, highlighted in Figure 4.17.

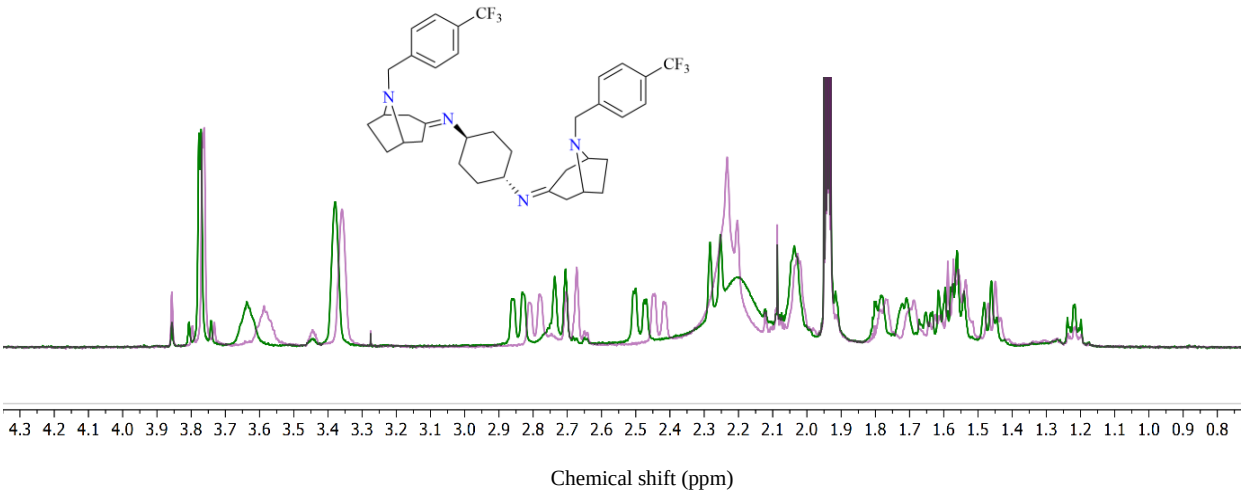

*Figure 4.17. ^{1}H NMR of aliphatic region of the 12:6 (green) and 8:6 (purple) M:L stoichiometry in the **L4.4**/AgOTf self-assembly system, with the structure of **L4.4** shown above*

In Figure 4.17, the green spectrum represents the 12:6 M:L stoichiometry, while the purple represents the 8:6 M:L stoichiometry. The signals for the tropinone α-protons and the tertiary tropinone CH protons are among those to shift furthest downfield by 0.5 ppm from the 8:6 M:L ratio to the 12:6 M:L ratio. From the early titration data, it can be seen that these signals shift downfield upon coordination to a silver(I) ion, relative to the free ligand. This suggests that at the 8:6 stoichiometry, the $M_{12}L_6$ complex has not fully formed, and the system contains excess ligand, which is then in equilibrium with the formed complex, causing the observed average signals to be further upfield than those in the 12:6 stoichiometry. For the purpose of understanding the $M_{12}L_6$ system, which is what is observed crystallographically in structurally similar ligands **L4.1** and **L4.2**, the 12:6 M:L stoichiometry was the focus of the subsequent solution studies.

Predictably, the species present at room temperature was concluded to be the thermodynamically stable product, as there were no changes to the ^{1}H NMR spectra throughout the heating process until the ligand again began to decompose (demonstrated by the appearance of the precursor α-proton doublet of doublets at 2.66 ppm). The decomposition in this case occurs after a much longer period of heating at 50 °C (relative to the **L4.1**/AgOTf system), with the additional peaks only beginning to appear after 72 hours of heating, with full decomposition after 144 hours (Figure 4.18).

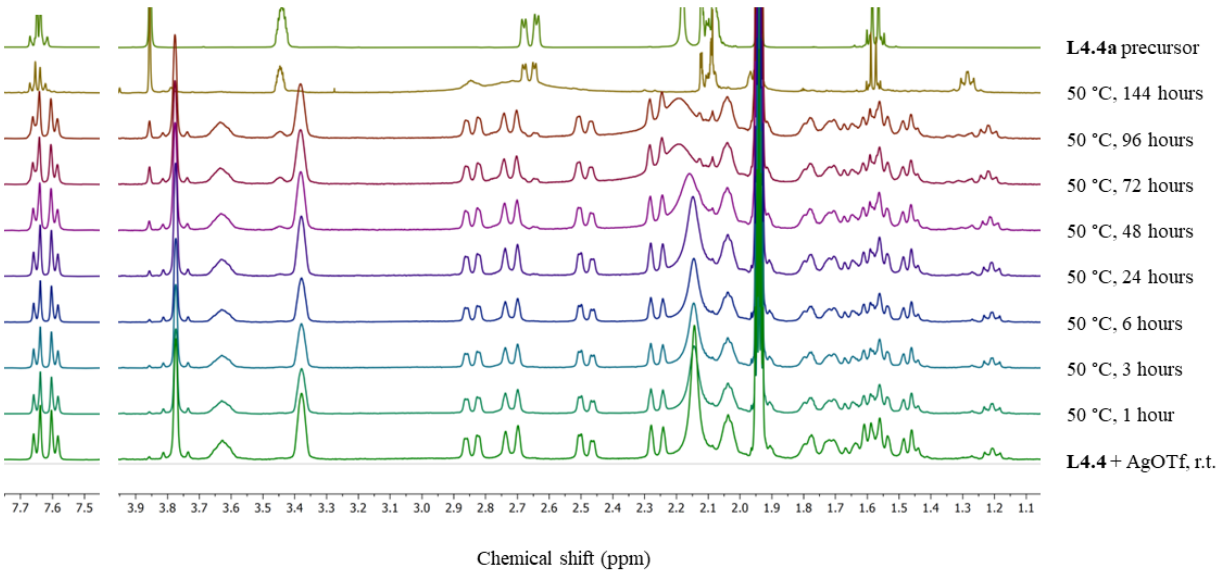

*Figure 4.18. ^{1}H NMR spectra of **L4.4**/AgOTf self-assembly system (50 °C in CD_3CN)*

As in the **L4.1**/AgOTf system, the ^{19}F NMR spectra throughout the **L4.4**/AgOTf self-assembly process are quite similar, however, due to the CF_3 moieties of the ligand, there are two signals in the spectra (one for the ligand and one for the triflate anion). Again, there are no separate signals for encapsulated and free anions, likely suggesting fast exchange between the two states of the anion, given the pore openings in the $M_{12}L_6$ cage are large enough to allow for the free movement of anions. As these spectra were of a much higher resolution to those of **L4.1**-containing systems, DOSY NMR (Figure 4.19) was used to both confirm the presence of a singular species in solution, and determine its average diffusion coefficient (D), which was 7.97×10^{-10} m^2 s^{-1}, corresponding to a hydrodynamic radius of 7.99 Å. The crystallographic radii of the discrete $M_{12}L_6$ cages **C4.1** and **C4.2a** are *ca.* 7.59 Å. As the $M_{12}L_6$ cages of analogous ligands **L4.1** and **L4.2** are roughly spherical in shape (*i.e.* no one axis is substantially longer than the others), the standard Stokes-Einstein equation (Equation 4.1) was used for the calculation of the hydrodynamic radii of each species discussed in this chapter.

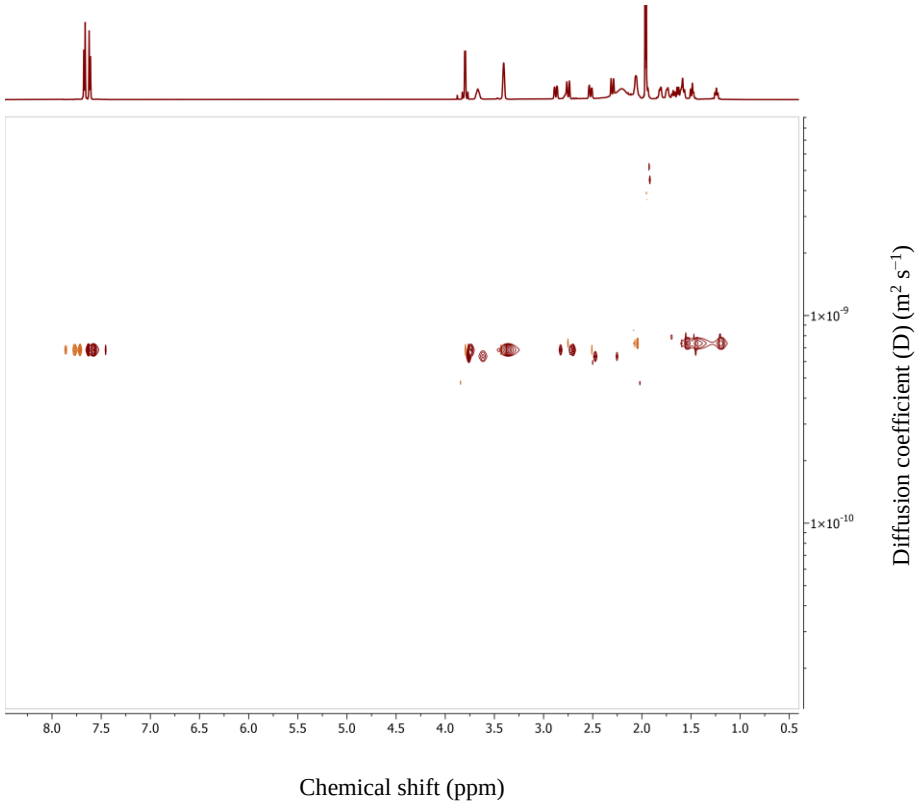

*Figure 4.19. DOSY NMR spectrum of the **L4.4**/AgOTf self-assembly system at room temperature*

Similar phenomena are observed when **L4.4** and $AgBF_4$ are combined, and again the 12:6 M:L stoichiometry was chosen for the analyses, as there was a difference in the signals in the ^{1}H NMR spectra that would suggest the formation of the $M_{12}L_6$ cage. The ^{1}H NMR spectra in this case were again well-resolved at room temperature, however, interestingly, the onset of ligand decomposition occurred after only 24 hours of heating at 50 °C in CD_3CN, which is a substantially shorter time than in the **L4.4**/AgOTf system, when the hydrolysis only begins after 72 hours of heating. The signals appearing at 2.68 ppm (representing the **L4.4a** tropinone α-protons) and 3.44 (representing the **L4.4a** tropinone tertiary CH moiety) are again, highly indicative of ligand hydrolysis, particularly when compared to the ^{1}H NMR spectrum of the ligand precursor (Figure 4.20).

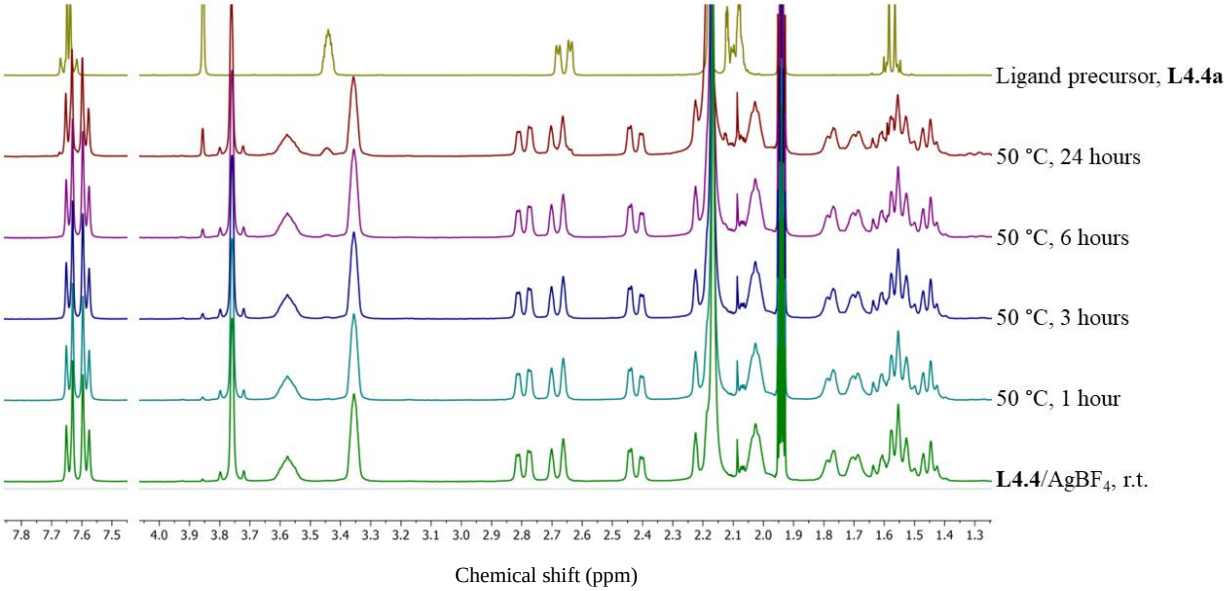

*Figure 4.20. ^{1}H NMR spectra of **L4.4**/$AgBF_4$ self-assembly system (50 °C in CD_3CN) compared to the ligand precursor **L4.4a** (top)*

Similarly, in the 12:6 M:L stoichiometry of the **L4.4**/$AgPF_6$ system (Figure 4.21), the onset of ligand hydrolysis occurs after a much shorter period of heating than the **L4.4**/AgOTf system, at only 24 hours. Interestingly, the signals arising from ligand decomposition in the self-assembly solutions correspond directly with the ^{1}H NMR signals of the ligand precursor, **L4.4a**, on its own. In the **L4.1** systems, it was noted that these signals were shifted downfield due to a deshielding effect, arising from the ligand

decomposition product (**L4.1a**) coordinating to the silver(I) ions in the self-assembly solutions. This does not appear to occur in the systems containing **L4.4**, as these shifts remain consistent with each other.

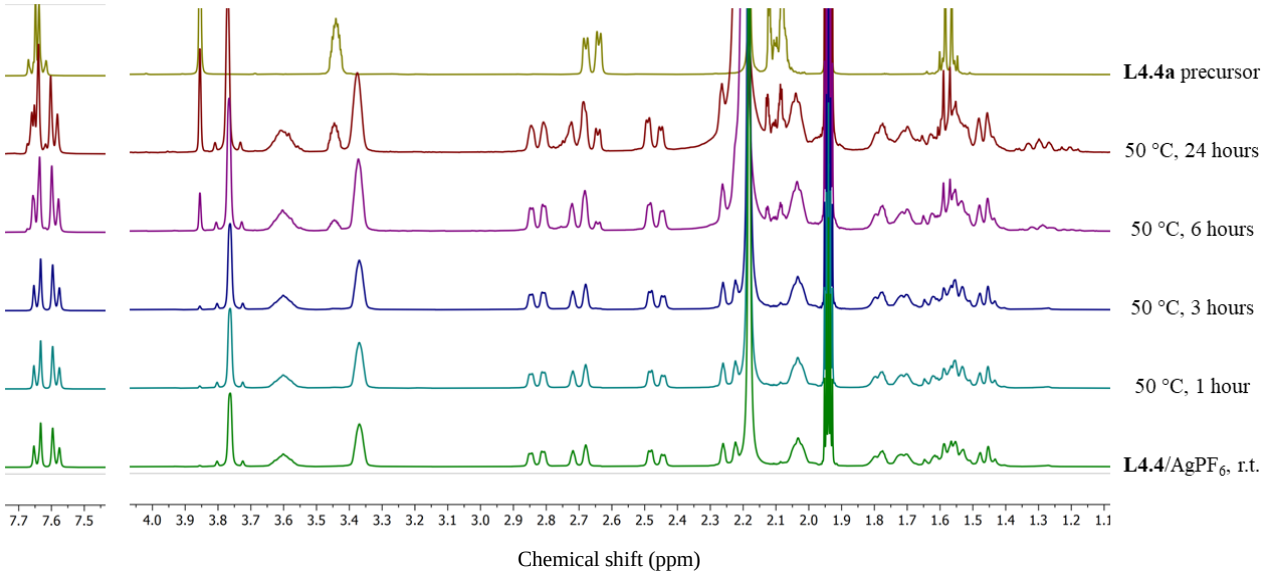

*Figure 4.21. ^{1}H NMR spectra of **L4.4**/$AgPF_6$ self-assembly system (50 °C in CD_3CN)*

Contrary to the triflate anion, BF_4^- and PF_6^- have the tendency to hydrolyse and release fluoride ions,[18] which will contribute to the hydrolysis of the **L4.4** ligands in the two self-assembly solutions. As well as this, in the **L4.4**/$AgPF_6$ and **L4.4**/$AgBF_4$ systems, there is a much larger quantity of water (presumably from the metal salt), evidenced by the large water peak at 2.18 ppm, relative to the smaller and further upfield water peak at 2.15 ppm in the room temperature **L4.4**/AgOTf ^{1}H NMR spectrum. The water signals that are further downfield (*i.e.* the BF_4 and PF_6 systems) suggest a higher pH of the self-assembly solutions, which is aided by the leaching of fluoride ions by BF_4^- and PF_6^- anions, thus likely increasing the rate of ligand hydrolysis in these systems, relative to the OTf system.

4.6.2 M_8L_6 System

L4.3 Systems

As with systems of the $M_{12}L_6$ stoichiometry, **L4.3** was first combined with AgOTf in both 12:6 and 8:6 M:L ratios in CD_3CN and heated to 50 °C to monitor the self-assembly process and determine the thermodynamically stable product. Relative to the difference in the two self-assembly stoichiometries observed in the **L4.4** systems, the difference in this case is much smaller, Figure 4.22.

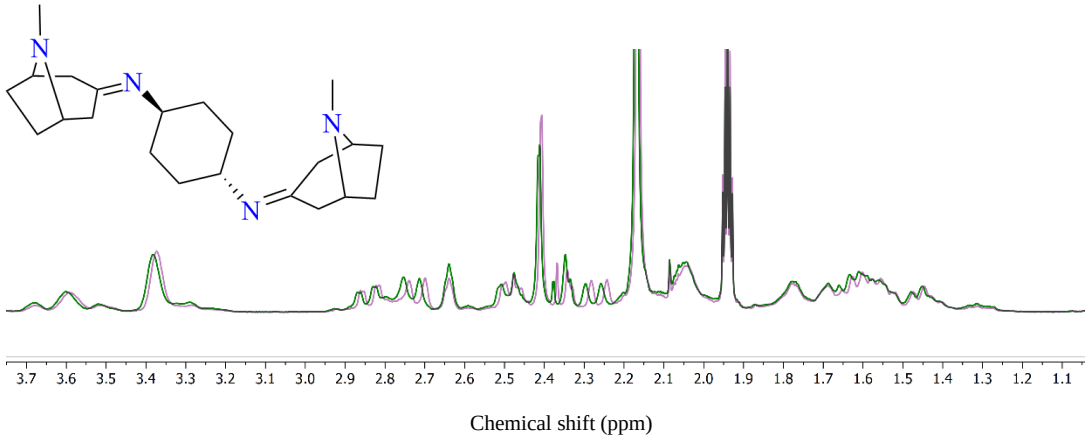

*Figure 4.22.[1]H NMR of the aliphatic region of the 12:6 (green) and 8:6 (purple) M:L stoichiometry in the **L4.3**/AgOTf self-assembly system, with the structure of **L4.3** shown above*

In Figure 4.22, the green spectrum represents the 12:6 M:L stoichiometry, while the purple represents the 8:6 M:L stoichiometry. The signals for the tropinone α-protons and the tertiary tropinone CH protons in this case shift downfield by only *ca*. 0.02 ppm from the 8:6 M:L ratio to the 12:6 M:L ratio, whereas in the **L4.4** system this shift was substantially larger, at *ca*. 0.5 ppm. This much smaller shift suggests that at the 8:6 M:L stoichiometry, the complex is fully formed, resulting in no significant change to the chemical shifts upon addition of more silver(I) into the system. For the purpose of understanding the M_8L_6 system, which is what is observed crystallographically in cage **C4.3**, the 8:6 M:L stoichiometry was the focus of the subsequent solution studies. Similarly to ligands **L4.1** and **L4.4**, the **L4.3** ligand on its own is insoluble in CD_3CN, therefore, any soluble species observable by NMR represent a coordination complex. Again, as

with cage **C4.1**, the ^{1}H NMR spectrum of the **L4.3**/AgOTf self-assembly solution was directly comparable to the ^{1}H NMR spectrum of the redissolved cage **C4.3** (Figure 4.23).

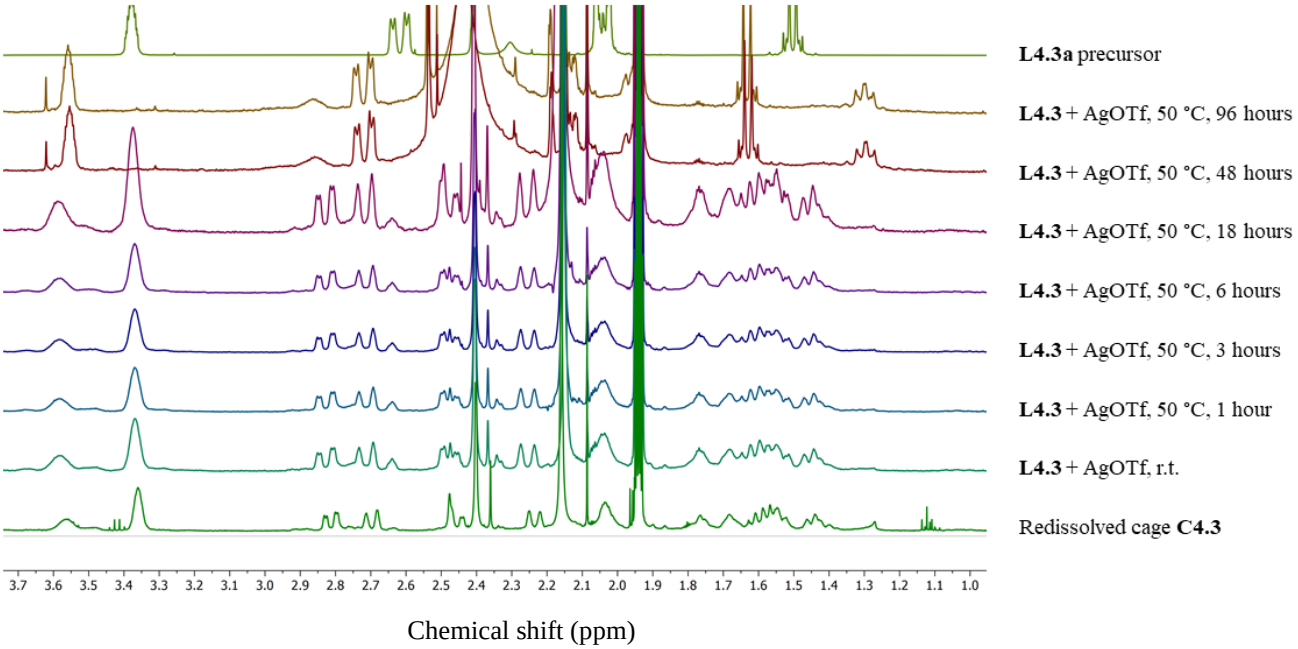

*Figure 4.23. ^{1}H NMR spectra of **L4.3**/AgOTf self-assembly system (50 °C in CD_3CN) compared to redissolved cage **C4.3** (bottom) and **L4.3a** (top)*

As is observed in previously discussed self-assembly systems, the species present at room temperature appear to be the thermodynamically stable material, as the only change to the spectrum occurs upon the onset of ligand decomposition, which for the **L4.3**/AgOTf system is after heating at 50 °C for 48 hours. The ^{1}H NMR spectra of the room temperature self-assembly solution and the redissolved cage **C4.3** appear to be reasonably similar at first glance. The only observable differences in the ^{1}H NMR spectra is the presence of two additional signals in the self-assembly solution that are not present in the spectrum of the redissolved cage, at 2.64 and 2.34 ppm, accompanied by a difference in appearance of the peak at 2.47 ppm, suggesting a difference in symmetry between the complexes present in the two solutions. The additional peaks in the self-assembly solution could also suggest the presence of a second complex, which is in slow exchange with

the first complex, suggested by the relatively well-resolved and narrow additional signals. This difference is much more clearly demonstrated by comparison of the corresponding COSY spectra (Figure 4.24)

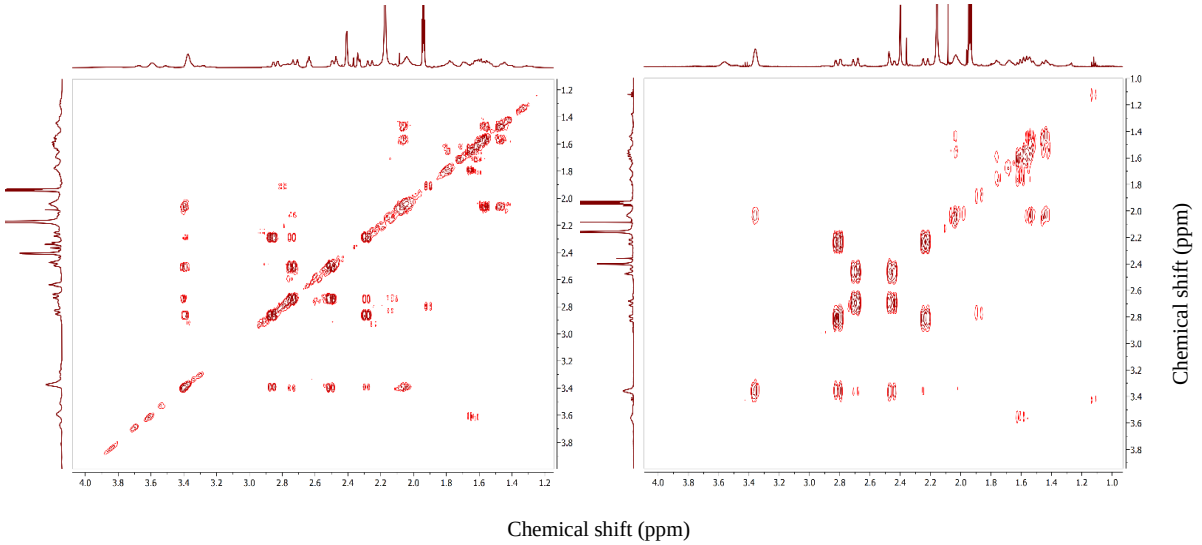

*Figure 4.24. COSY NMR spectra of the **L4.3**/AgOTf self-assembly system at room temperature (left) and redissolved cage **C4.3** (right)*

The significantly larger quantity of cross peaks in the self-assembly solution, relative to only two additional peaks in the one-dimensional ^{1}H NMR spectrum, suggests that there are overlapping signals in the ^{1}H NMR spectrum, *i.e.* if only one complex is present *in-situ*, not all ligand environments are equivalent. For example, the signal at 3.37 ppm in the **L4.3**/AgOTf self-assembly COSY NMR spectrum, which represents the tertiary tropinone CH moiety, is coupling to five other nuclei, which represent the four sets of tropinone α-protons and two of the four tropinone CH_2 protons. In the **C4.3** COSY NMR spectrum on the other hand, the analogous peak is only coupling to one other nucleus, which again corresponds to two of the four tropinone CH_2 protons.

The species present in the self-assembly solution appears to be a singular entity, which is confirmed by one signal in the ^{19}F NMR spectrum and the DOSY NMR spectrum, indicating that the species that forms upon combination of the individual components leads to a complex of lower symmetry, than in the redissolved cage **C4.3**. The redissolved cage **C4.3** and the **L4.3**/AgOTf self-assembly species also have significantly

different diffusion coefficients 9.00×10^{-10} m^2 s^{-1} and 7.09×10^{-10} m^2 s^{-1} which correspond to hydrodynamic radii of 7.08 Å and 8.98 Å for **C4.3** and **L4.3**/AgOTf, respectively (Figure 4.25). As with the $M_{12}L_6$ cage, crystallographically, the M_8L_6 cage is vaguely spherical, in which all axes are relatively similar to one another, and therefore the standard Stokes-Einstein equation (Equation 4.1) was used for all calculations of the hydrodynamic radii of **L4.3**-containing systems.

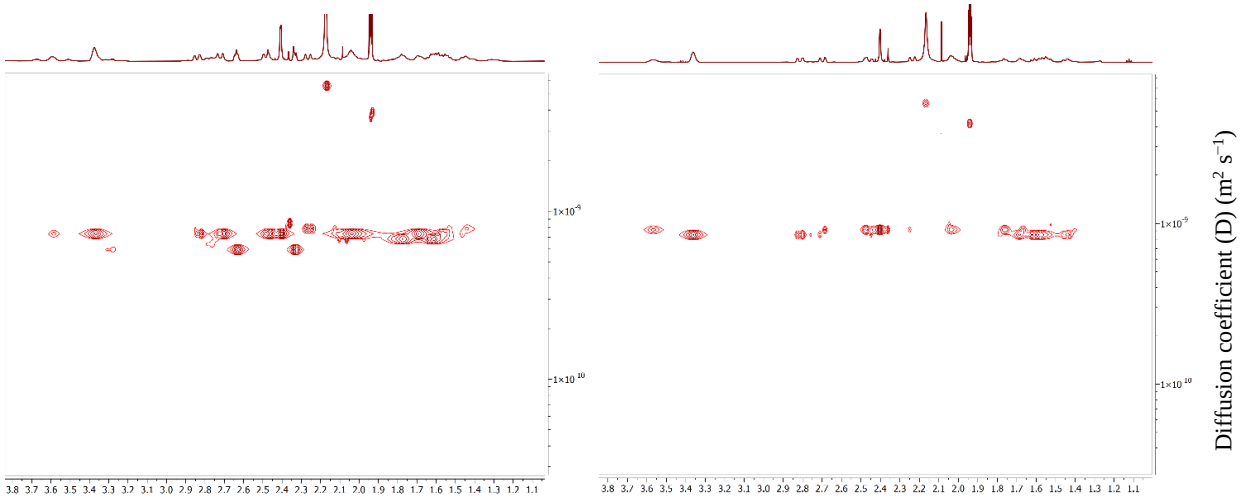

*Figure 4.25. DOSY NMR spectra of the **L4.3**/AgOTf self-assembly system at room temperature (left) and redissolved cage C4.3 (right)*

Interestingly, the lower symmetry of the self-assembly solution is more indicative of what is observed in the solid-state cage **C4.3**, as in the structure, not every **L4.3** ligand molecule is crystallographically (or chemically) equivalent, which would lead to multiple ligand environments in the NMR spectra if the same cage persisted in solution. The COSY NMR spectrum of the **L4.3**/AgOTf self-assembly system is highly suggestive of multiple ligand environments, whose signals overlap with one another, leading to a larger quantity of chemically non-equivalent correlation cross-peaks. This suggests that the self-assembly process is not straightforward to decipher, and is likely strongly affected by the dynamic behaviour of the imine bond *in-situ*, which is evident in the solid-state by observation of the partial displacement of a ligand tropinone moiety at the imine bond by a solvent acetone molecule in **C4.3**.

Despite the absence of crystallographic data, the self-assembly of the **L4.3**/$AgBF_4$ system was also studied for comparison with the **L4.3**/AgOTf system. The system appeared highly symmetric with regard to the ligand environments, perhaps more so than what is observed in the solid-state, as the partial replacement of two of the ligand tropinone moieties with acetone moieties can now no longer occur, possibly leading to a much more symmetric system. The ^{1}H NMR spectra closely resembled that of the redissolved cage **C4.3**, and did not have the additional signals that were present in the **L4.3**/AgOTf self-assembly system.

The species at room temperature was again determined to be the thermodynamically stable species as there are no observable changes to the ^{1}H NMR spectra throughout the heating process, until the onset of ligand decomposition was observed after approximately 24 hours of heating (Figure 4.26).

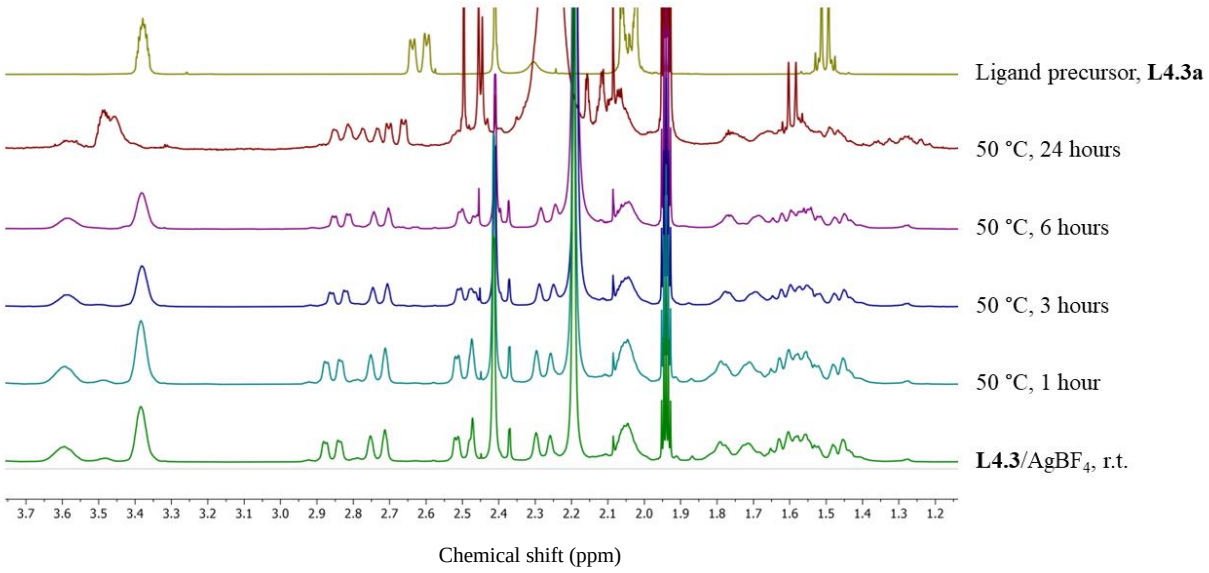

*Figure 4.26. ^{1}H NMR spectra of **L4.3**/$AgBF_4$ self-assembly system (50 °C in CD_3CN) compared to the ligand precursor **L4.3a** (top)*

Again, the appearance of the ligand precursor (tropinone) signals is indicative of imine hydrolysis with peaks appearing at 2.68 ppm (tropinone α-protons) and 3.48 ppm (tertiary tropinone CH moiety). These peaks do not directly align with the ^{1}H NMR signals of tropinone on its own, as each peak is shifted downfield by 0.09 ppm in the self-assembly solutions. This is likely due to the formation of a complex of tropinone with silver(I), as the ligand **L4.3** begins to decompose. As the multiplicity and appearance of each

tropinone peak is very similar to that of tropinone, it was assumed that **L4.3** does decompose upon heating the **L4.3**/$AgBF_4$ system, resulting in tropinone being present in solution.

The ^{19}F NMR and the DOSY NMR both confirmed the presence of only one species and the COSY NMR was very similar to that of the redissolved cage **C4.3**, with much fewer cross-peaks (*i.e.* much fewer unique correlations between nuclei) than in the **L4.3**/AgOTf self-assembly system. The DOSY NMR (Figure 4.27) revealed that the **L4.3**/$AgBF_4$ complex had a diffusion coefficient of 8.79×10^{-10} m^2 s^{-1}, resulting in a hydrodynamic radius of 7.24 Å, which again is much more similar to that of the redissolved cage **C4.3**. This, along with the other **L4.3** hydrodynamic radii, is consistent with solid-state data, as this radius is smaller than what is observed in the **L4.1** and **L4.4** systems, which are assumed to form $M_{12}L_6$ cages *in-situ*.

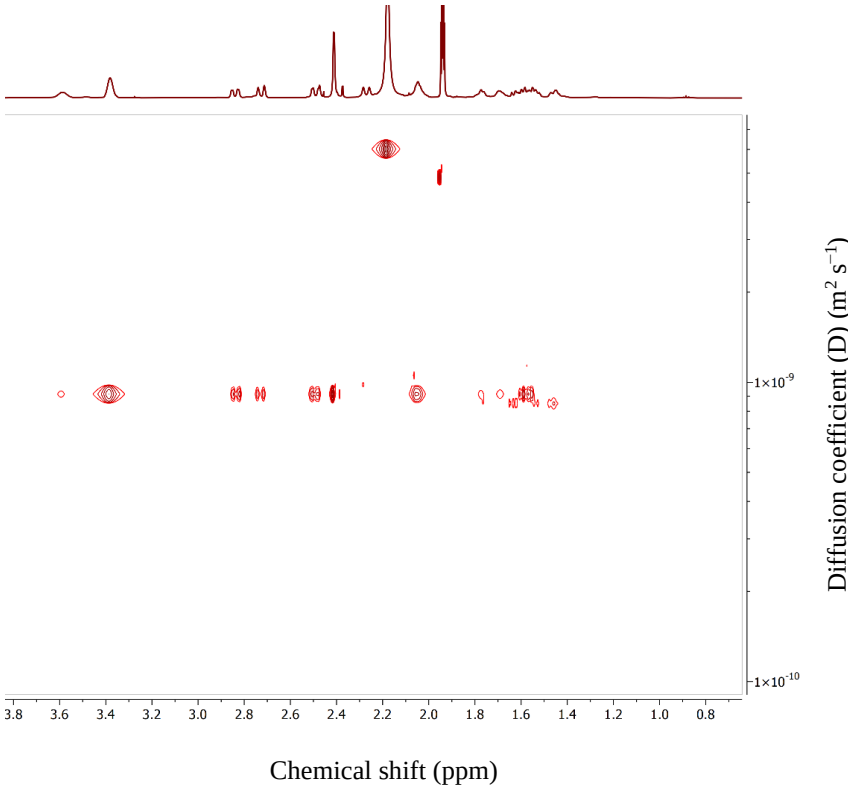

*Figure 4.27. DOSY NMR spectrum of **L4.3**/$AgBF_4$ self-assembly solution at room temperature*

Finally, the **L4.3**/$AgPF_6$ self-assembly species was also investigated. As with all previous systems, the species present at room temperature is the thermodynamically favoured product (Figure 4.28), and again highly suggestive of a very symmetric system in which the ligand molecules are chemically equivalent. This is demonstrated by the COSY NMR (Figure 4.29), which strongly resembles that of the redissolved **C4.3** and **L4.3**/$AgBF_4$ systems. The onset of ligand hydrolysis becomes observable after 24 hours of heating, at which time the majority of the species in the solution is the complex (Figure 4.28).

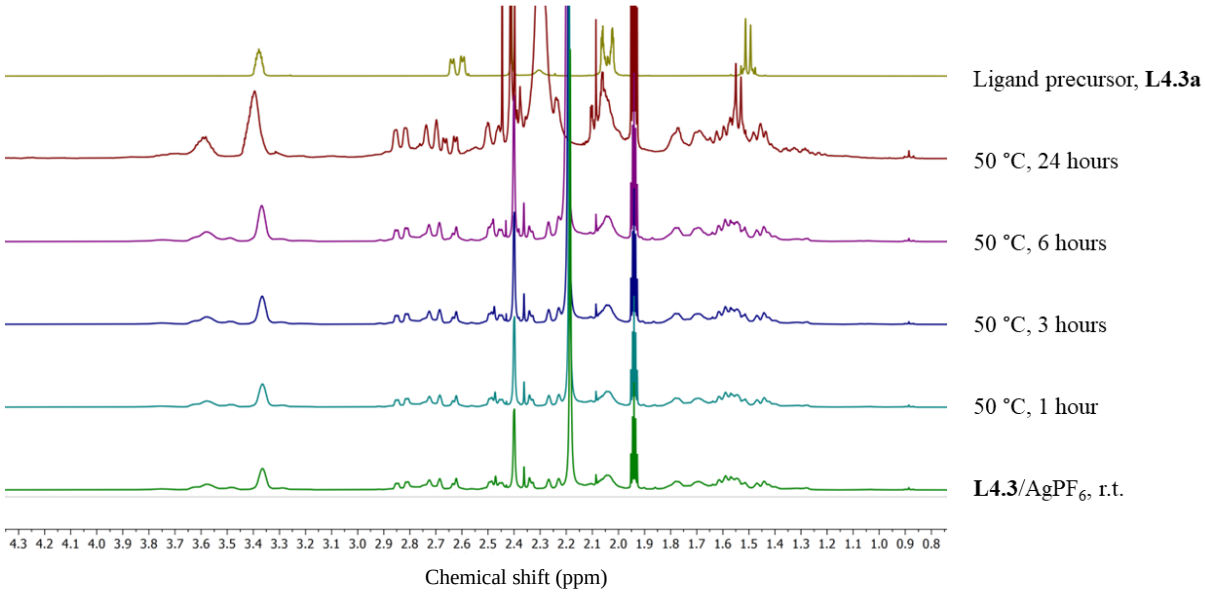

*Figure 4.28. ^1H NMR spectra of **L4.3**/$AgPF_6$ self-assembly system (50 °C in CD_3CN) compared to the ligand precursor **L4.3a** (top)*

All self-assembly solutions containing **L4.3** appear to have very similar thermal behaviours, *i.e.* they are less dependent on the anion or water content than the $M_{12}L_6$ system, however the dependence remains and follows the same trends as in the $M_{12}L_6$ systems. Crystallographically, the triflate anion appears to be less tightly bound in the M_8L_6 cage than in the $M_{12}L_6$ cage, as in the former the anion is much more disordered while in the latter, the anions are reasonably well-ordered despite the larger pore openings of the cage, therefore, it is possible that the M_8L_6 system is much more adaptable, *i.e.* the cage forms around a variety of anions.

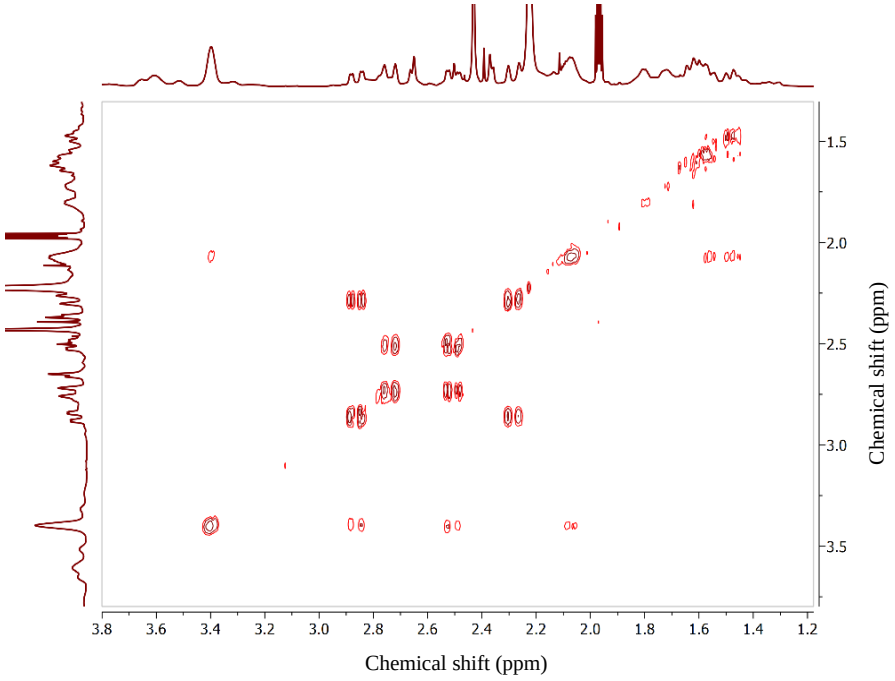

*Figure 4.29. COSY NMR spectrum of the **L4.3**/$AgPF_6$ self-assembly system at room temperature*

A similar phenomenon is observed with the ligand decomposition, in which the signals of tropinone do not have the same shifts as what is seen in the self-assembly decomposition of the ligand, however the multiplicity and appearance of the peaks are equivalent. In the self-assembly system, the peaks are shifted downfield by 0.03 ppm, again demonstrating a deshielding effect due to metal coordination. It is also interesting to note that the ^{1}H NMR spectra of this system closely resemble those of the **L4.3**/$AgBF_4$ system.

4.6.3 Anion Exchange Experiments

Finally, the persistence of each of these cages in solution was investigated, with respect to other anions. It was of interest to observe if the presence of a different anion in a large excess would alter the symmetry of the cage in solution, or if it would result in the formation of a second species, or some other change to its composition. Firstly, the $M_{12}L_6$ system was investigated, and as previously both the ^{1}H and ^{19}F NMR spectra were monitored after each subsequent addition of TBA salts of a variety of anions.

Firstly, equivalents of $TBABF_4$ were added to a solution of the redissolved **C4.1** cage, and despite the large excess of $TBABF_4$, there were no changes observed to the ligand environments in the ^1H NMR spectrum. The only observable change was the appearance and subsequent increase in intensity of the peaks representing the TBA^+ cation in the system. Similarly the ^{19}F NMR did not suggest any anion encapsulation, as only one additional signal for the presence of these anions was observed, instead of two – one for the encapsulated anions and one for the free anions. If this signal was broad, that would signify fast exchange between the free and encapsulated anions in solution, but the peaks are well-resolved and show splitting due to coupling to the ^{11}B nuclei of the BF_4^- anions. The resultant ^1H NMR spectra were compared to that of the **L4.1**/$AgBF_4$ self-assembly system (Figure 4.30), which revealed that the symmetry of the species in solution remains unchanged throughout the titration, but is also very similar to that of the **L4.1**/$AgBF_4$ system, suggesting that the species that forms is consistent and independent of anion choice. This also suggests that there is minimal interaction of the cage with the anions *in-situ*, as there is no difference in chemical shifts of the signals representing the ligand protons.

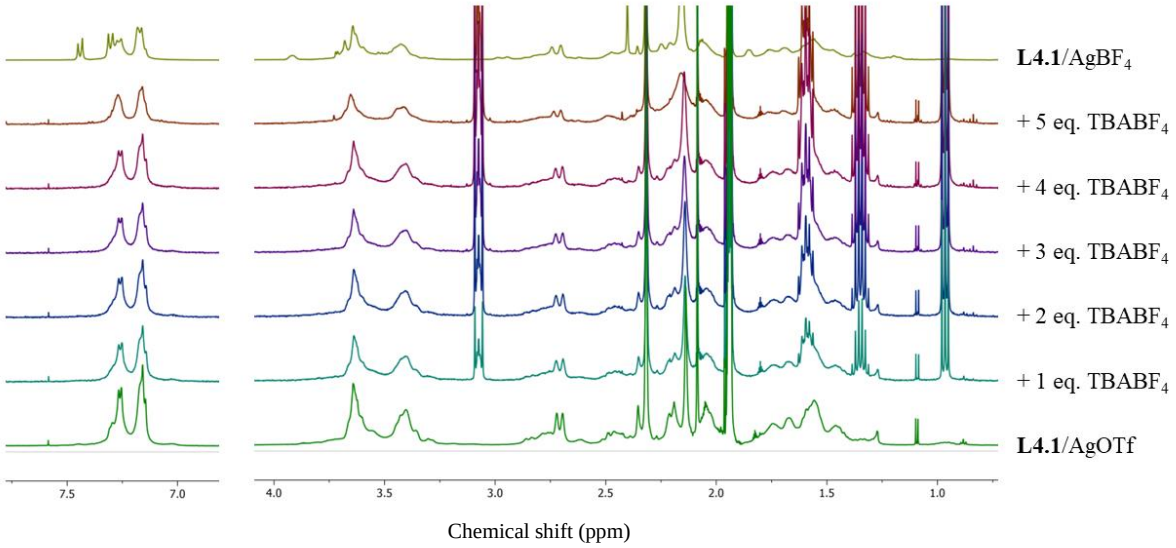

*Figure 4.30. ^{1}H NMR spectra showing the addition of TBABF$_4$ to the **L4.1**/AgOTf self-assembly system compared to the **L4.1**/AgBF$_4$ self-assembly system (top)*

Similar observations were made about the **L4.4**/AgOTf system, where the addition of TBABF$_4$, TBABPh$_4$ and TBAOTs did not have any observable effect on the symmetry of the cages in solution and there were no changes observed other than those arising from the TBA salts themselves. In the **L4.4**/AgOTf + TBABPh$_4$ system (Figure 4.31), there is a slight decrease in intensity of the tetraphenylborate signals in the aromatic region of the ^{1}H NMR spectrum are a result of the precipitation of AgBPh$_4$ when a certain concentration is reached. This also occurs upon combination of AgOTf and TBABPh$_4$, and a precipitate is observed in the NMR tube. Aside from this, there are no observable changes to the symmetry of the complex in solution upon addition of TBABPh$_4$, as is observed with TBABF$_4$ and TBAOTs, suggesting the complex, once formed, is relatively robust and does not form any significant interactions with the anions present in solution, even when they are present in large excess.

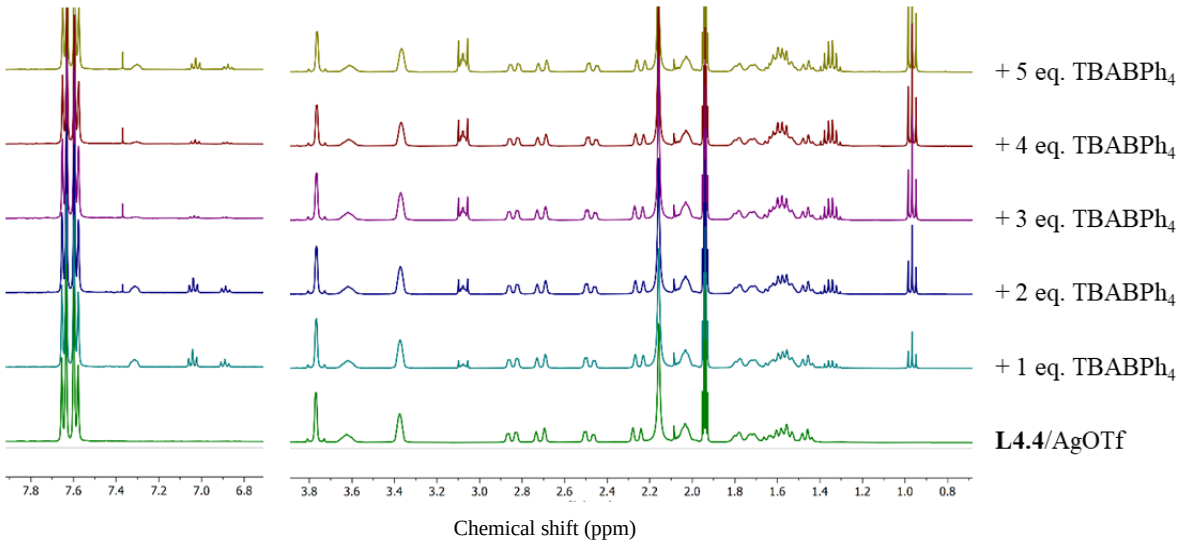

*Figure 4.31. ^{1}H NMR spectra showing the addition of $TBABPh_4$ to the **L4.4**/AgOTf self-assembly system*

As with the $M_{12}L_6$ system, TBA salts of various anions were added into the **L4.3**/AgOTf system to investigate the effect these would have on the complex in solution. Firstly, following the self-assembly studies of **L4.3**/$AgBF_4$, $TBABF_4$ was added into the **L4.3**/AgOTf system, in hopes of transforming the latter, lower symmetry complex into the higher symmetry system observed in the former system *via* self-assembly (Figure 4.32).

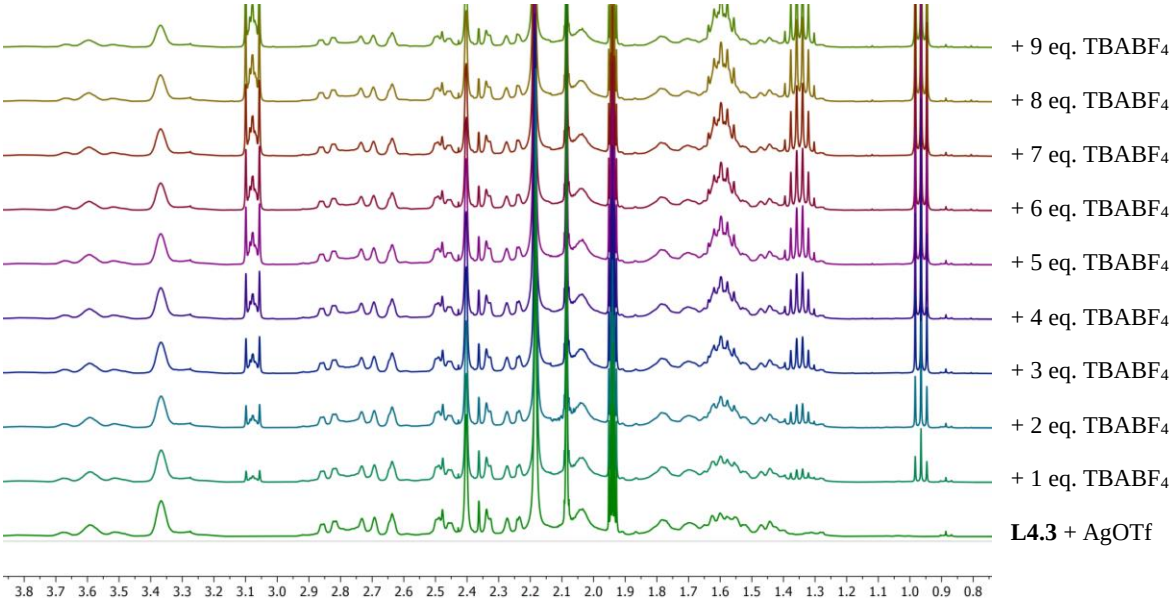

*Figure 4.32. ^{1}H NMR spectra showing the addition of $TBABF_4$ to the **L4.3**/AgOTf self-assembly system*

This would be monitored *via* the two additional peaks in the ^{1}H NMR spectrum observed in the triflate system, that are not present in the BF_4 system or in the redissolved crystals of **C4.3**. This, however, did not occur and the system remained constant, even when $TBABF_4$ was in a large excess (Figure 4.32).

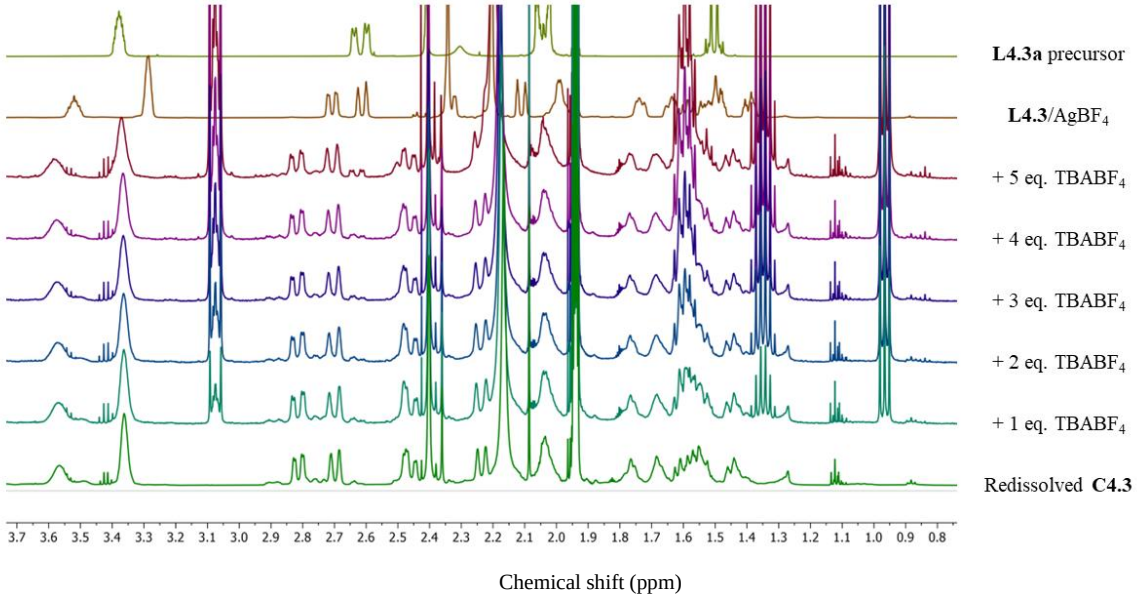

*Figure 4.33. ^{1}H NMR spectra showing the addition of $TBABF_4$ to the redissolved cage **C4.3**, with the **L4.3**/AgBF4 self-assembly system and **L4.3a** precursor for comparison (top)*

For comparison, $TBABF_4$ was also added to the redissolved cage **C4.3**, and in this case, there are some signals that begin to appear that do not correspond perfectly with the signals present in the **L4.3**/$AgBF_4$ self-assembly system. (Figure 4.33). The first of these signals is the signal representing a set of tropinone α-protons at 2.63 ppm, whereas the closest α-proton to that in the **L4.3**/$AgBF_4$ system is at 2.61 ppm. There is also a shoulder that begins to appear at 3.39 ppm, which is visible after five additions of $TBABF_4$, that again does not correspond to what is observed in the **L4.3**/$AgBF_4$ self-assembly system. Upon closer inspection, the two aforementioned changes to the ^{1}H NMR spectrum correspond with the signals of the ligand precursor **L4.3a**, suggesting possible ligand hydrolysis. This is consistent with the theory of fluoride ion leaching by the BF_4^-, which is theorised to be a contributing factor to the ligand decomposition after heating in the BF_4-containing self-assembly systems discussed previously. As this does not occur in the **L4.3**/AgOTf + $TBABF_4$ system, this may suggest that the increased symmetry of **C4.3**, relative to the complex that forms *in-situ* from **L4.3**/AgOTf may make it more vulnerable to hydrolysis. The addition of TBAOTs and $TBABPh_4$ to the **L4.3**/AgOTf system yielded similar results to $TBABF_4$ (*i.e.* no change to the

symmetry of the core cage) suggesting once the core itself has formed, it is difficult to alter it (or its symmetry), which is similar to what is observed with the $M_{12}L_6$ systems.

4.7 Discussion

The comparison of the self-assembly solutions of 12:6 and 8:6 M:L stoichiometries suggested that the aryl ligands **L4.1** and **L4.4**, preferably form an $M_{12}L_6$ complex *in-situ*, rather than also forming an M_8L_6 complex. A larger difference in chemical shifts between the spectra of the two stoichiometries is reflective of what is observed in the initial titration experiments, *i.e.* when the desired M:L ratio reached by the system, the titration curve begins to taper, resulting in smaller overall changes in chemical shifts after each subsequent addition of metal. These changes are larger, however, when a desired stoichiometry is not achieved *i.e.* when the M:L ratio in solution is 8:6, however the complex that is forming *in-situ* is of the 12:6 M:L stoichiometry. At the 8:6 M:L ratio in solution, the formed 12:6 complex is in equilibrium with the free ligand in solution resulting in an average signal that is further upfield from the complex itself. The free ligand molecules then coordinate upon further addition of metal into the system, forming more of the $M_{12}L_6$ complex, resulting in a decrease in free ligand in solution, until all ligands are coordinating. The opposite is true for when the complex that forms is of the 8:6 M:L stoichiometry, resulting in a much smaller observed change in chemical shifts between the two stoichiometries, as at the 8:6 M:L solution stoichiometry, the desired ratio has been achieved for the formation of the complex, and addition of any additional metal into the system, will have a much smaller relative effect on the ligand chemical shifts.

The hydrodynamic radii of the cages that formed in the self-assembly solution, and the crystallographic radii of the discrete solid-state cages **C4.1** and **C4.2** are summarised in Table 4.1.

Table 4.1. Summary of the DOSY and SCXRD radii of the $M_{12}L_6$ and M_8L_6 complexes discussed in this chapter

	DOSY radius (Å)	**SCXRD radius (Å)**
$M_{12}L_6$ stoichiometry		
Cage C4.1	n/a	7.59
L4.4/AgOTf	7.99	n/a
M_8L_6 stoichiometry		
Cage C4.3	7.08	6.11
L4.3/AgOTf	8.98	n/a
L4.3/$AgBF_4$	7.24	n/a

With the exception of the **L4.3**/AgOTf self-assembly system, the trends observed in the hydrodynamic radii of the $M_{12}L_6$ and M_8L_6 follow the same trends as is observed crystallographically, *i.e.* the complexes forming from the aryl ligands have a larger radius than those forming from **L4.3**. This could be due to some coordination or short contacts of the triflate anions with the silver(I) ions in the complex, contributing to both the lower symmetry (shown by the corresponding COSY NMR spectra) and the apparent larger radius. This coordination of triflate could distort the shape of the complex further from the roughly spherical shape that is observed in the solid-state, which could result in a decrease in efficacy of the idealized Stokes-Einstein equation (Equation 4.1), which could yield a falsely large hydrodynamic radius. This is not observed in the redissolved cage **C4.3**, as the concentration of the cage in solution is much lower than the concentration of the individual components in the self-assembly solution, and this coordination of triflate is likely encountered much less frequently.

It is important to note that even in the presence of an excess amount of AgOTf in the **L4.3**/AgOTf system, the changes in chemical shifts in the ^{1}H NMR spectra are negligible, as the M:L ratio in solution approaches 12:6, and does not result in the formation of a new 12:6 M:L complex. The opposite is true for the transformation of cage **C4.2** to **C4.2a**. This transformation in the presence of water, again highlights the solvent-dependency of the system. However, it also highlights that despite the ability of the system to leach silver(I) ions out of the polymeric $M_{15}L_6$ species, the aryl ligand still has a strong preference towards an

$M_{12}L_6$ cage, despite the possibility of forming an M_8L_6 complex, suggesting the role of the aromatic ligand component is central to the formation of the subsequent cages.

In order to better understand the effect of the aryl components on the cage formation, leading to the difference in cage radii between ligands **L4.1**, **L4.2(a)** and **L4.4**, versus **L4.3**, it is important to closely inspect the conformation of the common part of the ligands, *i.e.* the cyclohexyl-bridged tropinone units. An overlay of the ligand molecules in the $M_{12}L_6$ cage **C4.1** and the M_8L_6 cage **C4.3** is shown in Figure 4.34.

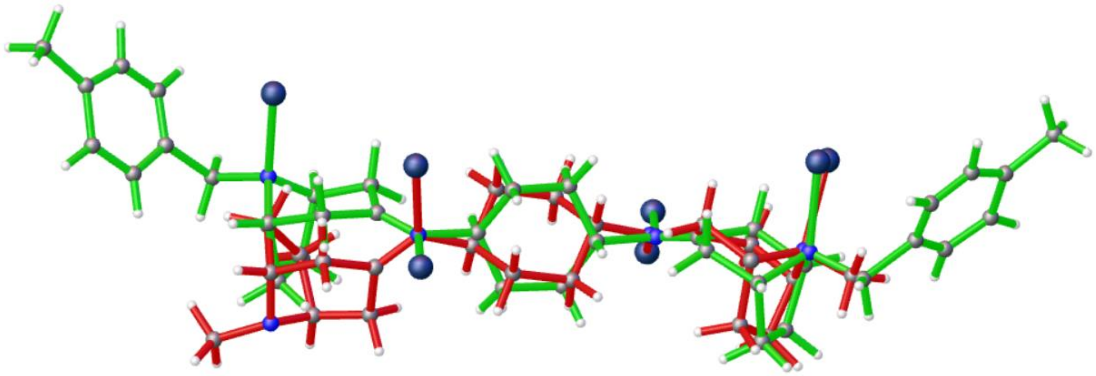

*Figure 4.34. Overlay of ligand molecules **L4.1** in cage **C4.1** (green) and **L4.3** in cage **C4.3** (red), using the three common coordinating nitrogen atoms as anchor points)*

In Figure 4.34, the ligand shown in green is the **L4.1** ligand from cage **C4.1** and the ligand shown in red is the **L4.3** ligand from cage **C4.3**. The components of the ligand molecules that are adjacent to coordinating nitrogen atoms are relatively similar in their conformations, with reasonable overlap between the ligand backbones, however, with significant difference in the orientation of the associated silver(I) ions. The tropinone unit of **L4.3** in which the tropinone amine nitrogen atom is not coordinating, differs significantly in its orientation to the corresponding coordinating *N*-substituted tropinone of **L4.1**. As not every amine nitrogen atom in **L4.3** is coordinating, the most informative torsion angles for comparison is the Ag-N(imine)-N(imine)-Ag torsion angle and an Ag-N(amine)-N(imine)-Ag torsion angle, both of which are summarised in Table 4.2.

*Table 4.2. Summary of relevant torsion angles in cages **C4.1** and **C4.3***

	Ag-N(imine)-N(imine)-Ag	**Ag-N(amine)-N(imine)-Ag**
Cage C4.1	175.249(4)°	81.4(5)°
Cage C4.3	148.0(4)°	96.2(4)°

The torsion angles involving the two different types of ligand nitrogen atoms are relatively similar, implying that the coordination modes of the coordinating nitrogen atoms are relatively similar between the two cage types. However, the torsion angles involving only the ligand imine nitrogen atoms differ significantly. The **L4.3** ligand molecule in cage **C4.3** appear to have a much more twisted motif, relative to cage **C4.1**, likely attributed to the significant reduction in steric bulk surrounding the amine nitrogen atoms. This in turn, results in a smaller sized cage, as the large aryl group at the amine moiety no longer needs to be accommodated for in the formation of the cage. This is also true for the remaining aryl $M_{12}L_6$ cages **C4.2** and **C4.2a**.

The cages consistently form at room temperature, at which they appear to be the thermodynamically stable product. Each of the complexes is prone to hydrolysis after a period of heating, and in each case this occurs *via* hydrolysis of the ligand at the imine functionality, yielding the ligand precursors, **L4.Xa**. This hydrolysis appears to occur more rapidly in self-assembly systems containing BF_4^- and PF_6^- anions, which hydrolyse to generate fluoride ions, which promote the hydrolysis of the ligands within the complexes. Perhaps unsurprisingly, the cages are also sensitive to the harsh conditions of electrospray mass spectrometry analysis, due to the particularly labile silver(I)-nitrogen coordination bonds and the sensitivity of the ligand imine bond to hydrolysis, and therefore only very small ML and M_2L fragments were observed in the respective spectra. The transformation of the cage **C4.2** to cage **C4.2a** highlights the lability of the silver(I) ion to nitrile nitrogen atom coordination bond, relative to the other silver(I) ion to nitrogen bonds, which in turn, highlights the robustness of the $M_{12}L_6$ cage itself. The more sterically encumbered imine and amine nitrogen atoms are surrounded by bulky aliphatic components (in the form of the bicyclic tropinone core

and the cyclohexyl moiety), which are possibly protecting the coordination bonds from the approach and subsequent hydrolysis by water. The formation of theses cages is highly sensitive to solvent choice, as demonstrated by the titration experiments. Indeed, in one crystallisation attempt using **L4.3** with silver hexafluoroantimonate which was left to crystallise in methanol for several weeks, we observed crystallisation of a silver(I) coordination polymer of *trans*-1,4-diaminocyclohexane, of an equivalent structure to that described by Braga *et. al.*[19] This observation confirms that complete hydrolysis of both imine bonds eventually occurs in these reaction solutions.

The cages appear to be much less sensitive to the presence of a variety of anions, as their symmetry remained unchanged throughout the titration experiments, with the only instances of anion sensitivity being observed in systems containing BF_4^- and PF_6^- anions, which could arise from the hydrolysis of these anions *in-situ*, generating species (such as fluoride ions) that could accelerate the hydrolysis of the ligands. The guests that have been introduced into these systems have thus far been limited to small, charged anions. As the interior surface chemistry of the cages could be reasonably non-polar due to the high degree of aliphatic character, small organic guests such as toluene or xylene could be more appropriate guests for future titration experiments. Alternatively, partially fluorinated analogues of those molecules could form favourable interactions with the walls of the cages, due to the formation of an increased overall dipole in the molecules, relative to the non-fluorinated analogues, but not as polar as anions such as triflate.

Beyond the library of ligands presented in this chapter, it would be of interest to expand the ligands to incorporate a bridging component different to cyclohexane, or perhaps introduce a significantly different *N*-tropinone substituent, to observe the effect of this on the subsequent complexes. Copper(I) is a soft acid metal ion that also pairs well with soft bases and *N*-donor ligands. This metal ion, similarly to silver(I), has a $[Ar]3d^{10}$ electron configuration, and therefore an absence of LFSE, which could result in similar coordination geometries in the subsequent complexes, which due to its improved stability could lead to the observation of these complexes in the mass spectra, to definitively confirm their presence *in-situ*.

4.8 References

1. T. K. Ronson, J. P. Carpenter and J. R. Nitschke, *Chem*, 2022, **8**, 557–568.

2. L. K. Macreadie, O. T. Qazvini and R. Babarao, *ACS. Appl. Mater. Interfaces*, 2021, **13**, 30885 – 30890.

3. K. B. Idrees, Z. Chen, X. Zhang, M. R. Mian, R. J. Drout, T. Islamoglu and O. K. Farha, *Chem. Mater.*, 2020, **32**, 3776 – 3782.

4. C. Cruickshank, *Proceedings of the Royal Society of London. Series A, Containing Papers of a Mathematical and Physical Character*, 1924, **106**, 724–749.

5. L. Avram and Y. Cohen, *Chem. Soc. Rev.*, 2014, **44**, 586–602.

6. Z. Qi, T. Heinrich, S. Moorthy and C. A. Schalley, *Chem. Soc. Rev*, 2015, **44**, 515 – 531.

7. A. J. McConnell, *Chem. Soc. Rev.*, 2022, **51**, 2957 – 2971.

8. E. W. Dean and D. D. Stark, *Ind Eng Chem*, 1920, **12**, 486–490.

9. R. D. Shannon, *Acta Crystallogr. A*, 1976, **32**, 751 – 767.

10. J. Singh, D. H. Kim, E. H. Kim, N. Singh, H. Kim, R. Hadiputra, J. Jung and K. W. Chi, *Chem. Commun.*, 2019, **55**, 6866–6869.

11. L. Yang, D. R. Powell and R. P. Houser, *Dalton Trans.*, 2007, 955 – 964.

12. H. Furukawa, F. Gándara, Y. B. Zhang, J. Jiang, W. L. Queen, M. R. Hudson and O. M. Yaghi, *J. Am. Chem. Soc.*, 2014, **136**, 4369–4381.

13. T. Harada, T. Sato and R. Kuroda, *Chem. Phys. Lett.*, 2005, **413**, 445–449.

14. A. K. Bain, in *Crystal Optics: Properties and Applications*, ed. A. K. Bain, Wiley VCH, Germany, 1st. edn, 2019, vol. 1, ch. 1, pp. 1 – 26.

15. M. Hochgürtel, R. Biesinger, H. Kroth, D. Piecha, M. W. Hofmann, S. Krause, O. Schaaf, C. Nicolau and A. V. Eliseev, *J. Med. Chem.*, 2003, **46**, 356–358.

16. P. T. Corbett, J. Leclaire, L. Vial, K. R. West, J. L. Wietor, J. K. M. Sanders and S. Otto, *Chem. Rev.*, 2006, **106**, 3652–3711.

17. H. W. Quinn, J. S. McIntyre and D. J. Peterson, *Proceedings of the 8th International Conference on Coordination Chemistry*, 1964, 221 – 223.

18. M. G. Freire, C. M. S. S. Neves, I. M. Marrucho, J. A. P. Coutinho and A. M. Fernandes, *J. Phys. Chem. A*, 2009, **114**, 3744–3749.

19. D. Braga, M. Curzi, F. Grepioni and M. Polito, *Chem. Commun.*, 2005, 2915–2917.

Chapter 5

· Complexes of Fecht's Acid ·

5.1 Introduction

Following the analysis of interactions present in coordination materials of amine-containing ligands, discussed in earlier chapters, it is evident that a large proportion of weak interactions and hydrogen bonding in those complexes involve the CH_2 moieties that are adjacent to an amine functionality. As these CH_2 moieties are polarised, they are much more likely to form weak interactions and hydrogen bond to one another as well as to water and solvent molecules. Fecht's acid, a spirocyclic aliphatic molecule, is presented here as a ditopic linear dicarboxylate ligand (Figure 5.1). The molecule contains no amine or other nitrogen atoms, which in theory will reduce the occurrence of strong interactions between adjacent networks and solvent molecules, and will serve as an interesting comparison to the ligands discussed thus far, which all contain an amine functionality.

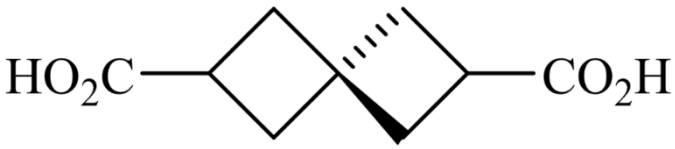

*Figure 5.1. Structure of spiro[3.3]heptane-2,6-dicarboxylic acid (**H_2L5.1**)*

The properties of spirocyclic aliphatic molecules have been well-documented, and their rigidity alongside their diverse geometries has been utilised in the discovery of new materials, such as drug molecules,[1] catalyst ligands,[2] and polymers.[3,4] Their rigidity is a result of a higher ring inversion or bond rotation energy barrier, due to two rings originating at one spiro carbon atom. Due to the steric bulk surrounding the spiro carbon atom, there is significant distortion from a perfect tetrahedral geometry, resulting in any further distortion being too energetically unfavourable. Four-membered rings in spirocyclic components incorporate an added degree of rigidity due to the already sterically strained nature of cyclobutane or other four-membered rings such as oxetanes, azetidines and thietanes.[5] A small number of spirocyclic ligands have previously been used as ligands in coordination materials, such as some spirocyclic diaminocarbenes in tungsten(0) complexes, reported by Hahn *et. al.*[6] Redox-active discrete coordination complexes containing a spirocyclic ligand have also been reported by Boskovic *et. al.* in which the distribution of electrons occurs between two metal centres *via* a conjugated spirocyclic bridge.[7]

No polymeric coordination materials (and therefore MOFs) have been reported to contain a spirocyclic component in the coordinating ligands. However, porous organic polymers incorporating a spirocyclic moiety have been shown to demonstrate excellent thermal stability and high surface areas.[8,9] As in medicinal chemistry, catalysis and polymer science, the use of these ligands in MOFs can impart similar advantages. Rigidity, as discussed in the context of fused-ring aliphatic ligands in previous chapters, can ensure permanent porosity in MOFs, resulting in an improved capacity for guest interactions. The non-planar nature results in geometries that can improve selectivity towards guest interactions,[10] as in catalysis. Finally, the aliphatic nature can result in a novel pore surface chemistry, which can again offer interesting guest interactions.

Spiro[3.3]heptane-2,6-dicarboxylic acid (**H_2L5.1**), more commonly known as Fecht's acid, was first synthesised in 1907 by Fecht,[11] and is shown in Figure 5.1. The structure consists of two cyclobutane rings, originating at the same tetrahedral spiro carbon atom, with two carboxylic acid moieties at the 2 and 6 positions of the spiro[3.3]heptane core. This molecule possesses rigidity comparable to its aromatic

counterparts arising from the high degree of ring strain in the two cyclobutane rings originating at one quaternary spiro carbon atom. Due to its size and orientation of the coordinating carboxylate groups, it is quite similar to a commercially available aromatic dicarboxylic acid ligand – terephthalic acid (benzene-1,4-dicarboxylic acid, **BDC**). Fecht's acid has an approximately 20% longer carbonyl-to-carbonyl carbon distance, relative to terephthalic acid, with the distance being *ca.* 6.9 Å in **L5.1** and *ca.* 5.8 Å in **BDC**. Thus, the coordination complexes obtained from Fecht's acid are nicely comparable to those of terephthalic acid, and the effects of replacing an aromatic component with a similarly sized rigid aliphatic component, are clearly identifiable. The results from this chapter were accepted for publication in November 2021.[12]

5.2 Ligand Synthesis

There are multiple approaches to the synthesis of spirocyclic compounds that have each been used extensively in literature, as many natural products contain a spirocyclic moiety. Examples of these include the antifungal drug griseofulvin, fungus-derived fumagillin, which has antiparasitic properties and Cleroindicin A from the *Clerodendrum japonicum* fungus (the structures of which are shown in Figure 5.2).[13]

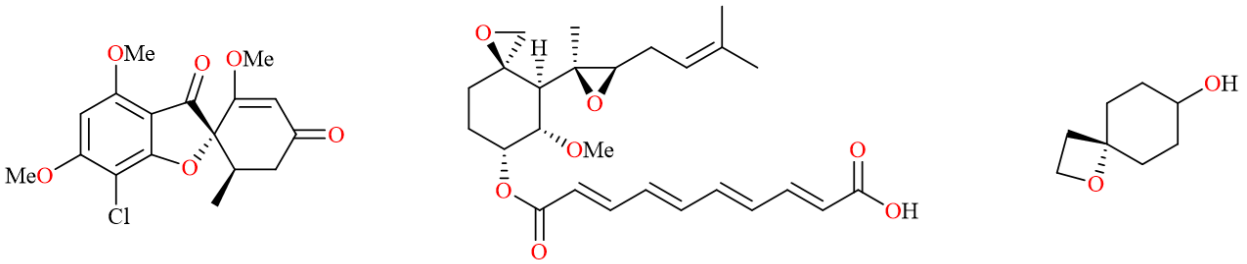

Figure 5.2. (left to right) Structures of griseofulvin, fumagillin and Cleroindicin A

The common synthetic approaches to making spirocycles are outlined in Figure 5.3, and tend to fall into one of six categories – alkylation, metal-catalysed synthesis, ring-closure methods, cycloaddition reactions, radical reactions and rearrangement approaches.[14]

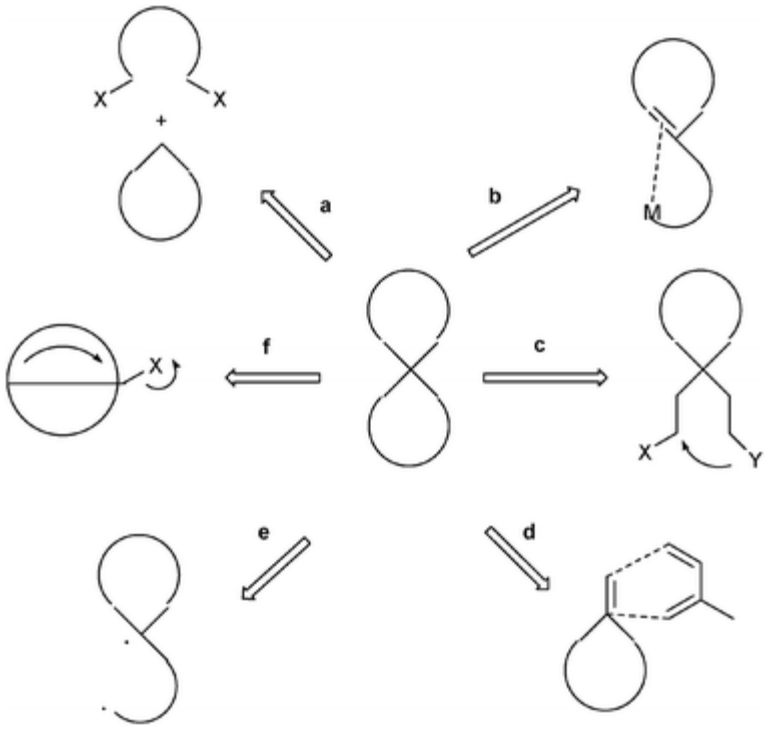

Figure 5.3. Common methods of synthesis of spirocyclic molecules, (a) alkylation, (b) metal-catalysed synthesis, (c) ring-closure methods, (d) cycloaddition reactions, (e) radical reactions and (f) rearrangement approaches[14]

The synthesis of Fecht's acid proceeds *via* an alkylation reaction, which is not among the common methods summarised by Rios, as this synthesis does not begin with a cyclic precursor.[14] This is likely due to the symmetry of Fecht's acid, *i.e.* the two rings on the spiro carbon atom are the same, whereas typically (as highlighted by the examples in Figure 5.2) it is desirable to have two different rings on the shared spiro atom. The synthetic procedure of Fecht's acid, **H_2L5.1**, is outlined in Scheme 5.1.

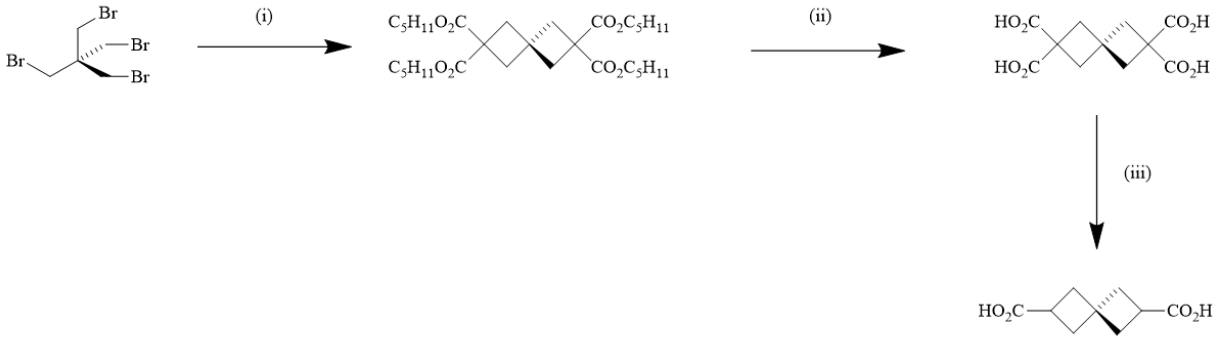

Scheme 5.1. Synthesis of ***H_2L5.1****, (i) diethyl malonate, Na(s), n-pentanol, (ii) KOH, EtOH, (iii) HCl(aq), Δ, H_2O*

The transformation of pentaerythritol tetrabromide to the tetraester of Fecht's acid was carried out *via* a metathesis reaction with diethyl malonate in the presence of sodium metal (forming NaBr) in 1-pentanol. An azeotropic distillation under N_2 was carried out to remove the solvent. The ester moieties were then hydrolysed under basic conditions, to form the tetracarboxylic acid. Finally, gradually heating the tetracarboxylic acid to 215 °C, resulted in a decarboxylation at both the 2 and 6 positions to give the racemic mixture of both enantiomers of Fecht's acid. It is the final double decarboxylation step (iii) in Scheme 5.1, which produces a racemic mixture of the final product, **H_2L5.1**.

Considering the tetrahedral geometry of each of the non-spiro quaternary carbon atoms, the face at which the decarboxylation occurs is important, leading to four possible combinations of decarboxylations from the precursor, as outlined in Figure 5.4. The four possible combinations of decarboxylations results in a set of four products which are related by either a rotation (resulting in equivalent molecules) or a mirror plane – which results in two possible enantiomers. These arise from the newly established axial chirality within the molecule, when considering the relationship between the two carboxylic acid moieties.

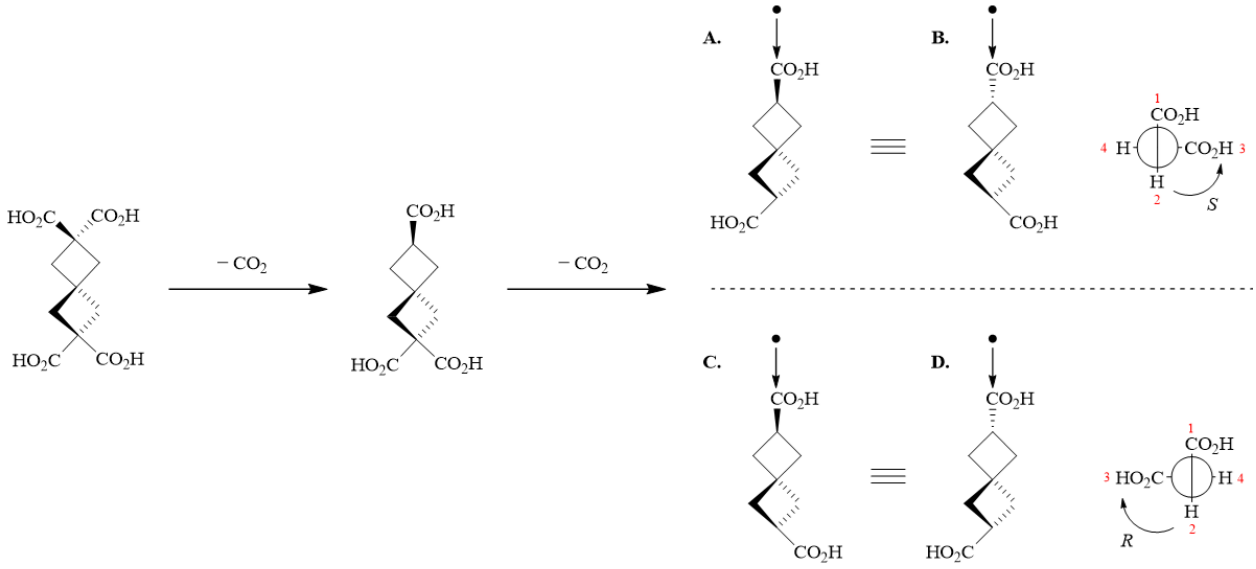

Figure 5.4. Description of the double decarboxylation step in the synthesis of ***H₂L5.1****, with the four possible combinations of decarboxylations leading to two enantiomers. A & B, and C & D are equivalent and related to one another by a rotation. A & D and B & C are enantiomers which are related to one another by reflection in the plane of the page and A & C and B & D are enantiomers by reflection perpendicular to the page. A & B are the (S)-enantiomer and B & C are the (R)-enantiomer.*

Following a screening process of a range of transition metal and lanthanide ion salts, coligands and synthetic conditions, two coordination polymers of Fecht's acid have been synthesised (and will be discussed further in Sections 5.3 and 5.4), which both involve the racemate in their respective syntheses. The separation of two enantiomers is a difficult process, however, there have been approaches proposed to achieve enantiomerically pure spirocyclic compounds in literature, mostly *via* catalysis.[15,16] The *R* and *S* enantiomers of Fecht's acid have been successfully separated (achieving 90% e.e.) by Backer and Schurink in 1931, by co-crystallisation with a chiral amine – brucine.[17] Later, the preparation of each enantiomer was shown to be achievable with higher enantiomeric purity using chiral HPLC separation of dicinnamyl spiro[3.3]heptane-2,6-dicarboxylate.[18] Future work involving this ligand could explore the separation of the two enantiomers or selective synthesis of one enantiomer, and the effect of using a single enantiomer in the synthesis of coordination complexes.

Though beyond the scope of this project, **H_2L5.1**, when dissolved in MeOH at 40 μM, is optically transparent in the 235 – 800 nm range, which further widens the scope for applications of these MOFs in the isolation of photophysically-active guests.

5.3 *Poly*-[Yb_6(L5.1)$_9$(DMF)$_2$]·0.5DMF·2.5H_2O, Complex 5.1

The combination of **H_2L5.1** with ytterbium(III) chloride hexahydrate in DMF and water at 100 °C yielded colourless rod-shaped crystals of *poly*-[Yb_6(**L5.1**)$_9$(DMF)$_2$]·0.5DMF·2.5H_2O, complex **5.1**. The structure of this complex (shown in Figure 5.10) was revealed to be a three-dimensional coordination polymer. The structure was solved and refined in the monoclinic space group $P2_1/n$. The asymmetric unit (shown in Figure 5.5) consists of three unique ytterbium(III) ions, with two complete **L5.1** molecules and five halves of **L5.1** molecules, in which the remainder of the ligand molecules are generated by an inversion, resulting in the two enantiomers of **L5.1** being superimposed onto one another. In the case of the five half ligand molecules in the asymmetric unit, it is the spiro carbon atom that lies on the crystallographic inversion centre.

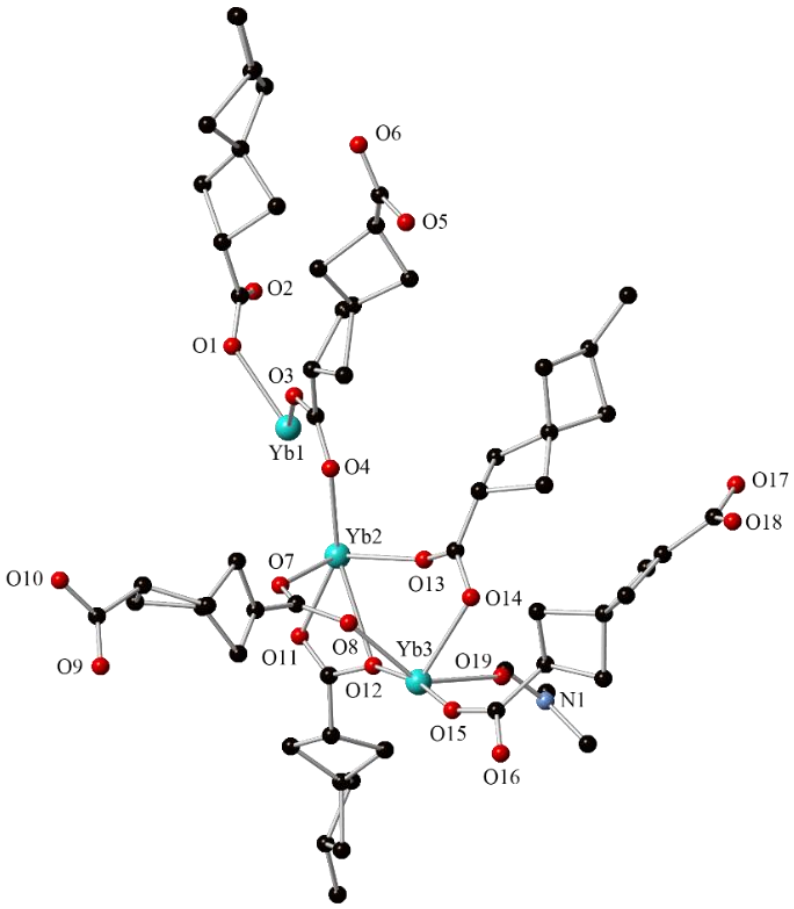

*Figure 5.5. Asymmetric unit of poly-[Yb_6(**L5.1**)$_9$(DMF)$_2$]·0.5DMF·2.5H_2O (complex **5.1**), with hydrogen atoms and disorder omitted for clarity*

This results in the two ligand enantiomers being superimposed onto one another between two metal ions, which leads to significant disorder (Figure 5.6). The representation in Figure 5.5, highlights one conformation of **L5.1** (out of the possible two), which demonstrates the superimposed half of one **L5.1** molecule as the other half of one conformation of the ligand occupying that space.

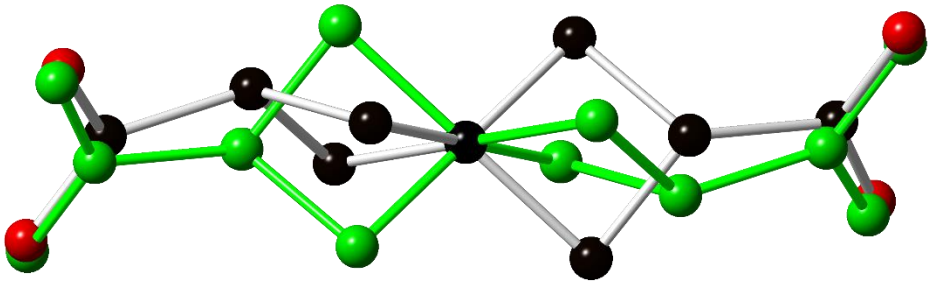

*Figure 5.6. Disorder mode of **L5.1** ligand observed in complexes **5.1** and **5.2**, with the spiro carbon atom at the same position for both ligand conformations, with hydrogen atoms omitted for clarity*

Examination of the crystal structure of complex **5.1** reveals the extent of the ring strain in the ligand molecules. The structure of one of the ligand molecules is shown in Figure 5.7. It is the bond angles surrounding the spiro carbon, C4, that are most informative, and are outlined in Table 5.1.

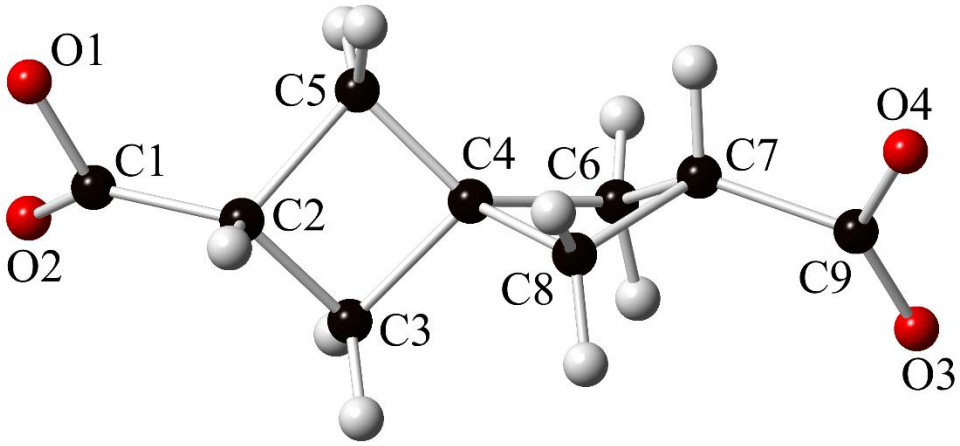

*Figure 5.7. Structure of **L5.1**, taken from complex **5.1***

.

*Table 5.1. Bond angles surrounding the spiro carbon (C4) in **L5.1***

Bond angle	Value
C3-C4-C8	118(3)°
C5-C4-C6	124(2)°
C5-C4-C8	116(2)°
C6-C4-C3	127(2)°
C5-C4-C3	86.1(19)°
C6-C4-C8	89(2)°

The angles all stray significantly from the expected 109.5° of a tetrahedral sp^3 carbon atom, and this is due to the cyclobutane rings. The internal ring angles surrounding C4 fall notably below 109.5° at 86° and 89°, and the external angles are significantly higher, ranging from 116 to 127°.

Each ytterbium(III) ion in the asymmetric unit has a different mode of coordination. Yb1 has a coordination number of 8, and has a square antiprismatic geometry, while Yb2 and Yb3 each have a coordination number of 7, with a capped octahedral geometry and a pentagonal bipyramidal geometry respectively. The coordination geometry surrounding each ytterbium(III) ion is shown in Figure 5.8.

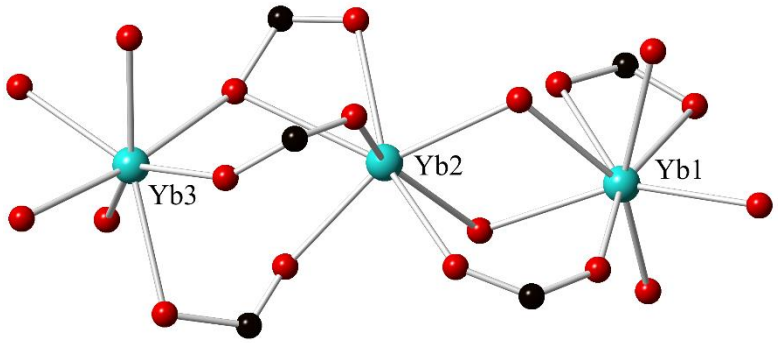

*Figure 5.8. The coordination geometry surrounding the three unique ytterbium(III) ions in poly-[Yb_6(**L5.1**)$_9$$(DMF)_2$]·0.5DMF·2.5$H_2O$ (complex **5.1**)*

One in three ytterbium(III) ions (Yb3) is also coordinated by a DMF solvent molecule *via* its oxygen atom. There are two bridging modes of the ligand molecules in the asymmetric unit – μ_3 and μ_4, shown in Figure 5.9.

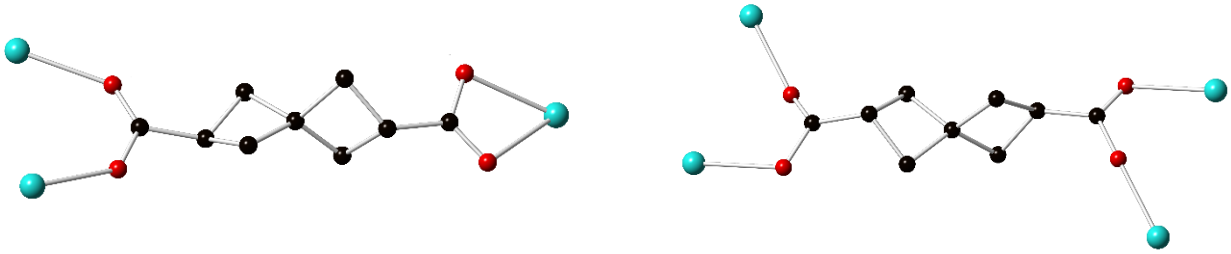

*Figure 5.9. The two bridging modes of **L5.1** in poly-[Yb_6(**L5.1**)$_9$(DMF)$_2$]·0.5DMF·2.5H_2O (complex **5.1**), μ-3 (left) and μ-4 (right), with hydrogen atoms omitted for clarity*

The polymeric structure has a hexagonal (**hex**) rod packing topology, consisting of one-dimensional ytterbium(III) carboxylate chains (shown in Figure 5.10), that are linked to six neighbouring chains *via* **L5.1** ligand molecules.

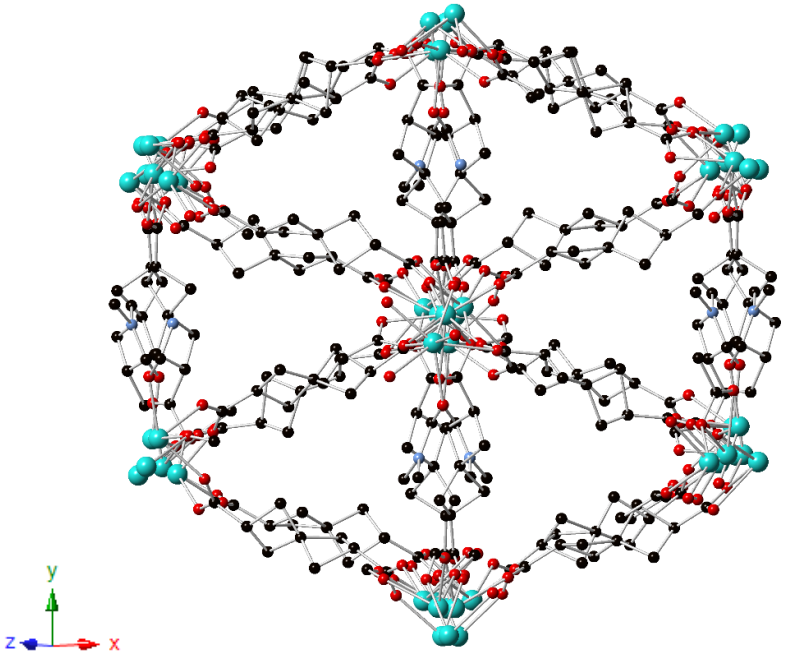

*Figure 5.10. Extended structure of poly-[Yb_6(**L5.1**)$_9$(DMF)$_2$]·0.5DMF·2.5H_2O (complex **5.1**) showing the **hex** rod-type packing topology*

Thermogravimetric analysis of complex **5.1** was carried out to analyse its thermal stability and to investigate any potential porosity. The TGA profile (shown in Figure 5.11) revealed that the loss of lattice solvent molecules occurs at a relatively high temperature range of 250-350 °C, accounting for an overall mass loss of 7.8 wt%, and no ligand decomposition is observed at this temperature. This figure is significantly larger than the calculated volatile mass, which was 2.8 wt%, which was calculated using elemental analysis of the filtered crystals of complex **5.1**, however, this does not account for the coordinating DMF molecules, in which case this would amount to 7.5 wt%. This suggests that the lattice and coordinating DMF molecules within the pores are either not easily accessible, or they are quite tightly bound. To investigate this, crystals of complex **5.1**, were soaked in methanol for several days, with regular replacement with fresh methanol. This was carried out as an attempt to displace the lattice solvent molecules from the complex. The TGA profile post-soaking was identical to the as-synthesised profile, confirming the immobility of the lattice solvent.

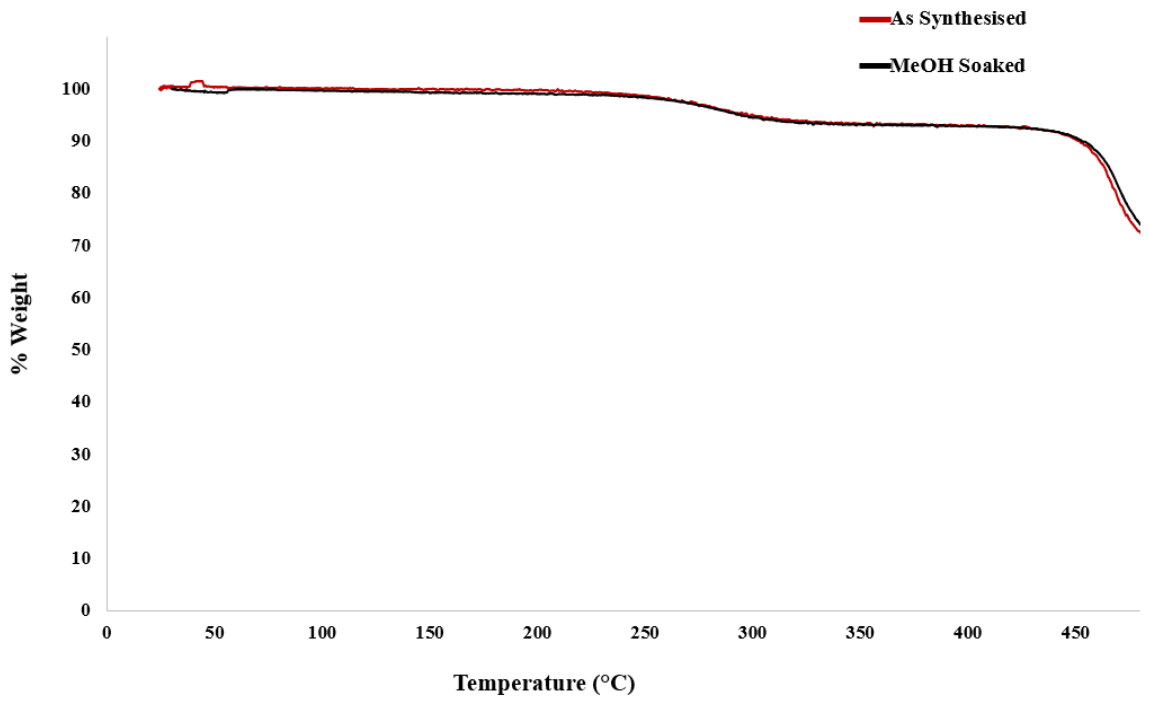

*Figure 5.11. TGA profile of as-synthesised complex **5.1** (black) and complex **5.1** post-MeOH soaking (red)*

The mass loss due to ligand decomposition, however, also occurs at an unexpectedly high temperature, beginning at 425 °C. This is surprising, given the nature of the highly strained cyclobutane rings within the ligand backbone, resulting in the highly distorted spiro carbon. This thermal stability is particularly impressive, when compared to an analogous cerium(III) terephthalate complex, in which the ligand decomposition begins at a much lower temperature, 360 °C. Despite allowing for the difference in metal ion between the two complexes, **L5.1** clearly imparts thermal stability to complex **5.1**, which is significantly higher than that of the cerium(III) terephthalate complex.

As expected, due to inaccessibility of the isolated pockets of solvation in the complex, the N_2 and CO_2 uptake of the material was particularly low, with mostly surface adsorption observed. The adsorption isotherms for N_2 and CO_2 are shown in Figure 5.12.

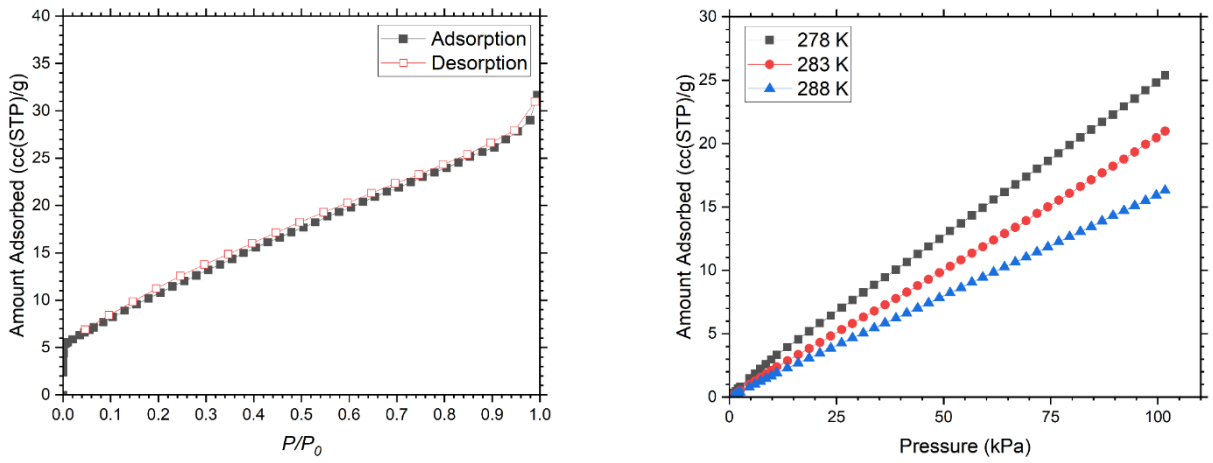

*Figure 5.12. N_2 adsorption (black, filled) and desorption (red, hollow) isotherms for complex **5.1** (left) and CO_2 adsorption isotherms at 278, 283 and 288 K for complex **5.1** (right)*

The complex exhibits a type II adsorption isotherm, with minimal filling of micropores, as evidenced by the sharp increase in the volume of gas adsorbed in the low P/P_0 values (between *ca.* 0.0 and 0.1) of the N_2 adsorption isotherms. As this sharp increase ends at the relatively small value of *ca.* 6 cc(STP) g^{-1}, this is indicative of the internal pore volume being very low, as the remainder of the adorption occurs at the surface of the material, as evidenced by the relatively flat shape to the remainder of the adsorption isotherm. The point where the sharp increase in volume of gas adsorbed begins to level out is the value which is used to

calculate BET surface area, which would not be accurately calculable at such a low value, and would result in a value much lower than 10 $m^2\ g^{-1}$.

The overall adsorption of N_2 at 77 K is relatively low, only reaching 32 cc(STP) g^{-1}. The CO_2 adsorption isotherms show similarly low adsorption, with the data suggesting mostly surface adsorption, with little to no filling of micropores, indicated by the absence of an inflection point in any of the CO_2 adsorption isotherms. The total volume of CO_2 adsorbed at 278 K at 100 Pa only reaches a maximum of 25 cc(STP) g^{-1}. Another indication of minimal adsorption is that the enthalpy of adsorption does not decrease significantly with loading, leading to a calculated enthalpy of adsorption of CO_2 of -37 kJ mol^{-1} at zero surface coverage.

While an analogous ytterbium(III) complex of terephthalic acid has not yet been reported in literature, a similar cerium(III) terephthalate complex, reported by D'Arras *et. al.*,[19] with the same **hex** rod-type topology offers an appropriate aromatic contrast. The structures of both complexes are shown in Figure 5.13. As in complex **5.1**, *poly*-[Ce_5(**BDC**)$_{7.5}$(DMF)$_4$] contains one-dimensional cerium(III) carboxylate chains, which are linked to six neighbouring chains *via* doubly deprotonated ligand molecules.

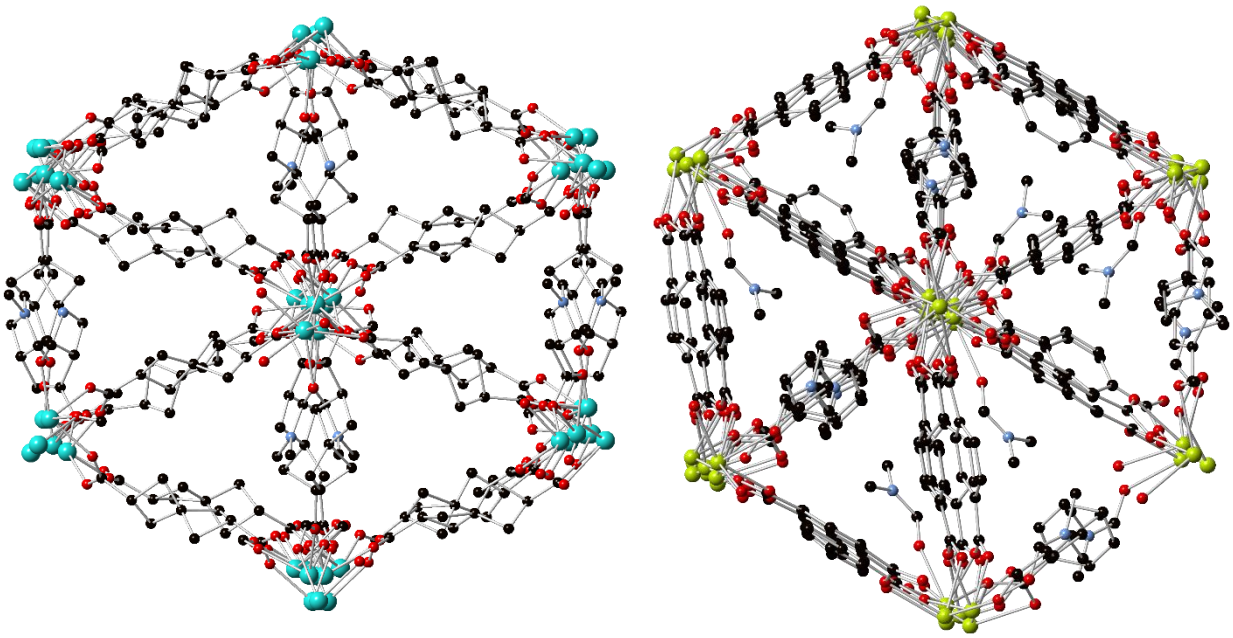

*Figure 5.13. Extended structure of poly-[Yb_6(**L5.1**)$_9$(DMF)$_2$]·0.5DMF·2.5H_2O (complex **5.1**) (left) and extended structure of isostructural poly-[Ce_5(**BDC**)$_{7.5}$(DMF)$_4$][19] (right)*

The internal surface chemistry of complex **5.1**, and *poly*-[Ce_5(**BDC**)$_{7.5}$(DMF)$_4$] will differ significantly, despite the topological similarities of the two materials. In complex **5.1**, the aliphatic backbone of **L5.1** results in -CH_2 moieties pointing inward into the pore, resulting in a potentially very hydrophobic interior. The pore surface will also be geometrically more complex than *poly*-[Ce_5(**BDC**)$_{7.5}$(DMF)$_4$], due to the three-dimensional nature of **L5.1**, relative to the two-dimensional **BDC** ligand. In the case of complex **5.1**, the pockets of solvation are not accessible, therefore any impact this would have on adsorption selectivity is in vain, which inspired the synthesis of complex **5.2**, a material with more accessible porosity.

5.4 *Poly*-[Zn(L5.1)(dpe)]·1.33DMF·1.33H_2O, Complex 5.2

Synthesis of a homoleptic zinc(II) complex of **L5.1**, isostructural to MOF-5 was unsuccessful, likely due to the slight curve of the **L5.1** ligand molecule, relative to terephthalic acid. Instead, a neutral N-donor co-ligand, 4,4′-dipyridyl ethylene (**dpe**) was employed in the synthesis. Combination of **H_2L5.1**, **dpe** and $Zn(NO_3)_2$·$6H_2O$ in DMF resulted in *poly*-[Zn(SHDC)(**dpe**)], complex **5.2**, shown in Figure 5.14, highlighting the coordination geometry surrounding the zinc(II) ions.

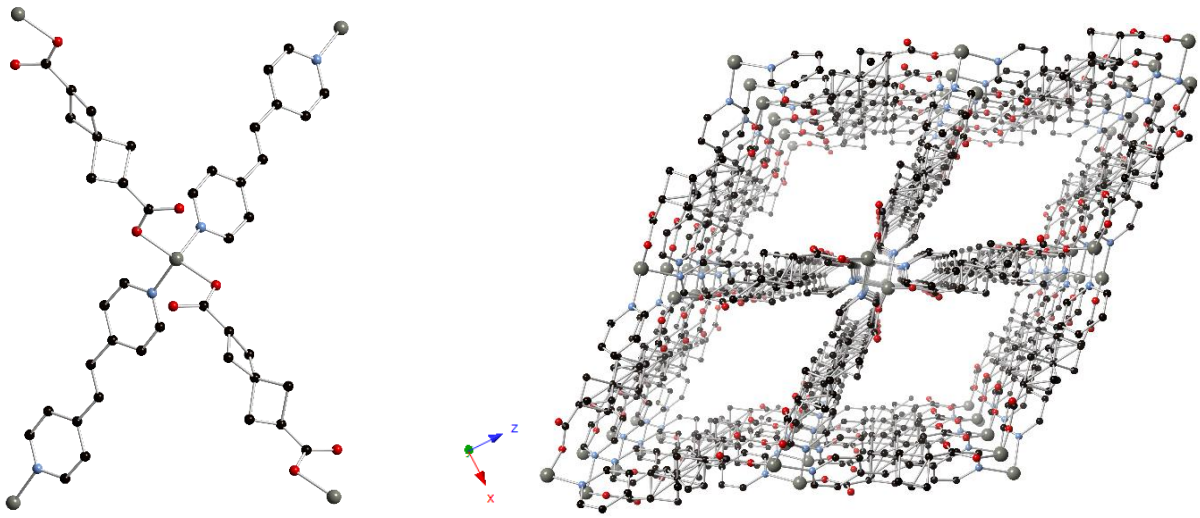

Figure 5.14. Coordination geometry surrounding zinc(II) in poly-*[Zn(SHDC)(**dpe**)] (complex **5.2**) (left) and extended structure of complex **5.2** (right)*

As is clear from Figure 5.14, the structure appears significantly more porous. The structure of complex **5.2** was solved and refined in the orthorhombic space group *Pnna*. The asymmetric unit, shown in Figure 5.15 consists of one half of one **L5.1** ligand molecule, coordinated to one zinc(II) ion *via* an oxygen atom and one half of a **dpe** ligand molecule, coordinated to the same zinc(II) ion *via* a pyridyl nitrogen atom.

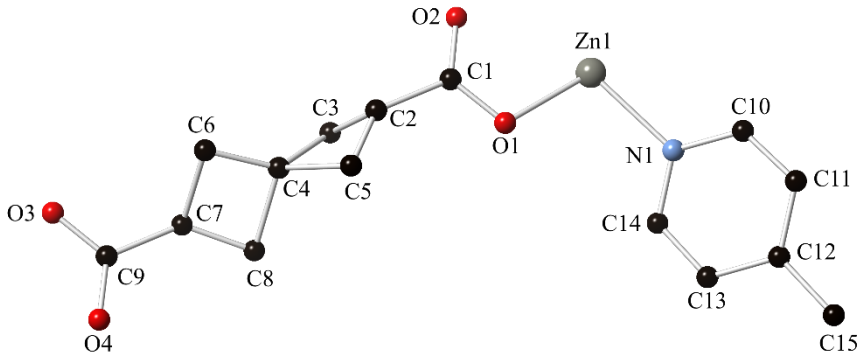

Figure 5.15. Asymmetric unit of poly-*[Zn(SHDC)(**dpe**)] (complex **5.2**), with disorder and hydrogen atoms omitted for clarity*

As in complex **5.1**, there is significant disorder surrounding the **L5.1** ligand molecule, again suggesting both enantiomers are superimposed within the structure. These are related by a fourfold improper rotation around

the spiro carbon atom. Each zinc(II) ion has a tetrahedral geometry, with two **L5.1** molecules and two **dpe** molecules coordinating to each metal ion, as shown in Figure 5.14.

The angles all significantly deviate from the expected 109.5° angles of a typical tetrahedral geometry. This is attributed to the ambiguity of the coordination mode of **L5.1** to the zinc(II) centre. The Zn1-O2 distance (2.47(3)Å) is significantly longer than the other bond lengths surrounding the zinc(II) ion, however it is short enough that in some cases it can be considered a bond. For the purposes of this description of the crystal structure, it is not considered a bond. What is more likely is that the coordination mode is a hybrid of a single coordination bond from one oxygen atom, O1, and a chelation coordination mode. Therefore, when considering the geometry surrounding the zinc(II), it is more reasonable to consider the C-Zn-C angles rather than the O-Zn-O angles, as these would be more representative of the true coordination geometry. Perhaps unsurprisingly, the geometry deviates from that of a perfect tetrahedron, as zinc(II) is a d^{10} metal ion, resulting in an absence of ligand field stabilisation energy.

The extended structure of complex **5.2** has a fourfold interpenetrated diamondoid (**dia)** topology, outlined in Figure 5.16, in which the different colours represent different interpenetrating networks. The dominating interactions between neighbouring networks which result in this interpenetration are weak interactions between a coordinating oxygen atom (O1) and a CH moiety (C14) of a **dpe** pyridyl ring in an adjacent network, (with a C···O distance of 3.48(3) Å and a C-H···O angle of 149.0(7)°), and π-π interactions between adjacent **dpe** molecules, with an interplanar distance of 3.701(3) Å and an offset of 1.145(7) Å.

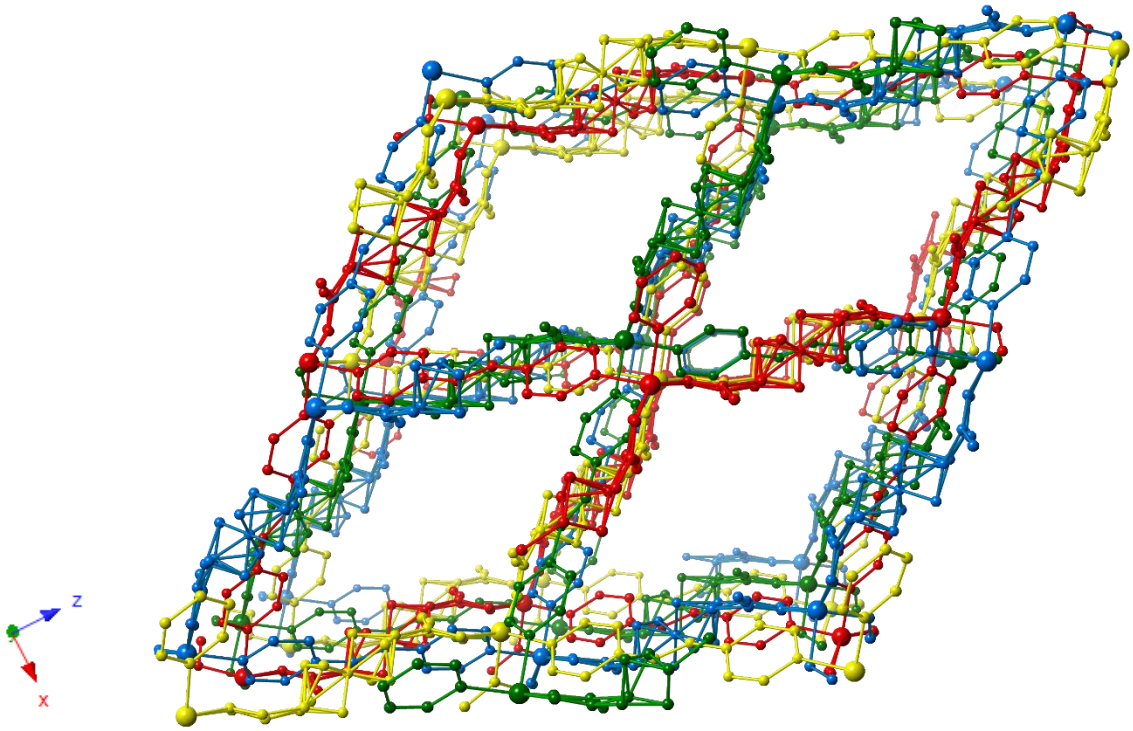

Figure 5.16. Fourfold interpenetration in poly-*[Zn(SHDC)(**dpe**)] (complex **5.2**), with individual interpenetrating networks shown in red, blue, green, and yellow*

Despite the interpenetration, however, there are linear solvent channels parallel to the crystallographic *b* axis with an approximate interatomic distance of 8.8 × 9.1 Å. Thermogravimetric analysis revealed that the solvent is much more mobile within the channels of complex **5.2**, and this was confirmed by the change in TGA profile following soaking crystals of complex **5.2** in methanol for several days. The TGA profiles of both the freshly synthesised sample and the sample post-soaking are shown in Figure 5.17.

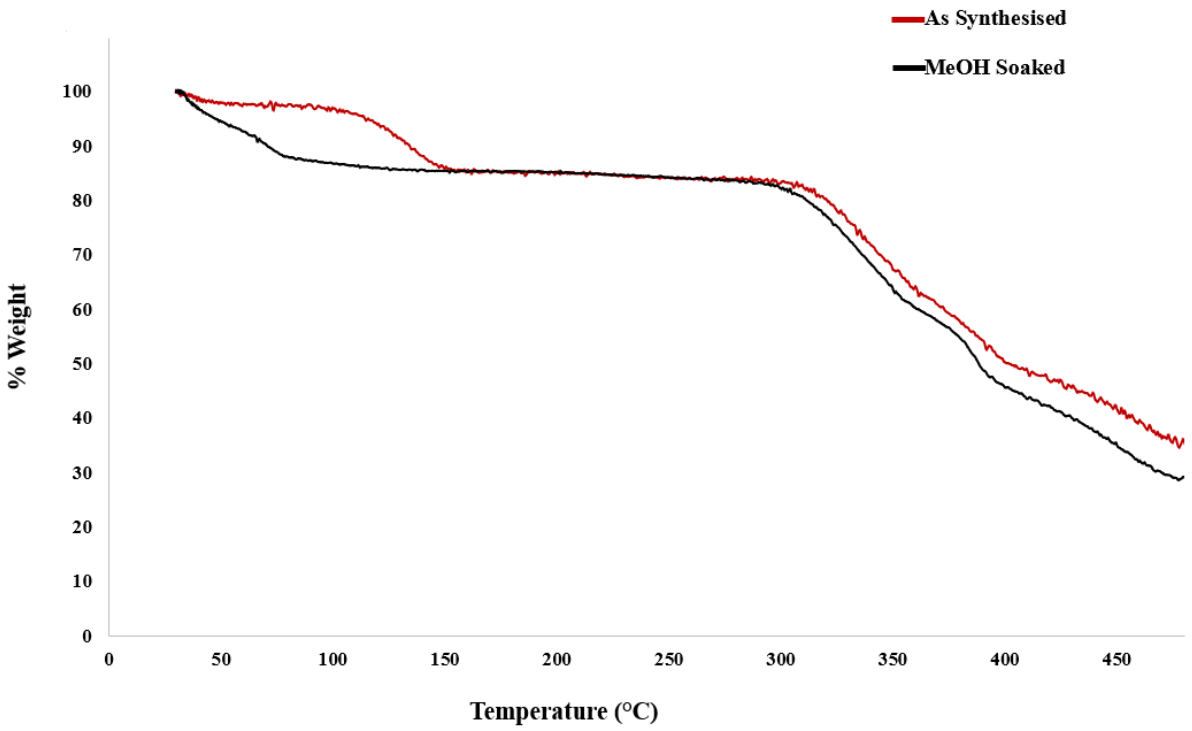

*Figure 5.17. TGA profile of as-synthesised complex **5.2** (black) and complex **5.2** post-MeOH soaking (red)*

TGA also revealed that this complex was significantly less thermally stable than complex **5.1**, with the onset of ligand decomposition occurring at 320 °C, and this is likely due to the introduction of the aromatic ligand, **dpe**. Desolvation of the fresh sample began at room temperature and only plateaued at 170 °C. Whereas, after soaking in methanol for several days, the desolvation was completed at 100 °C, confirming the improvement in volatility of the lattice solvent molecules.

A terephthalic acid zinc(II) analogue to this complex has been reported by Liu *et. al.*[20] in 2008 and the structure is shown in Figure 5.18. The structure of *poly*-[Zn(**BDC**)(**dpe**)] has the same **dia** topology as complex **5.2**, however in this case it is fivefold interpenetrated, resulting in no permanent porosity, and the individual networks are again highlighted in different colours in Figure 5.18.

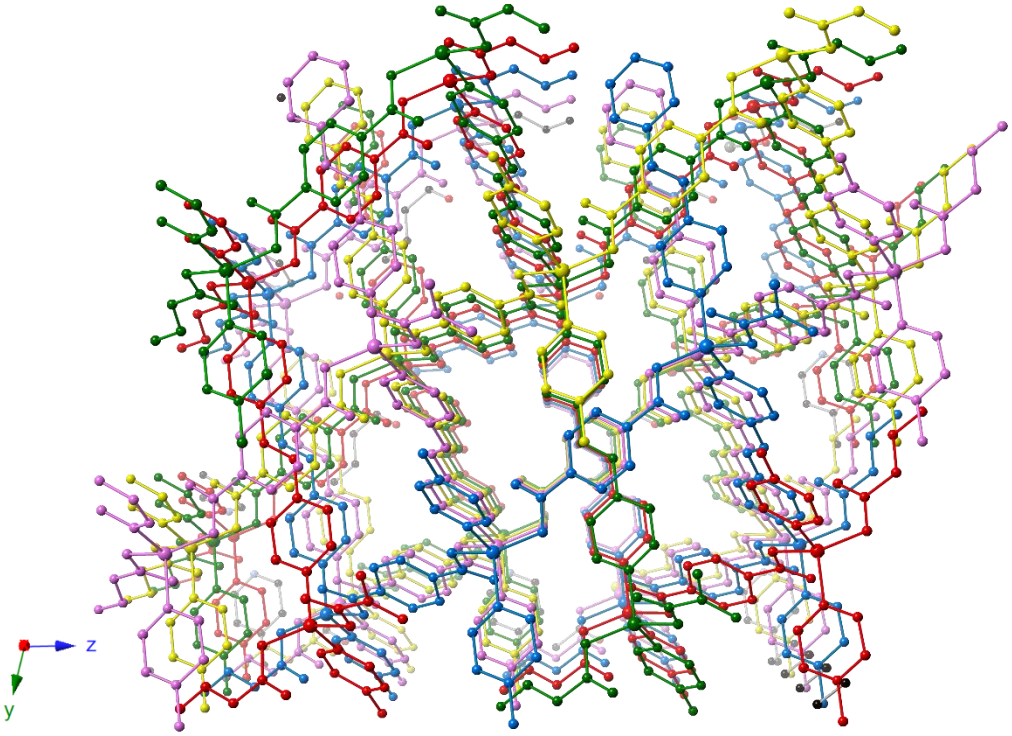

*Figure 5.18. Fivefold interpenetration in poly-[Zn(**BDC**)(**dpe**)], with individual interpenetrating networks shown in red, blue, green, yellow and pink*

The increase in the degree of interpenetration in this complex is attributed to the face-to-face π-π interactions between the π-systems of the terephthalic acid and the **dpe** coligand, with an interplanar distance of 3.8590(19) Å and a shift of 1.483(7) Å. Both values are significantly larger than the face-to-face π-π interactions between **dpe** pyridyl moieties in complex **5.2** (with an interplanar distance of 3.701(3) Å and an offset of 1.145(7) Å), suggesting a much looser association of adjacent networks in the zinc(II) terephthalate complex. This is also observed, when examining the alignment of adjacent networks in the crystal packing, in complex **5.2**, the ligands of the networks align parallel to each other, resulting in more favourable π-π interactions, and therefore a closer association, whereas this is not true for the zinc(II) terephthalate complex. Weaker C-H···O contacts are again present, however in this case they originate at a **dpe** ethylene CH moiety and a terephthalate oxygen atom (with a C···O distance of 3.187(4) Å, and a C-H···O angle of 164.5(3)°), which are significantly stronger than the analogous interactions in complex **5.2**

(C···O distance of 3.48(3) Å and a C-H···O angle of 149.0(7)°). The distance between zinc(II) ions (across the dicarboxylate ligand) is longer in complex **5.2** (11.8078(7) Å) relative to the zinc(II) terephthalate complex (10.792(3) Å), meaning the degree of interpenetration in theory should be higher in complex **5.2**, however that is not the case. The stronger C-H···O contacts in the terephthalate complex likely both contribute to the increased degree of interpenetration in the complex, but also interfere with the formation of better aligned π-systems of adjacent networks.

The π-π interactions in complex **5.2** are much less frequently encountered due to the reduced overall aromaticity of the material, relative to the analogous zinc(II) terephthalate complex. This implies that by replacing aromatic bridging ligands with aliphatic ligands, the interactions between adjacent networks that encourage interpenetration (namely π-π interactions) could be significantly reduced in quantity. This in turn could increase the probability of permanent porosity within a coordination polymer.

This porosity of complex **5.2** was again examined using N_2 and CO_2 adsorption measurements, and the results were expected to be a significant improvement from those of complex **5.1**, due to the confirmed increase in lattice solvent volatility. However, the adsorption isotherms show similarly low values for both N_2 and CO_2 adsorption (Figure 5.19).

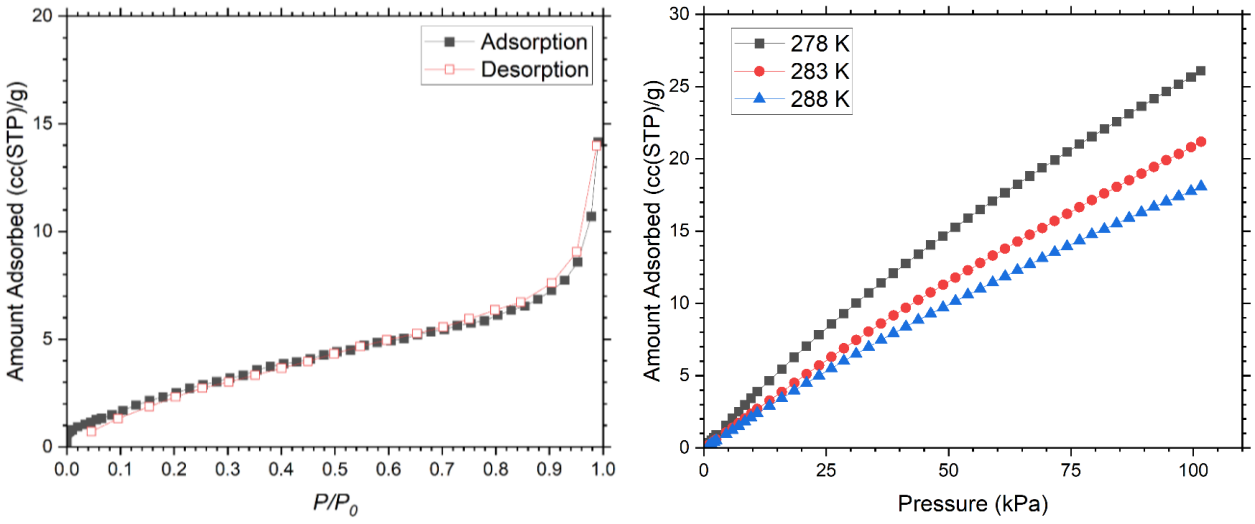

*Figure 5.19. N_2 adsorption (black, filled) and desorption (red, hollow) isotherms for complex **5.2** (left) and CO_2 adsorption isotherms at 278, 283 and 288 K for complex **5.2** (right)*

The overall adsorption of N_2 at 77K only reaches 14 cc(STP) g^{-1}, and the CO_2 adsorption is slightly higher than in complex **5.1**, reaching slightly above 26 cc(STP) g^{-1} at 278 K at 100 kPa. There is little to no filling of micropores, evidenced by the absence of any notable sharp increase in the N_2 adsorption isotherm at the lowest P/P_0 values. Similar issues were observed with the CO_2 adsorption isotherms and adsorption enthalpies as in those of complex **5.1**, with no significant inflections observed in the isotherms. The enthalpy of adsorption at zero surface loading of CO_2 was calculated to be a similar value to that of complex **5.1**, at –33 kJ mol^{-1}, and did not show any notable decrease with loading.

A closer inspection of the PXRD patterns of the material at each stage revealed the reason behind the unexpectedly low adsorption of complex **5.2**. The PXRD patterns of the freshly synthesised complex **5.2** and after MeOH soaking were identical, indicating that the solvent exchange resulted in no change to the framework structure or overall crystallinity (Appendix 2, Figure A2.20). The PXRD pattern after gas adsorption measurements, however, deviates significantly from that of the pristine material. The broadness and low resolution of the peaks in the PXRD pattern indicate a structural transformation and loss in crystallinity of the complex. This change combined with the gas adsorption data strongly suggest a loss in porosity of complex **5.2**, following solvent removal during the activation process of the material.

5.5 WIG-5

Soon after the publication of complexes **5.1** and **5.2**,[12] another coordination polymer containing Fecht's acid was reported by Földes *et. al.*[21] This structure makes a useful comparison to the materials described above and so is briefly discussed below. WIG-5, a homochiral zinc(II) MOF of (*R*)-Fecht's acid ((*R*)-spiro[3.3]heptane-2,6-dicarboxylate) demonstrates the effect of using only one enantiomer of Fecht's acid in a MOF synthesis. The (*R*)-enantiomer was isolated using a HPLC with a chiral stationary phase. The complex crystallises in the orthorhombic space group $P2_12_12_1$ and the asymmetric unit consists of four

zinc(II) ions, three (*R*)-**L5.1** molecules and five DMF solvent molecules, three of which are coordinating (Figure 5.20).

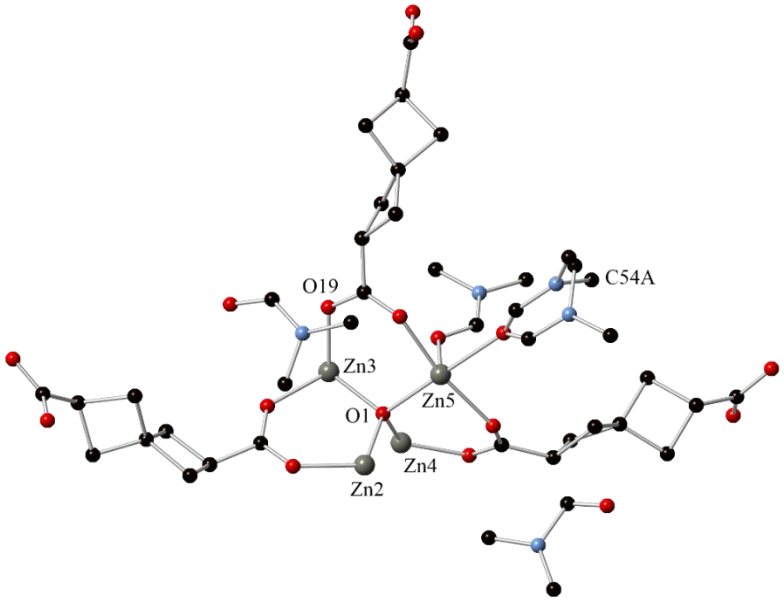

Figure 5.20. Asymmetric unit of WIG-5, with hydrogen atoms omitted for clarity

The four zinc(II) ions form a zinc(II) carboxylate cluster, with a tetrahedral oxygen atom, O1, at the centre of that cluster (Figure 5.20). The complex forms a distorted MOF-5-like structure,[22] with a **pcu** topology which interestingly, is two-fold interpenetrated (Figure 5.21).

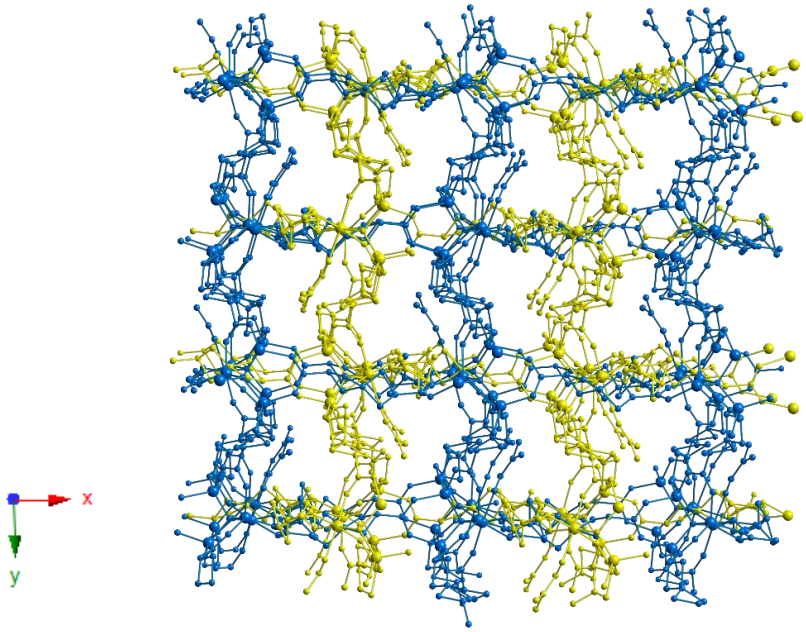

Figure 5.21. Twofold interpenetration in WIG-5, showing individual networks in blue and yellow, non-coordinating solvent molecules were omitted for clarity

Due to the enantiomeric purity of the ligand, the MOF is considered to be chiral, which is not true for any previously discussed complexes containing **L5.1**. The coordinating DMF molecules form short contacts with a carboxylate oxygen atom of an adjacent network (with a C54A···O19 distance of 3.482(15) Å and a C54A-H···O19 angle of 169.2(8)°) and these are the strongest interactions that associate adjacent networks. There are four channels parallel to the crystallographic *a* axis, two of which are occupied by coordinating DMF molecules and two of which are occupied by lattice DMF molecules, which are assumed to be much more volatile. No gas adsorption measurements were carried out, however, a theoretical gravimetric and volumetric surfaces areas were calculated to be 1700 $m^2\ g^{-1}$ and 1900 $m^2\ cm^{-3}$, respectively. This is much smaller than that of MOF-5, which has a gravimetric surface area of 3800 $m^2\ g^{-1}$.[23] This is likely due to the interpenetration in WIG-5, which is absent in MOF-5.

This increased interpenetration and reduced porosity, despite an absence of aromatic ligands (and therefore, π-π interactions) in WIG-5, relative to MOF-5, shows opposite trends to what was previously observed in complex **5.2** and the corresponding zinc(II) terephthalate complex. Földes *et. al.*[21] make structural comparisons of WIG-5 to MOF-5, attributing the porosity in MOF-5 to the planarity of the terephthalate linkers, whereas, in WIG-5, the carboxylate moiety is completely out of plane, relative to the cyclobutane rings of the (*R*)-**L5.1** linkers, which results in a much more complex pore network in WIG-5. WIG-5 shows relatively high thermal stability (up to 300 °C), which is consistent with what is observed in other complexes of **L5.1**, however, this is substantially lower than that of MOF-5, in which the onset of ligand decomposition only begins at *ca*. 400 °C.[24]

5.6 Discussion

Complexes of Fecht's acid have provided an interesting comparison to complexes of amine-containing ligands discussed in previous chapters. As previously mentioned, in amine-containing ligands most often it is the polarised CH_2 moieties adjacent to the amines that participate in hydrogen bonding or other weak interactions between neighbouring components. These interactions have led to diverse hydrogen bonding networks in their coordination complexes, which in turn have given rise to a variety of crystal packing

modes. On a wider scope, however, interactions such as these can lead to interpenetration, which for gas adsorption purposes is unfavourable. On the other hand, Fecht's acid contains no amine or other nitrogen atoms, which significantly reduces the range of possible interactions between adjacent networks in a coordination complex. Complexes of Fecht's acid have served two important purposes in the analysis of coordination complexes containing aliphatic ligands.

Firstly, the comparison of its complexes with analogous complexes of terephthalic acid identifies the direct effect of replacing the aromatic ligands in a MOF with similarly rigid aliphatic ligands. In the case of complex **5.1**, the aliphatic ligand notably imparted significant thermal stability onto its coordination complex, relative to the analogous cerium(III) terephthalate complex, despite the highly strained nature of **L5.1**. This thermal stability was a significant improvement from that of its aromatic analogue. Complex **5.2**, while not presenting the same degree of thermal stability (likely due to the aromatic coligand, **dpe**), offered an alternative benefit. Due to the reduced aromaticity, the degree of interpenetration, compared to the isostructural terephthalic acid MOF, was reduced, resulting in some porosity being maintained in the form of linear solvent channels. This porosity is non-existent in the aromatic MOF due to five-fold interpenetration owing to the increased π-π interactions.

Secondly, these complexes offer a comparison to complexes of amine-containing ligands discussed in previous chapters. The effects of removing any nitrogen atoms from the ligand structure has resulted in significantly weaker interactions playing a larger part in the crystal packing of complexes **5.1** and **5.2**. In complex **5.1** (which also contains no aromaticity), these interactions are limited to contacts between a -CH_2 moiety of one ligand molecule and an oxygen atom of an adjacent ligand molecule, which as expected are relatively weak. There are also some interactions between the -CH_3 moiety of a coordinating DMF molecule and an oxygen atom of a neighbouring ligand molecule, which appears to be one of the stronger interactions, due to the near-linearity of the C-H···O angle. However, relative to interactions observed in amine-containing ligands in Chapters 2, 3 and 4, the potential for any weak ligand interactions or hydrogen bonding are significantly reduced in complexes of **L5.1**. Where in previous ligands, there were multiple polarised

CH_2 moieties adjacent to hydrogen bond accepting moieties, the only heteroatoms in **L5.1** are the carboxylate oxygen atoms which are most often coordinating. The substantial disorder observed in the complexes of **L5.1**, further confirms the absence of any significant short contacts, as perhaps there would be less disorder observed (*i.e.* one enantiomer of **L5.1** would be preferred) if stronger interactions were possible.

Complex **5.2** has a slightly wider range of accessible interactions, due to the aromatic, pyridine-containing **dpe** coligand, which possibly contributes to the likelihood of interpenetration. The interactions in this case largely originate at the **dpe** coligand, with the ethylene CH moiety forming short contacts with an oxygen atom of a neighbouring **L5.1** ligand molecule along with expected face-to-face π-π interactions between adjacent networks, resulting in fourfold interpenetration. Given that complex **5.1** was not interpenetrated and complex **5.2** was interpenetrated to a lesser degree than its aromatic counterpart, a conclusion can be drawn that by reducing the degree of aromaticity that is present in a coordination complex, the risk of interpenetration will also be reduced. Again, the high degree of **L5.1** ligand disorder, as in complex **5.1**, is indicative of an absence of any strong short contacts that could potentially lead to the preference of one ligand conformation.

This disorder in the ligand molecule is absent, however, when the enantiomerically pure, (*R*)-**L5.1** is used, instead of the racemate, in WIG-5, which is a chiral MOF confirmed to only contain the (*R*)-enantiomer using VCD spectroscopy. This is expected, as the disorder arises from the two overlapping conformations of Fecht's acid in complexes **5.1** and **5.2**, but when only one enantiomer is used, there is no longer any disorder present. If stronger short contacts were present in the complexes, perhaps a preference for one enantiomer would be observed in the subsequent complexes and again, lead to an absence of ligand disorder. The use of a singular enantiomer interestingly added a degree of interpenetration relative to its zinc(II) terephthalate analogue, MOF-5, which is unlike the observed trends in complex **5.2**. The distance between zinc(II) ions in WIG-5 is larger than that in MOF-5, which is not surprising given the slightly larger size of

L5.1 relative to terephthalic acid, meaning interpenetration is more likely to occur in WIG-5, which is observed.

The comparability or significant improvement of thermal stability in complexes **5.2**, and **5.1** respectively, provides encouraging provisional data for the use of molecules of that nature as coordinating ligands in MOFs. While the direct comparison of complexes **5.1**, **5.2** and WIG-5 are not possible due to a variety in metal salts, coligands and enantiomeric purity between complexes, it is evident that the rigidity of **L5.1** has resulted in the ability to synthesise MOFs with topologies similar to early aromatic MOFs, however now providing novel properties and chemistries. The small library of aliphatic MOFs in literature (for example CUB-5, NU-403)[10,25] have begun to explore the unusual adsorption properties and novel optical properties of these materials, and have highlighted this novel space in the literature in the field of porous coordination materials.

5.7 References

1. K. Hiessinger, D. Dar'in, E. Proschak and M. Krasavin, *J. Med. Chem.*, 2021, **64**, 150 – 183.

2. A. J. Bourke, H. Federsel and G. J. Hermann, *J. Org. Chem.*, 2022, **87**, 1898 – 1924.

3. O. Bonjour, I. Liblikas, T. Pehk, T. Khai-Nghi, K. Rissanen, L. Vares and P. Jannasch, *Green Chem.*, 2020, **22**, 3940 – 3951.

4. N. G. Valsange, M. N. Garcia Gonzalez, N. Warlin, S. V. Mankar, N. Rehnberg, S. Lundmark, B. Zhang and P. Jannasch, *Green Chemistry*, 2021, **23**, 5706 – 5723.

5. E. M. Carreira and T. C. Fessard, *Chem. Rev.*, 2014, **114**, 8257 – 8322.

6. F. E. Hahn, M. Paas, D. L. Van and R. Fröhlich, *Eur. J. Chem.*, 2005, **11**, 5080 – 5085.

7. K. G. Alley, G. Poneti, P. S. D. Robinson, A. Nafady, B. Moubaraki, J. B. Aitken, S. C. Drew, C. Ritchie, B. F. Abrahams, R. K. Hocking, K. S. Murray, A. M. Bond, H. H. Harris, L. Sorace and C. Boskovic, *J. Am. Chem. Soc.*, 2013, **135**, 8304 – 8323.

8. Y. Rogan, L. Starannikova, V. Ryzhikh, Y. Yampolskii, P. Bernardo, F. Bazzarelli, J. C. Jansen and N. B. McKeown, *Polym. Chem.*, 2013, **4**, 3813 – 3820.

9. C. A. Terraza, L. H. Tagle, J. L. Santiago-García, R. J. Canto-Acosta, M. Aguilar-Vega, R. A. Hauyon, D. Coll, P. Ortiz, G. Perez, L. Herrán, B. Comesaña-Gándara, N. B. McKeown and A. Tundidor-Camba, *Polymer*, 2018, **137**, 283 – 292.

10. L. K. Macreadie, E. J. Mensforth, R. Babarao, K. Konstas, S. G. Telfer, C. M. Doherty, J. Tsanaktsidis, S. R. Batten and M. R. Hill, *J. Am. Chem. Soc.*, 2019, **141**, 3828 – 3832.

11. H. Fecht, *Chem. Ber.*, 1907, **40**, 3883 – 3891.

12. V. D. Slyusarchuk and C. S. Hawes, *CrystEngComm*, 2022, **24**, 484 – 490.

13. E. Chupakhin, O. Babich, A. Prosekov, L. Asyakina and M. Krasavin, *Molecules*, 2019, **24**, 4165.

14. R. Rios, *Chem. Soc. Rev.*, 2012, **41**, 1060 – 1074.

15. A. M. Kelley, E. Minerali, J. E. Wilent, N. J. Chambers, K. J. Stingley, G. T. Wilson and K. S. Petersen, *Tetrahedron Lett.*, 2019, **60**, 1262 – 1264.

16. C. Cassani, X. Tian, E. C. Escudero-Adán and P. Melchiorre, *Chem. Commun.*, 2010, **47**, 233 – 235.

17. H. J. Backer and H. B. J. Schurink, *Recueil des Travaux Chimiques des Pays-Bas*, 1931, **50**, 921 – 930.

18. H. Tang, H. Miura and Y. Kawakami, *Enantiomer*, 2010, **7**, 5 – 9.

19. L. D'Arras, C. Sassoye, L. Rozes, C. Sanchez, J. Marrot, S. Marre and C. Aymonier, *New J. Chem.*, 2014, **38**, 1477 – 1483.

20. D. Liu, H. Li, Y. Chen, Y. Zhang and J. Lang, *Chin. J. Chem.*, 2008, **26**, 2173 – 2178.

21. D. Földes, É. Kováts, G. Bortel, K. Kamarás, G. Tarczay, E. Jakab and S. Pekker, *J. Mol. Struct.*, 2022, **1257**, 132538.

22. H. Li, M. Eddaoudi, M. O'Keeffe and O. M. Yaghi, *Nature*, 1999, **402**, 276–279.

23. L. F. Herrera, L. Prasetyo and D. D. Do, *Adsorption*, 2019, **25**, 1075 – 1087.

24. M. M. Peng, U. J. Jeon, M. Ganesh, A. Aziz, R. Vinodh, M. Palanichamy and H. T. Jang, *Bull. Korean Chem. Soc.*, 2014, **35**, 3213 – 3218.

25. K. B. Idrees, Z. Chen, X. Zhang, M. R. Mian, R. J. Drout, T. Islamoglu and O. K. Farha, *Chem. Mater.*, 2020, **32**, 3776–3782.

Chapter 6

· Conclusions & Future Work ·

6.1 Conclusions

The results discussed in the preceding chapters have demonstrated the feasibility and versatility of incorporating rigid cyclic aliphatic units into the backbones of ligands in metallosupramolecular assemblies, resulting in the synthesis of a library of discrete and polymeric assemblies. The aim of this work was to investigate whether the aliphatic units would mimic the rigidity of traditional aromatic ligands, to then overcome the issues of flexibility associated with aliphatic coordination materials to sustain permanent porosity within these coordination materials. The geometric diversity provided by the non-planar cyclic, fused-ring or spirocyclic aliphatic components was also investigated, and compared to analogous aromatic coordination assemblies, which again contributed to the trends in short contacts observed in these materials.

In Chapter 2, piperidine and morpholine-substituted 4-picolylamine ligands, alongside the equivalent primary amine were investigated as simple representative alicyclic amine-containing ligands in discrete and polymeric coordination assemblies of copper(II), cobalt(II) and silver(I) salts. The SCXRD data was used in conjunction with Hirshfeld surface analysis to observe the general trends in short contacts arising from the aliphatic ligand backbones, that contribute to the observed crystal packing modes of the assemblies. The

protonated ligand heteroatoms were found to be the most likely to partake in short contacts, followed by the most polarised aliphatic protons (provided these were accessible), followed by the most accessible protons.

Chapter 3 applied the observations from Chapter 2 to more complex conjugated tropinone ligands, which also contain an alicyclic amine-containing functionality. This library of ditopic and tritopic divergent ligands were generated *via* functionalisation of the nortropinone secondary amine and the positions α- to the ketone, which were combined with transition metal and lanthanide ions to yield polymeric coordination assemblies, which displayed similar trends in short contacts to the complexes in Chapter 2.

Chapter 4 extended this work to the functionalisation of nortropinone at the apical amine and the carbonyl functionality. These functionalisations were used to design a library of convergent, nitrogen-rich cyclohexyl-bridged bis-*R*-tropinone ligands, which were combined with silver(I) salts to generate both discrete and polymeric coordination cages. The *N*-aryl ligands exclusively formed cages of an $M_{12}L_6$ stoichiometry which had a truncated tetrahedron shape, while the *N*-methyl ligand, on the other hand, led to a discrete cubic M_8L_6 cage. The dynamic assembly process of the discrete cages was probed *in-situ* using NMR analysis techniques, with a particular focus on DOSY NMR, which revealed the persistence of the cages in solution, in particular in the presence of a large excess of other anions. The preferred stoichiometry of the aryl cages, as well as the *N*-methyl cage *in-situ* were consistent with the solid-state observations, as were as the hydrodynamic radii obtained by DOSY NMR.

Finally, Chapter 5 explored the coordination chemistry of a spirocyclic dicarboxylate ligand, spiro[3.3]heptane-2,6-dicarboxylic acid (Fecht's acid) was investigated in zinc(II) and ytterbium(III) MOFs, which were compared with analogous MOFs of a similarly-sized aromatic ligand, terephthalic acid. The Fecht's acid MOFs demonstrated a relatively improved thermal stability, as well as reduced degree of interpenetration, however, no preservation of permanent porosity.

The results described in this thesis have highlighted the versatility of incorporating rigid aliphatic units into the backbones of coordinating ligands. There are some common trends observed between the coordination

assemblies of increasingly complex aliphatic units. The short contacts arising from the non-aromatic components are most likely to originate at the protonated ligand heteroatoms, as these are the strongest hydrogen bond donors. If these are not available, the interactions originate at the most polarised aliphatic protons, which are adjacent to the ligand heteroatoms, which in these complexes are limited to nitrogen and oxygen. If these aliphatic protons are not accessible, the close contacts will originate at the most sterically accessible aliphatic protons, such as the contacts observed in the complexes of Fecht's acid in Chapter 5, and in some complexes in Chapter 3, in which tropinone CH_2 moieties which are not adjacent to a heteroatom are involved in the short contacts. If no aliphatic protons are accessible, weak contacts with aromatic protons are most likely, and this trend is common among complexes of the picolyl-derived ligands, and tropinone-derived ligands. The incorporation of an aliphatic unit into these ligands (in particular in the ligands discussed in Chapter 3), prevent the formation of any significant π-π interactions to occur along the entire length of the ligand molecule, instead limiting them to the aromatic functionalities at the ends of the ligands. As the aromatic moieties are most often coordinating, they are close to the sterically encumbered metal centres, which further restricts the extent of overlap between adjacent π-systems.

The gas sorption properties of complex **3.6** demonstrate that fused-ring aliphatic ligands are capable of maintaining permanent porosity within MOFs, and the maintenance of this porosity after exposure to atmospheric water vapour suggests some level of protection of the metal-ligand coordination bond from hydrolysis or displacement by water, which possibly occurs due to the presence of the bulky hydrophobic tropinone core. Furthermore, the improved thermal stability and reduced interpenetration exhibited by complexes of the spirocyclic ligand **5.1**, relative to analogous aromatic MOFs, further reiterated the potential advantages to replacing aromatic ligands with rigid aliphatic ligands in the future development of the field of application-driven coordination assemblies.

Exploring a variety of coordinating and non-coordinating *N*-aryl substitutions of the cyclohexyl-bridged bis-*R*-tropinone core, unexpectedly led to the consistent formation of the truncated tetrahedron $M_{12}L_6$ silver(I) coordination cages. While maintaining the steric influence of an aryl substituent, its chemical

properties and associated close contacts can be fine-tuned with the careful selection of aryl functionalities, paving the way for further design of convergent ligands of this nature for coordination cages. The much less sterically hindered alkyl-substituted ligand led to a smaller, cubic M_8L_6 cage, which demonstrated a much higher degree of ligand flexibility. The dynamic assembly process of these cages was highlighted by the partial substitution of a ligand tropinone moiety with an acetone imine, and further exploration of the assembly process *via* NMR analysis revealed that the cages persist in solution and are relatively unaffected by the presence of other anions *in-situ*, which is reflective of the solid-state observations. The absence of any extended conjugated systems in the ligands, combined with their robustness *in-situ* and reliable preferred stoichiometries and geometries could present this method of ligand design as a desirable avenue for the formation of optically transparent robust coordination cages with novel but consistent structural types and tuneable chemical properties.

6.2 Future Work

While the work presented in this thesis demonstrates the feasibility of incorporating a variety of geometrically diverse rigid aliphatic ligands into both discrete and polymeric coordination materials, these results showcase the novel space for ligands of this nature within the field of metallosupramolecular chemistry. To this end, several promising routes for further ligand design were identified, and some preliminary work has been carried out in their syntheses. As much of this work has been carried out in the final weeks of this research, full characterisation has not been carried out due to time constraints, and the ligands discussed are offered as potential avenues for further expansion of the library of rigid aliphatic ligands.

6.2.1 Ligands Derived from α,α′-bis(*N*-tropinonyl)-*p*-xylene

The complexes of *N*-functionalised tropinone ligands discussed in Chapters 3 and 4 demonstrate the variety of ligands that can be achieved using relatively well-known chemistry, leading to both convergent and divergent coordinating ligands for both discrete and polymeric coordination assemblies. However, thus far, these functionalisations have been limited to mono-tropinone precursors. α,α′-bis(*N*-tropinonyl)-*p*-xylene (Figure 6.1), offers an interesting alternative starting point, allowing for the same established chemistry to be utilised for its functionalisation, however, yielding ligands with significantly different connectivities.

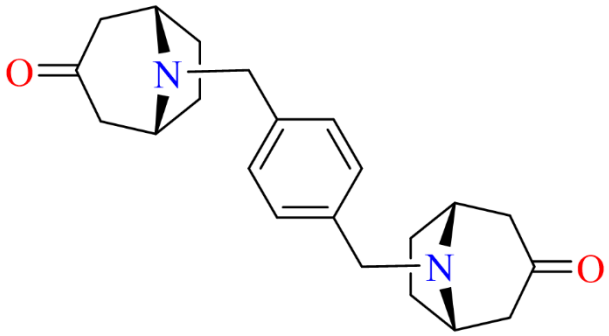

Figure 6.1. Structure of α,α′-bis(N-tropinonyl)-p-xylene

To expand the functionalisations explored in Chapter 3, some initial Claisen-Schmidt condensations were carried out to generate α-functionalised ligands with pyridyl, benzonitrile and benzoic acid moieties. The pyridyl-functionalised ligand was characterised using SCXRD to gain some initial insight into the potential coordination geometries of the ligand (Figure 6.2)

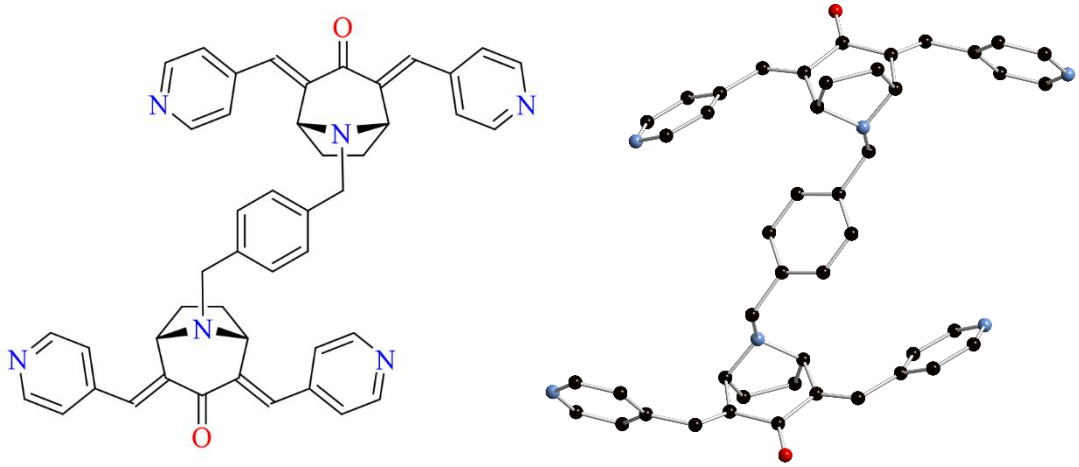

Figure 6.2. Schematic structure (left) and SCXRD-derived structure (right) of pyridyl-functionalised α,α′-bis(N-tropinonyl)-p-xylene, with hydrogen atoms omitted for clarity

The resultant divergent tetratopic ligands have not yet been screened with metal ions to investigate their coordination chemistry, however, this could lead to distinct coordination modes and crystal packing to those observed in the complexes discussed in Chapter 3. This starting point could also be used for the expansion of the convergent nitrogen-rich ligands discussed in the context of silver(I) coordination cages in Chapter 4, by functionalising at the carbonyl functionalities of both tropinone cores. To expand this further, an aliphatic linker such as cyclohexane could be used to replace the xylyl moiety that connects the two tropinone units, to further increase the aliphatic character of the resultant ligands, as well as to further diversify the ligand geometries.

6.2.2 Quaternary Tropinone Ligands

A second promising route for the expansion of tropinone-derived ligands for coordination assemblies is the synthesis of quaternary tropinone ligands, by the addition of a coordinating functionality to the apical amine of an *N*-functionalised tropinone precursor. There have been several instances in structures presented in this thesis in which an amine nitrogen atom (either in morpholine/piperidine in complexes **2.3**, **2.5**, **2.6** and **2.7** in Chapter 2, or in tropinone in complex **3.5** in Chapter 3) has been protonated in order to balance the overall

change of the coordination complex. In some cases, this has resulted in the formation of hydrogen bonds or other short contacts originating at the protonated NH moieties.

To achieve the desired charge balance of the overall complex without creating any strong hydrogen bond donors, the formation of a quaternary salt at the tropinone amine could be a desirable route to achieve this goal. The coordination geometries arising from these quaternisation reactions would also significantly differ from the ditopic and tritopic ligands discussed in this thesis. These transformations could also be combined with the aldol condensations exploited in Chapter 3, yielding a new library of ligands with more complex coordination geometries than have been previously discussed ditopic and tritopic ligands, without promoting strong interactions between adjacent networks by generating a strong hydrogen bond donor.

6.2.3 1,1′-Biadamantanyl-Derived Ligands

Finally, to expand the fused-ring ligands beyond the tropinone core, 1,1′-biadamantane-derived ligands contain a larger rigid aliphatic core to potentially impart water-stability to its resultant coordination complexes. 1,1′-Biadamantane (Figure 6.3) has been synthesised from the dimerization of 1-bromoadamantane in the presence of sodium.

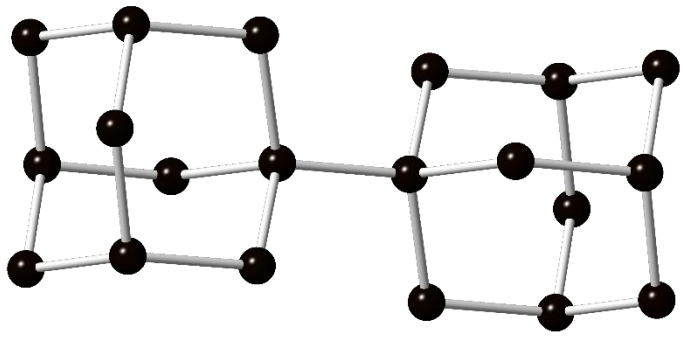

Figure 6.3. Structure of 1,1′-biadamantane, with hydrogen atoms omitted for clarity

This, in turn, can be brominated in the presence of a catalyst to yield 1,1′-biadamantane with varying numbers of bromine per molecule, according to Scheme 6.1.[1]

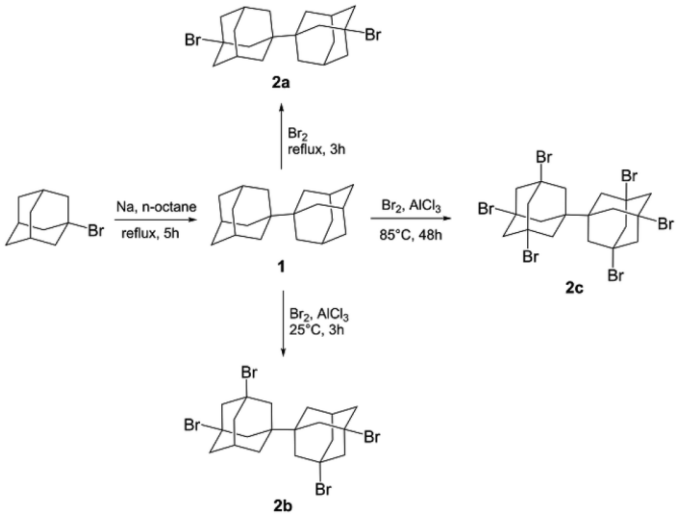

Scheme 6.1. Synthetic scheme for the synthesis and subsequent bromination of 1,1′-biadamantane[1]

From the brominated analogues of the biadamantyl core, a variety of coordinating functionalities can be added to this core, resulting in ditopic, tetratopic and hexatopic coordinating ligands, in which unique relative orientations of the coordinating groups arise from the non-planar core.

The work presented in the preceding chapters of this thesis highlight not only the possibility of incorporating these non-aromatic cores into the backbones of MOF ligands, but also the range of exciting geometries that are achievable with these novel and unusual coordinating ligands. Some examples demonstrate that the rigid aliphatic units are indeed capable of supporting permanent porosity within these materials which creates an interesting comparison to the traditional aromatic ligands often employed in metal-organic complexes. While a variety of complexes have been synthesised and discussed, the work reveals the wide scope for future investigations of tropinone-derived or other rigid aliphatic ligands in coordination materials. Beyond the work presented in this thesis, there are likely many routes to further explore the potential of these ligands, only some of which have been outlined in this chapter.

6.3 References

1. X. Lai, J. Guo, S. Fu and D. Zhu, *RSC Advances*, 2016, **6**, 8677–8680.

Chapter 7

· Experimental Data ·

7.1 Materials and Methods

All starting materials, reagents and solvents were purchased from Sigma-Aldrich, TCI, Alfa Aesar or Fluorochem, were of reagent grade or better and were used as received. Melting points were recorded in air using a Stuart digital melting point apparatus and are uncorrected. High-resolution mass spectra were recorded by the EPSRC National Mass Spectrometry Facility at Swansea University. All reactions were carried out in air, unless otherwise specified.

Infrared Spectroscopy

All infrared spectra were recorded using a Thermo Scientific Nicolet iS10 instrument operating in ATR sampling mode. The following abbreviations are used to describe the appearance of the peaks in the spectra: w (weak), m (medium), s (strong) and br (broad).

Elemental Analysis

Elemental analysis was performed using ThermoFlash 2000 CHNS analyser calibrated against sulfanilamide with vanadium pentoxide as a combustion aid. Elemental analysis for fluorine-containing coordination complexes was carried out by the Elemental Analysis service at London Metropolitan

University, and were weighed using Mettler Toledo high precision scale and analysed using a ThermoFlash 2000 analyser.

NMR Spectroscopy

NMR spectroscopy was performed on a Bruker Avance III HD 400 spectrometer operating at 400 MHz for ^{1}H NMR and 101 MHz for ^{13}C NMR at 298 K. The NMR spectra discussed in Chapter 4 and its related compounds were recorded on a Bruker Avance 200, a Bruker Avance NEO 500, or a Bruker Avance 600 spectrometer, also at 298 K. All samples were dissolved in commercially available deuterated solvents $CDCl_3$, d_6-DMSO, CD_3CN or d_6-C_3D_6O, which were obtained from the Cambridge Isotope Laboratories. Chemical shifts are reported in parts per million (ppm) and coupling constants (*J*) are reported in Hertz (Hz), and all spectra were referenced to the residual solvent signal and/or tetramethylsilane (at 0.00 ppm). The multiplicity of each reported signal is indicated by: s (singlet), d (doublet), t (triplet), q (quartet), p (pentet), dd (doublet of doublets) or m (multiplet). NMR titration experiments were carried out by dissolving the free ligand in 600 μL of deuterated solvent, and adding a solution of specified concentration of the metal ion in the same solvent in 3 μL additions, and measuring ^{1}H NMR spectra after each subsequent addition. All spectra were analysed using the MestReNova software, and all figures showing NMR spectra were created in the same software.[1]

Thermogravimetric Analysis

Thermogravimetric analysis was performed with an STA1500 thermal analyser (Thorn Scientific Services), under an atmosphere of nitrogen and with a heating rate of 5 °C per minute up to 500 °C.

Gas Sorption Measurements

Gas sorption measurements were carried out using a Quantachrome Autosorb iQ using N_2 and CO_2 at N4.5 grade or better. Temperature control was provided by a liquid nitrogen dewar for N_2 measurements and a Julabo recirculating chiller for CO_2 measurements. Samples were activated prior to the adsorption measurements by soaking them in methanol for three days, and the solvent was replaced with fresh solvent

every twelve hours. Initial activation of the samples was performed at 100 °C under dynamic vacuum provided by a rotary oil pump followed by soaking under high vacuum provided by a turbomolecular pump at 100 °C for twelve hours.

Single-Crystal X-Ray Diffraction

Structural and refinement parameters are presented in the crystallographic tables in Appendix 1. X-ray diffraction data were collected on a Bruker D8 Quest ECO with graphite monochromated Mo Kα (λ = 0.71073 Å) radiation. Crystals were mounted on Mitegen micromounts in NVH immersion oil, and all collections were carried out at 150 K using an Oxford cryostream. Data collections and reductions were carried out using the Bruker APEX-3 suite of programs,[2] with multi-scan adsorption corrections performed with SADABS.[3] All datasets were solved using intrinsic phasing methods with SHELXT[4] and refined on F^2 with SHELXL,+5 within the Olex-2 GUI.[6] Non hydrogen atoms were refined with anisotropic displacement parameters. Most hydrogen atoms were assigned in calculated positions with a riding model, with selected hydrogen atoms involved in hydrogen bonding interactions manually assigned from Fourier residuals with distance restraints when appropriate, and isotropic displacement parameters of 1.2 times the isotropic equivalent of their carrier atoms. Graphical representations of crystallographic data were prepared using CrystalMaker package,[7] and relevant Hirshfeld surface maps, discussed in Chapter 2, were prepared using the CrystalExplorer package.[8] In complexes containing significant voids (complexes **2.3**, **3.5**, **3.6**, **3.7**, **C4.1**, **C4.2**, **C4.2a** and **C4.3**) containing highly disordered solvent molecules which could not be modelled, the SQUEEZE routine was carried out.[9] In these instances, the lattice solvation was estimated by a combination of (where appropriate) elemental analysis, thermogravimetric analysis and the calculated residual electron count. Where appropriate, disorder was modelled by location of atoms from the Fourier residuals. Their positions and ADPs were refined either freely or with restraint strategies with mostly involved DFIX commands using bond lengths from well-resolved equivalent crystallographic components. The disordered components were assigned different part numbers to ensure that two chemical entities were not occupying the same crystallographic space at the same time. Chemical

occupancies of the disordered components were determined by the size of the corresponding ADPs and were either refined based on a free variable or fixed to the nearest sensible fractional occupancy, to avoid over-parameterizing. In the cases of complexes **3.1** and **3.4**, due to the relatively low data resolution, the data was used simply as a connectivity model. The RIGU command was used in the refinement of complexes **3.6**, **3.7**, **C4.1**, **C4.2**, **C4.2a** and **C4.3**, when rigid unit(s) had large ADPs which were beyond reason, in order to obtain a better model of the data. The AFIX66 command was used for complexes **C4.2** and **C4.2a**, to model the phenyl rings which were not sufficiently well-resolved. The FRAG command was used in complex **C4.3**, to model the encapsulated triflate anion within the cage, as this was highly disordered. Crystallographic data for all compounds is included in .cif format as electronic supplementary information, at https://bit.ly/3e4C8ev.

Powder X-Ray Diffraction

X-ray powder diffraction patterns were measured with a Bruker D8 Avance diffractometer with Cu Kα radiation (λ = 1.54178 Å). All samples were mounted on a zero-background silicon single crystal sample holder. All samples were measured at room temperature and compared against the simulated patterns from the single crystal datasets (150 K).

7.2 Ligand Synthesis

Chapter 2

Synthesis of *N*-(4-picolyl)piperidine, **L2.1**

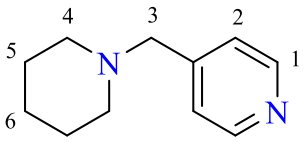

K_2CO_3 (0.500 g, 3.62 mmol), KI (20 mg, 0.12 mmol), piperidine (0.84 mL, 8.5 mmol) and 4-chloromethylpyridine (0.46 g, 2.8 mmol) were heated at reflux in MeCN (50 mL) for 2 hours. The solution was then filtered while hot, cooled to room temperature, and concentrated *in vacuo*, giving a brown solid. This was then dissolved in water (20 mL) and brought to pH 10 using 2M $NaOH_{(aq)}$ and the product was extracted with EtOAc (3 × 20 mL). The organic layers were combined and dried over $MgSO_4$, and the solvent was removed *in vacuo*, to give a red oil of mass 274 mg (55%). δ_H (400 MHz, $CDCl_3$) (ppm) 8.52 (dd, 2H, **H1**, *J* = 4.4, 1.5 Hz), 7.26 (dd, 2H, **H2**, *J* = 1.0, 4.4 Hz), 3.46 (s, 2H, **H3**), 2.37 (t, 4H, **H4**, *J* = 4.5 Hz), 1.59 (m, 4H, **H5**), 1.45 (m, 2H, **H6**); δ_C (101 MHz, $CDCl_3$) (ppm) 149.7 (**C1**), 148.2 (4-Py**C**), 123.9 (**C2**), 62.6 (**C3**), 54.7 (**C4**), 26.0 (**C5**), 24.2 (**C6**); $\tilde{\nu}_{max}/cm^{-1}$ (ATR): 3385 w br, 3070 w, 3026 w, 2932 s, 2852 m, 2793 m, 2758 m, 2727 w, 1930 w, 1724 w, 1639 w, 1602 s, 1560 m, 1493 w, 1468 w, 1454 m, 1442 m, 1414 s, 1392 w, 1370 m, 1349 m, 1319 m, 1299 m, 1278 m, 1255 w, 1220 w, 1197 w, 1154 m, 1112 s, 1064 m, 1038 s, 992 s, 962 w, 907 w, 863 s, 828 w, 803 s, 779 s, 728 w, 669 w, 645 w, 609 s; *m/z* (ESMS) 177.1386 ([M + H+], calculated for $C_{11}H_{17}N_2$ 177.1392).

Synthesis of *N*-(4-picolyl)morpholine, **L2.2**

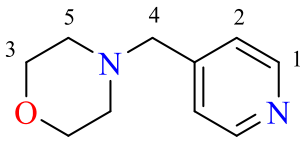

K_2CO_3 (0.500 g, 3.62 mmol), KI (20 mg, 0.12 mmol), morpholine (0.73 mL, 9.2 mmol) and 4-chloromethylpyridine (0.46 g, 2.8 mmol) were heated at reflux in MeCN (50 mL) for two hours. After this, the solution was filtered while hot, cooled to room temperature and concentrated *in vacuo*, giving an orange solid. This was dissolved in water (20 mL) and basified to pH 10 using 2M $NaOH_{(aq)}$ and the product was extracted with EtOAc (3 × 20 mL). The organic layers were combined and dried over $MgSO_4$, and the solvent was

removed *in vacuo*, to give an orange oil of mass 266 mg (53%). δ_H (400 MHz, $CDCl_3$) (ppm) 8.55 (dd, 2H, **H1**, *J* = 4.4, 1.5 Hz), 7.29 (m, 2H, **H2**), 3.73 (t, 4H, **H3**, *J* = 4.7 Hz), 3.50 (s, 2H, **H4**), 2.45 (t, 4H, **H5**, *J* = 4.4 Hz); δ_C (101 MHz, $CDCl_3$) (ppm) 149.8 (C1), 147.2 (4-Py**C**), 123.9 (**C2**), 66.9 (**C3**), 62.1 (**C4**), 53.7 (**C5**); $\tilde{\nu}_{max}/cm^{-1}$ (ATR): 3365 m br, 3231 w br, 3071 w, 3029 w, 3956 m, 2914 w, 2855 m, 2810 m, 2766 w, 2685 w, 1937 w, 1731 w, 1603 s, 1561 m, 1494 w, 1454 m, 1416 s, 1398 w, 1371 w, 1355 m, 1321 m, 1291 m, 1270 m, 1242 w, 1223 w, 1206 w, 1112 s, 1068 m, 1035 m, 1008 s, 959 w, 915 m, 866 s, 812 m, 789 m, 764 w, 729 w, 629 w, 602 m; *m/z* (ESMS) 179.1179 ([M + H+], calculated for $C_{10}H_{15}N_2O$ 179.1184).

Chapter 3

Synthesis of *N*-(4-cyanobenzyl)nortropinone, **L3.1a**

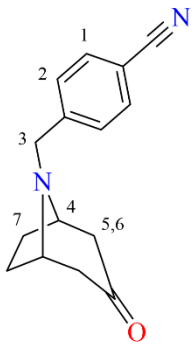

Nortropinone hydrochloride (0.720 g, 4.44 mmol), methyl-3-bromomethylbenzoate (1.02 g, 4.44 mmol), K_2CO_3 (1.84 g, 13.3 mmol) and KI (20 mg, 0.12 mmol) were heated at reflux in MeCN (30 mL) for 6 hours. The solution was then filtered while hot, cooled to room temperature and the solvent was removed *in vacuo*, yielding 0.88 g (83%) of a white crystalline solid. The structure was confirmed using SCXRD, m.p. 97 – 100 °C. δ_H (400 MHz, $CDCl_3$) (ppm) 7.64 (dt, 2H, **H1,** *J* = 1.7, 8.3 Hz), 7.56 (d, 2H, **H2,** *J* = 8.6 Hz), 3.86 (s, 2H, **H3**), 3.46 (m, 2H, **H4**), 2.67 (m, 2H, **H5**/**H6**), 2.24 (m, 2H, **H6**/**H5**), 2.13 (m, 2H, **H7**), 1.67 (m, 2H, **H7**); δ_C (101 MHz, $CDCl_3$) (ppm) 209.6 (R_2**C**=O), 145.1 (Ar**C**-CN), 132.3 (**C1**), 129.8 (**C2**), 118.9 (**C**N), 111.0 (Ar**C**-CH_2), 59.0 (**C3**), 55.1 (**C4**), 48.4 (**C5** & **C6**), 27.8 (**C7**); $\tilde{\nu}_{max}/cm^{-1}$ (ATR): 2955 w, 2900 w, 2883 w, 2222 m, 1709 s, 1604 m, 1503 m, 1471 w, 1454 w, 1439 m, 1413 w, 1394 m, 1371 w, 1349 m, 1344 s, 1324 w, 1306 m, 1274 m, 1264 m, 1236 w, 1193 s, 1163 w, 1161 w, 1158 w, 1121 m, 1110 m, 1087 m, 1085 m, 1056 w, 1042 m, 1007 s, 975 w, 954 w, 951 w, 907 m, 824 s, 822 s, 786 w, 781 m, 755 m, 733 w, 718 m, 701 w, 673 w, 651 m, 631 w, 601 w; *m/z* (ESMS) 241.1341 ([M + H+], calculated for $C_{15}H_{17}N_2O$ 241.1345).

Synthesis of *N*-((3-carboxymethyl)benzyl)nortropinone, **L3.3a**

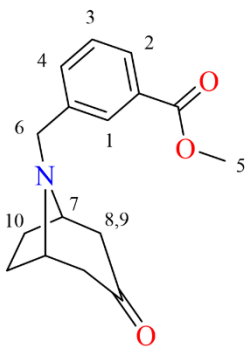

Nortropinone hydrochloride (0.720 g, 4.44 mmol), methyl-3-bromomethylbenzoate (1.02 g, 4.44 mmol), K_2CO_3 (1.84 g, 13.3 mmol) and KI (20 mg, 0.12 mmol) were heated at reflux in MeCN (30 mL) for 6 hours. The solution was then filtered while hot, cooled to room temperature and the solvent was removed *in vacuo*, yielding 1.00 g (82%) of a pale-yellow solid, m.p. 63 – 67 °C; δ_H (400 MHz, $CDCl_3$) (ppm) 8.07 (s, 1H, **H1**), 7.95 (dt, 1H, **H2,** *J* = 1.5, 7.6 Hz), 7.65 (d, 1H, **H3,** *J* = 7.6 Hz), 7.43 (t, 1H, **H4,** *J* = 7.6 Hz), 3.93 (s, 3H, **H5**) 3.77 (s, 2H, **H6**), 3.47 (p, 2H, **H7,** *J* = 2.2 Hz), 2.70 (dd, 2H, **H8**/**H9,** *J* = 4.2, 16.1 Hz), 2.25 (d, 2H, **H9**/**H8,** *J* = 15.7 Hz), 2.13 (m, 2H, **H10**), 1.65 (m, 2H, **H10**); δ_C (101 MHz, $CDCl_3$) (ppm) 210.1 (R_2**C**=O), 167.1 (R**C**O_2), 139.9 (Ar**C**-COOMe) 133.0 (**C3**), 130.3 (Ar**C**-CH_2), 129.6 (**C1**), 128.6 (**C2**), 128.5 (**C4**), 58.7 (**C5**), 55.0 (**C6**), 52.1 (**C7**), 48.4 (**C8** & **C9**), 27.8 (**C10**); $\tilde{\nu}_{max}/cm^{-1}$ (ATR): 3419 w br, 3070 w, 2976 m, 2952 m, 2942 m, 2903 w, 2886 m, 2833 w, 2825 m, 1981 w, 1934 w, 1887 w, 1725 s, 1705 s, 1601 w, 1589 m, 1484 w, 1465 w, 1455 w, 1425 m, 1416 m, 1372 w, 1356 m, 1344 m, 1301 m, 1300 m, 1285 s, 1231 m, 1193 s, 1004 w, 979 m, 956 m, 945 m, 913 m, 905 m, 863 m, 832 w, 828 m, 795 m, 781 m, 755 s, 734 m, 718 s, 695 m, 674 m, 630 w; *m/z* (ESMS) 274.1438 ([M + H+], calculated for $C_{16}H_{20}NO_3$ 274.1443).

Synthesis of *N*-((4-carboxymethyl)benzyl)nortropinone, **L3.4a**

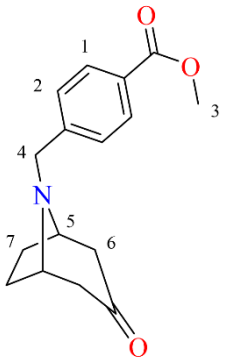

Nortropinone hydrochloride (0.720 g, 4.44 mmol), methyl-4-bromomethylbenzoate (1.02 g, 4.44 mmol), K_2CO_3 (1.84 g, 13.3 mmol) and KI (20 mg, 0.12 mmol) were heated at reflux in MeCN (30 mL) for 6 hours. The solution was then filtered while hot, cooled to room temperature and the solvent was removed *in vacuo*, yielding 0.92 g (75%) of a orange solid, m.p. 49 – 51 °C; δ_H (400 MHz, $CDCl_3$) (ppm) 8.02 (dt, 2H, **H1**, *J* = 2.0, 8.6 Hz), 7.51 (d, 2H, **H2** *J* = 8.6 Hz), 3.92 (s, 3H, **H3**) 3.80 (s, 2H, **H4**), 3.48 (m, 2H, **H5**), 2.68 (dd, 2H, **H6**, *J* = 4.4, 16.1 Hz), 2.23 (d, 2H, **H6**, *J* = 15.7 Hz), 2.13 (m, 2H, **H7**), 1.67 (m, 2H, **H7**); δ_C (101 MHz, $CDCl_3$) (ppm) 210.0 (R_2**C**=O), 167.0 (**C**O_2Me), 144.8

(Ar**C**-COOMe), 129.8 (Ar**C**-CH_2), 129.1 (**C1**), 128.3 (**C2**), 58.8 (**C3**), 55.2 (**C4**), 52.1 (**C5**), 48.4 (**C6**), 27.8 (**C7**); $\tilde{\nu}_{max}/cm^{-1}$ (ATR): 3410 w br, 2940 w, 2882 w, 1723 s, 1711 s, 1608 m, 1599 m, 1567 w, 1480 w, 1446 w, 1434 m, 1411 m, 1372 w, 1365 w, 1344 m, 1290 m, 1273 s, 1249 s, 1167 m, 1164 m, 1105 s, 1089 s, 1015 m, 1014 sm 961 m, 909 w, 865 m, 834 w, 829 w, 791 m, 755 s, 736 w, 693 m, 660 w, 627 w; *m/z* (ESMS) 274.1441 ([M + H+], calculated for $C_{16}H_{20}NO_3$ 274.1443).

Synthesis of *N*-(4′-cyanobenzyl)-2,4-bis(4-vinylpyridine)tropin-3-one, **L3.1**

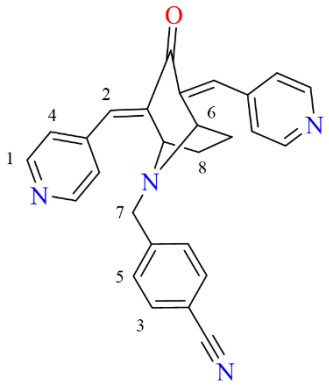

N-(4-cyanobenzyl)nortropinone (**L3.1a**) (0.350 g, 1.44 mmol) was dissolved in EtOH (10 mL) under the atmosphere of nitrogen. A solution of 4-pyridinecarboxaldehyde (0.27 mL, 2.9 mmol) in EtOH (10 mL) was added to this *via* syringe, and the combined solutions were stirred for 5 minutes. 2M $NaOH_{(aq)}$ (2 mL) was added dropwise, and the solution was stirred under N_2 for 2 hours at room temperature, after which a large amount of yellow precipitate had appeared in the flask. Water (20 mL) was added to this, and the yellow precipitate was isolated *via* vacuum filtration and washed with water several times, resulting in a yield of 0.460 g (76%), m.p. 176 – 179 °C. δ_H (400 MHz, DMSO-d_6) (ppm) 8.61 (d, 4H, **H1**, *J* = 5.1 Hz), 7.60 (s, 2H, **H2**), 7.54 (d, 2H, **H3**, *J* = 7.9 Hz), 7.33 (d, 4H, **H4**, *J* = 5.1 Hz), 7.27 (d, 2H, **H5**, *J* = 7.9 Hz), 4.26 (m, 2H, **H6**), 3.69 (s, 2H, **H7**), 2.55 (m, 2H, **H8**), 1.96 (m, 2H, **H8**); δ_C (101 MHz, DMSO-d_6) (ppm) 187.2 (**C**=O), 150.0 (**C1**), 144.3 (O=C-**C**), 141.7 (**C2**), 141.6 (Ar**C**-CN), 132.6 (α-Ar**C**-CH), 132.0 (**C3**), 129.3 (**C5**), 124.1 (**C4**), 118.7 (**C**N), 110.0 (*N*-Ar**C**-CH_2), 58.6 (**C7**), 51.9 (**C6**), 29.2 (**C8**); $\tilde{\nu}_{max}/cm^{-1}$ (ATR): 3330 br s, 2950 w, 2837 w, 2227 m, 1675 m, 1622 m, 1591 s, 1542 m, 1498 w, 1492 w, 1469 w, 1435 w, 1411 s, 1388 w, 1375 w, 1347 m, 1326 w, 1310 m, 1307 m, 1275 m, 1271 m, 1221 s, 1215 s, 1178 s, 1123 w, 1102 w, 1099 m, 1089 m, 1070 m, 1054 m, 1048 s, 1022 m, 998 w, 991 m, 970 w, 937 m, 932 s, 900 m, 899 m, 865 m, 865 m, 817 s, 774 w, 760 w, 735 m, 696 w, 660 w, 647 w, 615 m, 601 m; *m/z* (ESMS) 419.1870 ([M + H+], calculated for $C_{27}H_{23}N_4O$ 419.1872).

Synthesis of 2,4-bis(4-carboxybenzylidene)tropin-3-one, **L3.2**

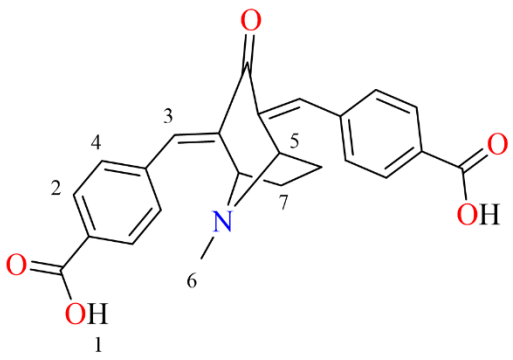

Tropinone (0.200 g, 1.44 mmol) was dissolved in EtOH (10 mL) under the atmosphere of nitrogen. A solution of 4-formylbenzoic acid (0.43 g, 2.9 mmol) in EtOH (10 mL) was added to this *via* syringe, and the combined solutions were stirred for 5 minutes. 2M $NaOH_{(aq)}$ (2 mL) was added dropwise, and the solution was stirred under N_2 for 2 hours at room temperature. After this, the solution was acidified with glacial acetic acid. The yellow solid was then isolated *via* vacuum filtration and washed several times with water, resulting in a yield of 0.320 g (55%), m.p. >300 °C. δ_H (400 MHz, DMSO-d_6) (ppm) 12.29 (s, 2H, **H1**), 8.05 (d, 4H, **H2**, *J* = 8.3), 7.83 (s, 2H, **H3**), 7.63 (d, 2H, **H4**, *J* = 8.4), 5.05 (m, 2H, **H5**), 3.03 – 2.79 (m, 5H, **H6** & **H7**), 2.33 (m, 2H, **H7**); δ_C (101 MHz, DMSO-d_6) (ppm) 193.1 (**C**=O), l66.7 (**C**OOH), 137.7 (O=C-**C**), 132.2 (**C3**), 131.2 (**C2**), 130.4 (Ar**C**-COOH), 130.2 (**C4**), 129.9 (Ar**C**-CH), 62.5 (**C6**), 46.5 (**C5**), 25.5 (**C7**); $\tilde{\nu}_{max}/cm^{-1}$ (ATR): 3460 w br, 3389 w, 3102 w, 2892 m, 2933 w, 2810 w, 2714 w, 2567 w, 1713 s, 1680 m, 1614 s 1584 m, 1566 m, 1505 w, 1481 w, 1444 w, 1414 m, 1379 s, 1310 m, 1293 m, 1241 s, 1226 s, 1190 s, 1182 m, 1156 s, 1107 s, 1059 s, 1020 w, 1016 m, 999 w, 968 w, 960 w, 955 m, 930 m, 905 w, 861 m, 852 m, 809 m, 772 m, 768 m, 754 s, 724 w, 723 m, 690 s, 680 m, 645 w, 600 w; *m/z* (ESMS) 200.5642 ([M − 2H+], calculated for $C_{24}H_{19}NO_5$ 200.5637).

Synthesis of *N*-(3′-carboxybenzyl)-2,4-bis(4-carboxybenzylidene)tropin-3-one, **L3.3**

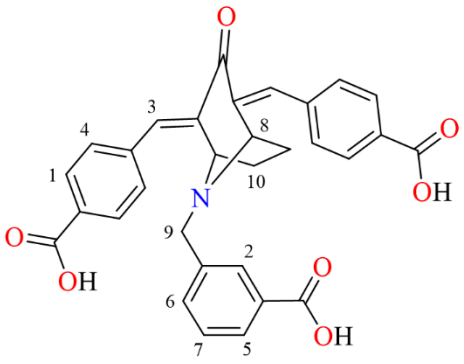

N-((3-carboxymethyl)benzyl)nortropinone (**L3.3a**) (0.790 g, 2.88 mmol) and methyl-4-formylbenzoate (0.950 g, 5.76 mmol) were dissolved in EtOH (30 mL). KOH (3.38 g, 60 mmol) was dissolved in H_2O (10 mL) and this was added dropwise to the first solution. This was sealed and stirred at room temperature for 72 hours. This solution was slowly acidified with glacial acetic acid until there was no more yellow precipitate forming upon addition of the acid. The yellow solid was then isolated *via* vacuum filtration and washed with EtOH, MeOH and finally with Et_2O, to give 1.130 g of the dry product as a yellow solid (75%), m.p. >300 °C. δ_H (400 MHz, DMSO-d_6) (ppm) 7.93 (d, 4H, **H1**, *J* = 7.8 Hz), 7.71 (s, 1H, **H2**), 7.70 (s, 2H, **H3**), 7.42 (d, 4H, **H5**, *J* = 8.0 Hz), 7.19 (d, 1H, **H6**, *J* = 7.6 Hz), 7.10 (t, 1H, **H7**, *J* = 7.6 Hz), 4.35 (m, 2H, **H8**), 3.64 (s, 2H, **H9**), 2.57 (m, 2H, **H10**), 1.94 (m, 2H, **H10**); δ_C (101 MHz, DMSO-d_6) (ppm) 187.3 (**C**=O), 167.7 (**C**OOH), 139.6 (**C2**), 138.5 (*N*-**C**-COOH), 137.0 (O=C-**C**), 135.1 (**C5**), 134.4 (**C6**), 132.9 (**C7**), 131.9 (**C3**), 129.8 (**C1**), 129.5 (α-Ar**C**-COOH), 129.3 (**C4**), 127.8 (α-Ar**C**-CH), 58.6 (**C9**), 52.2 (**C8**), 29.4 (**C10**); $\tilde{\nu}_{max}/cm^{-1}$ (ATR): 3572 w, 3406 w br, 2845 w, 2496 w br, 1922 w br, 1688 s, 1671 s, 1605 s, 1584 s, 1499 m, 1435 w, 1394 s, 1323 w, 1297 w, 1264 s, 1234 m, 1221 w, 1206 w, 1176 s, 1128 w, 1109 m, 1085 m, 1028 m, 1013 m, 954 w, 935 m, 924 w, 907 w, 866 m, 854 w, 842 w, 832 w, 791 m, 782 m, 779 s, 757 s, 740 s, 700 s, 690 m, 683 m, 660 m, 650 m, 632 w, 613 w; *m/z* (ESMS) 522.1553 ([M − H+], calculated for $C_{31}H_{24}NO_7$ 522.1558).

Synthesis of *N*-(3′-carboxybenzyl)-2,4-bis(4-carboxybenzylidene)tropin-3-one, **L3.4**

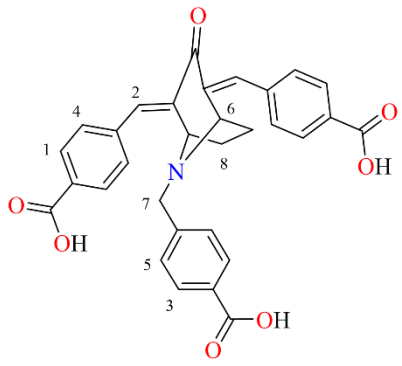

N-((4-carboxymethyl)benzyl)nortropinone (**L3.4a**) (0.790 g, 2.88 mmol) and methyl-4-formylbenzoate (0.950 g, 5.76 mmol) were dissolved in EtOH (30 mL). KOH (3.38 g, 60 mmol) was dissolved in H_2O (10 mL) and this was added dropwise to the first solution. This was sealed and stirred at room temperature for 72 hours. This solution was slowly acidified with glacial acetic acid until there was no more yellow precipitate forming upon addition of the acid. The yellow solid was then isolated *via* vacuum filtration and washed with EtOH, MeOH and finally with Et_2O, to give 1.260 g of the dry product as a yellow solid (84%), m.p. >300 °C. δ_H (400 MHz, DMSO-d_6) (ppm) 7.95 (d, 4H, **H1**, *J* = 8.3 Hz), 7.70 (s, 2H, **H2**), 7.63 (d, 2H, **H3**, *J* = 8.2 Hz), 7.48 (d, 4H, **H4**, *J* = 8.3 Hz), 7.16 (d, 2H, **H5**, *J* = 8.2 Hz), 4.33 (m, 2H, **H6**), 3.65 (s, 2H, **H7**), 2.56 (m, 2H, **H8**), 1.95 (m, 2H, **H8**); δ_C (101 MHz, DMSO-d_6) (ppm) 187.2 (**C**=O), 167.0 (*N*-**C**OOH), 166.9 (α-**C**OOH), 143.4 (Ar**C**-CH_2), 140.2 (O=C-**C**), 138.4 (*N*-**C**-COOH), 134.1 (**C3**), 131.2 (**C5**), 130.1 (**C2**), 129.6 (**C1**), 129.5(α-**C**-COOH), 129.0 (**C4**), 128.4 (α-Ar**C**-CH), 58.7 (**C7**), 52.0 (**C6**), 29.4 (**C8**); $\tilde{\nu}_{max}$/cm^{-1} (ATR): 2830 w, 2668 w br, 2544 w br, 2225 w, 1681 s, 1606 s, 1585 m, 1562 m, 1529 w, 1505 w, 1457 w, 1425 s, 1418 s, 1365 w, 1303 s, 1289 s, 1260 s, 1245 m, 1219 m, 1177 s, 1175 s, 1113 m, 1111 m, 1082 w, 1032 m, 1018 m, 983 w, 931 s, 863 s, 852 m, 834 m, 776 s, 755 s, 715 m, 696 m, 674 w, 646 w, 611 w; *m/z* (ESMS) 522.1553 ([M − H+], calculated for $C_{31}H_{24}NO_7$ 522.1558).

Chapter 4

Synthesis of *N*-(4-methylbenzyl)nortropinone, **L4.1a**

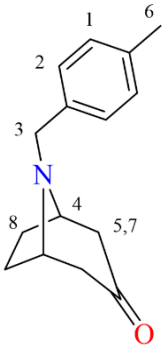

Nortropinone hydrochloride (0.720 g, 4.44 mmol), 4-methylbenzyl bromide (0.820 g, 4.44 mmol), K_2CO_3 (1.840 g, 13.31 mmol) and KI (20 mg, 0.12 mmol) were heated in MeCN (30 mL) at reflux for 6 hours. The solution was then filtered while hot, cooled to room temperature and the solvent was removed *in vacuo*, yielding a pale-brown solid of mass 0.88 g (86%), m.p. 41 – 42 °C. δ_H (400 MHz, $CDCl_3$) (ppm) 7.30 (d, 2H, **H1**, *J* = 7.9 Hz), 7.15 (d, 2H, **H2**, *J* = 7.8 Hz), 3.71 (s, 2H, **H3**), 3.49 (m, 2H, **H4**), 2.68 (dd, 2H, **H5**/**H7**, *J* = 16.4, 5.1 Hz), 2.35 (s, 3H, **H6**), 2.20 (m, 2H, **H7**/**H5**), 2.11 (m, 2H, **H8**), 1.62 (m, 2H, **H8**); δ_C (101 MHz, $CDCl_3$) (ppm) 210.6 (R_2**C**=O), 136.9 (Ar**C**-CH_3), 136.4 (Ar**C**-CH_2), 129.2 (**C1**), 128.5 (**C2**), 58.6 (**C3**), 55.0 (**C4**), 48.4 (**C5**), 27.9 (**C6**), 21.2 (**C7**); $\tilde{\nu}_{max}$/cm^{-1} (ATR): 3046 w, 3021 w, 3004 w, 2961 m, 2947 m, 2941 m, 2898 w, 2877 w, 2840 w, 2080 w br, 1910 w, 1808 w, 1709 s, 1696 s, 1673 m, 1657 m, 1619 w, 1514 m, 1463 w, 1447 w, 1411 m, 1369 w, 1345 s, 1321 m, 1302 m, 1277 m, 1235 w, 1229 m, 1217 w, 1193 m, 1178 w, 1147 m, 1132 s, 1107 m, 1068 w, 1058 w, 1022 m, 1010 m, 952 w, 942 m, 905 m, 864 w, 851 m, 813 s, 794 m, 774 s, 755 m, 727 m, 725 m, 703 m, 665 w, 615 s; *m/z* (ESMS) 230.1545 ([M + H+], calculated for $C_{15}H_{20}NO$ 230.1545).

Synthesis of *N*-((4-trifluoromethyl)benzyl)nortropinone, **L4.4a**

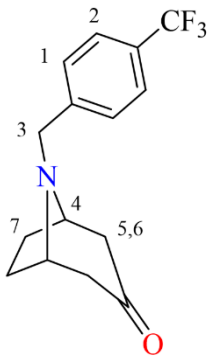

Nortropinone hydrochloride (0.720 g, 4.44 mmol), 4-(trifluoromethyl)benzyl bromide (1.60 g, 4.44 mmol), K_2CO_3 (1.840 g, 13.31 mmol) and KI (20 mg, 0.12 mmol) were heated in MeCN (30 mL) at reflux for 6 hours. The solution was then filtered while hot, cooled to room temperature and the solvent was removed *in vacuo*, yielding a brown oil of mass 1.14 g (91%). δ_H (400 MHz, $CDCl_3$) (ppm) 7.60 (d, 2H, **H1**, *J* = 8.1 Hz), 7.55 (d, 2H, **H2**, *J* = 8.0 Hz), 3.80 (s, 2H, **H3**), 3.47 (m, 2H, **H4**), 2.68 (dd, 2H, **H5**/**H6**, *J* = 16.2, 4.8 Hz), 2.23 (m, 2H, **H6**/**H5**), 2.12 (m, 2H, **H7**), 1.66 (m, 2H, **H7**);

δ_C (101 MHz, $CDCl_3$) (ppm) 210.0 (R_2**C**=O), 143.7 (Ar**C**-CH_2**)**, 129.6 (q, Ar**C**-CF_3, *J* = 32.2 Hz), 128.7 (**C1**), 125.5 (q, **C2**, *J* = 3.7 Hz), 124.4 (q, **C**F_3, *J* = 272.4 Hz), 58.9 (**C3**), 55.1 (**C4**), 48.5 (**C5**), 27.9 (**C6**); $\tilde{\nu}_{max}/cm^{-1}$ (ATR): 3399 w, 3052 w, 2954 m, 2882 w, 2826 w, 2077 w, 1713 s, 1618 m, 1586 w, 1508 w, 1472 w, 1446 w, 1416 m, 1372 w, 1336 m, 1321 s, 1279 m, 1239 w, 1203 w, 1183 m, 1159 s, 1116 s, 1100 s, 1064 s, 1022 m, 1017 s, 1008 s, 971 w, 948 m, 907 m, 850 m, 826 s, 824 s, 782 m, 755 w, 721 m, 648 w, 642 m, 613 w, 611 w; *m/z* (ESMS) 284.1257 ([M + H+], calculated for $C_{15}H_{17}F_3NO$ 284.1262).

Synthesis of *trans*-1,4-di-[*N*-(4′′-methylbenzyl)-nortropin-3′-yliden]-diaminocyclohexane, **L4.1**

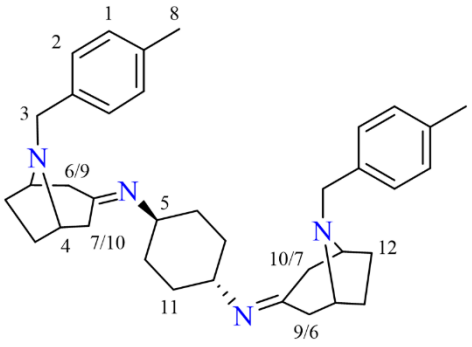

N-(4-methylbenzyl)nortropinone (**L4.1a**) (0.66 g, 2.88 mmol), *trans*-1,4-diaminocyclohexane (0.150 g, 1.31 mmol) and *para*-toluenesulfonic acid monohydrate (10 mg, 0.05 mmol) were added to toluene (30 mL), which was then heated under reflux in an apparatus equipped with a Dean-Stark condenser for 24 hours. and a Dean-Stark condensation was carried out for 24 hours at 160 °C. The solution was then filtered while hot and the solvent was removed *in vacuo* yielding a brown oil as the crude product, which was allowed to stand for 24 hours. This was then triturated with MeCN (50 mL), resulting in precipitation of a white solid which was isolated *via* vacuum filtration and washed several times with fresh MeCN, resulting in the pure product with a final mass of 0.290 g (41%), m.p. 187 – 188 °C. δ_H (400 MHz, $CDCl_3$) (ppm) 7.28 (d, 4H, **H1**, *J* = 8.1 Hz), 7.14 (d, 4H, **H2**, *J* = 8.3 Hz), 3.63 (s, 4H, **H3**), 3.40 – 3.28 (m, 6H, **H4** & **H5**), 2.67 (dd, 2H, **H6**/**H9**, *J* = 14.7, 3.7 Hz), 2.53 (m, 2H, **H7**/**H10**), 2.34 (s, 6H, **H8**), 2.29 (dd, 2H, **H9**/**H6**, *J* = 14.9, 3.8), 2.14 (m, 2H, **H10**/**H7**), 2.00 (m, 4H, **H12**/**H11**), 1.81 – 1.39 (m, 12H, **H11**/**H12** & **H12**/**H11**); δ_C (101 MHz, $CDCl_3$) (ppm) 167.5 (R_2**C**=N), 136.8 (Ar**C**-CH_3), 136.6 (Ar**C**-CH_2), 129.1 (**C1**), 128.6 (**C2**), 59.0 (**C4**), 58.4 (**C5**), 57.4 (**C4**), 55.3 (**C3**), 45.1 (**C6**/**C9**), 35.6 (**C7**/**C10**), 32.8 (**C11**), 32.7 (**C11**), 32.1 (**C11**), 32.0 (**C11**), 27.9 (**C12**), 26.9 (**C12**), 21.2 (**C8**); $\tilde{\nu}_{max}/cm^{-1}$ (ATR): 3042 w, 3017 w, 2946 m, 2926 m, 2889 w, 2885 m, 2854 m, 2821 w, 1898 w, 1715 w, 1658 s, 1616 w, 1513 s, 1466 m, 1444 s, 1417 m, 1379 w, 1373 w, 1348 s, 1336

s, 1317 s, 1313 m, 1292 m, 1264 m, 1242 m, 1227 w, 1210 m, 1177 w, 1157 m, 1134 m, 1101 s, 1079 m, 1066 w, 1046 w, 1011 s, 971 m, 964 m, 939 m, 913 w, 893 m, 888 w, 856 m, 845 m, 815 s, 795 m, 776 s, 757 m, 741 w, 703 w, 658 w, 608 m; *m/z* (ESMS) 537.3958 ([M + H+], calculated for $C_{36}H_{49}N_4$ 537.3957).

Synthesis of *trans*-1,4-di-[*N*-(4″-cyanobenzyl)-nortropin-3′-yliden]-diaminocyclohexane, **L4.2**

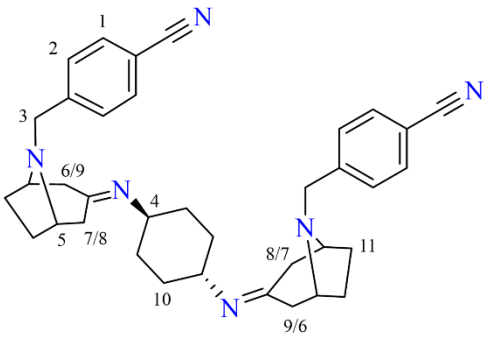

N-(4-cyanobenzyl)nortropinone (**L3.1a**) (0.830 g, 3.44 mmol), *trans*-1,4-diaminocyclohexane (0.200 g, 1.72 mmol) and *para*-toluenesulfonic acid monohydrate (10 mg, 0.05 mmol) were added to toluene (30 mL), which was then heated under reflux in an apparatus equipped with a Dean-Stark condenser for 24 hours. The solution was then filtered while hot and the solvent was removed *in vacuo* yielding a brown oil as the crude product, which was allowed to stand for 24 hours. This was then triturated with MeCN (50 mL), resulting in precipitation of a white solid which was isolated *via* vacuum filtration and washed several times with fresh MeCN, resulting in the pure product with a final mass of 0.440 g (46%), m.p. 160 – 162 °C. δ_H (400 MHz, $CDCl_3$) (ppm) 7.62 (d, 4H, **H1**, *J* = 8.3 Hz), 7.53 (d, 4H, **H2**, *J* = 8.2 Hz), 3.72 (s, 4H, **H3**), 3.39 – 3.28 (m, 6H, **H4** & **H5**), 2.67 (m, 2H, **H6**/**H9**), 2.57 (m, 2H, **H7**/**H8**), 2.29 (m, 2H, **H9**/**H6**), 2.17 (m, 2H, **H8**/**H7**), 2.02 (m, 4H, **H10**), 1.76 – 1.41 (m, 12H, **H10** & **H11**); δ_C (101 MHz, $CDCl_3$) (ppm) 166.9 (R_2**C**=N), 145.7 (R**C**≡N), 132.3 (**C1**), 129.1 (**C2**), 119.1 (Ar**C**-CN), 110.9 (Ar**C**-CH_2), 59.5 (**C5**), 58.8 (**C4**), 57.5 (**C5**), 55.5 (**C3**), 45.2 (**C6**/**C9**), 35.8 (**C7**/**C8**), 32.7 (**C10**), 32.6 (**C10**), 32.1 (**C10**), 32.0 (**C10**), 27.8 (**C11**), 26.9 (**C11**); $\tilde{\nu}_{max}/cm^{-1}$ (ATR): 3243 w br, 3068 w, 3049 w, 2934 m, 2933 m, 2923 m, 2898 w, 2883 m, 2852 m, 2230 s, 1710 w, 1658 s, 1610 m, 1568 m, 1506 m, 1466 m, 1445 s, 1414 m, 1375 w, 1347 s, 1337 m, 1315 m, 1294 w, 1262 w, 1242 m, 1227 w, 1209 m, 1196 w, 1178 m, 1158 m, 1133 m, 1105 m, 1078 m, 1065 w, 1044 m, 1037 m, 1009 s, 975 w, 963 m, 947 w, 938 m, 910 w, 893 m, 884 m, 863 s, 842 m, 830 m, 821

s, 795 m, 781 s, 755 w, 742 m, 701 m, 656 w, 605 m; *m/z* (ESMS) 559.3547 ([M + H+], calculated for $C_{36}H_{43}N_6$ 559.3549).

Synthesis of *trans*-1,4-di-[tropin-3′-yliden]-diaminocyclohexane, **L4.3**

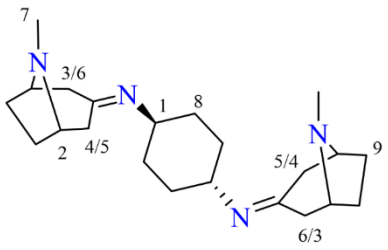

Tropinone (0.480 g, 3.44 mmol), *trans*-1,4-diaminocyclohexane (0.200 g, 1.72 mmol) and *para*-toluenesulfonic acid monohydrate (10 mg, 0.05 mmol) were added to toluene (30 mL), which was then heated under reflux in an apparatus equipped with a Dean-Stark condenser for 24 hours. The solution was then filtered while hot and the solvent was removed *in vacuo* yielding a brown oil as the crude product, which was allowed to stand for 24 hours. The product was then recrystallised from hot hexane, yielding the pure product as a white solid of mass 0.320 g (52%), m.p. 142 – 145 °C. δ_H (400 MHz, $CDCl_3$) (ppm) 3.34 (m, 2H, **H1**), 3.31 (m, 4H, **H2**), 2.67 (dd, 2H, **H3**/**H6**, *J* = 14.8, 3.7), 2.54 (m, 2H, **H4**/**H5**), 2.41 (s, 6H, **H7**), 2.29 (m, 2H, **H5**/**H4**), 2.16 (m, 2H, **H6**/**H3**), 2.02 (m, 4H, **H8**/**H9**), 1.72 – 1.35 (m, 12H, **H8**/**H9** & **H9**/**H8**); δ_C (101 MHz, $CDCl_3$) (ppm) 166.9 (**C**=N), 61.3 (**C2**), 60.6 (**C1**), 57.4 (**C2**), 44.5 (**C7**), 39.0 (**C3**/**C6**), 35.2 (**C4**/**C5**), 32.7 (**C8**), 32.6 (**C8**), 32.1 (**C8**), 32.0 (**C8**), 27.6 (**C9**), 26.6 (**C9**); $\tilde{\nu}_{max}/cm^{-1}$ (ATR): 3350 m br, 3186 m br, 2936 s, 2921 s, 2896 m, 2870 m, 2856 s, 2821 m, 2797 m, 2245 w br, 1979 w, 1711 m, 1648 s, 1473 m, 1445 s, 1418 m, 1413 m, 1354 s, 1323 w, 1308 w, 1297 m, 1275 w, 1233 m, 1211 s, 1140 m, 1109 s, 1080 s, 1064 m, 1046 w, 1012 s, 988 m, 975 w, 964 w, 943 m, 909 m, 898 m, 860 w, 839 s, 798 m, 756 s, 737 m, 658 m, 610 s; *m/z* (ESMS) 357.3019 ([M + H+], calculated for $C_{22}H_{37}N_4$ 357.3018).

Synthesis of *trans*-1,4-di-[*N*-(4′′-(trifluoromethyl)benzyl)-nortropin-3′-yliden]-diaminocyclohexane, **L4.4**

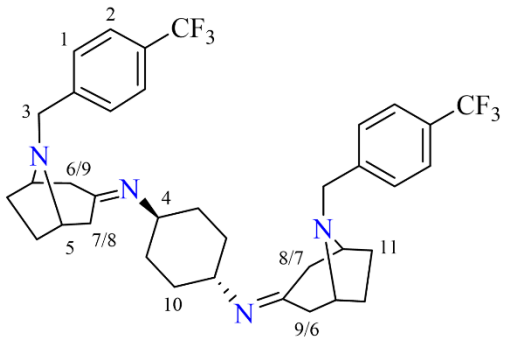

N-((4-trifluoromethyl)benzyl)nortropinone (**L4.4a**) (0.860 g, 2.24 mmol), *trans*-diaminocyclohexane (0.130 g, 1.16 mmol) and *para*-toluenesulfonic acid monohydrate (10 mg, 0.05 mmol) were added to toluene (30 mL), which was then heated under reflux in an apparatus equipped with a Dean-Stark condenser for 24 hours. The solution was then filtered while hot and the solvent was removed *in vacuo* yielding a brown oil as the crude product, which was allowed to stand for 24 hours. This was then triturated with MeCN (50 mL), resulting in precipitation of a white solid which was isolated *via* vacuum filtration and washed several times with fresh MeCN, resulting in the pure product with a final mass of 0.440 g (46%), m.p. 160 – 162 °C. δ_H (400 MHz, $CDCl_3$) (ppm) 7.58 (d, 4H, **H1**, *J* = 8.2 Hz), 7.53 (d, 2H, **H2**, *J* = 8.2 Hz), 3.72 (s, 4H, **H3**), 3.39 – 3.29 (m, 6H, **H4** & **H5**), 2.68 (dd, 2H, **H6**/**H9**, *J* = 14.9, 3.7 Hz), 2.57 (m, 2H, **H7**/**H8**), 2.29 (dd, 2H, **H9**/**H6**, *J* = 14.8, 3.7 Hz), 2.18 (m, 2H, **H8**/**H7**), 2.03 (m, 4H, **H11**/**H10**), 1.74 – 1.41 (m, 12H, **H10**/**H11** & **H11**/**H10**); δ_C (101 MHz, $CDCl_3$) (ppm) 167.1 (**C**=N), 144.1 (Ar**C**-CH_2), 129.4 (q, Ar**C**-CF_3, *J* = 32.4 Hz), 128.8 (**C1**), 125.4 (q, **C2**, *J* = 3.8 Hz), 124.4 (q, **C**F_3, *J* = 270.7 Hz), 59.4 (**C5**), 58.8 (**C4**), 57.5 (**C5**), 55.4 (**C3**), 45.2 (**C6**/**C9**), 35.8 (**C7**/**C8**), 32.7 (**C10**), 32.6 (**C10**), 32.1 (**C10**), 32.0 (**C10**); $\tilde{\nu}_{max}/cm^{-1}$ (ATR): 3292 w br, 2961 m, 2946 m, 2923 s, 2897 m, 2855 m, 2824 m, 2644 w, 1920 w, 1809 w, 1656 s, 1619 m, 1586 w, 1466 m, 1449 s, 1435 w, 1418 m, 1367 w, 1352 m, 1331 s, 1319 s, 1266 m, 1244 m, 1229 w, 1217 w, 1199 w, 1198 m, 1186 w, 1154 s, 1135 s, 1113 s, 1100 s, 1068 s, 1044 m, 1022 s, 1010 s, 981 m, 963 w, 949 m, 939 w, 910 w, 900 m, 882 w, 850 m, 833 s, 821 s, 792 m, 784 m, 756 m, 742 m, 719 m, 665 m, 633 m; *m/z* (ESMS) 645.3392 ([M + H+], calculated for $C_{36}H_{43}F_6N_4$ 645.3392).

Chapter 5

Synthesis of spiro[3.3]heptane-2,6-dicarboxylic acid, **H_2L5.1**

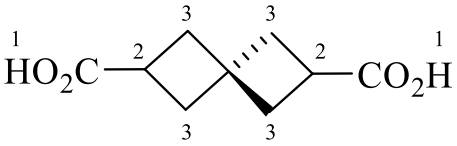

H_2L5.1 was prepared according to a modified literature procedure reported by Rice *et. al.*[1] Sodium (0.575 g, 25.01 mmol) was added to *n*-pentanol (25 mL) under a N_2 atmosphere and was stirred with gentle heating (*ca.* 55 – 60 °C) until most of the sodium had dissolved. Diethyl malonate (3.80 mL, 24. 9 mmol) was added to this and was stirred until the remained of the sodium had dissolved. Pentaerythritol tetrabromide (2.000 g, 5.158 mmol) was then added in one portion and the mixture was heated to reflux under N_2 for 48 hours. After this, the solution was cooled to room temperature and any solids were removed *via* vacuum filtration and immersed into isopropanol to quench any remaining sodium solids. The *n*-pentanol was then removed from the filtrate *via* distillation under N_2. To aid this, when near dryness the solution was cooled to *ca.* 80 – 90 °C and water (5 mL) was added, and the solution was reheated to remove the water:pentanol azeotrope. This was repeated 1-2 more times to ensure complete removal of pentanol. The resulting oil was cooled to room temperature and combined with water (5 mL) and extracted into diethyl ether (3 × 100 mL). The organic layers were combined, dried over $MgSO_4$, filtered and the solvent was removed *in vacuo* to give a viscous brown oil consisting of a mixture of the ethyl and pentyl esters of the tetracarboxylate. This was dissolved in ethanol (40 mL) and KOH (4.500 g, 80.21 mmol) was added. This was stirred at room temperature for 72 hours. After this, the yellow solid that had formed was isolated *via* vacuum filtration and dissolved in water (5 mL). This was acidified to pH ~3 using 5M $HCl_{(aq)}$. The resulting solution was poured into a large evaporating dish and left to dry completely for several days. The resulting pale-yellow solid was then isolated and heated to 150 °C, and the temperature was gradually increased in ~20 °C increments until a temperature of 215 °C was reached, at which it was allowed to dwell for 5 minutes, after which it was allowed to cool to room temperature. The black solid was then recrystallised from boiling water, which was filtered while hot. Cooling the filtrate yielded colourless crystals of mass 160 mg (18%), m.p. 207-209 °C (lit. 212 °C).[10] δ_H (400 MHz, $CDCl_3$) (ppm) 11.25 (s, 2H,

H1), 3.03 (p, 2H, **H2**, *J* = 8.3 Hz), 2.23-2.39 (m, 8H, **H3**); δ_C (101 MHz, $CDCl_3$) (ppm) 180.6, 37.7, 37.3, 36.8, 32.5; $\tilde{\nu}_{max}/cm^{-1}$ (ATR): 2969 w, 2931 w, 2848 w, 2736 w, 2664 w br, 2554 w br, 1681 s, 1415 m, 1333 w, 1247 s, 1215 s, 1112 w, 931 s, 738 m, 702 m, 541 w, 467 w; *m/z* (ESMS) 183.0668 ([M – H+], calculated for $C_9H_{11}O_4$ 183.0657).

7.3 Coordination Complex Synthesis

Chapter 2

Synthesis of $[Cu_4OCl_6(\mathbf{L2.1})_4]\cdot MeCN\cdot H_2O$, complex **2.1**

L2.1 (10.6 mg, 0.06 mmol) was dissolved in MeCN (3 mL). $CuCl_2\cdot 2H_2O$ (5.0 mg, 0.03 mmol) was dissolved in MeCN (3 mL) and the two solutions were combined and left in a sealed vial. After three days, brown crystals had formed and were isolated by filtration. Yield 2.4 mg (27%); m.p. 270 – 272 °C (decomp.); $\tilde{\nu}_{max}/cm^{-1}$ (ATR): 3059 w, 2889 m, 2846 m, 2809 m, 2774 m, 2159 w, 1943 w, 1851 w, 1619 s, 1557 w, 1506 m, 1470 m, 1447 w, 1434 m, 1425 s, 1399 w, 1369 m, 1349 m, 1333 m, 1300 m, 1277 m, 1260 m, 1226 s, 1213 s, 1193 m, 1158 m, 1147 m, 1116 s, 1097 s, 1068 s, 1035 s, 997 s, 981 m, 967 m, 913 m, 853 s, 852 s, 818 s, 780 s, 733 m, 665 w, 628 s; Found C, 44.43; H, 5.40; N, 10.31%; calculated for $C_{44}H_{69}N_9O_2Cl_6Cu_4$ C, 44.30; H, 5.58; N, 10.11%.

Synthesis of $[Cu_4OCl_6(\mathbf{L2.2})_4]\cdot MeOH\cdot 3H_2O$, complex **2.2**

L2.2 (10.8 mg, 0.06 mmol) was dissolved in MeOH (2 mL). $CuCl_2\cdot 2H_2O$ (5.0 mg, 0.03 mmol) was dissolved in MeOH (2 mL) and the two solutions were combined and left in a sealed vial. After six days, brown crystals had formed and were isolated by filtration. On drying, the solid loses lattice methanol molecules and absorbs atmospheric water. Yield 7.1 mg (79%); m.p. 167 – 169 °C (decomp.); $\tilde{\nu}_{max}/cm^{-1}$ (ATR): 3558 w br, 3066 w br, 2955 w, 2906 w, 2896 w, 2840 m, 2812 m, 2769 w, 1620 s, 1564 w, 1505 m, 1452 m, 1429 s, 1401 m, 1368 w, 1356 m, 1323 m, 1291 s, 1275 m, 1223 m, 1210 m, 1127 m, 1114 m,

1063 s, 1036 s, 1009 s, 912 s, 863 s, 851 s, 821 s, 795 s, 727 w, 719 w, 658 w, 622 s; Found C, 39.36; H, 4.61; N, 9.90%; calculated for $C_{42}H_{62}N_8O_9Cl_6Cu_4$ C, 39.20; H, 4.78; N, 9.80%.

Synthesis of $[Cu_4OCl_7(\mathbf{L2.2})_2(\mathbf{L2.2H})]\cdot 2MeCN\cdot 9H_2O$, complex **2.3**

L2.2 (10.8 mg, 0.06 mmol) was dissolved in MeCN (1.5 mL). $CuCl_2\cdot 2H_2O$ (5.0 mg, 0.03 mmol) was dissolved in MeCN (1.5 mL) and the two solutions were combined. Water (20 μL) was added to the combined solution, and this was left in a sealed vial. After one day, brown crystals had formed and were isolated by filtration. Yield 6.3 mg (63%); m.p. 156 – 159 °C (decomp.); $\tilde{\nu}_{max}/cm^{-1}$ (ATR): 3340 m br, 3092 w, 3058 w, 3048 w, 3026 w, 2979 w, 2963 w, 2927 w, 2863 w, 2827 w, 2584 w, 2530 m br, 2461 m, 2399 w, 2348 w, 2317 w, 2287 w, 2251 m, 1623 s, 1565 w, 1495 w, 1457 m, 1445 s, 1428 s, 1405 s, 1374 m, 1353 m, 1331 w, 1303 w, 1295 m, 1268 m, 1251 m, 1224 s, 1215 s, 1122 s, 1117 s, 1082 m, 1066 s, 1059 m, 1035 s, 1011 w, 1008 m, 974 m, 963 m, 912 m, 868 s, 825 s, 790 m, 738 m, 659 w, 627 s; Found C, 30.95; H, 3.94; N, 8.77%; calculated for $C_{34}H_{67}N_8O_{13}Cl_7Cu_4$ C, 31.45; H, 5.20; N, 8.63%.

Synthesis of $[Cu_2(OAc)_4(\mathbf{L2.1})_2]$, complex **2.4**

L2.1 (10.6 mg, 0.06 mmol) was dissolved in MeCN (3 mL). $Cu(OAc)_2\cdot H_2O$ (6.0 mg, 0.03 mmol) was dissolved in MeCN (3 mL) and the two solutions were combined and left in a sealed vial. After one day, green crystals had formed and were isolated by filtration. Yield 3.4 mg (32%); m.p. 215 – 218 °C; $\tilde{\nu}_{max}/cm^{-1}$ (ATR): 2944 w, 2928 w, 2921 m, 2844 w, 2813 w, 2774 w, 2758 w, 2726 w, 2711 w, 1610 s, 1618 s, 1560 m, 1498 m, 1466 w, 1422 s, 1397 m, 1374 m, 1371 m, 1352 m, 1333 w, 1325 w, 1298 m, 1274 w, 1267 w, 1252 w, 1222 m, 1209 w, 1198 w, 1153 m, 1122 m, 1114 m, 1109 m, 1089 w, 1065 m, 1052 w, 1040 m, 1020 m, 994 m, 985 m, 958 w, 934 w, 904 w, 890 w, 863 m, 843 m, 814 m, 807 m, 785 m, 731 w, 679 s, 627 s, 617 s; Found C, 49.75; H, 6.15; N, 8.27%; calculated for $C_{30}H_{44}N_4O_8Cu_2$ C, 50.34; H, 6.20; N, 7.87%.

Synthesis of [$CoCl_3$(**L2.1H**)]·MeCN, complex **2.5**

L2.1 (10.6 mg, 0.06 mmol) was dissolved in MeCN (3 mL). $CoCl_2 \cdot 6H_2O$ (14.5 mg, 0.06 mmol) was dissolved in MeCN (3 mL) and the two solutions were combined and left in a sealed vial. After several days, blue crystals had formed and were isolated by filtration. Yield 5.1 mg (22%); m.p. 270 – 272 °C; $\tilde{\nu}_{max}/cm^{-1}$ (ATR): 3548 w br, 3011 m, 2956 w, 2931 w, 2781 w, 2752 w, 2249 w, 1624 s, 1464 m, 1430 s, 1368 w, 1250 w, 1227 m, 1192 w, 1153 w, 1130 w, 1107 w, 1075 m, 1063 w, 1035 s, 964 w, 954 s, 944 s, 912 w, 873 w, 853 s, 816 s, 796 w, 773 w, 666 w, 620 s; Found C 40.53; H, 5.21; N, 10.41%; calculated for $C_{13}H_{20}N_3Cl_3Co$, C, 40.70; H, 5.26; N, 10.95%.

Synthesis of [$CoCl_3$(**L2.2H**)], complex **2.6**

L2.2 (5.3 mg, 0.03 mmol) was dissolved in MeCN (3 mL). $CoCl_2 \cdot 6H_2O$ (14.5 mg, 0.06 mmol) was dissolved in MeCN (3 mL) and the two solutions were combined and left in a sealed vial. After several days, blue crystals had formed and were isolated by filtration. Yield 5.3 mg (51%); m.p. 162 – 163 °C; $\tilde{\nu}_{max}/cm^{-1}$ (ATR): 3449 w br, 3090 w, 3060 w, 3044 w, 2995 m, 2958 m, 2764 w, 2743 m, 2684 w, 2622 w, 1621 s, 1559 w, 1510 w, 1459 m, 1430 s, 1405 m, 1371 s, 1353 m, 1335 w, 1306 w, 1262 m, 1231 m, 1214 m, 1209 w, 1120 s, 1119 m, 1073 s, 1058 m, 1045 s, 1031 s, 1015 m, 968 s, 960 m, 909 m, 866 s, 858 s, 826 m, 822 s, 790 m, 739 w, 623 m, 609 m; Found C, 35.09; H, 4.43; N, 8.33%; calculated for $C_{10}H_{15}N_2OCl_3Co$, C, 34.86; H, 4.39; N, 8.13%.

Synthesis of [$CoCl_3$(**L2.3H**)], complex **2.7**

L2.3 (0.003 mL, 0.030 mmol) was dissolved in MeCN (3 mL). $CoCl_2 \cdot 6H_2O$ (14.5 mg, 0.06 mmol) was dissolved in MeCN (3 mL) and the two solutions were combined. Small blue needle-like crystals had formed after 24 hours of crystallisation by vapour diffusion in diethyl ether, which were isolated *via* filtration. After several days, blue crystals had formed in the smaller vial and were isolated by filtration. Yield 6.9 mg (84%); m.p. 265 – 268 °C (decomp.); $\tilde{\nu}_{max}/cm^{-1}$ (ATR): 3045 m br, 2990 m, 2939 w, 2661 w, 2550 w, 1955 w, 1621 m, 1598 m, 1560 m, 1510 w, 1474 s, 1434 s, 1399 m, 1346 w, 1317 m, 1239 w,

1233 s, 1211 w, 1135 m, 1102 m, 1074 s, 1031 s, 994 s, 974 m, 881 s, 803 m, 791 s, 719 w; Found C, 26.43; H, 3.30; N, 10.40%; calculated for $C_6H_9N_2Cl_3Co$, C, 26.26; H, 3.31; N, 10.21%.

Synthesis of *poly*-[Ag**L2.1**]SbF_6·0.5THF, complex **2.8**

L2.1 (10.6 mg, 0.06 mmol) was dissolved in THF (2 mL). $AgSbF_6$ (18.0 mg, 0.06 mmol) was dissolved in THF (2 mL) and the two solutions were combined and left in a sealed vial which was wrapped in foil. After three days, colourless crystals had formed and were isolated by filtration. Yield 3.2 mg (10%); m.p. 138 – 141 °C (decomp.); $\tilde{\nu}_{max}/cm^{-1}$ (ATR): 2973 w br, 2949 w, 2909 w br, 2852 m, 1618 s, 1564 m, 1503 w, 1471 m, 1451 m, 1444 m, 1433 s, 1392 w, 1373 w, 1361 m, 1343 m, 1337 w, 1304 m, 1281 m, 1251 w, 1234 m, 1186 m, 1145 w, 1113 w, 1090 m, 1082 m, 1066 s, 1059 s, 1035 s, 985 m, 971 s, 960 m, 916 m, 897 m, 891 w, 862 s, 855 s, 820 s, 803 m, 781 s, 744 w, 652 s, 644 s, 633 s; Found C, 25.86; H, 3.33; N, 5.50%; calculated for $C_{22}H_{32}N_4F_{12}Sb_2Ag_2$ (accounting for loss of the lattice THF), C, 25.41; H, 3.10; N, 5.39%.

Synthesis of *poly*-[Ag(**L2.2**)]SbF_6·0.5THF, complex **2.9** and $[Ag_2(\mathbf{L2.2})_2(THF)_4(SbF_6)_2]$, complex **2.9a**

L2.2 (10.8 mg, 0.06 mmol) was dissolved in THF (2 mL). $AgSbF_6$ (18.0 mg, 0.06 mmol) was dissolved in THF (2 mL) and the two solutions were combined and left in a sealed vial which was wrapped in foil. After two days, colourless crystals had formed and were isolated by filtration. Yield 10.9 mg (33%); m.p. 155 – 157 °C (decomp.); $\tilde{\nu}_{max}/cm^{-1}$ (ATR): 2963 w br, 2858 w, 2822 w, 2755 w, 1619 s, 1564 w, 1467 w, 1458 m, 1450 m, 1431 s, 1400 m, 1363 w, 1346 m, 1335 m, 1309 w, 1296 s, 1267 s, 1245 w, 1234 m, 1212 w, 1136 s, 1128 s, 1113 s, 1100 m, 1088 s, 1066 s, 1058 s, 1031 m, 1025 m, 992 s, 975 m, 923 s, 893 w, 870 s, 840 m, 822 s, 795 s, 742 w, 649 s, 646 s; Found C, 26.25; H, 3.19; N, 5.07%; calculated for $C_{24}H_{36}N_4O_3F_{12}Sb_2Ag_2$ (again accounting for loss of the lattice THF) C, 25.83; H, 3.25; N, 5.02%. The PXRD pattern (Appendix 2, Figure A2.8) confirms that the majority of the bulk phase consists of the discrete complex **2.9a**, with only trace amounts of complex **2.9**.

Synthesis of *poly*-[Ag(**L2.1**)(CO_2CF_3)], complex **2.10**

L2.1 (10.6 mg, 0.06 mmol) was dissolved in THF (3 mL). $AgCO_2CF_3$ (7.0 mg, 0.03 mmol) was dissolved in THF (3 mL) and the two solutions were combined and left in a sealed vial which was wrapped in foil. After four days, colourless crystals had formed and were isolated by filtration. Yield 6.2 mg (52%); m.p. 165 – 168 °C (decomp.); $\tilde{\nu}_{max}/cm^{-1}$ (ATR): 2979 w, 2945 w, 2923 w, 2847 w, 2831 w, 2779 w, 1660 s, 1610 s, 1594 m, 1557 w, 1496 w, 1474 w, 1461 w, 1425 w, 1423 m, 1410 s, 1387 w, 1375 w, 1348 w, 1326 w, 1302 m, 1279 w, 1223 m, 1213 m, 1192 s, 1170 s, 1115 s, 1100 s, 1083 m, 1064 m, 1060 m, 1008 m, 982 m, 979 m, 920 m, 872 w, 865 m, 854 s, 816 s, 815 s, 782 s, 780 s, 724 m, 720 s, 616 s, 606 w; Found C, 39.48; H, 3.94; N, 6.94%; calculated for $C_{13}H_{16}N_2O_2F_3Ag$, C, 39.32; H, 4.06; N, 7.05%.

Chapter 3

Synthesis of *poly*-[Zn(**L3.1**)$_2$($BDC)_2$]·$2H_2O$, complex **3.1**

L3.1 (12.5 mg, 0.03 mmol), terephthalic acid (2.5 mg, 0.02 mmol) and $Zn(NO_3)_2·6H_2O$ (3.5 mg, 0.02 mmol) were combined with H_2O (1 mL) and DMF (1 mL) and this was sonicated for several minutes. This was heated to 100 °C in a heat block for 24 hours, after which yellow crystals had formed, which were isolated *via* vacuum filtration. On drying, the solid loses lattice one lattice water molecule. Yield 4.1 mg (44%); m.p. >300 °C; $\tilde{\nu}_{max}/cm^{-1}$ (ATR): 3592 w, 3401 w br, 2944 w, 2846 w, 2226 m, 1675 m, 1605 s, 1573 s, 1543 m, 1498 m, 1456 w, 1434 w, 1424 m, 1399 m, 1372 s, 1340 s, 1323 s, 1311 m, 1289 m, 1271 w, 1243 w, 1224 w, 1216 s, 1177 s, 1139 w, 1109 w, 1103 m, 1066 m, 1034 m, 1017 m, 961 w, 933 m, 909 w, 884 w, 860 m, 827 s, 815 m, 772 m, 755 m, 743 s, 698 m, 684 w, 656 w, 606 m; Found C, 62.99; H, 4.19; N, 8.81%; calculated for $C_{70}H_{56}N_8O_{12}Zn$, C, 63.23; H, 4.77; N, 8.43%.

Synthesis of *poly*-[Zn(**L3.1**)(HBTC)]·$2H_2O$·DMF, complex **3.2**

L3.1 (12.5 mg, 0.03 mmol), 1,3,5-benzenetricarboxylic acid (3.0 mg, 0.015 mmol) and $Zn(NO_3)_2·6H_2O$ (3.5 mg, 0.02 mmol) were combined with H_2O (1 mL) and DMF (1 mL) and this was sonicated for several minutes. This was heated to 100 °C in a heat block for 24 hours, after which yellow crystals had formed,

which were isolated *via* vacuum filtration. Yield 5.6 mg (54%); m.p. >300 °C; $\tilde{\nu}_{max}/cm^{-1}$ (ATR): 3190 m br, 2925 w, 2863 w, 2228 m, 2161 w, 1668 m, 1660 m, 1608 s, 1562 s, 1502 m, 1425 s, 1380 w, 1348 s, 1316 m, 1251 w, 1220 m, 1178 m, 1137 w, 1105 m, 1096 m, 1071 m, 1035 s, 932 m, 870 m, 829 s, 817 m, 764 s, 732 s, 698 w, 683 w, 661 w, 647 w, 601 m; Found C, 57.97; H, 3.97; N, 8.94%; calculated for $C_{39}H_{37}N_5O_{10}Zn$, C, 58.47; H, 4.66; N, 8.74%.

Synthesis of *poly*-[Co(**L3.1**)(HBTC)]·2.5H_2O, complex **3.3**

L3.1 (12.5 mg, 0.03 mmol), 1,3,5-benzenetricarboxylic acid (3.0 mg, 0.02 mmol) and $CoCl_2 \cdot 6H_2O$ (4.5 mg, 0.02 mmol) were combined with H_2O (1 mL) and DMF (1 mL) and this was sonicated for several minutes. This was heated to 100 °C in a heat block for 24 hours, after which dark red crystals had formed, which were isolated *via* vacuum filtration. Yield 4.8 mg (47%); m.p. >300 °C; $\tilde{\nu}_{max}/cm^{-1}$ (ATR): 3337 w br, 3042 w, 2951 w, 2885 w, 2839 w, 2227 m, 1717 m, 1687 m, 1658 w, 1605 s, 1580 s, 1539 m, 1538 s, 1500 m, 1459 w, 1448 w, 1423 m, 1416 s, 1374 s, 1336 w, 1316 w, 1260 s, 1240 w, 1217 m, 1183 s, 1108 w, 1096 m, 1070 w, 1053 s, 1015 m, 961 w, 944 w, 927 m, 922 m, 896 m, 876 w, 826 s, 817 m, 793 m, 753 s, 745 m, 720 s, 680 m, 662 w, 649 w, 616 m, 602 w; Found C, 59.11; H, 3.86; N, 8.14%; calculated for $C_{72}H_{62}N_8O_{19}Co_2$, C, 59.18; H, 4.28; N, 7.67%.

Synthesis of *poly*-[Zn_3(**L3.1**)$_2$(BTC)$_2$(H_2O)$_2$]·4H_2O·DMF, complex **3.4**

L3.1 (12.5 mg, 0.03 mmol), 1,3,5-benzenetricarboxylic acid (3.0 mg, 0.02 mmol) and $ZnCl_2 \cdot H_2O$ (3.0 mg, 0.02 mmol) were combined with H_2O (1 mL) and DMF (1 mL) and this was sonicated for several minutes. This was heated to 100 °C in a heat block for 24 hours, after which yellow crystals had formed, which were isolated *via* vacuum filtration. Yield 2.2 mg (30%); m.p. 278 – 280 °C (decomp.); $\tilde{\nu}_{max}/cm^{-1}$ (ATR): 3164 w br, 2227 w, 1668 w, 1657 w, 1609 s, 1559 m, 1501 w, 1439 w, 1424 m, 1348 s, 1251 w, 1221 m, 1179 m, 1136 w, 1105 w, 1096 w, 1070 m, 1035 m, 931 m, 872 w, 829 m, 815 w, 764 s, 732 s, 699 w, 682 w, 662 w, 646 w, 602 w; Found C, 55.27; H, 3.89; N, 7.91%; calculated for $C_{75}H_{65}N_9O_{21}Zn_3$, C, 55.62; H, 4.23; N, 7.78%.

Synthesis of *poly*-[Yb_3(**L3.2**)$_4$(**HL3.2**)]·4H_2O·6DMF complex **3.5**

L3.2 (12 mg, 0.03 mmol) and $YbCl_3·6H_2O$ (4.0 mg, 0.02 mmol) were combined with DMF (2 mL) and this was sonicated for several minutes. This was heated to 100 °C in a heat block for 72 hours after which brown crystals had formed, which were isolated *via* vacuum filtration. Yield 2.4 mg (14%); m.p. >300 °C $\tilde{\nu}_{max}/cm^{-1}$ (ATR): 3408 m br, 2930 m, 2868 w, 2810 w, 2565 w, 1712 m, 1653 s, 1652 s, 1621 w, 1591 m, 1583 m, 1537 m, 1524 m, 1505 m, 1457 w, 1409 s, 1385 s, 1328 w, 1306 w, 1281 w, 1251 m, 1215 m, 1180 m, 1168 m, 1096 s, 1059 s, 1015 m, 955 w, 945 w, 937 m, 894 w, 863 m, 850 m, 788 s, 778 s, 752 m, 719 w, 709 m, 692 m, 660 m, 634 w, 612 w; Found C, 54.67; H, 4.64; N, 5.26%; calculated for $C_{138}H_{145}N_{11}O_{35}Yb_3$, C, 54.57; H, 4.81; N, 5.07%.

Synthesis of *poly*-[Gd(**L3.3**)$(DMF)_2$]·2DMF·H_2O, complex **3.6**

L3.3 (16 mg, 0.03 mmol), 1,2-di(4-pyridyl)ethylene (5.4 mg, 0.03 mmol) and $Gd(NO_3)_3·H_2O$ (10.0 mg, 0.03 mmol) were combined with DMF (1 mL) and this was sonicated for several minutes. This was heated to 100 °C in a heat block for 48 hours after which brown crystals had formed, which were isolated *via* vacuum filtration. Yield 6.6 mg (27%); m.p. 263 – 265 °C (decomp.); $\tilde{\nu}_{max}/cm^{-1}$ (ATR): 3389 m br, 2931 w, 1646 s, 1635 s, 1629 s, 1606 s, 1594 s, 1538 m, 1504 m, 1489 w, 1425 m, 1398 s, 1392 s, 1317 w, 1292 w, 1249 m, 1222 m, 1177 s, 1145 w, 1096 m, 1062 w, 1031 m, 1014 m, 996 w, 975 w, 934 m, 906 w, 870 m, 849 m, 822 m, 788 s, 775 s, 759 m, 734 w, 717 m, 701 m, 677 s, 659 m, 618 w; Found C, 52.32; H; 5.04; N; 6.90%; calculated for $C_{43}H_{52}N_5O_{12}Gd$, C 52.26; H, 5.31, N 7.09%.

Synthesis of *poly*-[Co_3(**L3.4**)$_2$(**dpe**)$_2$(H_2O)]·8H_2O·2DMF, complex **3.7**

L3.4 (8.0 mg, 0.02 mmol), 1,2-di(4-pyridyl)ethylene (2.7 mg, 0.02 mmol) and $CoCl_2·6H_2O$ (9 mg, 0.04 mmol) were combined with DMF (2 mL) and H_2O (1 mL) and this was sonicated for several minutes. This was heated to 100 °C in a heat block for 72 hours after which red crystals

had formed, which were isolated *via* vacuum filtration. Yield 7.3 mg (61%); m.p. >300 °C (decomp.); $\tilde{\nu}_{max}/cm^{-1}$ (ATR): 3313 w br, 3060 w, 2924 w, 2864 w, 1662 s, 1651 s, 1603 s, 1575 m, 1568 m, 1516 w, 1497 m, 1429 m, 1390 s, 1338 w, 1316 w, 1310 w, 1294 w, 1254 m, 1221 m, 1190 m, 1176 m, 1144 w, 1096 m, 1070 w, 1029 m, 1015 m, 971 w, 953 w, 933 m, 862 m, 840 w, 827 m, 787 s, 767 w, 753 m, 713 m, 698 w, 683 w, 672 m, 659 m, 640 w, 603 w; Found C, 58.45; H, 4.76; N, 6.12%; calculated for $C_{92}H_{96}N_8O_{25}Co_3$, C, 58.44; H, 5.12; N, 5.93%.

Chapter 4

Synthesis of $[Ag_{12}(\mathbf{L4.1})_6(OTf)_{12}]$, cage **C4.1**

L4.1 (8.0 mg, 0.02 mmol) was added to acetone (3 mL). A solution of AgOTf (6.0 mg, 0.02 mmol) in acetone (3 mL) was added to the initial solution. This solution was then left to stand in a sealed vial which was wrapped in foil. The combined solutions were sonicated until complete dissolution of all solids. Colourless crystals had formed after 72 hours of crystallisation by vapour diffusion in toluene, which were isolated *via* filtration. Yield 1.4 mg (12%); m.p. 202 – 204 °C (decomp.); $\tilde{\nu}_{max}/cm^{-1}$ (ATR): 3478 m br, 2925 w br, 1702 w, 1636 m, 1514 w, 1496 w, 1470 w, 1448 w, 1406 w, 1378 w, 1345 w, 1321 w, 1271 s, 1246 s, 1223 s, 1151 s, 1115 w, 1086 m, 1072 m, 1025 s, 1008 s, 957 m, 947 m, 902 w, 874 w, 849 w, 819 m, 809 m, 790 m, 757 w, 732 m, 713 w, 696 m, 634 s.

Synthesis of *poly*-$[Ag_{15}(\mathbf{L4.2})_6(BF_4)_{12}]$, cage **C4.2**

L4.2 (11.6 mg, 0.021 mmol) was added to dry acetone (1.5 mL) and sonicated for several minutes. $AgBF_4$ (6.6 mg, 0.03 mmol) was dissolved in dry acetone (1.5 mL) and the two solutions were combined and sonicated until complete dissolution of all solids. This solution was then left to stand in a sealed vial (wrapped in foil and parafilm to keep dry) for 30 minutes. After this, the solution was filtered using a 0.2 μM PTFE syringe filter, and placed in a fresh vial (also wrapped in foil and parafilm to keep dry). After 24 hours, colourless crystals had formed and were isolated *via* filtration. Yield 0.7 mg (5%); m.p. 211 – 213 °C (decomp.); $\tilde{\nu}_{max}/cm^{-1}$ (ATR): 3598 m br, 2934 m br, 2884 w, 2841 w, 2360 s, 2339 s, 2227

m, 2068 w, 1982 w, 1708 w, 1632 m, 1607 w, 1547 w, 1529 w, 1503 w, 1468 w, 1449 w, 1412 m, 1352 m, 1321 w, 1299 w, 1203 w, 1053 s, 1015 s, 957 w, 903 w, 882 w, 840 w, 833 m, 783 w, 668 m, 650 w; Found C, 41.77; H, 4.43; N, 7.63%; calculated for $C_{216}H_{252}N_{36}B_{15}F_{60}Ag_{15}$, C, 41.36; H, 4.05; N, 8.04%.

Synthesis of $[Ag_{12}(\mathbf{L4.2})_6(BF_4)_{12}]\cdot H_2O\cdot 2C_3H_6O$, cage **C4.2a**

L4.2 (11.6 mg, 0.021 mmol) was added to dry acetone (1.5 mL) and sonicated for several minutes. $AgBF_4$ (6.6 mg, 0.03 mmol) was dissolved in dry acetone (1.5 mL) and the two solutions were combined and sonicated until complete dissolution of all solids. This solution was then left to stand in a sealed vial (wrapped in foil and parafilm to keep dry) for 30 minutes. After this, the solution was filtered using a 0.2 μM PTFE syringe filter, and placed in a fresh vial (also wrapped in foil and parafilm to keep dry). After approximately 6 hours, some crystals started to form on the walls of the vial, and at this stage water (20 μL) was added to the vial. After 48 hours Yield 1.2 mg (8%); m.p. 214 – 216 °C (decomp.); $\tilde{\nu}_{max}/cm^{-1}$ (ATR): 3588 m br, 3398 m br, 2939 w br, 2359 w, 2336 w, 2227 w, 2162 w, 1635 m, 1607 w, 1558 w, 1540 w, 1506 w, 1472 w, 1448 w, 1411 w, 1349 w, 1323 w, 1296 w, 1202 w, 1052 s, 1038 s, 1010 s, 957 m, 902 w, 882 w, 840 w, 832 m, 763 w, 649 w; Found C, 44.60; H, 4.64; N, 8.30%; calculated for $C_{220}H_{268}N_{36}O_5B_{12}F_{48}Ag_{12}$, C, 45.30; H, 4.63; N, 8.65%.

Synthesis of $[Ag_8(\mathbf{L4.3})_5(\mathbf{L4.3'})^*(OTf)_8]\cdot 5H_2O$, cage **C4.3**

L4.3 (6.0 mg, 0.02 mmol) was added to acetone (1 mL). A solution of AgOTf (5.0 mg, 0.02 mmol) in acetone (1 mL) was added to this and the combined solution was sonicated until complete dissolution of all solids. This solution was then left to stand in a sealed vial which was wrapped in foil. Colourless crystals had formed after 24 hours of crystallisation by vapour diffusion in diethyl ether, which were isolated *via* filtration. Yield 3.2 mg (31%); m.p. 175 – 177 °C (decomp.); $\tilde{\nu}_{max}/cm^{-1}$ (ATR): 344 w br, 2927 m, 2887 w, 2850 w, 2810 w, 1709 m, 1669 w, 1632 m, 1605 w, 1582 w, 1525 w, 1458 w, 1451 w, 1408 m, 1358 m, 1314 w, 1261 s, 1247 s, 1221 s, 1152 s, 1116 m, 1092 w, 1062 w, 1058 w, 1027 s, 1011

m, 967 w, 947 w, 905 m, 851 w, 846 w, 780 m, 756 m, 691 w, 634 s; Found C, 38.10; H, 4.92; N, 8.66%; calculated for $C_{135}H_{219}N_{23}O_{23}F_{24}S_8Ag_8$, C, 38.57; H, 5.25; N, 7.66%.

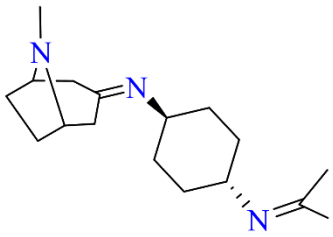

***L4.3′**:

Chapter 5

Synthesis of *poly*-[Yb_6(**L5.1**)$_9$$(DMF)_2$]·0.5DMF·2.5$H_2O$, complex **5.1**

H_2L5.1 (10.0 mg, 0.054 mmol) was dissolved in DMF (2 mL) and H_2O (1 mL), to which was added $YbCl_3·6H_2O$ (5.0 mg, 0.01 mmol). The resulting mixture was heated in a heat block to 100 °C for 24 hours. Colourless block crystals formed in the vial after 24 hours which were isolated by vacuum filtration while the solution was hot. Yield 4.6 mg (41%); mp >300 °C; $\tilde{\nu}_{max}/cm^{-1}$ (ATR): 2952 w, 2921 w, 1660 w, 1612 m, 1539 s, 1427 s, 1281 m, 1112 w, 859 w, 778 w, 675 w, 566 w, 498 m; Found C, 36.30; H, 3.71; N, 1.52%; calculated for $C_{177}H_{225}N_5O_{82}Yb_{12}$, C, 36.58; H, 3.90; N, 1.21%.

Synthesis of *poly*-[Zn(**L5.1**)(**dpe**)]·1.33DMF·1.33H_2O, complex **5.2**

H_2L5.1 (10.0 mg, 0.054 mmol) was dissolved in DMF (1 mL), to which was added $Zn(NO_3)_2·6H_2O$ (6.0 mg, 0.030 mmol) and **dpe** (9 mg, 0.049 mmol). The resulting mixture was heated in a heat block to 100 °C for 24 hours. Orange needle crystals formed in the vial after 24 hours which were isolated by vacuum filtration while the solution was hot. Yield 6 mg (41%); mp >300 °C. ; $\tilde{\nu}_{max}/cm^{-1}$ (ATR): 3421 w br, 3063 w, 2995 w, 2920 w, 2845 w, 1668 m, 1611 s, 1567 s, 1506 w, 1429 s, 1387 s, 1274 m, 1207 w,

1097 w, 1069 w, 1025 m, 984 w, 834 m, 772 w, 737 w, 660 w, 552 s, 515 w; Found C, 54.19; H, 5.23; N, 8.91%; calculated for $C_{75}H_{96}N_{10}O_{20}Zn_3$, C, 54.47; H, 5.85; N, 8.47%.

7.4 Preparation of NMR Solutions

The titration and self-assembly solutions were prepared according to the details described below. In the experiments where it was necessary to heat the samples, light was excluded by wrapping the NMR tubes in foil and placed in an oil bath or NMR heat block which was set to 50 °C. ^{1}H NMR spectra were then typically measured at room temperature, after 1 hour of heating, 3 hours, 6 hours, 24 hours and several days. Each self-assembly solution was prepared in CD_3CN.

Titration Experiments

L4.2 (6.0 mg, 0.011 mmol) was dissolved in a 11:5 CD_3CN:$CDCl_3$ mixture (800 μL) and a ^{1}H NMR spectrum was measured of the solution. Following this, 3 μL additions of a stock solution of $AgBF_4$ (62.7 mg, 0.322 mmol) in a 11:5 CD_3CN:$CDCl_3$ mixture (1.350 mL) and a ^{1}H NMR spectrum was measured after each subsequent addition.

L4.1 Systems

L4.1/AgOTf

L4.1 (6 mg, 0.011 mmol) and AgOTf (5.76 mg, 0.022 mmol, for the 12:6 M:L stoichiometry, or 3.84 mg, 0.015 mmol for the 8:6 stoichiometry) were combined in CD_3CN (600 μL). ^{1}H NMR and ^{19}F NMR spectra were measured at room temperature and after heating to 50 °C for 1, 3, 6, 24 and 48 hours.

Crystals of cage **C4.1** (8.0 mg, 0.001 mmol) were dissolved in CD_3CN (600 μL). $TBABF_4$ (21.50 mg, 0.065 mmol) was dissolved in CD_3CN (300 μL) and 6 μL additions of this (0.43 mg, 0.001 mmol per addition) were added to the solution of dissolved cage **C4.1**, and ^{1}H NMR and ^{19}F NMR spectra were measured after each addition.

L4.1/$AgBF_4$

L4.1 (6 mg, 0.011 mmol) and AgOTf (4.36 mg, 0.022 mmol, for the 12:6 M:L stoichiometry, or 2.91 mg, 0.015 mmol for the 8:6 stoichiometry) were combined in CD_3CN (600 μL), and ^1H NMR and ^{19}F NMR spectra were measured at room temperature and after heating to 50 °C for 1 and 3 hours.

L4.3 Systems

L4.3/AgOTf

L4.3 (6 mg, 0.015 mmol) and AgOTf (7.1 mg, 0.030 mmol, for the 12:6 M:L stoichiometry, or 5.14 mg, 0.02 mmol for the 8:6 stoichiometry) were combined in CD_3CN (600 μL). ^1H NMR and ^{19}F NMR spectra were measured at room temperature and after heating to 50 °C for 1, 3, 6 and 17 hours.

Crystals of cage **C4.3** (7.0 mg, 0.002 mmol) were also dissolved in CD_3CN (600 μL). $TBABF_4$ (27.99 mg, 0.085 mmol) was dissolved in CD_3CN (300 μL) and 6 μL additions of this (0.55 mg, 0.002 mmol per addition) were added to the solution of dissolved cage **C4.1**, and ^1H NMR and ^{19}F NMR spectra were measured after each addition.

The 8:6 M:L stoichiometry was again prepared in CD_3CN (600 μL). $TBABF_4$ (246.9 mg, 0.750 mmol) was dissolved in CD_3CN (300 μL) and 6 μL additions of this (4.94 mg, 0.015 mmol per addition) were added to the solution, and ^1H NMR and ^{19}F NMR spectra were measured after each addition. This was repeated for additions of $TBABPh_4$ – 6 μL additions of the stock solution (421.3 mg, 0.750 mmol) dissolved in CD_3CN (300 μL), and TBAOTs (310.2 mg, 0.750 mmol) dissolved in CD_3CN (300 μL).

L4.3/$AgBF_4$

L4.3 (6 mg, 0.015 mmol) and $AgBF_4$ (6.54 mg, 0.030 mmol, for the 12:6 M:L stoichiometry, or 4.36 mg, 0.020 mmol for the 8:6 stoichiometry) were combined in CD_3CN (600 μL). ^1H NMR and ^{19}F NMR spectra were measured at room temperature and after heating to 50 °C for 1, 3, 6 and 24 hours.

L4.3/$AgPF_6$

L4.3 (6 mg, 0.015 mmol) and $AgPF_6$ (8.54 mg, 0.030 mmol, for the 12:6 M:L stoichiometry, or 5.71 mg, 0.020 mmol for the 8:6 stoichiometry) were combined in CD_3CN (600 μL). ^1H NMR and ^{19}F NMR spectra were measured at room temperature and after heating to 50 °C for 1, 3, 6 and 24 hours.

L4.4 Systems

L4.4/AgOTf

L4.4 (6 mg, 0.009 mmol) and AgOTf (4.55 mg, 0.018 mmol, for the 12:6 M:L stoichiometry, or 3.10 mg, 0.012 mmol for the 8:6 stoichiometry) were combined in CD_3CN (600 μL). ^1H NMR and ^{19}F NMR spectra were measured at room temperature and after heating to 50 °C for 1, 3, 6, 24, 48, 72, 96 and 144 hours.

The 12:6 M:L stoichiometry was again prepared in CD_3CN (600 μL). $TBABF_4$ (142.5 mg, 0.450 mmol) was dissolved in CD_3CN (300 μL) and 6 μL additions of this (2.85 mg, 0.009 mmol per addition) were added to the solution, and ^1H NMR and ^{19}F NMR spectra were measured after each addition. This was repeated for additions of $TBABPh_4$ – 6 μL additions of the stock solution (252.7 mg, 0.450 mmol) dissolved in CD_3CN (300 μL), and TBAOTs (186.1 mg, 0.450 mmol) dissolved in CD_3CN (300 μL).

L4.4/$AgPF_6$

L4.4 (6 mg, 0.009 mmol) and $AgPF_6$ (4.62 mg, 0.018 mmol, for the 12:6 M:L stoichiometry, or 3.03 mg, 0.012 mmol for the 8:6 stoichiometry) were combined in CD_3CN (600 μL). ^{1}H NMR and ^{19}F NMR spectra were measured at room temperature and after heating to 50 °C for 1, 3, 6 and 24 hours.

L4.4/$AgBF_4$

L4.4 (6 mg, 0.009 mmol) and $AgPF_6$ (3.50 mg, 0.018 mmol, for the 12:6 M:L stoichiometry, or 2.34 mg, 0.012 mmol for the 8:6 stoichiometry) were combined in CD_3CN (600 μL). ^{1}H NMR and ^{19}F NMR spectra were measured at room temperature and after heating to 50 °C for 1, 3, 6 and 24 hours.

7.5 References

1. M. R. Willcott, *J. Am. Chem. Soc.*, 2009, **131**, 13180.

2. *Bruker APEX-3*, Bruker-AXS Inc., Madison, WI, 2016.

3. *SADABS 2016/2*, Bruker-AXS Inc., Madison, WI, 2016.

4. G. M. Sheldrick, *Acta Crystallogr., SA: Found. Adv*., 2015, **71**, 3 – 8.

5. G. M. Sheldrick, *Acta Crystallogr., Sect. C: Struct. Chem*., 2015, **71**, 3 – 8.

6. O. V. Dolomanov, L. J. Bourhis, R. J. Gildea, J. A. K. Howard and H. Puschmann, *J. Appl. Crystallogr.*, 2009, **42**, 339–341.

7. D. C. Palmer, *CrystalMaker*, CrystalMaker Software Ltd., Begbroke, Oxfordshire, England, 2014.

8. P. R. Spackman, M. J. Turner, J. J. McKinnon, S. K. Wolff, D. J. Grimwood, D. Jayatilaka and M. A. Spackman, *J. Appl. Cryst.*, 2021, **54**, 1006 – 1011.

9. A. L. Spek, *Acta Crystallogr. C*, 2015, **71**, 9 – 18.

10. L. M. Rice and C. H. Grogan , *J. Org. Chem.*, 1961, **26** , 54 – 58

Appendix 1

· Crystallographic Refinement Data ·

*Table A1.1. Crystallographic data for complexes **2.1** and **2.2***

Identification code	complex **2.1**	complex **2.2**
Empirical formula	$C_{45}H_{68}Cl_6Cu_4N_8O_2$	$C_{42}H_{60}Cl_6Cu_4N_8O_7$
Formula weight	1219.93	1255.84
Temperature/K	150	150
Crystal system	tetragonal	triclinic
Space group	$I4_1/a$	P-1
a/Å	14.0363(6)	11.0233(4)
b/Å	14.0363(6)	13.1480(5)
c/Å	26.9125(18)	18.2426(7)
α/°	90	96.2980(10)
β/°	90	90.0800(10)
γ/°	90	97.8290(10)
Volume/$Å^3$	5302.2(6)	2603.17(17)
Z	4	2
$\rho_{calc}g/cm^3$	1.528	1.602
μ/mm^{-1}	1.929	1.974
F(000)	2512	1284
Crystal size/mm^3	0.21 × 0.15 × 0.13	0.41 × 0.26 × 0.22
Radiation	MoKα (λ = 0.71073)	MoKα (λ = 0.71073)
2Θ range for data collection/°	6.548 to 55.214	5.5 to 61.432
Index ranges	$-18 \leq h \leq 15$, $-18 \leq k \leq 18$, $-34 \leq l \leq 34$	$-15 \leq h \leq 15$, $-18 \leq k \leq 18$, $-26 \leq l \leq 26$
Reflections collected	28121	59409
Independent reflections	3067 [R_{int} = 0.0735, R_{sigma} = 0.0356]	16082 [R_{int} = 0.0276, R_{sigma} = 0.0271]
Data/restraints/parameters	3067/0/163	16082/2/608
Goodness-of-fit on F^2	1.04	1.033
Final R indexes [I>=2σ (I)]	R_1 = 0.0393, wR_2 = 0.0871	R_1 = 0.0373, wR_2 = 0.0962
Final R indexes [all data]	R_1 = 0.0718, wR_2 = 0.1029	R_1 = 0.0507, wR_2 = 0.1047
Largest diff. peak/hole / e $Å^{-3}$	0.32/-0.43	1.18/-1.31

*Table A1.2. Crystallographic data for complexes **2.3** and **2.4***

Identification code	complex **2.3**	complex **2.4**
Empirical formula	$C_{30}H_{49}Cl_7Cu_4N_6O_7$	$C_{30}H_{44}Cu_2N_4O_8$
Formula weight	1108.06	715.77
Temperature/K	150	150
Crystal system	trigonal	monoclinic
Space group	P-3	$P2_1/n$
a/Å	15.5475(9)	13.4883(11)
b/Å	15.5475(9)	7.1824(6)
c/Å	13.0392(13)	17.0115(14)
α/°	90	90
β/°	90	91.746(2)
γ/°	120	90
Volume/$Å^3$	2729.6(4)	1647.3(2)
Z	2	2
$\rho_{calc}g/cm^3$	1.348	1.443
μ/mm^{-1}	1.919	1.344
F(000)	1124	748
Crystal size/mm^3	0.25 × 0.23 × 0.2	0.18 × 0.09 × 0.07
Radiation	MoKα (λ = 0.71073)	MoKα (λ = 0.71073)
2Θ range for data collection/°	6.102 to 61.288	6.044 to 55.036
Index ranges	$-18 \leq h \leq 22$, $-22 \leq k \leq 22$, $-18 \leq l \leq 18$	$-17 \leq h \leq 17$, $-9 \leq k \leq 9$, $-22 \leq l \leq 22$
Reflections collected	38451	22784
Independent reflections	5604 [R_{int} = 0.0854, R_{sigma} = 0.0497]	3772 [R_{int} = 0.0544, R_{sigma} = 0.0331]
Data/restraints/parameters	5604/0/166	3772/0/201
Goodness-of-fit on F^2	1.058	1.05
Final R indexes [I>=2σ (I)]	R_1 = 0.0496, wR_2 = 0.1264	R_1 = 0.0417, wR_2 = 0.1003
Final R indexes [all data]	R_1 = 0.0736, wR_2 = 0.1370	R_1 = 0.0602, wR_2 = 0.1113
Largest diff. peak/hole / e $Å^{-3}$	0.89/-0.70	1.12/-0.57

*Table A1.3. Crystallographic data for complexes **2.5**, **2.6** and **2.7***

Identification code	complex **2.5**	complex **2.6**	complex **2.7**
Empirical formula	$C_{13}H_{20}Cl_3CoN_3$	$C_{10}H_{15}Cl_3CoN_2O$	$C_6H_9Cl_3CoN_2$
Formula weight	383.6	344.52	274.43
Temperature/K	150	150	150
Crystal system	monoclinic	monoclinic	monoclinic
Space group	$P2_1/c$	$P2_1/n$	$P2_1/n$
a/Å	10.1383(5)	10.5474(5)	12.061(2)
b/Å	13.6020(6)	9.1427(3)	6.5567(10)
c/Å	12.8828(6)	15.2850(6)	13.712(2)
α/°	90	90	90
β/°	91.018(2)	108.233(2)	110.528(6)
γ/°	90	90	90
Volume/Å^3	1776.27(14)	1399.95(10)	1015.5(3)
Z	4	4	4
ρ_{calc}g/cm^3	1.434	1.635	1.795
μ/mm^{-1}	1.411	1.783	2.425
F(000)	788	700	548
Crystal size/mm^3	0.14 × 0.13 × 0.08	0.26 × 0.16 × 0.1	0.16 × 0.14 × 0.05
Radiation	MoKα (λ = 0.71073)	MoKα (λ = 0.71073)	MoKα (λ = 0.71073)
2Θ range for data collection/°	5.888 to 61.07	5.266 to 61.236	6.1 to 55.984
Index ranges	-14 ≤ h ≤ 14, -19 ≤ k ≤ 19, -18 ≤ l ≤ 18	-15 ≤ h ≤ 15, -9 ≤ k ≤ 13, -21 ≤ l ≤ 14	-15 ≤ h ≤ 15, -8 ≤ k ≤ 8, -18 ≤ l ≤ 18
Reflections collected	23548	18303	11395
Independent reflections	5434 [R_{int} = 0.0706, R_{sigma} = 0.0575]	4279 [R_{int} = 0.0266, R_{sigma} = 0.0222]	2441 [R_{int} = 0.0620, R_{sigma} = 0.0440]
Data/restraints/parameters	5434/1/185	4279/1/157	2441/0/111
Goodness-of-fit on F^2	1.016	1.044	1.074
Final R indexes [I>=2σ (I)]	R_1 = 0.0403, wR_2 = 0.0649	R_1 = 0.0232, wR_2 = 0.0521	R_1 = 0.0553, wR_2 = 0.1278
Final R indexes [all data]	R_1 = 0.0765, wR_2 = 0.0742	R_1 = 0.0304, wR_2 = 0.0551	R_1 = 0.0740, wR_2 = 0.1370
Largest diff. peak/hole / e Å^{-3}	0.45/-0.38	0.44/-0.39	1.56/-0.64

*Table A1.4. Crystallographic data for complexes **2.8** and **2.9***

Identification code	complex **2.8**	complex **2.9**
Empirical formula	$C_{13}H_{20}AgF_6N_2O_{0.5}Sb$	$C_{24}H_{36}Ag_2F_{12}N_4O_3Sb_2$
Formula weight	555.93	1115.81
Temperature/K	150	150
Crystal system	monoclinic	monoclinic
Space group	$P2_1/n$	$P2_1/c$
a/Å	9.2354(3)	13.0527(4)
b/Å	14.1425(5)	16.4295(5)
c/Å	14.6604(5)	16.8553(5)
α/°	90	90
β/°	95.5360(10)	108.1260(10)
γ/°	90	90
Volume/Å^3	1905.89(11)	3435.23(18)
Z	4	4
ρ_{calc}g/cm^3	1.937	2.157
μ/mm^{-1}	2.499	2.777
F(000)	1072	2144
Crystal size/mm^3	0.22 × 0.19 × 0.1	0.2 × 0.13 × 0.09
Radiation	MoKα (λ = 0.71073)	MoKα (λ = 0.71073)
2Θ range for data collection/°	5.46 to 59.348	5.348 to 61.246
Index ranges	$-12 \le h \le 12$, $-19 \le k \le 19$, $-20 \le l \le 20$	$-17 \le h \le 18$, $-23 \le k \le 23$, $-24 \le l \le 24$
Reflections collected	23805	60065
Independent reflections	5380 [R_{int} = 0.0297, R_{sigma} = 0.0233]	10565 [R_{int} = 0.0795, R_{sigma} = 0.0565]
Data/restraints/parameters	5380/45/253	10565/84/460
Goodness-of-fit on F^2	1.073	1.046
Final R indexes [I>=2σ (I)]	R_1 = 0.0329, wR_2 = 0.0788	R_1 = 0.0399, wR_2 = 0.0658
Final R indexes [all data]	R_1 = 0.0449, wR_2 = 0.0857	R_1 = 0.0814, wR_2 = 0.0774
Largest diff. peak/hole / e Å^{-3}	1.22/-0.62	0.80/-0.97

*Table A1.5. Crystallographic data for complexes **2.9a** and **2.10***

Identification code	complex **2.9a**	complex **2.10**
Empirical formula	$C_{36}H_{60}Ag_2F_{12}N_4O_6Sb_2$	$C_{13}H_{16}AgF_3N_2O_2$
Formula weight	1332.12	397.15
Temperature/K	150	150
Crystal system	triclinic	monoclinic
Space group	P-1	$P2_1/n$
a/Å	8.2200(3)	8.7468(4)
b/Å	10.9459(4)	18.2566(8)
c/Å	12.8714(5)	9.3738(5)
α/°	95.9600(10)	90
β/°	93.8840(10)	110.6800(10)
γ/°	93.4670(10)	90
Volume/Å^3	1146.54(7)	1400.42(12)
Z	1	4
ρ_{calc}g/cm^3	1.929	1.884
μ/mm^{-1}	2.102	1.479
F(000)	656	792
Crystal size/mm^3	0.24 × 0.1 × 0.04	0.2 × 0.16 × 0.11
Radiation	MoKα (λ = 0.71073)	MoKα (λ = 0.71073)
2Θ range for data collection/°	6.026 to 58.474	6.442 to 61.108
Index ranges	-11 ≤ h ≤ 11, -15 ≤ k ≤ 15, -17 ≤ l ≤ 17	-12 ≤ h ≤ 11, -26 ≤ k ≤ 16, -13 ≤ l ≤ 13
Reflections collected	19463	13086
Independent reflections	6194 [R_{int} = 0.0312, R_{sigma} = 0.0353]	4283 [R_{int} = 0.0227, R_{sigma} = 0.0238]
Data/restraints/parameters	6194/0/280	4283/0/190
Goodness-of-fit on F^2	1.054	1.124
Final R indexes [I>=2σ (I)]	R_1 = 0.0285, wR_2 = 0.0517	R_1 = 0.0285, wR_2 = 0.0572
Final R indexes [all data]	R_1 = 0.0405, wR_2 = 0.0551	R_1 = 0.0349, wR_2 = 0.0591
Largest diff. peak/hole / e Å^{-3}	0.89/-0.55	0.53/-0.76

Chapter 3

*Table A1.6. Crystallographic data for complexes **3.1**, **3.2** and **3.3***

Identification code	complex **3.1**	complex **3.2**	complex **3.3**
Empirical formula	$C_{70}H_{54}N_8O_{13}Zn_2$	$C_{36}H_{28}N_4O_8Zn$	$C_{36}H_{27}CoN_4O_8$
Formula weight	1345.95	709.99	702.54
Temperature/K	150	150	150
Crystal system	triclinic	triclinic	triclinic
Space group	P-1	P-1	P-1
a/Å	9.811(3)	10.2435(4)	10.2113(4)
b/Å	16.447(4)	11.0718(4)	11.0701(5)
c/Å	19.774(5)	13.8513(5)	13.9758(5)
α/°	86.596(6)	93.6090(10)	93.9180(10)
β/°	77.642(7)	92.3960(10)	92.2310(10)
γ/°	73.397(7)	106.2710(10)	106.3670(10)
Volume/Å^3	2986.8(14)	1502.12(10)	1509.47(11)
Z	2	2	2
ρ_{calc}g/cm^3	1.497	1.57	1.546
μ/mm^{-1}	0.88	0.883	0.633
F(000)	1388	732	724
Crystal size/mm^3	0.13 × 0.09 × 0.06	0.18 × 0.13 × 0.12	0.22 × 0.2 × 0.19
Radiation	MoKα (λ = 0.71073)	MoKα (λ = 0.71073)	MoKα (λ = 0.71073)
2Θ range for data collection/°	4.494 to 40	5.65 to 56.982	6.428 to 61.296
Index ranges	-9 ≤ h ≤ 9, -15 ≤ k ≤ 15, -19 ≤ l ≤ 19	-13 ≤ h ≤ 13, -14 ≤ k ≤ 14, -18 ≤ l ≤ 18	-14 ≤ h ≤ 14, -15 ≤ k ≤ 15, -20 ≤ l ≤ 20
Reflections collected	33853	28687	33785
Independent reflections	5553 [R_{int} = 0.1483, R_{sigma} = 0.0908]	7564 [R_{int} = 0.0390, R_{sigma} = 0.0368]	9294 [R_{int} = 0.0422, R_{sigma} = 0.0420]
Data/restraints/parameters	5553/2/386	7564/0/446	9294/3/449
Goodness-of-fit on F^2	1.143	1.032	1.061
Final R indexes [I>=2σ (I)]	R_1 = 0.1642, wR_2 = 0.3650	R_1 = 0.0394, wR_2 = 0.0885	R_1 = 0.0552, wR_2 = 0.1267
Final R indexes [all data]	R_1 = 0.1975, wR_2 = 0.3835	R_1 = 0.0516, wR_2 = 0.0935	R_1 = 0.0727, wR_2 = 0.1356
Largest diff. peak/hole / e Å^{-3}	1.04/-0.96	1.16/-0.57	1.25/-0.65

*Table A1.7. Crystallographic data for complexes **3.4** and **3.5***

Identification code	complex **3.4**	complex **3.5**
Empirical formula	$C_{72}H_{54}N_8O_{18.5}Zn_3$	$C_{119}H_{92}N_4O_{25}Yb_3$
Formula weight	1523.34	2497.08
Temperature/K	150	150
Crystal system	orthorhombic	monoclinic
Space group	Pcca	C2/m
a/Å	20.710(4)	26.24(3)
b/Å	10.128(2)	39.86(4)
c/Å	32.240(7)	20.753(19)
α/°	90	90
β/°	90	94.614(14)
γ/°	90	90
Volume/Å^3	6763(2)	21634(36)
Z	4	4
ρ_{calc}g/cm^3	1.496	0.767
μ/mm^{-1}	1.136	1.324
F(000)	3120	4976
Crystal size/mm^3	0.19 × 0.17 × 0.09	0.43 × 0.25 × 0.19
Radiation	MoKα (λ = 0.71073)	MoKα (λ = 0.71073)
2Θ range for data collection/°	3.934 to 41.81	4.33 to 53.218
Index ranges	$-20 \le h \le 20$, $-10 \le k \le 10$, $-32 \le l \le 32$	$-32 \le h \le 33$, $-49 \le k \le 49$, $-25 \le l \le 25$
Reflections collected	32907	228931
Independent reflections	3566 [R_{int} = 0.2979, R_{sigma} = 0.1137]	22719 [R_{int} = 0.0694, R_{sigma} = 0.0380]
Data/restraints/parameters	3566/12/462	22719/106/711
Goodness-of-fit on F^2	1.019	1.066
Final R indexes [I>=2σ (I)]	R_1 = 0.0754, wR_2 = 0.1821	R_1 = 0.0831, wR_2 = 0.2283
Final R indexes [all data]	R_1 = 0.1523, wR_2 = 0.2345	R_1 = 0.1062, wR_2 = 0.2536
Largest diff. peak/hole / e Å^{-3}	0.92/-0.55	5.88/-3.83

*Table A1.8. Crystallographic data for complexes **3.6** and **3.7***

Identification code	complex **3.6**	complex **3.7**
Empirical formula	$C_{37}H_{36}GdN_3O_9$	$C_{74}H_{62}Co_3N_4O_{18}$
Formula weight	823.94	1472.06
Temperature/K	150	150
Crystal system	monoclinic	triclinic
Space group	C2/c	P-1
a/Å	26.3795(18)	12.2599(6)
b/Å	31.348(2)	12.5508(5)
c/Å	12.5430(8)	14.3055(6)
α/°	90	84.4700(10)
β/°	114.801(2)	81.7290(10)
γ/°	90	72.7310(10)
Volume/Å^3	9415.7(11)	2076.76(16)
Z	8	1
ρ_{calc}g/cm^3	1.162	1.177
μ/mm^{-1}	1.453	0.654
F(000)	3320	759
Crystal size/mm^3	0.12 × 0.05 × 0.04	0.25 × 0.13 × 0.04
Radiation	MoKα (λ = 0.71073)	MoKα (λ = 0.71073)
2Θ range for data collection/°	5.022 to 52.892	6.142 to 52.214
Index ranges	$-33 \le h \le 31$, $-39 \le k \le 39$, $-15 \le l \le 14$	$-15 \le h \le 15$, $-15 \le k \le 15$, $-17 \le l \le 17$
Reflections collected	55731	48954
Independent reflections	9683 [R_{int} = 0.1521, R_{sigma} = 0.1264]	8230 [R_{int} = 0.0555, R_{sigma} = 0.0436]
Data/restraints/parameters	9683/48/451	8230/49/452
Goodness-of-fit on F^2	0.983	1.058
Final R indexes [I>=2σ (I)]	R_1 = 0.0610, wR_2 = 0.1300	R_1 = 0.0637, wR_2 = 0.1798
Final R indexes [all data]	R_1 = 0.1068, wR_2 = 0.1448	R_1 = 0.0837, wR_2 = 0.1920
Largest diff. peak/hole / e Å^{-3}	1.31/-1.09	1.57/-0.55

Chapter 4

*Table A1.9. Crystallographic data for cages **C4.1** and **C4.2***

Identification code	cage **C4.1**	cage **C4.2**
Empirical formula	$C_{228}H_{288}Ag_{12}F_{36}N_{24}O_{36}S_{12}$	$C_{216}H_{252}Ag_{15}B_{15}F_{60}N_{36}$
Formula weight	6303.97	6272.72
Temperature/K	150	150
Crystal system	cubic	cubic
Space group	I23	P-43n
a/Å	25.317(2)	25.1713(6)
b/Å	25.317(2)	25.1713(6)
c/Å	25.317(2)	25.1713(6)
α/°	90	90
β/°	90	90
γ/°	90	90
Volume/Å^3	16227(5)	15948.4(11)
Z	2	2
ρ_{calc}g/cm^3	1.29	1.306
μ/mm^{-1}	0.86	0.977
F(000)	6384	6240
Crystal size/mm^3	0.17 × 0.16 × 0.1	0.38 × 0.3 × 0.28
Radiation	MoKα (λ = 0.71073)	MoKα (λ = 0.71073)
2Θ range for data collection/°	4.55 to 41.668	4.578 to 52.746
Index ranges	-25 ≤ h ≤ 25, -25 ≤ k ≤ 25, -25 ≤ l ≤ 25	-31 ≤ h ≤ 31, -31 ≤ k ≤ 23, -26 ≤ l ≤ 31
Reflections collected	49242	64887
Independent reflections	2840 [R_{int} = 0.1617, R_{sigma} = 0.0481]	5468 [R_{int} = 0.0745, R_{sigma} = 0.0426]
Data/restraints/parameters	2840/235/287	5468/185/205
Goodness-of-fit on F^2	1.034	1.132
Final R indexes [I>=2σ (I)]	R_1 = 0.0558, wR_2 = 0.1436	R_1 = 0.0992, wR_2 = 0.2829
Final R indexes [all data]	R_1 = 0.0663, wR_2 = 0.1521	R_1 = 0.1702, wR_2 = 0.3694
Largest diff. peak/hole / e Å^{-3}	0.45/-0.30	0.89/-0.63
Flack parameter	0.47(2)	0.48(12)

*Table A1.10. Crystallographic data for cages **C4.2a** and **C4.3***

Identification code	cage **C4.2a**	cage **C4.3**
Empirical formula	$C_{228}H_{276}Ag_{12}B_{12}F_{48}N_{36}O_4$	$C_{135.06}H_{211.11}Ag_{11}F_{21}N_{23}O_{26}S_8$
Formula weight	5920.99	4415.08
Temperature/K	150	150
Crystal system	orthorhombic	monoclinic
Space group	$P2_12_12$	$P2_1/n$
a/Å	22.116(3)	18.6822(8)
b/Å	25.223(4)	16.8613(7)
c/Å	28.915(5)	31.1992(13)
α/°	90	90
β/°	90	100.144(2)
γ/°	90	90
Volume/Å^3	16129(4)	9674.3(7)
Z	2	2
ρ_{calc}g/cm^3	1.219	1.516
μ/mm^{-1}	0.785	1.254
F(000)	5968	4449
Crystal size/mm^3	0.19 × 0.16 × 0.08	0.2 × 0.17 × 0.17
Radiation	MoKα (λ = 0.71073)	MoKα (λ = 0.71073)
2Θ range for data collection/°	4.524 to 53.002	4.454 to 52.884
Index ranges	$-27 \leq h \leq 27$, $-31 \leq k \leq 29$, $-36 \leq l \leq 36$	$-23 \leq h \leq 23$, $-21 \leq k \leq 21$, $-39 \leq l \leq 39$
Reflections collected	216308	142702
Independent reflections	32971 [R_{int} = 0.2177, R_{sigma} = 0.1950]	19836 [R_{int} = 0.0788, R_{sigma} = 0.0610]
Data/restraints/parameters	32971/1331/1478	19836/405/1024
Goodness-of-fit on F^2	0.933	1.036
Final R indexes [I>=2σ (I)]	R_1 = 0.0762, wR_2 = 0.1573	R_1 = 0.1101, wR_2 = 0.3048
Final R indexes [all data]	R_1 = 0.1524, wR_2 = 0.1855	R_1 = 0.1547, wR_2 = 0.3397
Largest diff. peak/hole / e Å^{-3}	0.56/-0.52	1.66/-1.04
Flack parameter	0.40(4)	n/a

Chapter 5

*Table A1.11. Crystallographic data for complexes **5.1** and **5.2***

Identification code	complex **5.1**	complex **5.2**
Empirical formula	$C_{88}H_{104}N_2O_{38}Yb_6$	$C_{21}H_{20}N_2O_4Zn$
Formula weight	2835.97	429.76
Temperature/K	150	150
Crystal system	monoclinic	orthorhombic
Space group	$P2_1/n$	Pnna
a/Å	12.4079(8)	11.3429(10)
b/Å	20.8937(14)	12.4311(10)
c/Å	19.4442(12)	18.5115(14)
α/°	90	90
β/°	90.801(2)	90
γ/°	90	90
Volume/Å^3	5040.4(6)	2610.2(4)
Z	2	4
ρ_{calc}g/cm^3	1.869	1.094
μ/mm^{-1}	5.593	0.963
F(000)	2740	888
Crystal size/mm^3	0.15 × 0.14 × 0.05	0.35 × 0.31 × 0.16
Radiation	MoKα (λ = 0.71073)	MoKα (λ = 0.71073)
2Θ range for data collection/°	4.19 to 53.074	6.556 to 53
Index ranges	$-13 \le h \le 15$, $-26 \le k \le 26$, $-24 \le l \le 22$	$-12 \le h \le 14$, $-15 \le k \le 15$, $-23 \le l \le 23$
Reflections collected	50050	15765
Independent reflections	10423 [R_{int} = 0.0868, R_{sigma} = 0.0597]	2688 [R_{int} = 0.0469, R_{sigma} = 0.0297]
Data/restraints/parameters	10423/640/703	2688/81/171
Goodness-of-fit on F^2	1.019	1.054
Final R indexes [I>=2σ (I)]	R_1 = 0.0599, wR_2 = 0.1446	R_1 = 0.0501, wR_2 = 0.1293
Final R indexes [all data]	R_1 = 0.0952, wR_2 = 0.1663	R_1 = 0.0758, wR_2 = 0.1502
Largest diff. peak/hole / e Å^{-3}	3.51/-1.85	0.33/-0.36

Ligands

*Table A1.12. Crystallographic data for ligands **L3.1a** and **L4.1a***

Identification code	ligand **L3.1a**	ligand **L4.1a**
Empirical formula	$C_{15}H_{16}N_2O$	$C_{15}H_{19}NO$
Formula weight	240.3	229.31
Temperature/K	150	150
Crystal system	monoclinic	monoclinic
Space group	$P2_1/n$	$P2_1/n$
a/Å	10.4822(12)	6.1493(3)
b/Å	11.4330(14)	27.8065(12)
c/Å	10.5661(12)	7.4666(3)
α/°	90	90
β/°	93.394(4)	100.8420(10)
γ/°	90	90
Volume/Å^3	1264.1(3)	1253.93(10)
Z	4	4
ρ_{calc}g/cm^3	1.263	1.215
μ/mm^{-1}	0.08	0.075
F(000)	512	496
Crystal size/mm^3	0.23 × 0.2 × 0.11	0.33 × 0.26 × 0.19
Radiation	MoKα (λ = 0.71073)	MoKα (λ = 0.71073)
2Θ range for data collection/°	5.254 to 55.314	5.86 to 61.054
Index ranges	$-13 \leq h \leq 13$, $-14 \leq k \leq 14$, $-13 \leq l \leq 13$	$-8 \leq h \leq 8$, $-39 \leq k \leq 39$, $-10 \leq l \leq 10$
Reflections collected	13768	30058
Independent reflections	2935 [R_{int} = 0.0870, R_{sigma} = 0.0594]	3825 [R_{int} = 0.0255, R_{sigma} = 0.0150]
Data/restraints/parameters	2935/0/163	3825/0/155
Goodness-of-fit on F^2	1.014	1.063
Final R indexes [I>=2σ (I)]	R_1 = 0.0556, wR_2 = 0.1115	R_1 = 0.0469, wR_2 = 0.1205
Final R indexes [all data]	R_1 = 0.1194, wR_2 = 0.1400	R_1 = 0.0515, wR_2 = 0.1236
Largest diff. peak/hole / e Å^{-3}	0.18/-0.20	0.37/-0.24
Flack parameter	0.40(4)	n/a

Appendix 2

· Powder X-Ray Diffraction Patterns ·

Chapter 2

Complex 2.1

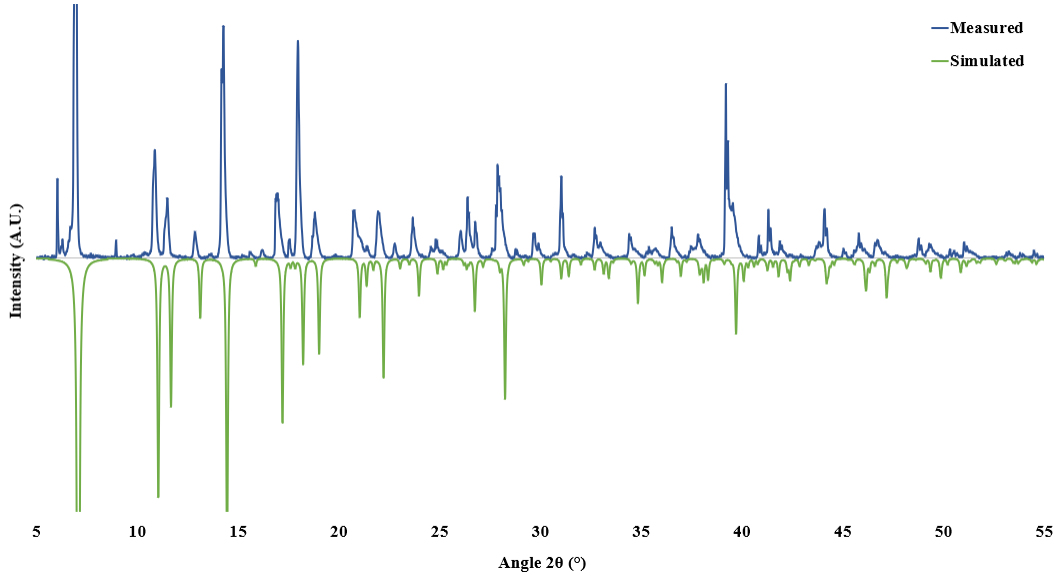

*Figure A2.1. X-ray powder diffraction pattern for complex **2.1** (blue, room temperature) compared against the simulated pattern from the single crystal dataset (green, 150 K)*

Complex 2.3

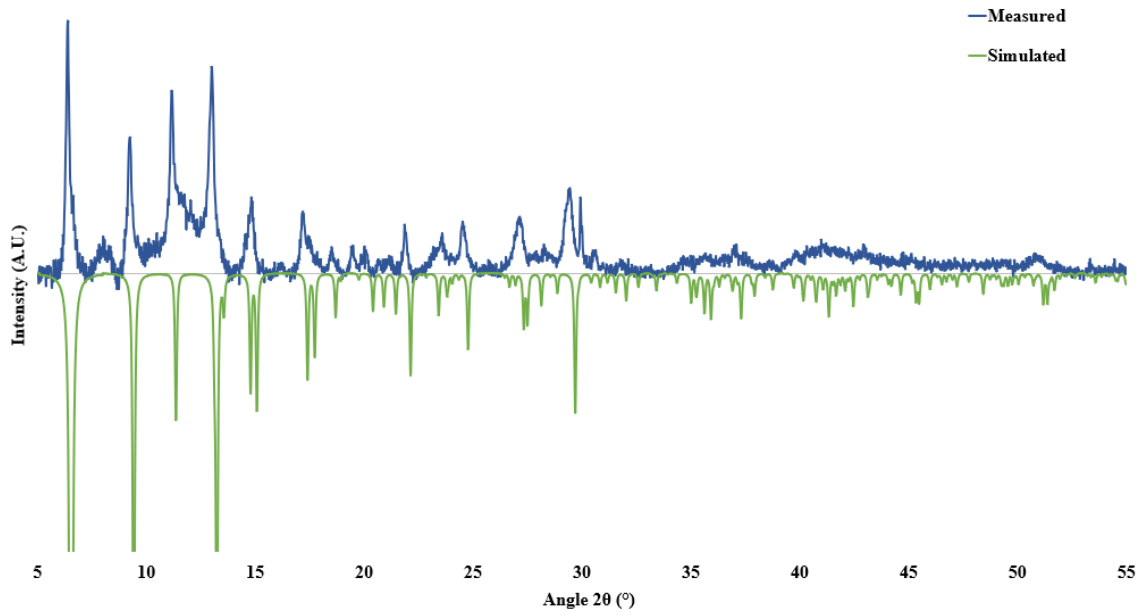

*Figure A2.2. X-ray powder diffraction pattern for complex **2.3** (blue, room temperature) compared against the simulated pattern from the single crystal dataset (green, 150 K)*

Complex 2.4

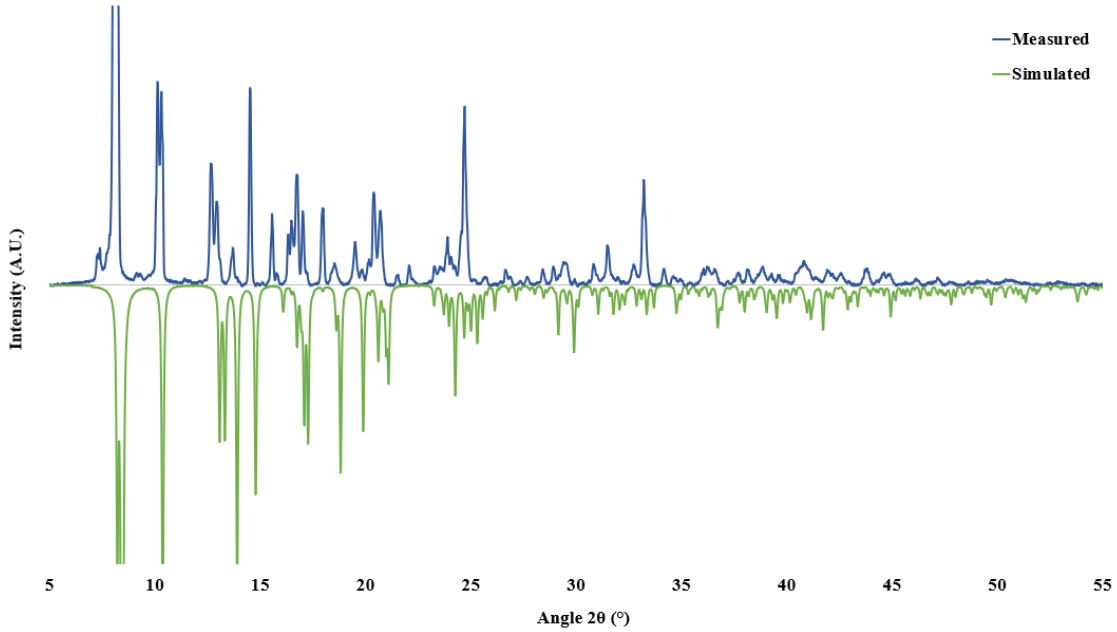

*Figure A2.3. X-ray powder diffraction pattern for complex **2.4** (blue, room temperature) compared against the simulated pattern from the single crystal dataset (green, 150 K)*

Complex 2.5

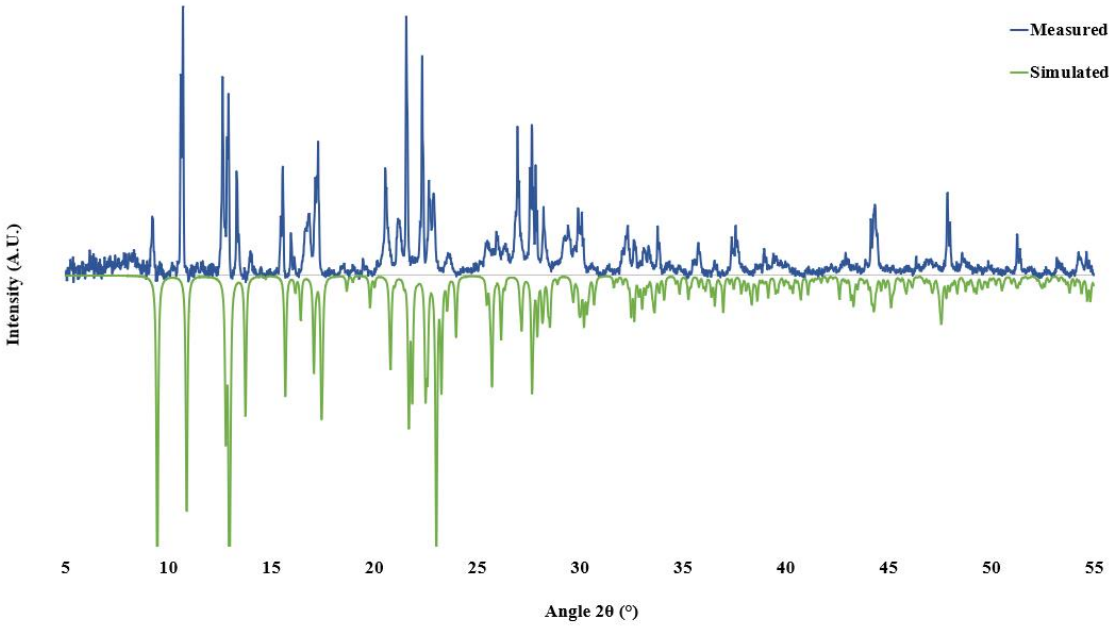

*Figure A2.4. X-ray powder diffraction pattern for complex **2.5** (blue, room temperature) compared against the simulated pattern from the single crystal dataset (green, 150 K)*

Complex 2.6

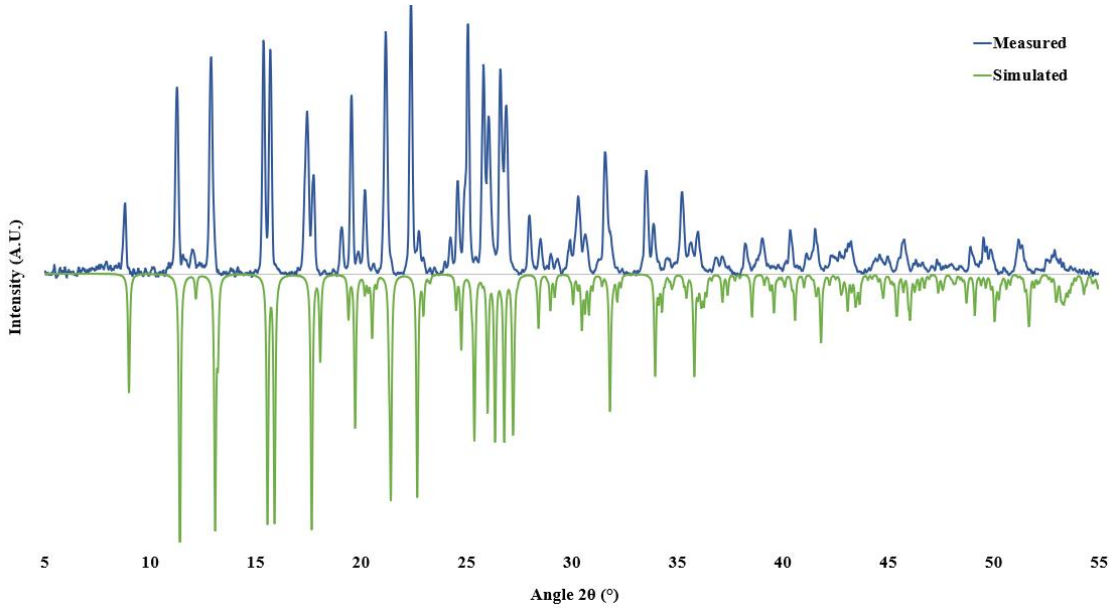

*Figure A2.5. X-ray powder diffraction pattern for complex **2.6** (blue, room temperature) compared against the simulated pattern from the single crystal dataset (green, 150 K)*

Complex 2.7

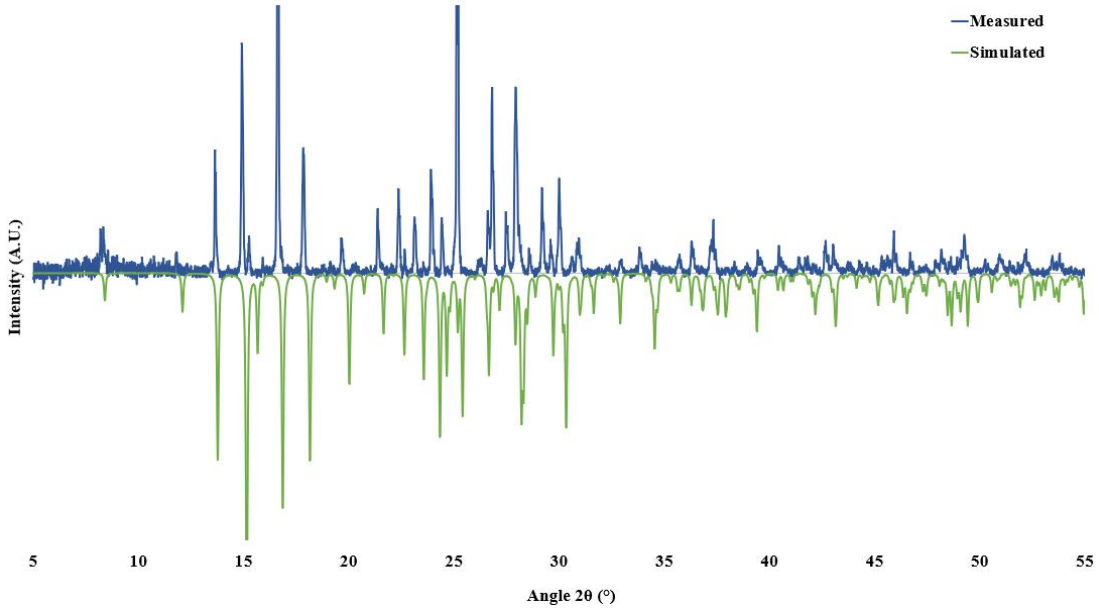

*Figure A2.6. X-ray powder diffraction pattern for complex **2.7** (blue, room temperature) compared against the simulated pattern from the single crystal dataset (green, 150 K)*

Complex 2.8

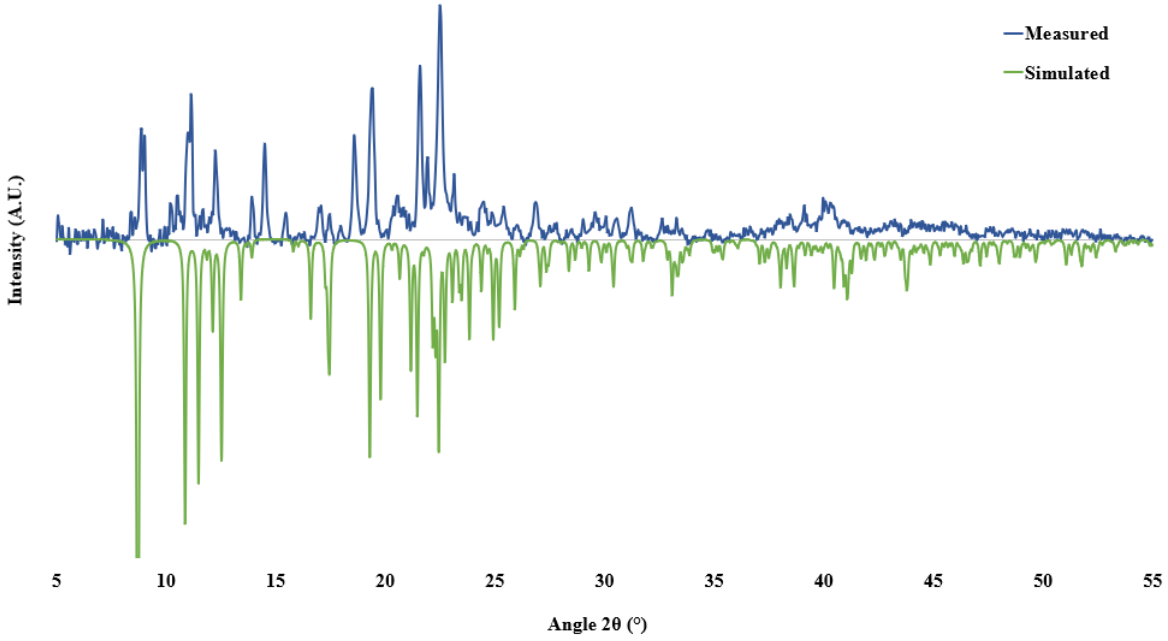

*Figure A2.7. X-ray powder diffraction pattern for complex **2.8** (blue, room temperature) compared against the simulated pattern from the single crystal dataset (green, 150 K)*

Complex 2.9/2.9a

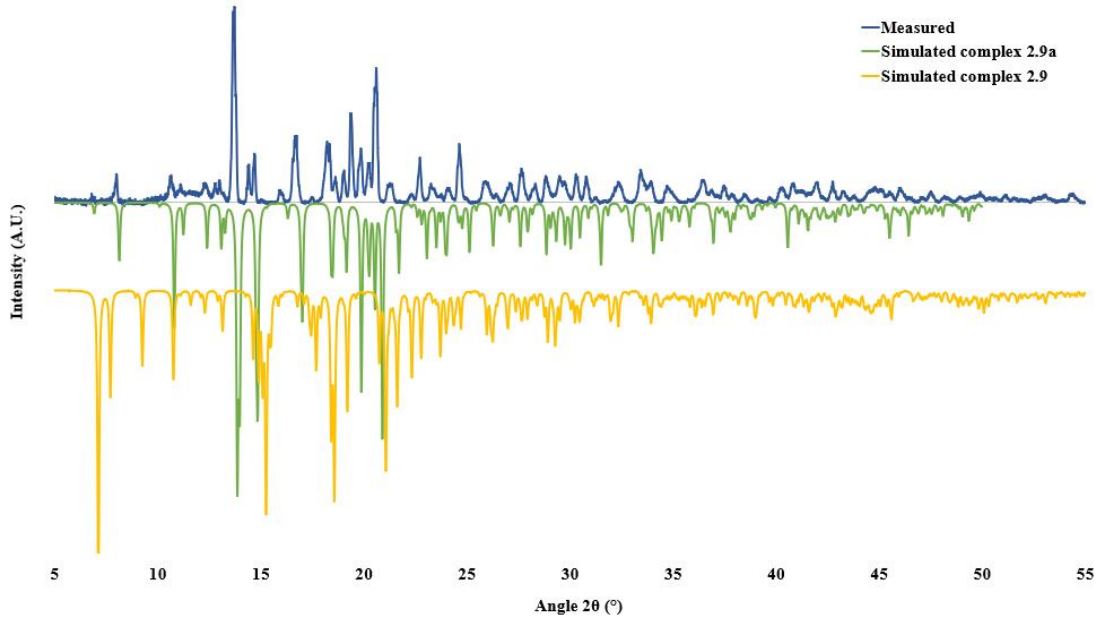

*Figure A2.8. X-ray powder diffraction pattern for complex **2.9/2.9a** (blue, room temperature) compared against the simulated patterns from the single crystal dataset for complex **2.9** (yellow) and **2.9a** (green) at 150 K, confirming that the solid is predominantly complex **2.9a** with only trace quantities of complex **2.9***

Complex 2.10

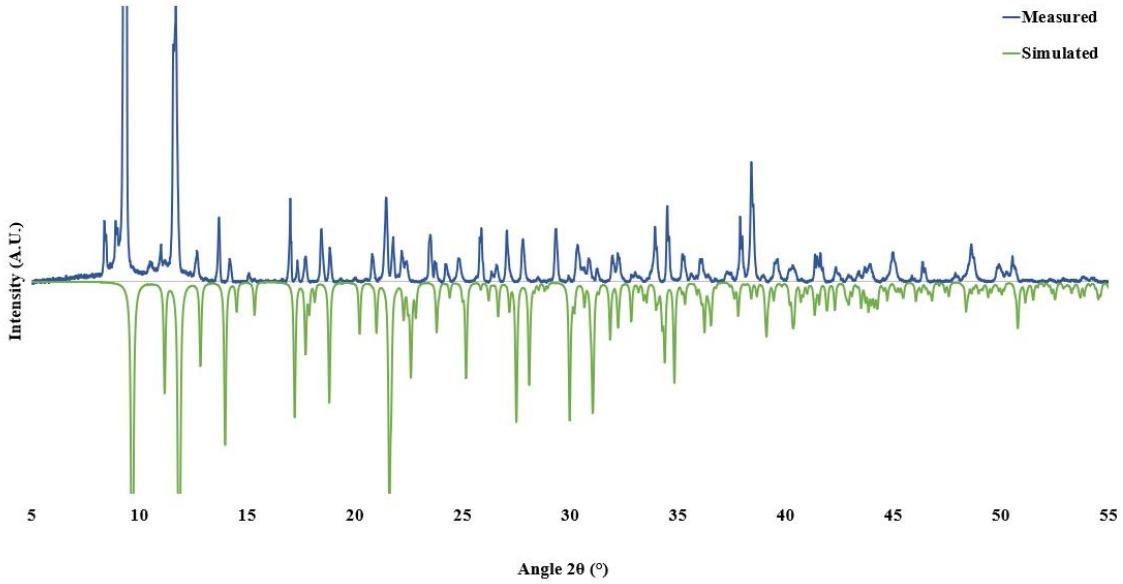

*Figure A2.9. X-ray powder diffraction pattern for complex **2.10** (blue, room temperature) compared against the simulated pattern from the single crystal dataset (green, 150 K)*

Chapter 3

Complex 3.1

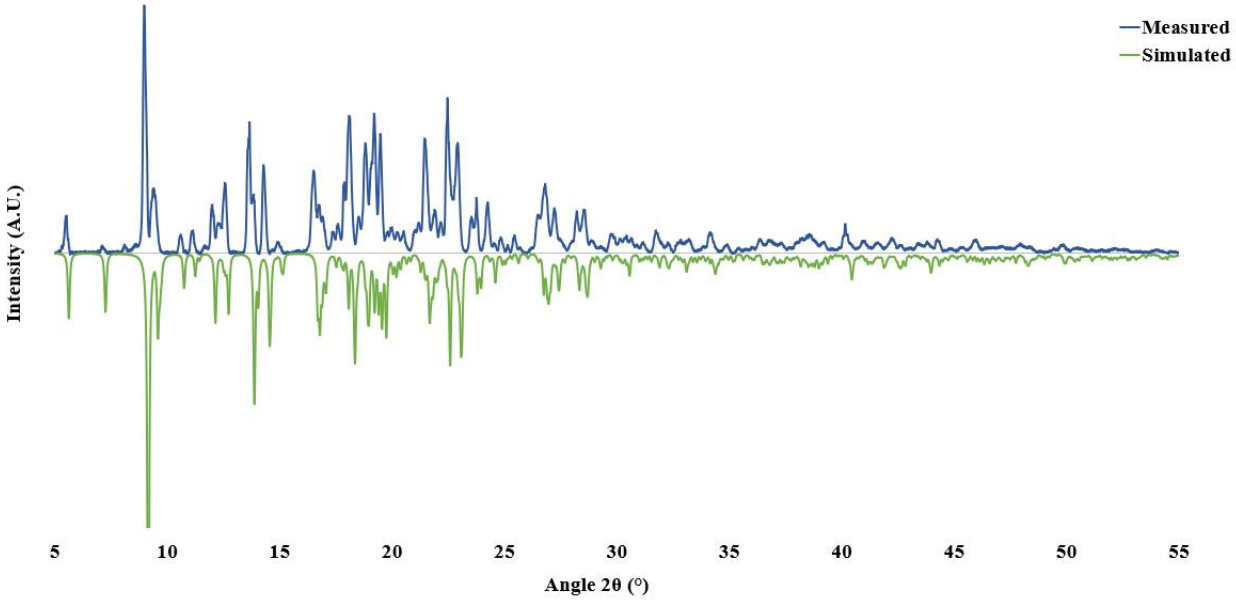

*Figure A2.10. X-ray powder diffraction pattern for complex **3.1** (blue, room temperature) compared against the simulated pattern from the single crystal dataset (green, 150 K)*

Complex 3.2

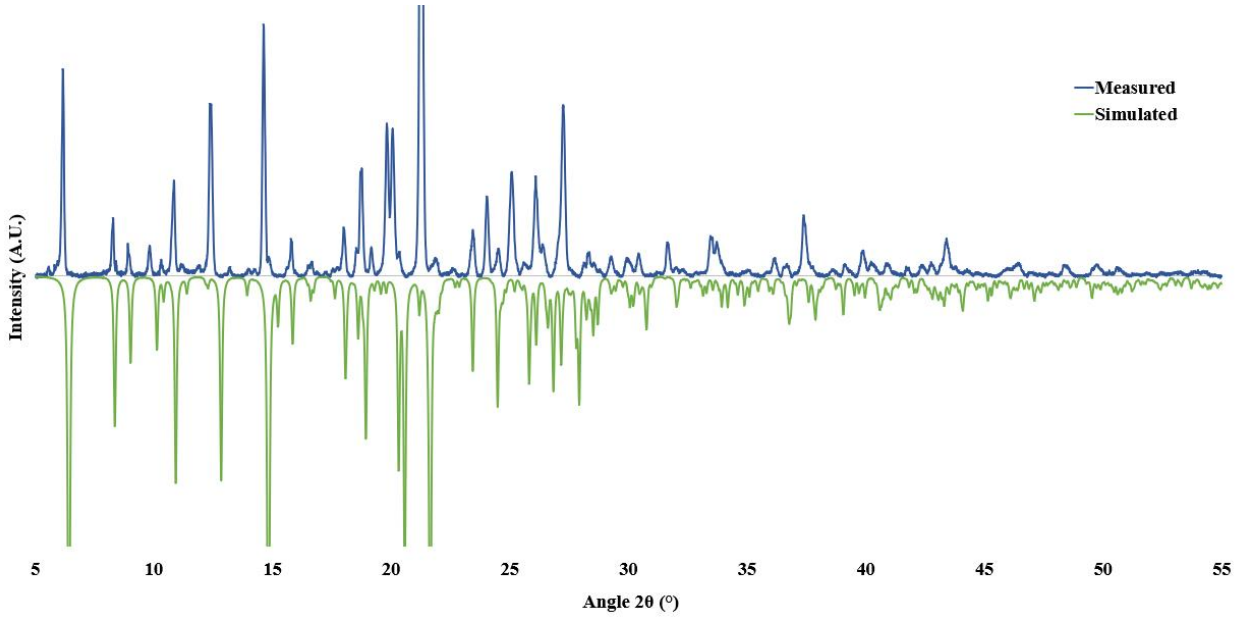

*Figure A2.11. X-ray powder diffraction pattern for complex **3.2** (blue, room temperature) compared against the simulated pattern from the single crystal dataset (green, 150 K)*

Complex 3.3

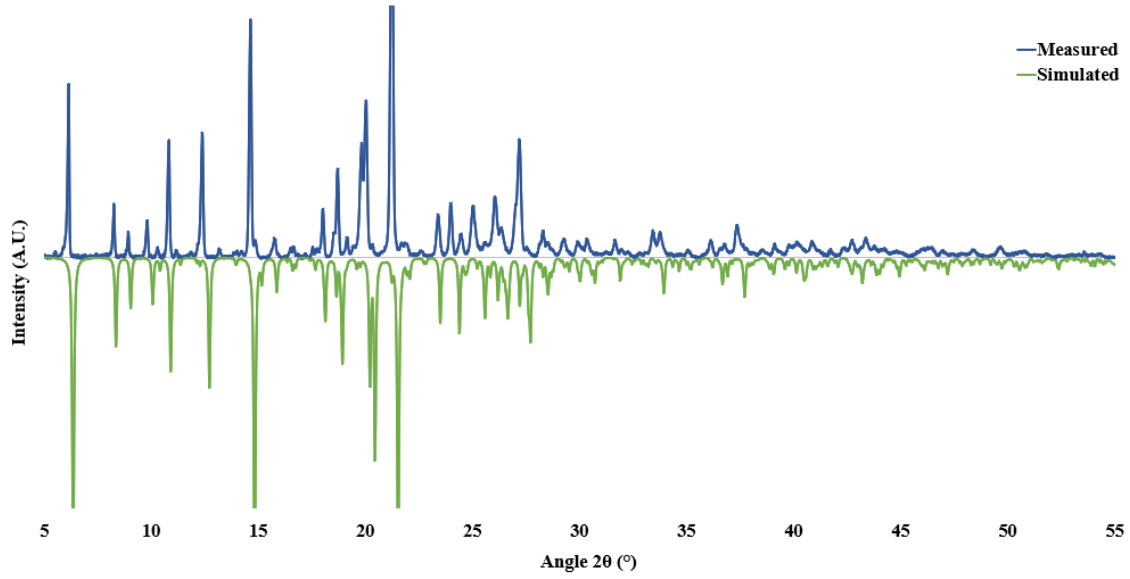

*Figure A2.12. X-ray powder diffraction pattern for complex **3.3** (blue, room temperature) compared against the simulated pattern from the single crystal dataset (green, 150 K)*

Complex 3.4

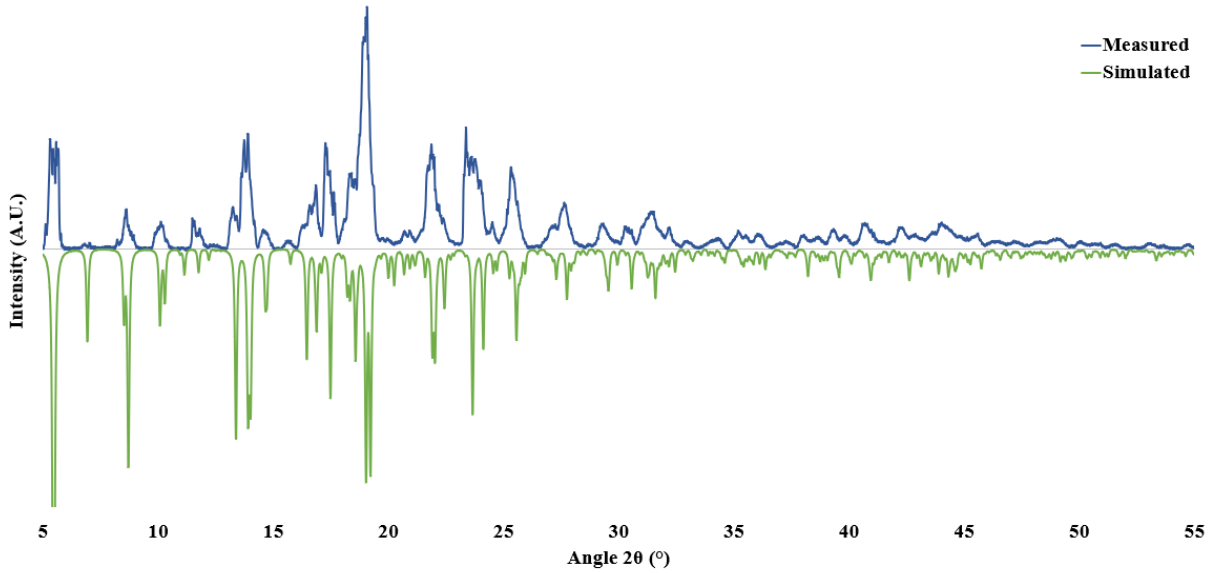

*Figure A2.13. X-ray powder diffraction pattern for complex **3.4** (blue, room temperature) compared against the simulated pattern from the single crystal dataset (green, 150 K)*

Complex 3.5

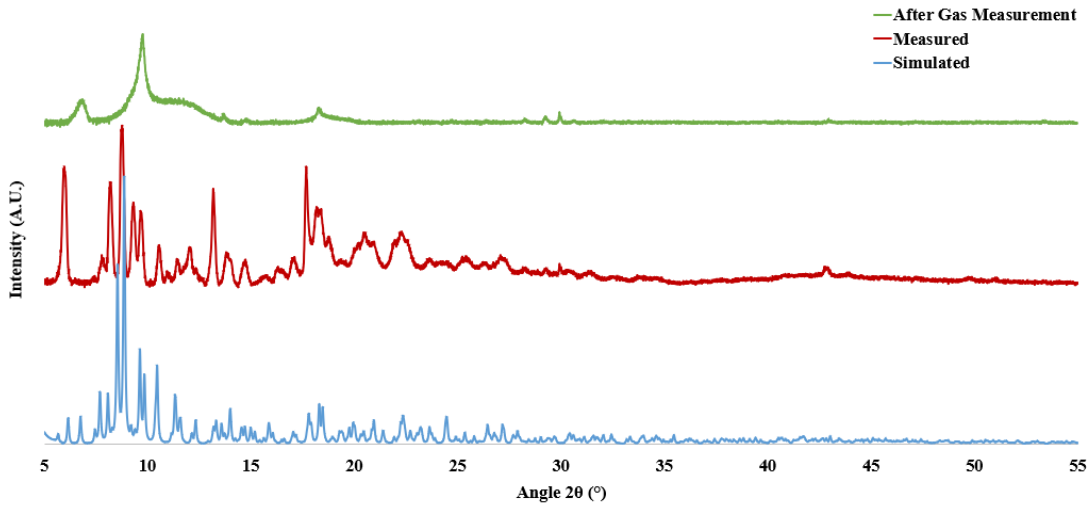

*Figure A2.14. X-ray powder diffraction data for complex **3.5** showing pattern simulated from single crystal data at 150K (blue), measured as synthesised (red, room temperature) and measured after gas adsorption measurements (green, room temperature)*

Complex 3.7

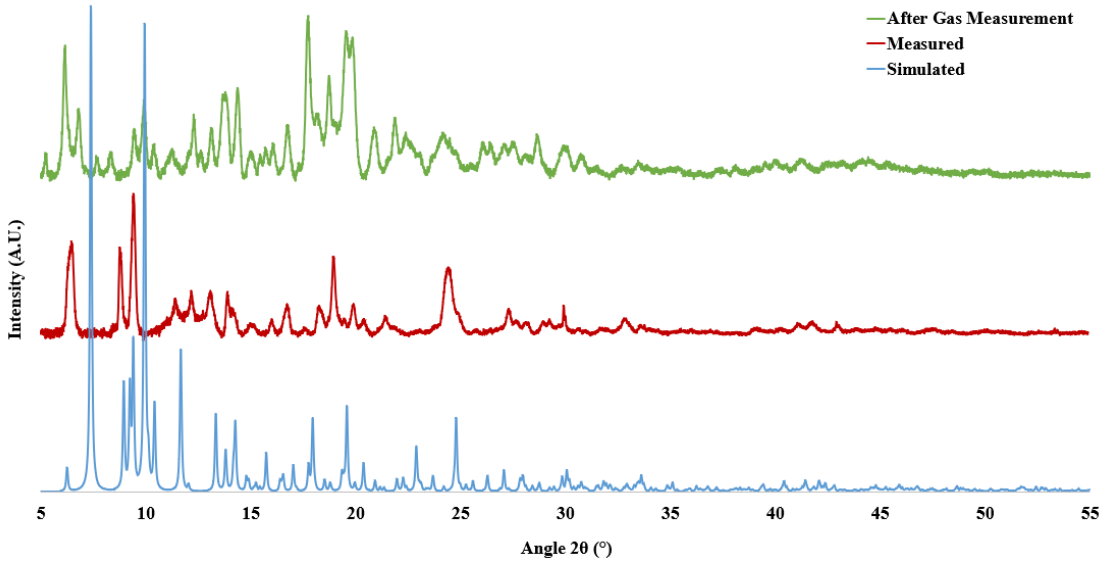

*Figure A2.15. X-ray powder diffraction data for complex **3.7** showing pattern simulated from single crystal data at 150K (blue), measured as synthesised (red, room temperature) and measured after gas adsorption measurements (green, room temperature)*

Chapter 4

*Cage **C4.1***

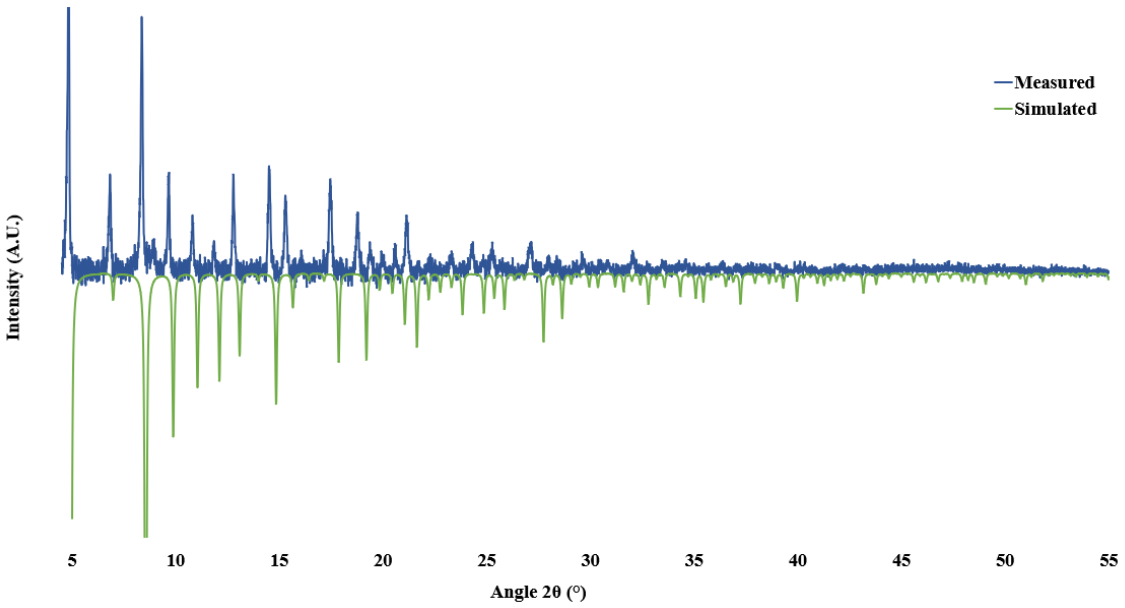

*Figure A2.16. X-ray powder diffraction pattern for cage **C4.1** (blue, room temperature, capillary) compared against the simulated pattern from the single crystal dataset (green, 150 K)*

*Cage **C4.2***

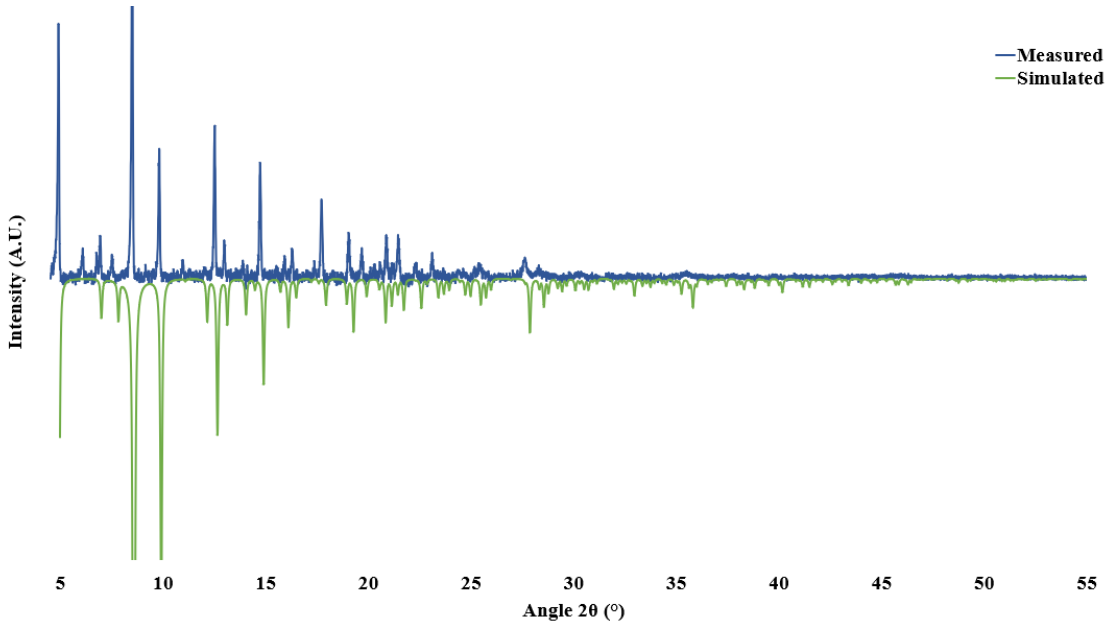

*Figure A2.17. X-ray powder diffraction pattern for cage **C4.2** (blue, room temperature, capillary) compared against the simulated pattern from the single crystal dataset (green, 150 K)*

Cage C4.2a

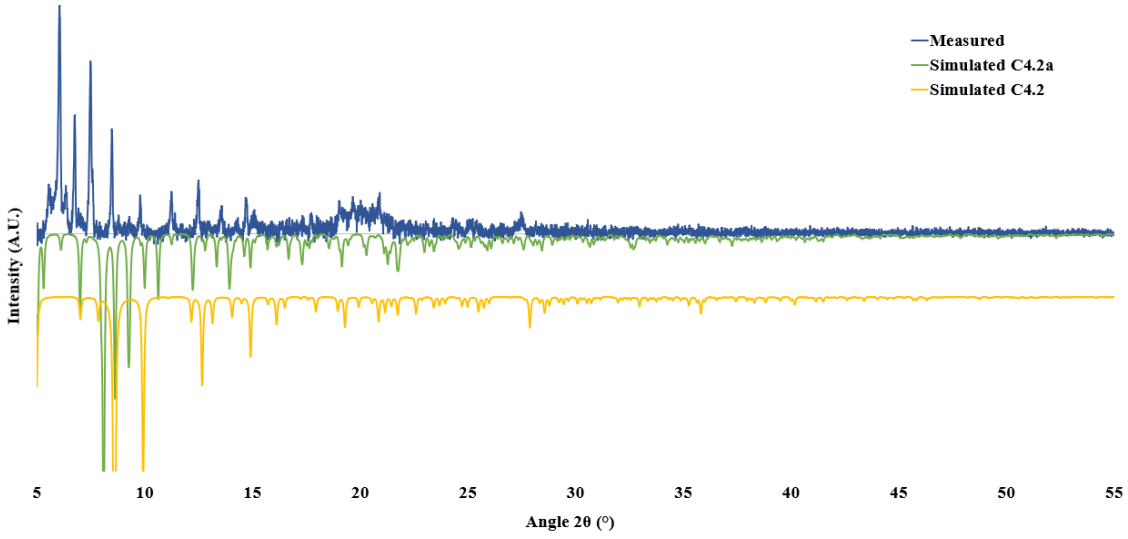

*Figure A2.18. X-ray powder diffraction pattern for cage **C4.2a** (blue, room temperature, capillary) compared against the simulated pattern from the single crystal dataset for cage **C4.2a** (green, 150 K) and **C4.2** (yellow, 150 K)*

Cage C4.3

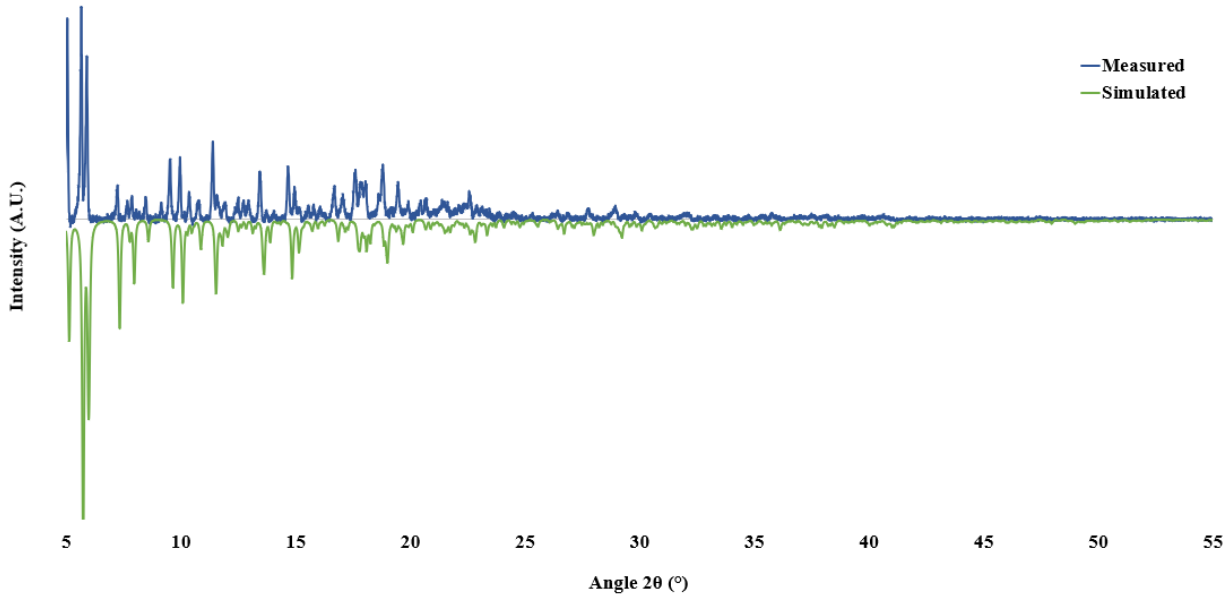

*Figure A2.19. X-ray powder diffraction pattern for cage **C4.3** (blue, room temperature, capillary) compared against the simulated pattern from the single crystal dataset (green, 150 K)*

Chapter 5

Complex 5.1

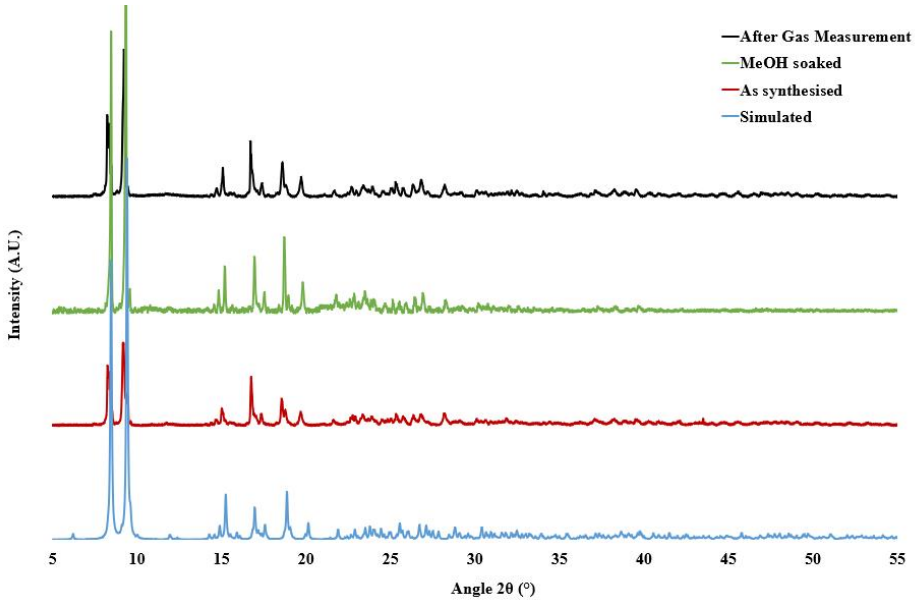

*Figure A2.20. X-ray powder diffraction data for complex **5.1** showing pattern simulated from single crystal data at 150K (blue), measured as synthesised (red, room temperature), measured after soaking in methanol (green, room temperature, capillary) and measured after gas adsorption measurements (green, room temperature)*

Complex 5.2

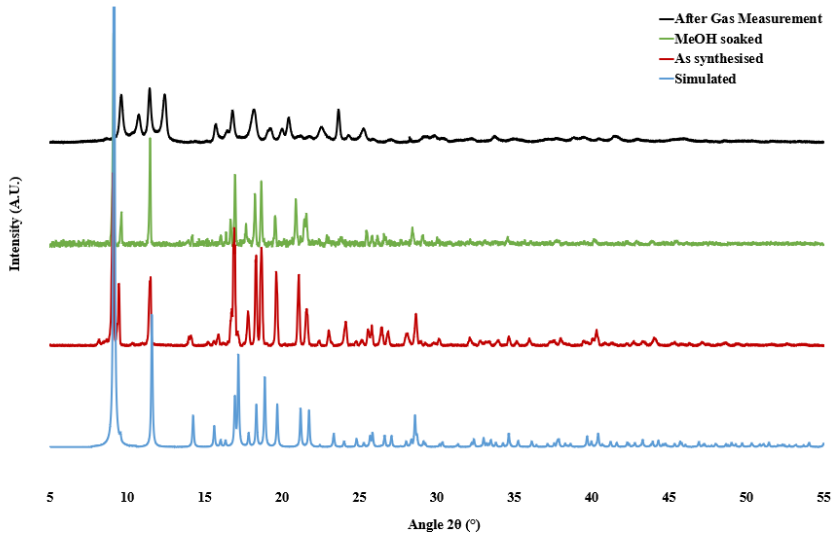

*Figure A2.21. X-ray powder diffraction data for complex **5.2** showing pattern simulated from single crystal data at 150K (blue), measured as synthesised (red, room temperature), measured after soaking in methanol (green, room temperature, capillary) and measured after gas adsorption measurements (green, room temperature)*

Appendix 3

· Thermogravimetric Analysis ·

Chapter 2

Complex 2.3

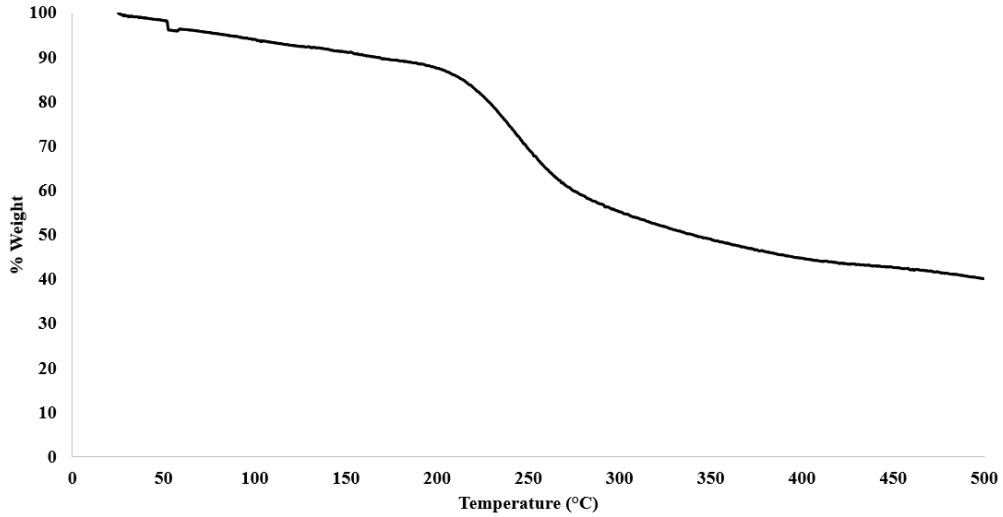

*Figure A3.1. TGA profile of complex **2.3***

Chapter 3

Complex 3.5

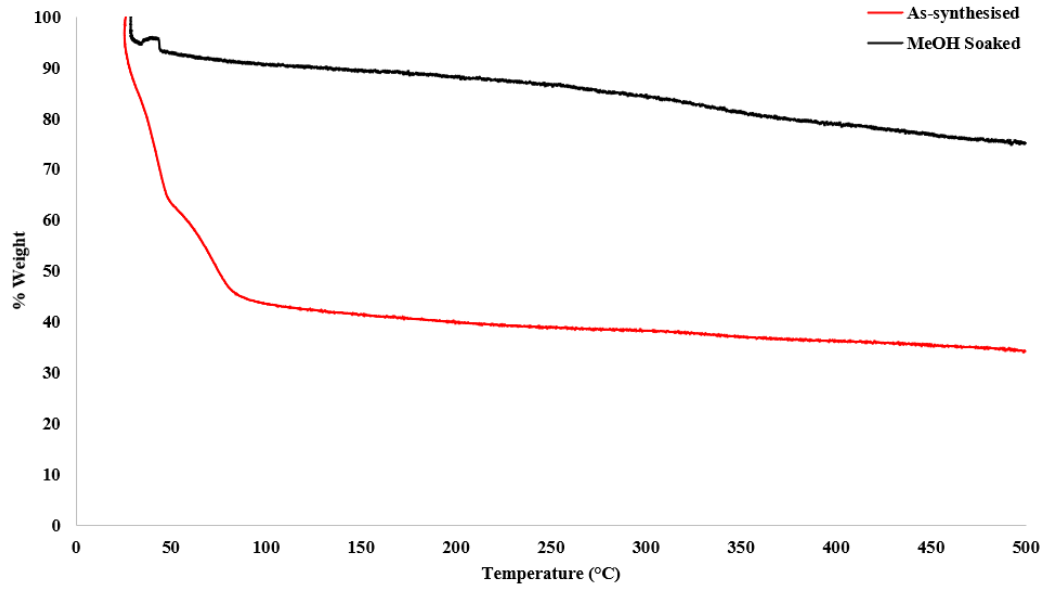

*Figure A3.2. TGA profile of as-synthesised complex **3.5** (red) and post soaking in MeOH (black)*

Complex 3.7

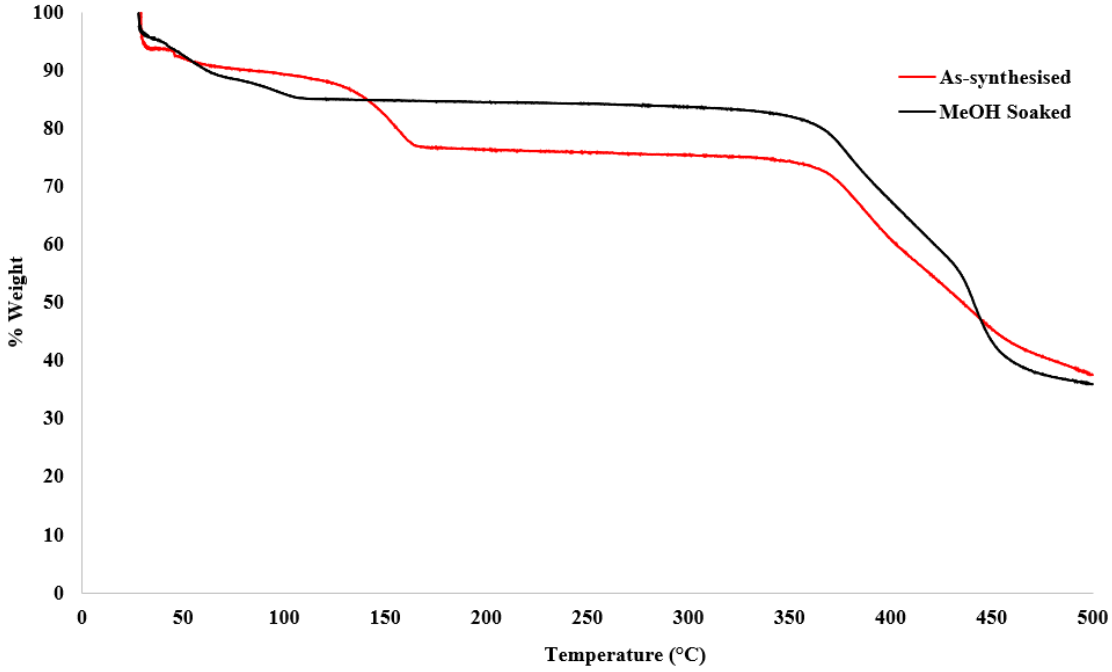

*Figure A3.3. TGA profile of as-synthesised complex **3.7** (red) and post soaking in MeOH (black)*

Chapter 5

Complex 5.1

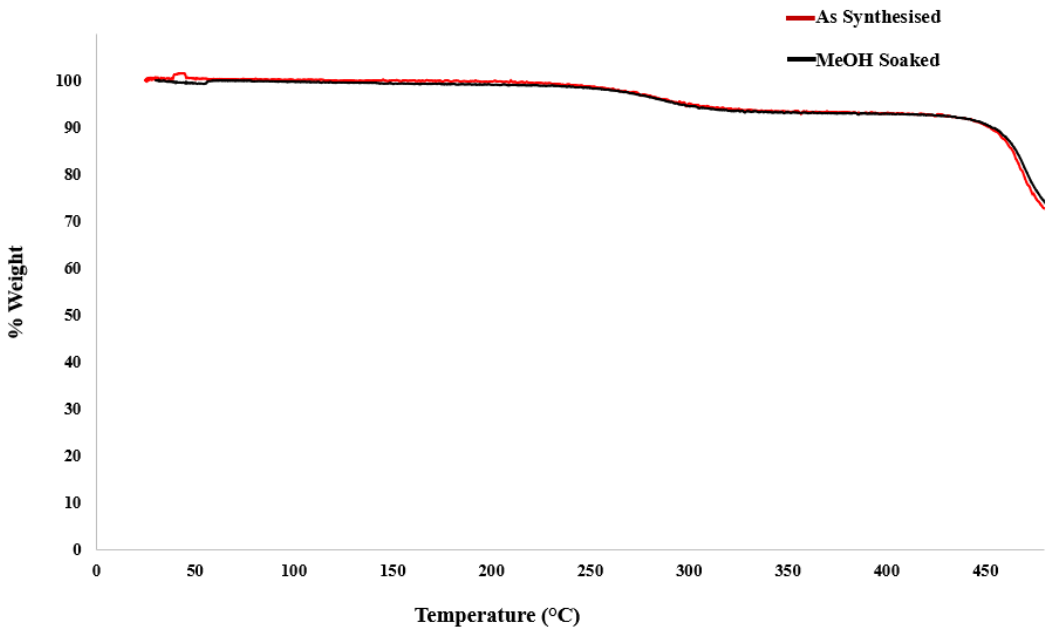

*Figure A3.4. TGA profile of as-synthesised complex **5.1** (red) and post soaking in MeOH (black)*

Complex 5.2

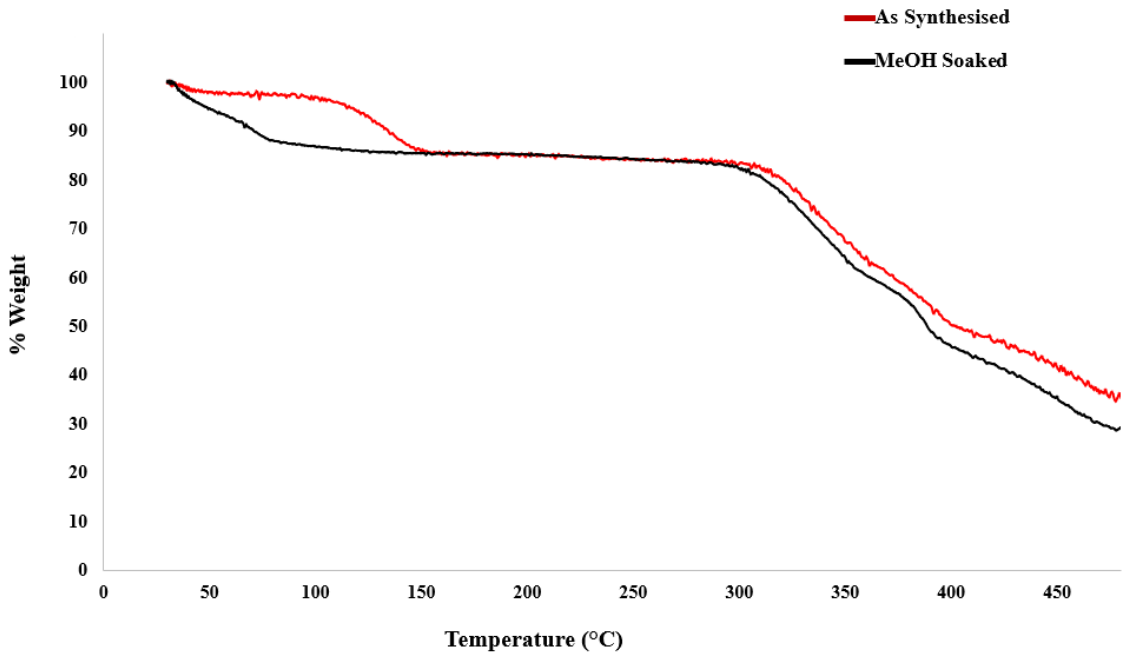

*Figure A3.5. TGA profile of as-synthesised complex **5.2** (red) and post soaking in MeOH (black)*

Appendix 4

· Additional Figures & Data ·

A4.1 Proof

Proof A4.1. Concentration of [ML] in an [M]=[L] system at low concentrations

The relative concentrations of a complex to its individual components becomes easier to understand if a 2,2′-bipyridine ligand (L) is used as an example in a simple 1:1 M:L coordination complex, ML. The association or binding constant, K, is defined by the following equation (Equation A4.1):

Equation A4.1

$$K = \frac{[ML]}{[M][L]}$$

Taking the special case where [M] = [L] to simplify the calculation, the denominator can be simplified to $[M]^2$. Typical NMR concentrations are to the order of 10^{-3} M, which can be substituted for the [ML] value in the equation, as this is the concentration of the complex in the NMR tube. 2,2′-bipyridine has a binding constant, K, range of *ca.* 10^3 to 10^5 M^{-1}.[1] Taking the median value, 10^4 M^{-1}, the [M] is calculated to be $10^{-3.5}$ M. Therefore, at NMR concentrations, given a ligand binding constant of *ca.* 10^4, there are roughly equal quantities of metal/ligand and complex in solution when [M] = [L]. With smaller binding constants (such as in silver(I) complexes), or more complex systems involving multiple binding constants (for multiple coordination bonds) this ratio will lean further towards the concentration of the individual components. The same can be said for lower concentrations. Typical concentrations for mass spectrometry measurements are in the order of 10^{-7} M. If again, the special case of [M] = [L] is taken, [ML] can be equated to 10^{-7} M. Taking 10^4 M^{-1} as the binding constant, K, the concentration of [M] (and therefore, [L]) is calculated to be *ca*. 3×10^{-6} M, which is significantly larger than the concentration of the complex, [ML]. This is further exacerbated by kinetically labile systems and those involving the formation of multiple coordination bonds, which will drive the system further towards the concentration of the individual components.

A4.2 Additional Figures

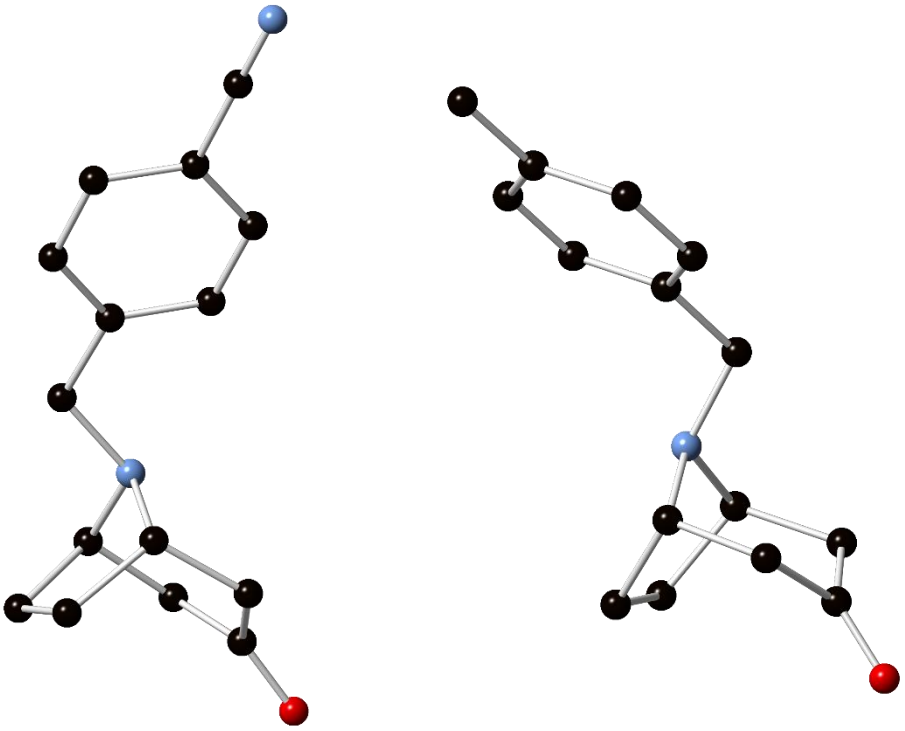

*Figure A4.1. Structures of **L3.1a** (left) and **L4.1a** (right)*

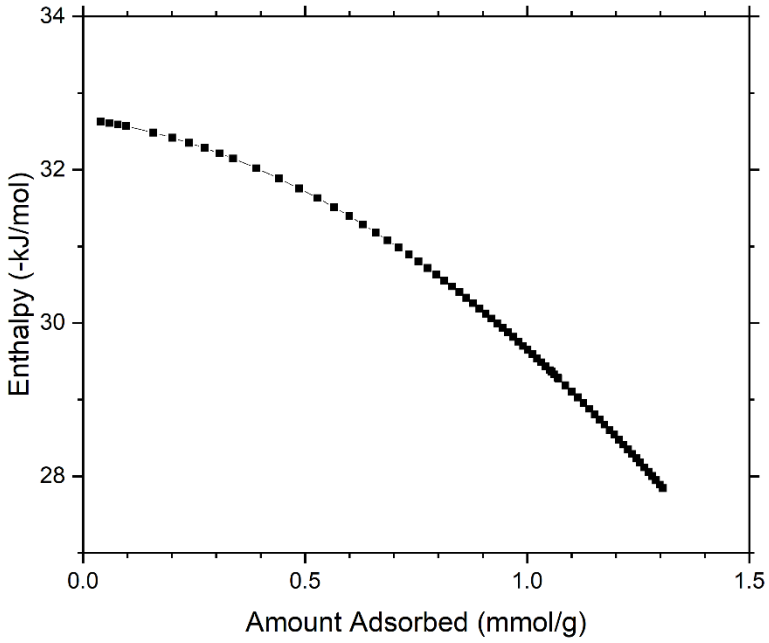

*Figure A4.2. Estimated CO_2 adsorption enthalpy as a function of gas loading for complex **3.6***

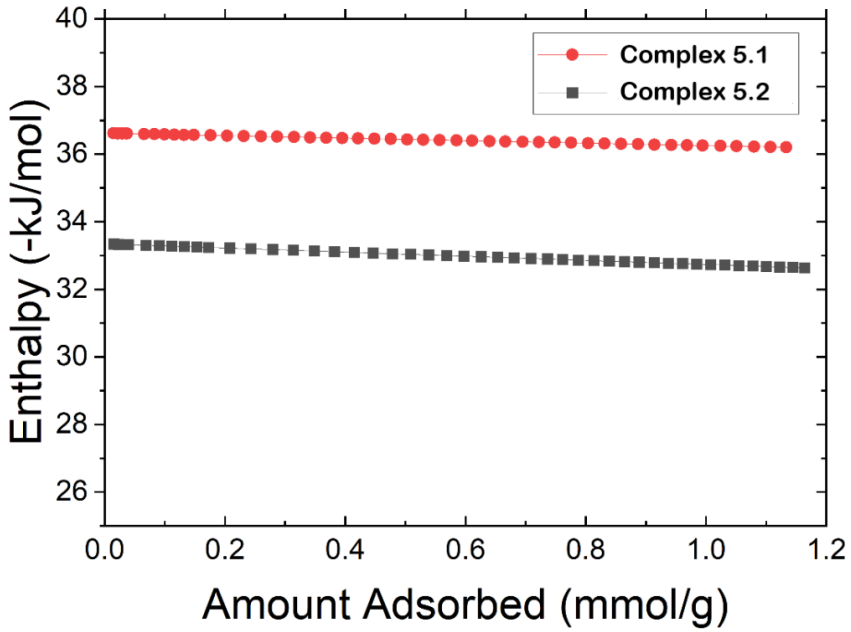

*Figure A4.2. Estimated CO_2 adsorption enthalpy as a function of gas loading for complexes **5.1** (red) and **5.2** (black)*

A4.3 List of Publications

1. Supramolecular structural influences from remote functionality in coordination complexes of 4-picolylamine ligands, **V. D. Slyusarchuk**, B. O'Brien, and C. S. Hawes, *J. Coord. Chem.*, **2022**, *75*, 2039 – 2061, DOI: 10.1080/00958972.2022.2130059.

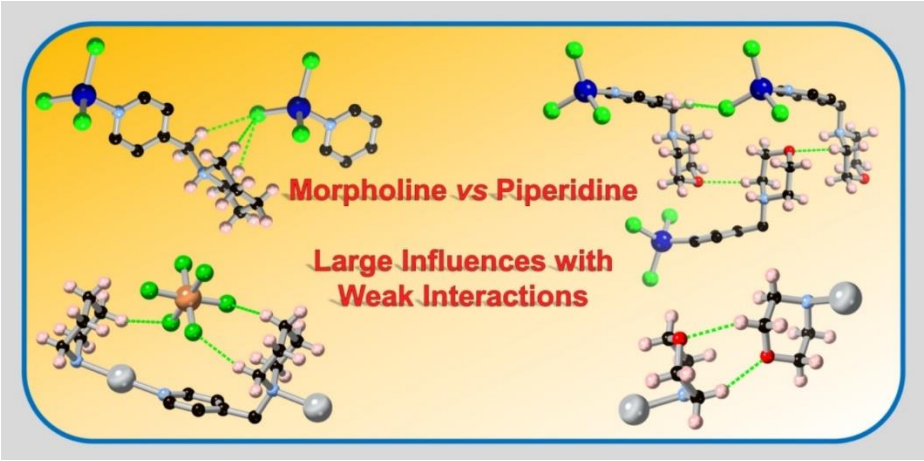

The work in this publication comprises the research presented in Chapter 2 of this thesis.

2. Fecht's acid revisited: a spirocyclic dicarboxylate for non-aromatic MOFs, **V. D. Slyusarchuk**, and C. S. Hawes, *CrystEngComm*, **2022**, *24*, 484 – 490, DOI: 10.1039/D1CE01542G.

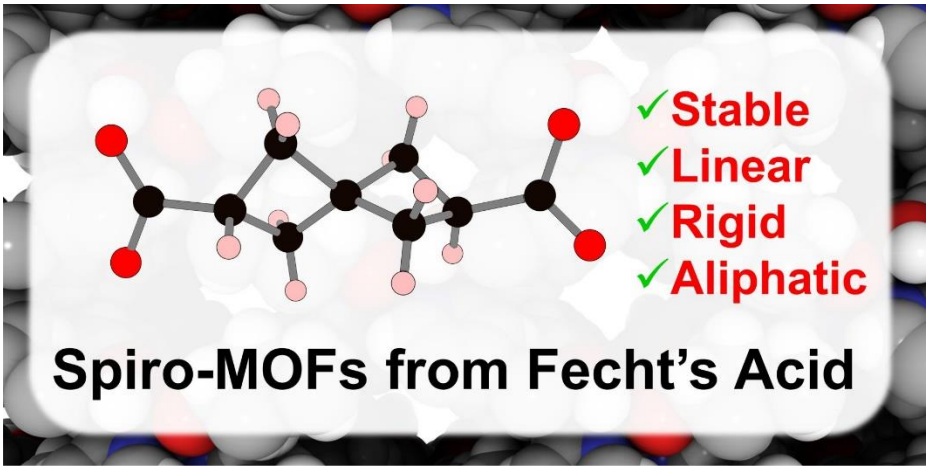

The work in this publication comprises the research presented in Chapter 5 of this thesis.

3. Cyclic Aliphatic Hydrocarbons as Linkers in Metal-Organic Frameworks: New Frontiers for Ligand Design, **V. D. Slyusarchuk** , P. E. Kruger, and C. S. Hawes, *ChemPlusChem*, **2020**, *85*, 845-854, DOI: 10.1002/cplu.202000206.

A4.4 References

1. R. Dobrawa and F. Würthner, *J. Polym. Sci., Part A: Polym. Chem.*, 2005, **43**, 4981–4995.